Solid-State Nanopores: Fabrication, Application, and Analysis

Kyle Briggs

Thesis submitted in partial fulfillment of the requirements for the Doctorate in Philosophy degree in Physics

Ottawa-Carleton Institute of Physics
Department of Physics
Faculty of Science
University of Ottawa
Ottawa, Canada

Contents

Summary

The work presented in this thesis is divided loosely into three main areas of interest: development of a novel method of solid-state nanopore fabrication; applications of this method to some of the open problems in the field; and analysis of nanopore data.

The first of these occupies the majority of the research presented in this thesis, covering research dedicated to the development and characterization of a novel method of solid-state nanopore fabrication which achieves nanometer scale control over matter using simple and low cost circuitry. Termed controlled breakdown (CBD), this technique is in the process of revolutionizing the field of nanopore research, and in the few short years I have been part of its development it has seen adoption in nanopore labs across the globe, both academic and industrial.

Due to the simple nature of CBD, this technique also enables novel applications of nanopores in device architectures that were inaccessible to the expensive and inflexible methods used previously. The second part of this thesis takes advantage of the unique opportunities presented by CBD to develop a device architecture comprising two nanopores in series. This nanodevice tackles one of the main problems standing between nanopores and the promise of cheap genomic analysis: control of the motion and conformation of the polymer both prior to and during translocation through the pore.

Finally, because the field of nanopore research is still relatively young, very few tools are available which provide high-quality analysis of nanopore data. The last part of this thesis is dedicated to a thorough discussion of the complexities involved in analysing nanopore signals, as well as the development of several tools which directly address this knowledge gap.

Sommaire

Le travail présenté dans cette thèse se divise principalement en trois champs d'intérêt: le développement d'une nouvelle méthode de fabrication de nanopore à l'état solide; l'application de cette méthode à certains problèmes ouverts du domaine; et l'analyse de données de nanopore.

La majorité de la recherche présentée dans cet ouvrage est consacrée au premier de ces trois points. Elle décrit le développement et la caractérisation d'une nouvelle méthode de fabrication de nanopore à l'état solide atteignant un contrôle nanométrique de la matière en ne nécessitant qu'un simple circuit peu coûteux. Dénommée claquage diéléctrique controllé (Controlled breakdown - CBD), cette technique révolutionne présentement le domaine de recherche des nanopores à l'échelle internationale, aux niveaux académique et industriel.

Dû à sa simplicité, le CBD rend possible de nouvelles applications dans des architectures d'appareils qui auparavant étaient inaccessibles pour les autres méthodes de fabrication coûteuses et peu flexibles. La deuxième partie de cette thèse exploite l'opportunité unique que présente le CBD en développant une architecture d'appareil contenant deux nanopores en série. Ce nanodispositif aborde un des problèmes majeurs qui fait obstacle à l'analyse génomique bon marché: le contrôle du mouvement et de la conformation des polymères lors de leur passage à travers le pore.

Finalement, puisque le domaine de recherche des nanopores est relativement jeune, la disponibilité d'outils capables de produire une analyse de haute qualité des données de nanopore se fait très rare. La dernière partie de cette thèse est dédiée à une discussion approfondie des complexités présentes lors de l'analyse de signaux de nanopore et au développement de plusieurs outils adressant cette lacune dans nos connaissances.

Acknowledgements

This thesis was a collaborative work from start to finish. Thank you in particular to my colleagues in the Tabard-Cossa lab, the University of Rochester, NIST, and the University of Ontario Institute of Technology. Collaborating with each of you brought a unique and complementary set of skills to bear on the problems we solved together, and I have learned from all of you.

Thank you to Vincent for the numerous opportunities you have given me over my years as your student. Your support, both in the lab and outside of it, have been invaluable, and it has been a privilege and a pleasure to be your student through my graduate work.

Thank you to Lora, Eddie, Nicolas, and Konstantin for your mentorship during my first experiences of research as an undergraduate student. The skills I developed with your guidance have served me well, and my time working with you laid the foundation for the success that followed.

Getting to the end of this chapter in my life has been a long process, made much more difficult by my injury part way through. To my colleagues in the lab who helped pick up the slack without complaint when my back interfered with my basic functioning, and to everyone who went out of their way to help me outside the lab as well, particularly Matt and Eric, I can't thank you all enough. When I say this would not have been possible without all of you, I mean it quite literally.

Finally and most importantly to Lindsay: your unwavering support through some of the most personally challenging years of my life was at times the only thing that enabled to me progress at all. A few words of acknowledgement are hopelessly inadequate to express this sentiment properly, but thank you from the bottom of my heart for the time we spent together.

Statement of Originality

The work presented in this thesis resulted directly from my work as a Ph.D. student, and contains a mixture of adaptations of peer-reviewed papers, book chapters, and software manuals to which I have made significant contributions during my work at the University of Ottawa. With the exception of Chapter 7, I am the first author or co-first author on all of the sections in this thesis. In several places changes have been made to already published works. Unless otherwise noted in this section, these changes represent only cosmetic alterations to formatting for consistency with the rest of work, and corrections to references when errors were found.

Chapter 2 is a draft version of a book chapter which is due to be published as part of a nanopore textbook in the near future. It will likely undergo further editing before the final version is published, but it serves in this thesis as a thorough introduction to nanopore fabrication techniques in general, and places the rest of the thesis in context. I wrote the first draft, which was then edited by Vincent Tabard-Cossa. Written permission has been obtained from the publisher for all images used in this chapter.

Chapter 3 represents my first independent project as a graduate student. I performed and analysed all of the experiments and wrote the first draft of the paper.

Chapter 4 represents my first project leading other team members. Myself, and two undergraduate summer students under my mentorship, Sanmeet Chahal and Timothea Le, generated most the data, which I analysed and compiled into the first draft of the paper. The data concerning DNA translocations in ethanol-based salts were collected by Martin Charron.

Chapter 5 was a direct collaboration between myself and Dr. Autumn Carlsen, a

postdoctoral fellow in the research group. Between us, we evenly split the workload of performing the experiments and analysing the data, and Autumn wrote the first draft of the paper. The version presented in this thesis is changed slightly from the online version, due to the need to coherently incorporate the supplementary information section into the main text. This has been done without significantly changing the message of the paper, though in some cases text has been added or deleted or figures omitted where redundancies existed between the main text and the supplementary information, or where a segue was necessary to transition smoothly between the two documents.

Chapter 6 is a collaborative project undertaken between three distinct research groups, including a materials science laboratory from the University of Rochester NY, (USA) and a simulation group from University of Ontario Institute of Technology, supported by Simpore Inc, a membrane manufacturing company based in Rochester. My role was to perform and analyse all of the nanopore experiments, as well as to assemble the devices to be studied after assembly protocols had been worked out between myself and Gregory Madejski, a graduate student at the University of Rochester. Interpretation of the results was largely collaborative between myself and the simulation group of Prof. Hendrick W. de Haan, and I wrote several versions of major drafts for the paper. Like the previous chapter, the need to incorporate the supplementary information into the main text in a coherent manner necessitated changes to the text and figures both for the sake of flow and to remove redundancies, though this has been done in such a way as to preserve the message of the paper.

Chapter 7 represents a collaboration with the National Institute of Standards and Technology (NIST, Gaithersburg, Maryland) that came about as a result of my independent work developing analysis tools for nanopore data. My contribution to this work is primarily the implementation and testing of the CUSUM+ algorithm

within the framework of MOSAIC, an open-source nanopore analysis software suite, as well as writing sections 7.3.1, 7.4.1, and 7.6.1. As with the previous two chapters, the supplementary information has been worked into the main text, while preserving the message of the paper.

Finally, Chapter 8 is a user manual for most of the nanopore analysis software I have written during my Ph.D., which details the theory, implementation, and application of a comprehensive suite of nanopore analysis tools which I wrote from scratch during my graduate work and have released as open source software.

Summary of Contributions

Publications

[1] H. Kwok*, K. **Briggs***, and V. Tabard-Cossa, "Nanopore fabrication by controlled dielectric breakdown," *PLoS ONE*, vol. 9, no. 3, 2014

[2] H. Kwok, M. Waugh, J. Bustamante, K. **Briggs**, and V. Tabard-Cossa, "Long passage times of short ssDNA molecules through metallized nanopores fabricated by controlled breakdown," *Advanced Functional Materials*, vol. 24, no. 48, pp. 7745–7753, 2014

[3] K. **Briggs**, H. Kwok, and V. Tabard-Cossa, "Automated Fabrication of 2-nm Solid-State Nanopores for Nucleic Acid Analysis," *Small*, vol. 10, no. 10, pp. 2077–2086, 2014

[4] M. Waugh, A. Carlsen, D. Sean, G. W. G. Slater, K. **Briggs**, H. Kwok, and V. Tabard-Cossa, "Interfacing solid-state nanopores with gel media to slow DNA translocations," *Electrophoresis*, vol. 36, no. 15, pp. 1759–1767, 2015

[5] K. **Briggs**, M. Charron, H. Kwok, T. Le, S. Chahal, J. Bustamante, M. Waugh, and V. Tabard-Cossa, "Kinetics of nanopore fabrication during controlled breakdown of dielectric membranes in solution," *Nanotechnology*, vol. 26, no. 8, 2015

[6] T. T. J. Morin, T. Shropshire, X. Liu, K. **Briggs**, C. Huynh, V. Tabard-Cossa, H. Wang, and W. W. B. Dunbar, "Nanopore-Based Target Sequence Detection.," *PLoS One*, vol. 11, no. 5, p. e0154426, 2016

[7] J. H. Forstater, K. **Briggs**, J. W. F. Robertson, J. Ettedgui, O. Marie-Rose, C. Vaz, J. J. Kasianowicz, V. Tabard-Cossa, and A. Balijepalli, "MOSAIC: A Modular Single Molecule Analysis Interface for Decoding Multi-state Nanopore Data," *Analytical Chemistry*, vol. 88, no. 23, pp. 11900–11907, 2016

[8] A. T. Carlsen*, K. **Briggs***, A. R. Hall, and V. Tabard-Cossa, "Solid-state nanopore localization by controlled breakdown of selectively thinned membranes," *Nanotechnology*, vol. 28, no. 8, 2017

[9] R. Tahvildari, E. Beamish, K. **Briggs**, S. Chagnon-Lessard, A. N. Sohi, S. Han, B. Watts, V. Tabard-Cossa, and M. Godin, "Manipulating Electrical and Fluidic Access in Integrated Nanopore-Microfluidic Arrays Using Microvalves," *Small*, vol. 13, no. 10, pp. 1–7, 2017

[10] D. Cossa, A. S. Fanget, J. F. Chiffoleau, M. A. Bassetti, R. Buscail, B. Dennielou, K. **Briggs**, M. Arnaud, S. Guédron, and S. Berné, "Chronology and

*These authors contributed equally to this work

sources of trace elements accumulation in the Rhône pro-delta sediments (Northwestern Mediterranean) during the last 400 years," *Progress in Oceanography*, pp. 1–11, 2017

[11] K. **Briggs**, G. Madejski, M. Magill, K. Kastritis, H. W. De Haan, J. L. McGrath, and V. Tabard-Cossa, "DNA Translocations through Nanopores under Nanoscale Preconfinement," *Nano Letters*, vol. 18, no. 2, pp. 660–668, 2018

Manuscripts in Preparation

[12] M. Lam, K. Kastritis, K. **Briggs**, M. Magill, H. W. de Haan, and V. Tabard-Cossa, "Entropic Trapping of DNA using Nanoporous Nitride," *Target: Nano Letters*, 2018

[13] J. DesOrmeaux, G. Madesjki, K. **Briggs**, J. Miller, V. Tabard-Cossa, and J. L. McGrath, "Monolithic Fabrication of Serial Nanopore System using Nanoporous Nitride," *Target: Advanced Functional Materials*, 2018

[14] M. Charron, S. King, K. **Briggs**, M. Waugh, and V. Tabard-Cossa, "Improved Concentration Measurements with Nanopores using an Internal Standard," *Target: Nature Methods*, 2018

[15] M. Waugh, K. **Briggs**, S. King, S. Berryman, Q. Ingram, M. Jiminez, G. S. Pregnolato, M. Gibeault, D. Gunn, and V. Tabard-Cossa, "Instrumentation and Protocols for Nanopore Fabrication using Controlled Breakdown," *Invited: Nature Protocols*, 2018

Book Chapters

[16] K. **Briggs** and V. Tabard-Cossa, "Fabricating Solid-State Nanopores for Single-Molecule Sensing," in *Nanoscience and Nanotechnology* (M. Wanunu and A. Meller, eds.), ch. TBD, WORLD SCIENTIFIC, 2019

Patents

[17] W. H. Kwok, V. Tabard-Cossa, and K. A. Z. **Briggs**, "Fabrication of nanopores using high electric fields," May 2012. WO2013167955A1, Issued, Licensed

[18] J. Bustamante, K. **Briggs**, and V. Tabard-Cossa, "Localizing nanopore fabrication on a membrane by laser illumination during controlled breakdown," February 2015. US20180043310A1, Licensed

[19] C. C. Striemer, J. J. Miller, J.-P. DesOrmeaux, J. A. Roussie, K. **Briggs**, and V. Tabard-Cossa, "Methods for creating fluidic cavities by transmembrane etching through porous membranes and structures made thereby and uses of such structures," October 2015. WO2017075598A1, Licensed

[20] K. **Briggs**, V. Tabard-Cossa, G. Madejski, and J. McGrath, "Controlling Translocating Molecules Through A Nanopore," April 2017. US2018029939, Licensed

Conference Presentations

[21] K. **Briggs**, H. Kwok, and V. Tabard-Cossa, "Poster: In Situ Creation of Solid-State Nanopores," (Baltimore, Maryland, USA), American Physical Society Annual March Meeting, 2013

[22] K. **Briggs**, H. Kwok, and V. Tabard-Cossa, "Poster: Fabrication of 2-nm Solid-State Nanopores by Dielectric Breakdown," (Lucca, Barga, Italy), Gordon Research Conference: Single Molecule Approaches to Biology, 2014

[23] K. **Briggs**, H. Kwok, M. Waugh, A. Carlsen, J. Bustamante, and V. Tabard-Cossa, "Poster: Applications of Nanopore Fabrication by Controlled Breakdown," (Lenzerheide, Switzerland), Swissnanopore Conference, 2015

[24] K. **Briggs**, G. Madejski, M. Magill, K. Kastritis, H. W. de Haan, and V. Tabard-Cossa, "Talk: Kinetics of Polymer Translocation Through Nanopores under Nanoscale Preconfinement," (Montreal, Quebec, Canada), Biophysical Society of Canada Annual Meeting, 2017

[25] K. **Briggs**, G. Madejski, M. Magill, K. Kastritis, H. W. de Haan, and V. Tabard-Cossa, "Talk: DNA Translocations Through Nanopores under Nanoscale Preconfinement," (Ottawa, Ontario, Canada), Ottawa-Carleton Institute of Physics, 2018

[26] K. **Briggs**, G. Madejski, M. Magill, K. Kastritis, H. W. de Haan, and V. Tabard-Cossa, "Poster: Controlling Molecular Conformation Before Passage Through a Nanopore," (San Francisco, California, USA), Biophysical Society 62$^{\text{nd}}$ Annual Meeting, 2018

Software

[27] K. **Briggs**, "CUSUM: Cumulative Sum Analysis of Nanopore Data," 2015. Online: `https://github.com/shadowk29/CUSUM`

[28] K. **Briggs**, M. Charron, P. Karau, and E. Beamish, "cusumtools: An Eclectic Collection of Nanopore Analysis Tools," 2015. Online: `https://github.com/shadowk29/cusumtools`

[29] A. Balijepalli, K. **Briggs**, J. Forstater, J. Robertson, and C. Vaz, "MOSAIC: MOSAIC: Modular Single-Molecule Analysis Interface," 2014. Online: `https://github.com/usnistgov/mosaic`

List of Figures

List of Tables

Chapter 1

Introduction:
Down the Tiniest Rabbit Hole

Kyle Briggs

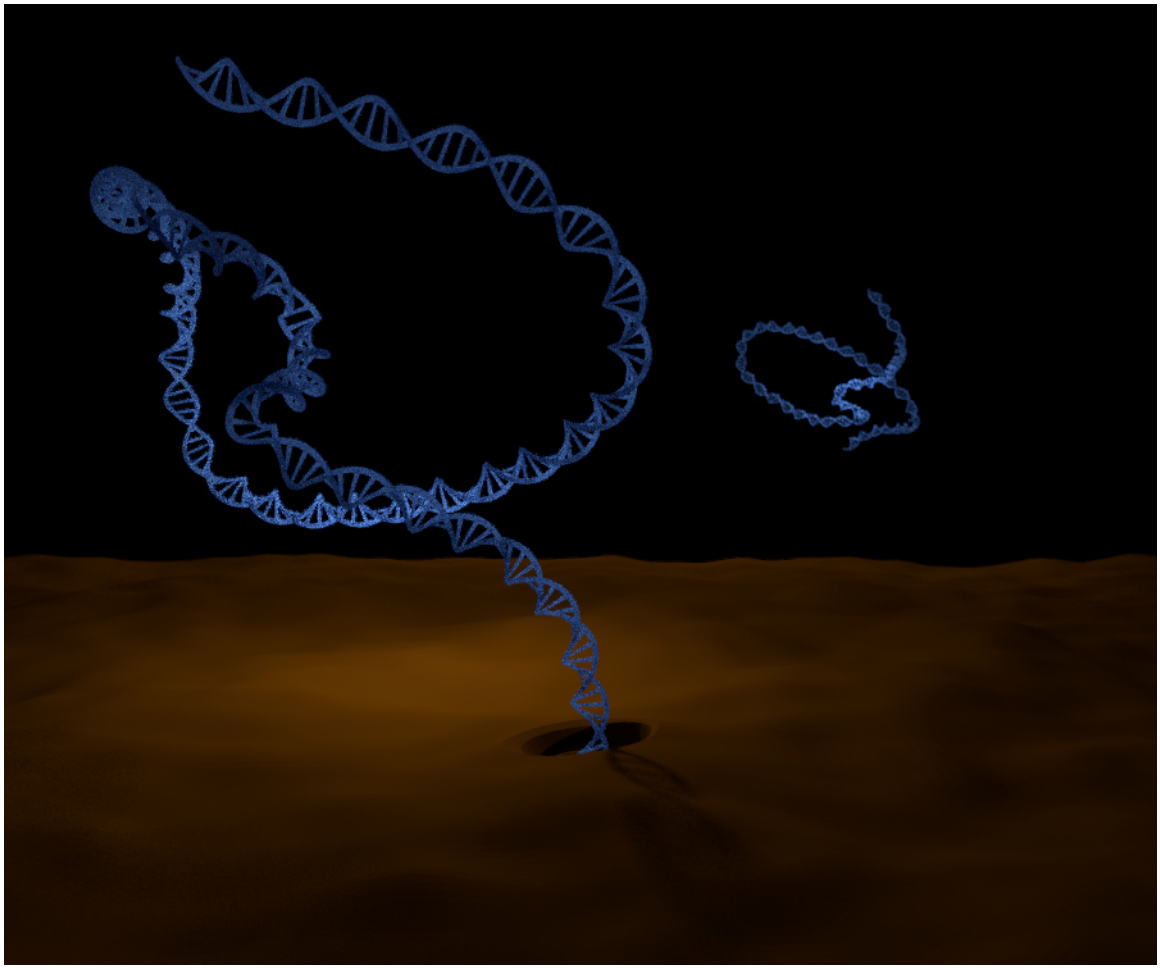

1.1 Context

The exact origin of the idea behind using nanopores to study single biomolecules depends on who you ask[1–3], but like most great ideas it probably began with a crudely scribbled diagram on a bar napkin: if single-stranded DNA could be forced through a tiny hole in a membrane that was passing electrical current, then the blockage caused by each base could be used to directly read the sequence. While the practical implementation of this idea turned out to be much more complicated than initially envisioned, from these humble beginnings was born an entire field of multidisciplinary research that today comprises thousands of researchers, hundreds of laboratories worldwide, and the beginnings of commercial enterprise.

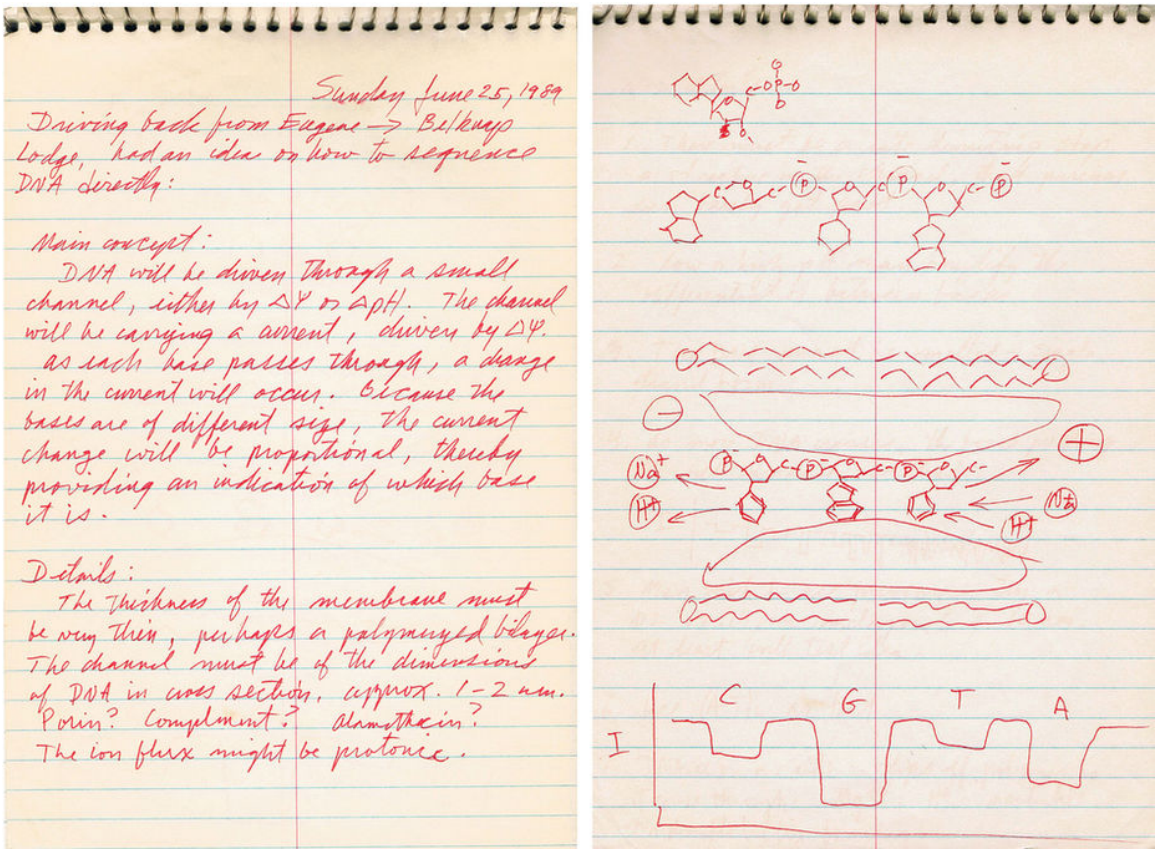

Figure 1.1: An early conceptual diagram and explanation of a nanopore sensing scheme, drawn by David Deamer in 1989[1].

Despite the complexities involved in using nanopores for sequencing, the basic premise of using them to interrogate individual biomolecules really is sufficiently simple to be drawn on a napkin. An insulating membrane containing a nanometre-scale pore is immersed between two fluidic reservoirs containing electrolyte solution, such that the only connection between the two reservoirs is through the pore. When a potential difference is applied across the membrane, ionic current is driven through the pore. If charged biomolecules are also present in the solution, they are driven through the pore as well, producing transient current blockades from which information about the biomolecule can be extracted. Figure 1.1 shows an early conceptual diagram of the nanopore sensing modality.

Once this idea was realized experimentally it became immediately apparent that the naïve idea of simple nanopore sequencing was not going to work, for several reasons. While polymers were clearly being captured by the pore, they were moving far too quickly to resolve the signal arising from individual bases. Typical residence times for a single base in a nanopore were of the order of 1 μs, faster even than the sampling period of the electronics. Even with sufficient time-resolution, however, the thickness of the pore meant that the signal being read was actually a convolution of several bases, making it much more difficult to identify a particular current blockage signal with a sequence of bases. Finally, even with accurate base-calling of the combinations of bases in the pore, polymers which are moving slow enough to provide time-resolution of the nucleotides in the pore are subject to Brownian motion and do not necessarily translocate smoothly and in a single direction, making it difficult to relate temporal information in the signal to spatial information on the polymer. These problems have provided fertile ground for three decades of research.

There are two major classes of nanopores. The first consists of biological protein pores derived from cell membrane proteins. These pores exist in every cell in every

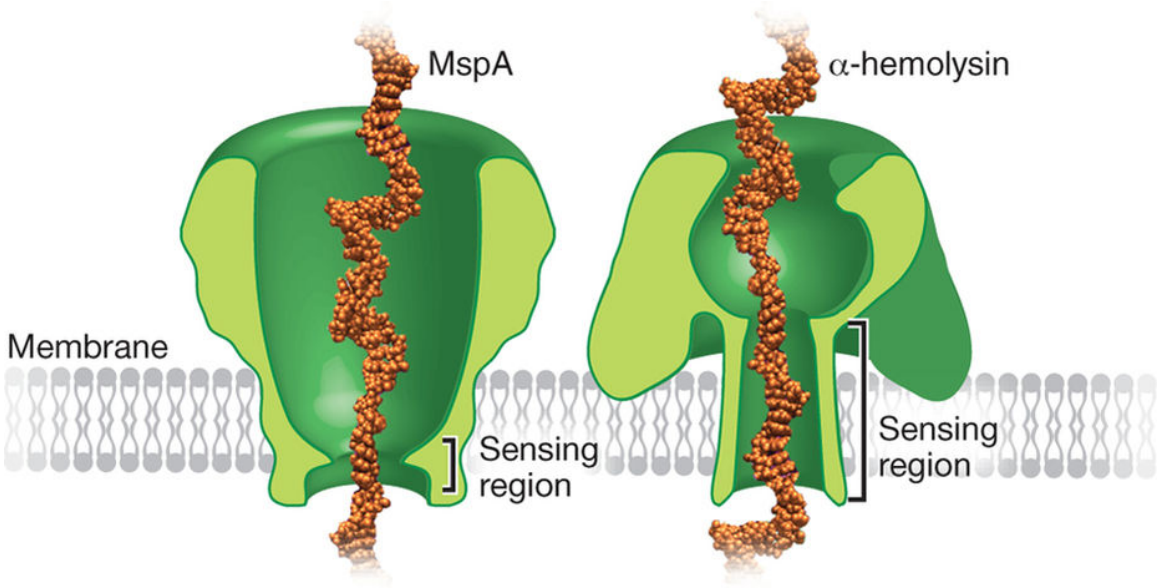

Figure 1.2: Illustrations of the two more common biological nanopores, MspA (left) and α-HL (right)[1]. The sensing region indicates the most narrow segment of the pore, which is the part of the pore to which the measured electrical current is most sensitive.

living thing on the planet, and are used in vivo for an astonishing variety of purposes, including ion pumps for chemical energy generation; maintaining electrolyte imbalances for nerve signalling; mediating selective biomolecular transport through cell membranes; and much more. From among the near-infinite variety of wild-type pores available, two in particular have come to be widely used for research purposes: α-Hemolysin (αHL)[4–14], a pore derived from the toxin *Staphylococcus aureus*, and *Mycobacterium smegmatis* porin A (MspA)[15–21]. The first DNA translocation experiments were performed using αHL pores[4]. Currently, the MinION sequencer available from Oxford Nanopore uses a heavily engineered mutant of the CsgG pore, an amyloid secretion channel found in *Escherichia coli*, to achieve long read sequencing[22,23]. These pores have numerous desirable properties: they can be maintained in the open state indefinitely; they can be engineered at the amino acid level to tweak their physical properties for a particular application; the lipid bilayers into which they

insert themselves are well-behaved electrically and have very low capacitance, allowing for incredibly sensitive measurement of current signals; and the sensing region of the pore, corresponding to the narrowest restriction to which the electrical signal is most sensitive, is only a few bases long, allowing for the sensitivity required for sequencing. Schematic illustrations αHL and MspA are shown in Figure 1.2. These biological nanopores achieved motion control for sequencing by pairing the pore with a processive enzyme to slowly move the DNA through the pore one base at a time, overcoming bandwidth limitations and extending the molecular passage time sufficiently to resolve the underlying sequence[15–19,24–30]. While this technique has enabled sequencing[21,31–34], biological nanopores are ill-suited to mass-manufacturing, where a fully solid-state solution provides a much more scalable approach.

Once it became apparent that biological pores could be used to study biomolecules at the individual level, a second class of nanopore was developed. These biomimetic synthetic pores are simply nanometre scale holes in thin solid-state membranes, most commonly silicon nitride (SiN_x). While these are generally less sensitive than their biological counterparts due to the electrical properties of the membranes themselves, they offer greater robustness and flexibility than biological pores. This arises from the fact that they can be made in any suitable material and at almost any size, and the resulting solid-state structures are more stable than lipid bilayers. The development of techniques for fabricating these devices has provided for more than twenty years of research alone, which is discussed in detail in Chapter 2.

While biological nanopore research is thriving to this day, these pores suffer from having fixed size, being dependent on lipid or synthetic membranes for support, and being highly sensitive to environmental conditions like salt concentration and pH. By comparison, solid-state nanopores are robust, flexible, and can relatively easily be integrated into other solid-state electronic devices[35], making them preferable as

a long-term solution over biological pores if the shortcomings of their comparatively lower sensitivity can be addressed. On the other hand, solid-state nanopores have yet to achieve the level of motion control required for reliable interpretation of translocation signals of complex biopolymers for anything beyond gross molecular structure (e.g. effective thickness and length) and conformation (e.g. the presence of hairpins). In this thesis, we will outline and attempt to address many of the problems that stand between synthetic nanopores and the enormous variety of potential applications in which they could find utility.

1.2 Nanopore Measurements

1.2.1 Nanopore Instrumentation

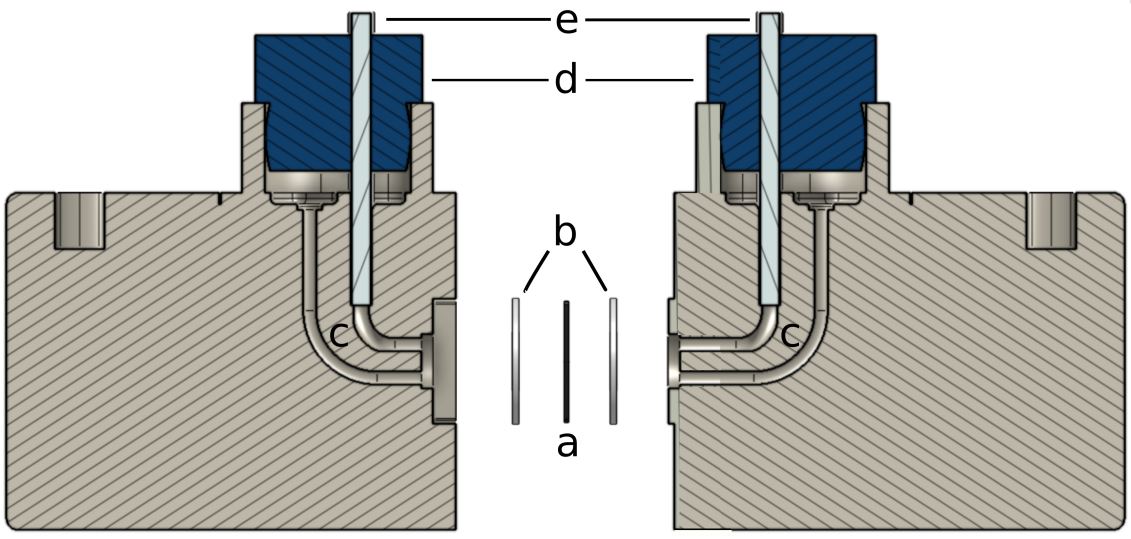

Figure 1.3: A schematic diagram of the fluidic flow cell used for nanopore experiments. a) The nanopore support chip. b) Gaskets used to pressure-seal around the nanopore. c) Flow channels used to fluidically connect electrodes to the nanopore and to easily introduce samples. d) Caps that hold the electrode and prevent evaporation of the electrolyte. e) Ag/AgCl electrodes used to electrically connect to the nanopore.

Solid-state nanopores are fabricated in thin free-standing SiN_x, membranes deposited on silicon support chips by one of several methods that are discussed in detail in Chapter 2. These chips are sandwiched between two fluidic reservoirs, and an Ag/AgCl electrode is connected to each reservoir to control the voltage and sense the resulting current through the device. The electrode type must be ion-matched to the electrolyte used for sensing, since this facilitates the transition between electronic and ionic current at the interface between solution and electrode. The basic setup is shown in Figure 1.3.

The current through the system is most commonly measured using one of two commercial current amplifiers that are sensitive to picoampere currents: the Axopatch 200B, which has a maximum bandwidth of 100 kHz, or the Chimera VC100, which has a maximum bandwidth of 1 MHz. In the former case, current is then digitized using a National Instruments data acquisition (DAQ) card, while the latter has a custom DAQ. Both DAQs interface with a standard desktop computer via USB. A schematic diagram of the full system is shown in Figure 1.4.

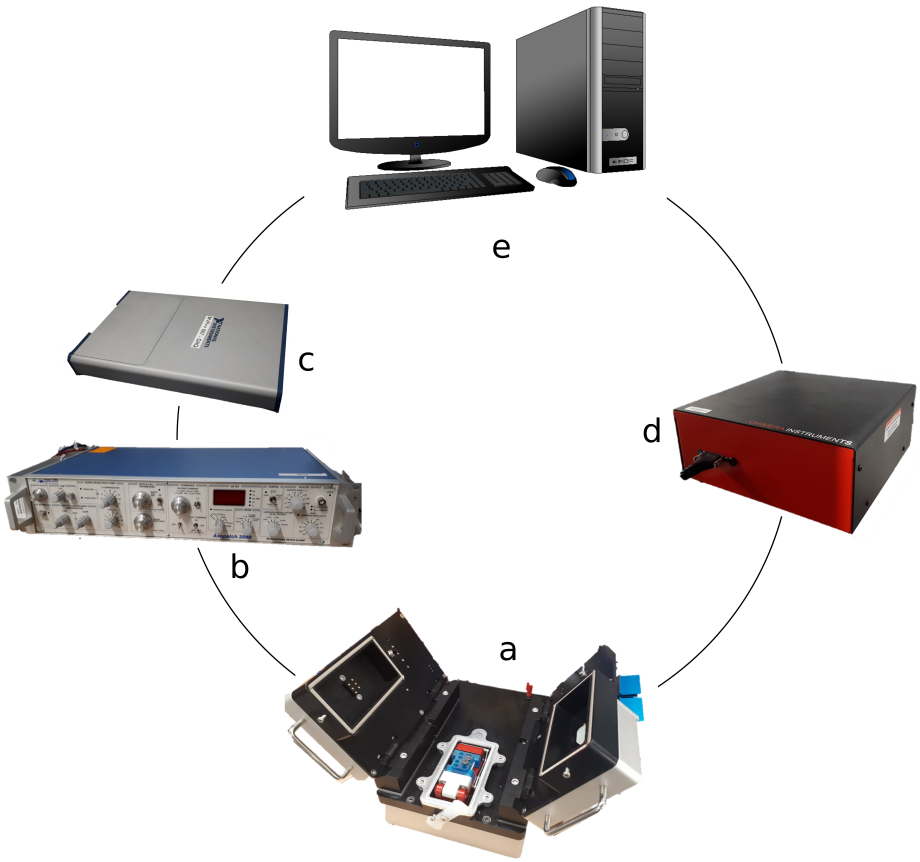

Figure 1.4: A schematic diagram of experimental setup for nanopore experiments. a) The custom device for fabricating and sensing with nanopores. The flow cell shown in Figure 1.3 is housed here. b) The Axopatch 200B, used for low-bandwidth current recording. c) A National Instruments DAQ card, used to digitize signals from the Axopatch 200B. d) The Chimera VC100, used for high-bandwidth current recording. e) A typical PC, which controls the entire equipment array. Which signal pathway is chosen depends on bandwidth requirements for a given experiment.

1.2.2 Nanopore Geometry Characterization

While it is in principle possible to directly image pores using an electron microscope, for example, this is a time-consuming process that yields less informaton than it might seem at first glance. Nanopores are dynamic objects that are very sensitive to a variety of stressors, not the least of which is the extensive cleaning and handling required to transfer between the TEM and a fluidic measurement setup, with the

net result that the pore size measured visually does not necessarily reflect the pore size once it is liquid and actually taking measurements. For the approach used to fabricate pores in this thesis, the nanopore is formed at a random location on the membrane, and takes up such a tiny fraction of the active area that finding it is like searching a football field for a penny while only being able to see a few hundred square centimetres at a time. While this can be done[36,37], it is preferable, and generally more informative, to measure the pore indirectly using the same electrical signal from which DNA translocation data is extracted. This framework can provide information about the pore diameter and, combined with translocation of a molecule which produces a known blockage depth, the aspect ratio.

The conductance of a nanopore is divided into three terms. The first, given by[38,39]

$$G_{bulk} = \sigma \frac{\pi d^2}{4L}, \tag{1.1}$$

represents the contribution of bulk conductivity of a cylinder of length L, diameter d, and conductivity σ. The second term relates to the fact that the finite conductivity of the solution means that there will be some electric field drop in the solution itself outside the pore. The origin of this term lies in solving the resistance between a conducting disk with the same diameter as the pore and a hemispherical electrode at infinity[40], which yields

$$G_{access} = \sigma d. \tag{1.2}$$

The final term represents the contribution of electroosmotic flow to the current, wherein the surface charge γ of the pore walls causes an accumulation of oppositely charged counterions that move coherently through electroosmotic flow under an applied voltage with electrophoretic mobility μ. The origin of this term is explored in

some detail by Stein *et al*[41], and is given by

$$G_{EOF} = \pi \frac{d}{L} \mu\gamma. \tag{1.3}$$

Combining these three terms by considering the EOF and bulk contributions to be in parallel, both in series with the access term, one obtains

$$G = \sigma \left(\frac{1}{d} + \frac{4L}{\pi d^2} \left(\frac{1}{1 + \frac{4\mu\gamma}{\sigma d}} \right) \right)^{-1}. \tag{1.4}$$

Most experimental work, including the work in this thesis, completely ignores electroosmostic flow, setting $\gamma = 0$. This is done for convenience, since the surface charge of the pore is rarely known and difficult to extract[42], as is the mobility of the counterions. This approximation is reasonable as long as the concentration of electrolyte is high[38], which suppresses surface effects.

With this in mind, the size of nanopores in solution is usually inferred using just the bulk and access resistance terms[43],

$$G = \sigma \left(\frac{1}{d} + \frac{4L}{\pi d^2} \right)^{-1}. \tag{1.5}$$

By assuming an effective membrane thickness L, which for CBD pores is generally taken to simply be the nominal membrane thickness, one can use the pore conductance G, measured as slope of an I-V curve, to infer a pore diameter d. A schematic diagram of the equivalent circuit represented by equation 1.5 is given in Figure 1.5.

The pore size estimate can be somewhat improved using an analyte of known size to obtain an improved estimate of the effective length of the nanopore. Assuming that an analyte only significantly blocks the bulk portion of the nanopore conductance without affecting the access resistance, one can expect a blockage depth for double-

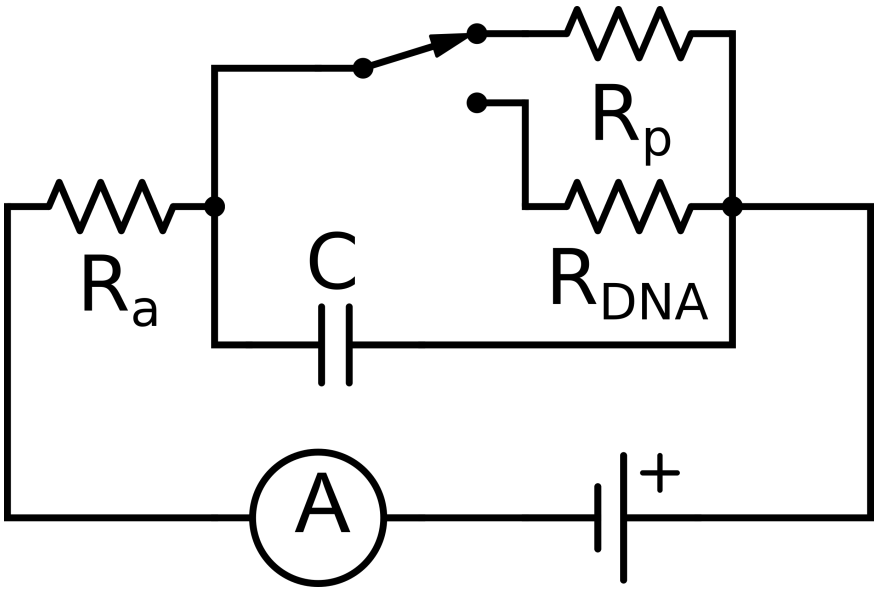

Figure 1.5: The schematic circuit diagram representing a nanopore and the sensing electronics required to use it. The passage of an analyte is represented by an instantaneous switch between R_p and R_{DNA} while current through the whole circuit is measured under constant voltage. C refers to the membrane capacitance, while R_a refers to the electrical resistance of the electrolyte and the access resistance of the nanopore. The current through the system is measured using a picoammeter denotes A.

stranded DNA (dsDNA) of

$$\Delta G \approx \sigma \frac{\pi d_{DNA}^2}{4L}. \tag{1.6}$$

Knowing $d_{DNA} \approx 2.2$ nm allows extraction of L, which can then be used to refine the pore diameter estimate by feeding back into Equation 1.5[44]. More complex models for solving both simultaneously also exist[43], but care must be taken when using them as the range of pore geometries over which they apply is fairly limited. In general, these formulas are rough approximations, since any deviation at all from a cylindrical geometry introduces errors that make it difficult to actually assign a physical meaning to the quantities generated, though work done using this formula to extract pore sizes near the limit of being able to pass DNA molecules, as well as direct TEM images of the fabricated nanopores, suggest that this is a reasonable approximation[36,44,45].

Nevertheless, in the absence of better models, these estimates provide a reasonably quantitative estimate of pore geometry with minimal effort, and actually perform surprisingly well as long as the salt concentration is very high (greater than 3 M) so that the effects of surface charge are suppressed[45].

More sophisticated treatments exist that in principle allow determination of geometric parameters for non-cylindrical pore models. These are based on observing the conductance change of a pore as a function of time while growing or shrinking the pore at a known rate[46–49]. While these have been validated experimentally[49], they are generally not in use due to the difficulty involved in growing or shrinking a pore while still having a useful pore at the end of the process.

1.2.3 Nanopore Noise Characterization

The dominant contributions to the power spectrum of a typical nanopore are of the form

$$S(f) = a_0 \frac{\langle i \rangle^2}{f^\alpha} + a_1 \frac{k_B T}{R_a + R_p} + a_2 k_B T D C f + a_3 \sigma_V^2 C^2 f^2, \tag{1.7}$$

where $\langle i \rangle$ is the DC current, $R_a + R_p$ is the nanopore resistance including access resistance, which sets the thermal noise floor, D is the dielectric loss constant, σ_V^2 is the RMS voltage noise at the input in $\mathrm{V^2\ Hz^{-1}}$, C is the total capacitance of the device and instrumentation, $\alpha \approx 1$ is the low-frequency noise exponent, and the a_i values are fitting parameters which determine the relative strength of each contribution to the noise[50]. Figure 1.6 shows a typical power spectrum for a solid-state nanopore.

The first term, $\frac{1}{f}$ or pink noise, dominates the low frequency spectrum. This type of noise is ubiquitous in almost any physical system, and the exact origins in nanopores are the subject of debate, though there is evidence that the presence of nanobubbles in the pore itself can be a factor if this term is particularly dominant[51].

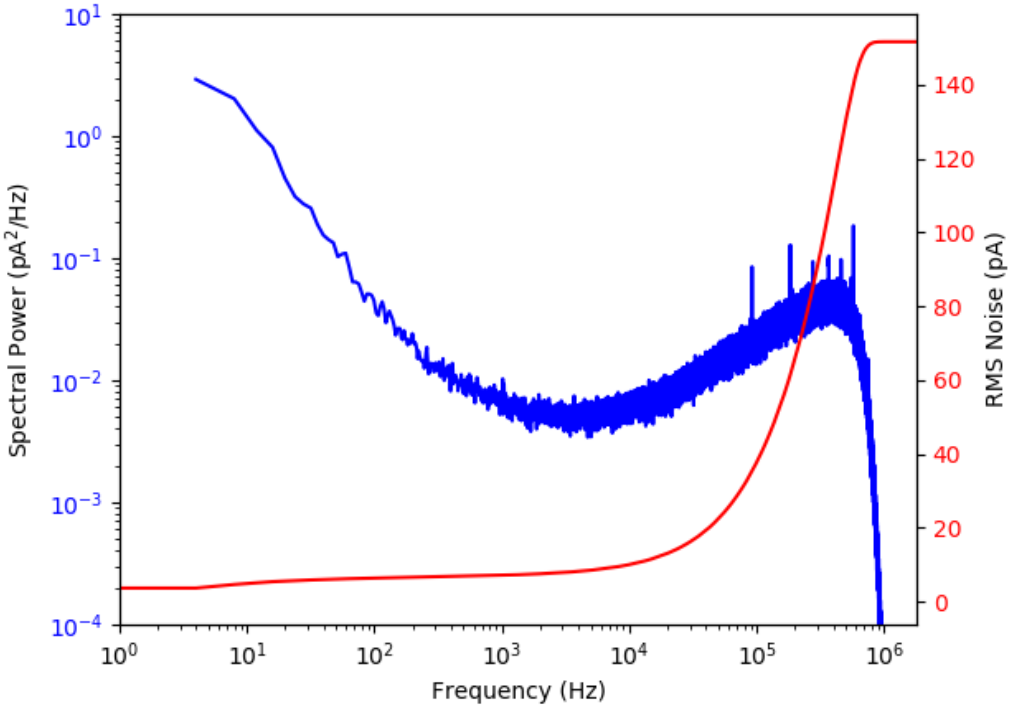

Figure 1.6: The power spectrum of a 5.4 nm nanopore painted with PDMS, showing the characteristic shape given by Equation 1.7. The signal is low-pass filtered at 900 kHz using an 8 pole zero-phase Bessel filter. The high frequency spikes are a consequence of the interaction between the digitizing electronics and noise generated by the computer itself, and do not integrate for significant noise.

It is often possible to tell whether a particular pore will be useful or not simply by the magnitude of the $\frac{1}{f}$ noise, where a large value for a_0 generally renders a pore useless.

The second term is due to thermal effects and depends entirely on the electrical resistance of the pore. Unless the pore is extremely large, this term is negligibly small compared to the others, and is certainly negligible for all of the pores used in this thesis.

At high frequencies we see two regimes of noise that increase with frequency, both mediated by the capacitance of the device under test. Dielectric noise increases lin-

early with frequency and is determined by the dieletric properties of the membrane and support structure, while capacitive noise scales with the square of the frequency. This capacitively coupled last noise term is inevitably the limiting factor in the usable bandwidth for nanopores, since even though amplifiers exist that can accurately record current measurements up to 10 MHz bandwidth[52], the capacitive noise eventually reduces the signal-to-noise ratio below a usable value. In practice, state of the art nanopore measurements typically work with up to 1 MHz bandwidth[53].

1.3 Polymer Physics

1.3.1 Polymer Capture

Due to the finite access resistance $R_a = (\sigma d)^{-1}$, there is a non-zero electric field outside the nanopore that decays approximately radially away from the mouth of the pore. The voltage in the vicinity of the pore mouth can be approximated as

$$V(r) = \frac{d^2}{8Lr}\Delta V, \tag{1.8}$$

where d is the pore diameter, L the membrane thickness, r the radial distance from the pore mouth and ΔV the total voltage drop across the system[54]. More sophisticated treatments of the local field exist for specific pore geometries[55], but this suffices for a qualitative discussion. Far from the pore, where no electric field exists, DNA freely diffuses. As DNA approaches the pore, there exists a characteristic length scale at which DNA motion becomes dominated by electrophoretic drift, called the capture radius $r^\star$. This is obtained by balancing diffusive motion against electrophoretic drift by setting $V(r^\star) = D\mu^{-1}$ where D is the DNA diffusion coefficient and μ the

electrophoretic mobility. This gives a capture radius of[54]

$$r^{\star} = \frac{d^2\mu}{8LD}\Delta V. \tag{1.9}$$

If we treat the capture radius as an absorbing hemisphere we find a capture rate of

$$R_c = \frac{\pi d^2\mu}{4L}c\Delta V, \tag{1.10}$$

where c is the analyte concentration. This formalism predicts that capture by the pore in this diffusion-limited regime is independent of polymer length, which appears to be true for long polymers. For short polymers, Equation 1.10 breaks down, anthe capture rate instead has power law dependence on length[56], a prediction that has been born out experimentally[54]. Rowghanian *et al.* provide a more thorough theoretical treatment, in which they show that the crossover length between these two regimes depends on the aspect ratio of the nanopore, with thicker membranes pushing the crossover to larger and larger polymers for a given pore size[56]. Since the vast majority of the experiments performed in this thesis are done in the diffusion-limited regime, we will not concern ourselves with the barrier-limited regime beyond noting its existence.

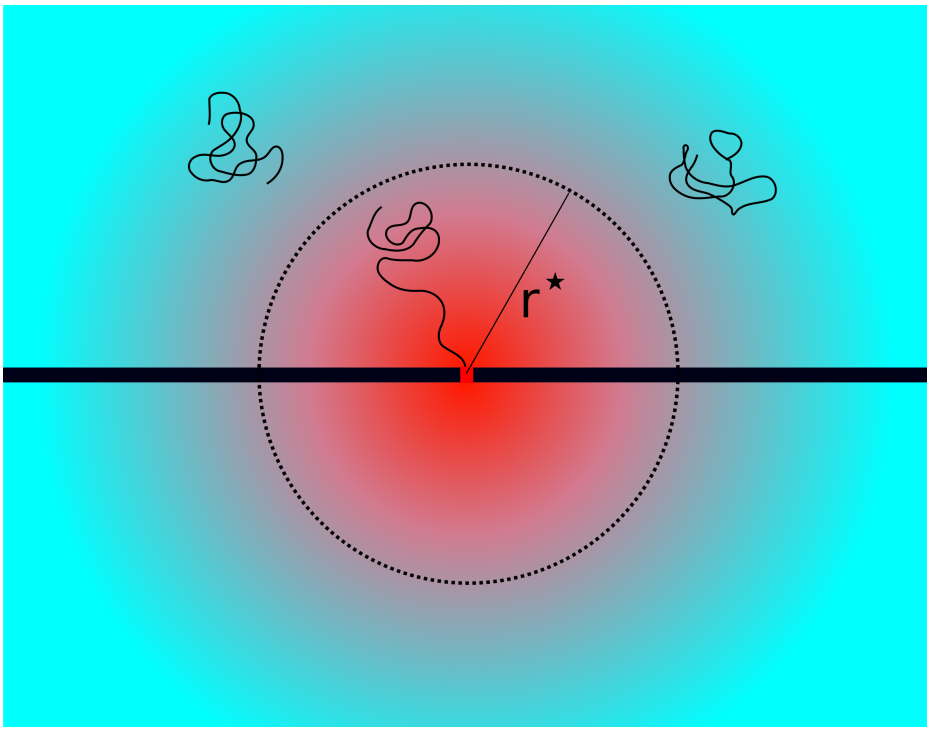

Figure 1.7: The capture radius of the nanopore, with the absolute voltage represented as a color scale. On one side of the pore, polymers that enter the capture radius are pulled toward the pore and captured. On the opposite side, a symmetric region exists in which polymers are actively pushed away from the pore. Image is not to scale.

1.3.2 Translocation Dynamics

Once the polymer is close to the pore, the dynamics of the translocation process are challenging to analyze theoretically. The driving force is usually too strong and the translocation process too fast for any sort of quasistatic approximation to be valid[57,58]. In fact, the translocation occurs so quickly that it is reasonable to assume that except for the leading end, the polymer is frozen in time during the translocation process. Consequently, translocation dynamics are determined completely by the details of the molecular conformation of the polymer at the moment of capture by the nanopore[59].

The theoretical framework that so far best approximates translocation dynamics is tension-propagation theory, which postulates that when a polymer is captured by

a pore, the polymer is pulled through the pore at a rate so fast that the leading end of the polymer experiences highly driven motion before the tail end of the polymer is even aware it has been captured, resulting in a propagating tension front that moves backwards along the chain. At any given time, only a portion of the polymer is experiencing driven motion and directed fluid drag, whereas the tail is still unaware that the front of the polymer is undergoing driven motion until near the end of the process. By treating the fluid drag of the polymer as time-dependent in this manner, this approach has yielded reasonable approximations for the polymer length scaling of the translocation time, predicting a time $\tau \sim N^{\alpha}$, with α varying depending on the details of the model. Various works have predicted $\alpha = \frac{1+\nu+2\nu^2}{1+\nu} \approx 1.45$[60–62] and $\alpha = 1 + \nu \approx 1.6$[63–66] where ν is the Flory exponent for the polymer size. The variation in α has been attributed to finite polymer length effects not accounted for in earlier work[63]. These exponents are in reasonable if not exact agreement with the handful of experimental studies that have attempted to extract this scaling law, which typically show smaller exponents, ranging from $\alpha \approx 1.19 - 1.27$[35,67–70], with significant deviations and even the appearance of new scaling regimes in very small pores where polymer-pore interactions can no longer be ignored[71,72]. This formalism also implies that the translocation speed of the portion of the polymer that is in the pore is not constant, but rather starts out fast when the portion of the polymer under tension is short and fluid drag is low, slows down toward the middle of the translocation as the tension front propagates through the polymer, and speeds up at the end as the tension front reaches the end of the polymer and the tail escapes through the pore. This general pattern has been observed in experiment[59,73] and simulation[74].

To further confuse the issue, in addition to mediating the actual capture process, due to the radial decay of the electric field near the pore mouth, there exists a strong electric field gradient outside the pore that results in stretching of charged polymers

as they approach the nanopore, which has important consequences for the conformation and subsequent translocation kinetics of polymers[66], an effect which is generally not taken into account in theoretical work on translocation phenomena. This should have minimal effect, if any, on the capture rate, since for the work done in this thesis, molecular capture is limited by the diffusion of molecules into this electric field gradient, not what occurs inside it, but it does have important implications for the translocation process itself. Because the translocation kinetics are governed entirely by the molecular conformation at the moment of capture, any deviation from equilibrium prior to this point has profound consequences for the resulting translocation event. Finally, almost all of the theory relating to polymer translocation assume capture by an end, and makes no attempt to deal with folded passage, with one notable exception[68].

What is clear from the available evidence is that translocation is a non-uniform, non-equilibrium process that is strongly dictated by the conformation of the polymer at the moment of capture by the pore[59,69,75]. In addition to making this a theoretically difficult problem, this presents enormous challenges in interpreting the time-series data extracted during experimental nanopore measurements. In this highly driven regime, most of the randomness in the translocation kinetics arises from conformational entropy rather than Brownian motion. In contrast, biological pores have managed to control the speed of passage to the point that sequencing is possible, but this reduced speed comes at the cost of making Brownian motion and backstepping a major contributor to measurement errors. Solid-state and biological nanopores represent two ends of a spectrum, both of which have downsides. An approach that balances deterministic motion against translocation speed has yet to be developed.

1.4 Thesis Overview

The previous sections have alluded to three major categories of problems in the nanopore field: development of simple nanopore fabrication methods; precise control of the motion of DNA as it translocates a nanopore; and analysis and interpretation of the resulting signals. This thesis presents significant contributions toward all three, and is roughly divided into three corresponding themes.

The first part of the thesis is concerned with nanopore fabrication. First, Chapter 2 presents a thorough review of all of the major nanopore fabrication techniques that are commonly in use today. Chapter 3 is the first of three chapters to begin a much deeper look at one method in particular, termed controlled breakdown (CBD)[44], in which nanopores are made by harnessing the normally destructive process of dielectric breakdown to easily sculpt matter on the nanoscale directly in electrolyte solution. Research into this method began in my undergraduate years, and Chapter 3 represents the first work of my graduate research, taking the form of a detailed study of the limits of the size of pores that can be reliably fabricated[45]. Chapter 4 goes deeper still, exploring the kinetics underlying the controlled breakdown process and the various control parameters by which it can be affected[76]. Finally, Chapter 5 studies the possibility of using pre-patterned membranes to precisely control the location of nanopores formed using CBD[36]. Because Chapter 2 covers nanopore fabrication generally there is by necessity some redundancy with Chapters 3-5.

The central part of the thesis presents efforts toward control of the motion of dsDNA as it translocates a nanopore. Chapter 6 presents a novel nanodevice that realizes two nanopores in series using a nanoporous membrane separated from a sensing pore by a nanoscale gap. In this work, we demonstrate that the presence of the nanofilter causes dsDNA to stretch as it approaches the pore, removing conforma-

tional entropy from the polymer and improving the consistency of translocation[69], an approach which not only simplifies experimental analysis of nanopore data, but should also simplify the theoretical problem of accurately describing polymer motion going forward.

Finally, Chapters 7 and 8 are concerned with digital signal processing and analysis of nanopore data, presenting two open-source software suites suitable for high-quality analysis of time-series data generated by nanopores[77]. Each chapter serves as a user manual that provides sufficient detail to use the software, while also discussing the theoretical framework on which each tool is based.

Bibliography

[1] D. Deamer, M. Akeson, and D. Branton, "Three decades of nanopore sequencing," *Nature Biotechnology*, vol. 34, no. 5, pp. 518–524, 2016.

[2] J. J. Kasianowicz and S. M. Bezrukov, "On 'three decades of nanopore sequencing' Reply," *Nature Biotechnology*, vol. 34, no. 5, p. 482, 2016.

[3] C. G. Brown and J. Clarke, "Nanopore development at Oxford Nanopore," *Nature Biotechnology*, vol. 34, no. 8, pp. 810–811, 2016.

[4] J. J. Kasianowicz, E. Brandin, D. Branton, and D. W. Deamer, "Characterization of individual polynucleotide molecules using a membrane channel," *Proc. Natl. Acad. Sci. U.S.A.*, vol. 93, no. November, p. 13770, 1996.

[5] M. Akeson, D. Branton, J. J. Kasianowicz, E. Brandin, and D. W. Deamer, "Microsecond time-scale discrimination among polycytidylic acid, polyadenylic acid, and polyuridylic acid as homopolymers or as segments within single RNA molecules," *Biophysical Journal*, vol. 77, no. 6, pp. 3227–3233, 1999.

[6] A. Meller, L. Nivon, E. Brandin, J. Golovchenko, and D. Branton, "Rapid nanopore discrimination between single polynucleotide molecules.," *Proceedings of the National Academy of Sciences of the United States of America*, vol. 97, pp. 1079–84, feb 2000.

[7] A. Meller, L. Nivon, and D. Branton, "Voltage-driven DNA translocations through a nanopore," *Physical Review Letters*, vol. 86, no. 15, pp. 3435–3438, 2001.

[8] H. Wang, J. E. Dunning, A. P.-H. Huang, J. A. Nyamwanda, and D. Branton, "DNA heterogeneity and phosphorylation unveiled by single-molecule electrophoresis," *Proceedings of the National Academy of Sciences*, vol. 101, no. 37, pp. 13472–13477, 2004.

[9] J. Mathe, A. Aksimentiev, D. R. Nelson, K. Schulten, and A. Meller, "Orientation discrimination of single-stranded DNA inside the -hemolysin membrane channel," *Proceedings of the National Academy of Sciences*, vol. 102, no. 35, pp. 12377–12382, 2005.

[10] T. Z. Butler, J. H. Gundlach, and M. A. Troll, "Determination of RNA orientation during translocation through a biological nanopore," *Biophysical Journal*, vol. 90, no. 1, pp. 190–199, 2006.

[11] N. Ashkenasy, J. Sanchez-Quesada, H. Bayley, and M. R. Ghadiri, "Recognizing a Single Base in an Individual DNA Strand: A Step Toward DNA Sequencing in Nanopores," *Angewandte Chemie*, vol. 117, pp. 1425–1428, 2005.

[12] D. Stoddart, A. J. Heron, E. Mikhailova, G. Maglia, and H. Bayley, "Single-nucleotide discrimination in immobilized DNA oligonucleotides with a biological nanopore," *Proceedings of the National Academy of Sciences*, vol. 106, no. 19, pp. 7702–7707, 2009.

[13] D. Stoddart, A. J. Heron, J. Klingelhoefer, E. Mikhailova, G. Maglia, and H. Bayley, "Nucleobase recognition in ssDNA at the central constriction of the α-hemolysin pore," *Nano Letters*, vol. 10, no. 9, pp. 3633–3637, 2010.

[14] D. Stoddart, G. Maglia, E. Mikhailova, A. J. Heron, and H. Bayley, "Multiple base-recognition sites in a biological nanopore: Two heads are better than one," *Angewandte Chemie - International Edition*, vol. 49, no. 3, pp. 556–559, 2010.

[15] E. A. Manrao, I. M. Derrington, A. H. Laszlo, K. W. Langford, M. K. Hopper, N. Gillgren, M. Pavlenok, M. Niederweis, and J. H. Gundlach, "Reading DNA at single-nucleotide resolution with a mutant MspA nanopore and phi29 DNA polymerase.," *Nature Biotechnology*, vol. 30, pp. 349–53, apr 2012.

[16] A. H. Laszlo, I. M. Derrington, H. Brinkerhoff, K. W. Langford, I. C. Nova, J. M. Samson, J. J. Bartlett, M. Pavlenok, and J. H. Gundlach, "Detection and mapping of 5-methylcytosine and 5-hydroxymethylcytosine with nanopore MspA," *Proceedings of the National Academy of Sciences*, vol. 110, no. 47, pp. 18904–18909, 2013.

[17] J. Schreiber, Z. L. Wescoe, R. Abu-Shumays, J. T. Vivian, B. Baatar, K. Karplus, and M. Akeson, "Error rates for nanopore discrimination among cytosine, methylcytosine, and hydroxymethylcytosine along individual DNA strands," *Proceedings of the National Academy of Sciences*, vol. 110, no. 47, pp. 18910–18915, 2013.

[18] A. H. Laszlo, I. M. Derrington, B. C. Ross, H. Brinkerhoff, A. Adey, I. C. Nova, J. M. Craig, K. W. Langford, J. M. Samson, R. Daza, K. Doering, J. Shendure, and J. H. Gundlach, "Decoding long nanopore sequencing reads of natural DNA," *Nature Biotechnology*, vol. 32, no. 8, pp. 829–833, 2014.

[19] Z. L. Wescoe, J. Schreiber, and M. Akeson, "Nanopores discriminate among five C5-cytosine variants in DNA," *Journal of the American Chemical Society*, vol. 136, no. 47, pp. 16582–16587, 2014.

[20] T. Z. Butler, M. Pavlenok, I. M. Derrington, M. Niederweis, and J. H. Gundlach, "Single-molecule DNA detection with an engineered MspA protein nanopore," *Proceedings of the National Academy of Sciences*, vol. 105, no. 52, pp. 20647–20652, 2008.

[21] I. M. Derrington, T. Z. Butler, M. D. Collins, E. Manrao, M. Pavlenok, M. Niederweis, and J. H. Gundlach, "Nanopore DNA sequencing with MspA.," *Proceedings of the National Academy of Sciences of the United States of America*, vol. 107, pp. 16060–5, sep 2010.

[22] J.-M. Carter and S. Hussain, "Robust long-read native DNA sequencing using the ONT CsgG Nanopore system," *Wellcome Open Research*, vol. 2, no. May, p. 23, 2017.

[23] M. Jain, S. Koren, K. H. Miga, J. Quick, A. C. Rand, T. A. Sasani, J. R. Tyson, A. D. Beggs, A. T. Dilthey, I. T. Fiddes, S. Malla, H. Marriott, T. Nieto, J. O'Grady, H. E. Olsen, B. S. Pedersen, A. Rhie, H. Richardson, A. R. Quinlan, T. P. Snutch, L. Tee, B. Paten, A. M. Phillippy, J. T. Simpson, N. J. Loman, and M. Loose, "Nanopore sequencing and assembly of a human genome with ultra-long reads," *Nature Biotechnology*, vol. 36, no. 4, pp. 338–345, 2018.

[24] S. Benner, R. J. Chen, N. A. Wilson, R. Abu-Shumays, N. Hurt, K. R. Lieberman, D. W. Deamer, W. B. Dunbar, and M. Akeson, "Sequence-specific detection of individual DNA polymerase complexes in real time using a nanopore," *Nature Nanotechnology*, vol. 2, no. 11, pp. 718–724, 2007.

[25] B. Hornblower, A. Coombs, R. D. Whitaker, A. Kolomeisky, S. J. Picone, A. Meller, and M. Akeson, "Single-molecule analysis of DNA-protein complexes using nanopores.," *Nature Methods*, vol. 4, pp. 315–7, apr 2007.

[26] S. L. Cockroft, J. Chu, M. Amorin, and M. R. Ghadiri, "A single-molecule nanopore device detects DNA polymerase activity with single-nucleotide resolution.," *Journal of the American Chemical Society*, vol. 130, pp. 818–20, jan 2008.

[27] F. Olasagasti, K. R. Lieberman, S. Benner, G. M. Cherf, J. M. Dahl, D. W. Deamer, and M. Akeson, "Replication of individual DNA molecules under electronic control using a protein nanopore," *Nature Nanotechnology*, vol. 5, no. 11, pp. 798–806, 2010.

[28] J. Chu, M. González-López, S. L. Cockroft, M. Amorin, and M. R. Ghadiri, "Real-time monitoring of DNA polymerase function and stepwise single-nucleotide DNA strand translocation through a protein nanopore.," *Angewandte Chemie*, vol. 49, pp. 10106–9, dec 2010.

[29] K. R. Lieberman, G. M. Cherf, M. J. Doody, F. Olasagasti, Y. Kolodji, and M. Akeson, "Processive replication of single DNA molecules in a nanopore catalyzed by phi29 DNA polymerase.," *Journal of the American Chemical Society*, vol. 132, pp. 17961–72, dec 2010.

[30] G. M. Cherf, K. R. Lieberman, H. Rashid, C. E. Lam, K. Karplus, and M. Ake-

son, "Automated forward and reverse ratcheting of DNA in a nanopore at 5-Å precision," *Nature Biotechnology*, vol. 30, no. 4, pp. 344–348, 2012.

[31] M. Jain, I. T. Fiddes, K. H. Miga, H. E. Olsen, B. Paten, and M. Akeson, "Improved data analysis for the MinION nanopore sequencer," *Nature Methods*, vol. 12, no. 4, pp. 351–356, 2015.

[32] N. J. Loman, J. Quick, and J. T. Simpson, "A complete bacterial genome assembled de novo using only nanopore sequencing data," *Nature Methods*, vol. 12, no. 8, pp. 733–735, 2015.

[33] M. A. Madoui, S. Engelen, C. Cruaud, C. Belser, L. Bertrand, A. Alberti, A. Lemainque, P. Wincker, and J. M. Aury, "Genome assembly using Nanopore-guided long and error-free DNA reads," *BMC Genomics*, vol. 16, no. 1, pp. 1–11, 2015.

[34] T. Szalay and J. A. Golovchenko, "De novo sequencing and variant calling with nanopores using PoreSeq," *Nature Biotechnology*, vol. 33, no. 10, pp. 1087–1091, 2015.

[35] C. Dekker, R. Article, and C. Dekker, "Solid-state nanopores," *Nature Nanotechnology*, vol. 2, no. 4, pp. 209–215, 2007.

[36] A. T. Carlsen, K. Briggs, A. R. Hall, and V. Tabard-Cossa, "Solid-state nanopore localization by controlled breakdown of selectively thinned membranes," *Nanotechnology*, vol. 28, no. 8, p. 085304, 2017.

[37] I. Yanagi, R. Akahori, T. Hatano, and K.-i. Takeda, "Fabricating nanopores with diameters of sub-1 nm to 3 nm using multilevel pulse-voltage injection.," *Scientific reports*, vol. 4, p. 5000, 2014.

[38] R. M. M. Smeets, U. F. Keyser, D. Krapf, M.-Y. Wu, H. Nynke, C. Dekker, N. H. Dekker, and C. Dekker, "Salt-dependence of ion transport and DNA translocation through solid-state nanopores," *Nano Letters*, vol. 6, no. 1, pp. 89–95, 2006.

[39] M. Wanunu, T. Dadosh, V. Ray, J. Jin, L. McReynolds, and M. Drndić, "Rapid electronic detection of probe-specific microRNAs using thin nanopore sensors," *Nature Nanotechnology*, vol. 5, no. 11, pp. 807–814, 2010.

[40] J. E. Hall, "Access resistance of a small circular pore," *The Journal of General Physiology*, vol. 66, no. 4, pp. 531–532, 1975.

[41] D. Stein, M. Kruithof, and C. Dekker, "Surface-Charge-Governed Ion Transport in Nanofluidic Channels," *Physical Review Letters*, vol. 93, no. 3, p. 035901, 2004.

[42] M. Firnkes, D. Pedone, J. Knezevic, M. Döblinger, and U. Rant, "Electrically facilitated translocations of proteins through silicon nitride nanopores: Conjoint and competitive action of diffusion, electrophoresis, and electroosmosis," *Nano Letters*, vol. 10, no. 6, pp. 2162–2167, 2010.

[43] S. W. Kowalczyk, A. Y. Grosberg, Y. Rabin, and C. Dekker, "Modeling the conductance and DNA blockade of solid-state nanopores.," *Nanotechnology*, vol. 22, no. 31, p. 315101, 2011.

[44] H. Kwok, K. Briggs, and V. Tabard-Cossa, "Nanopore fabrication by controlled dielectric breakdown.," *PLoS One*, vol. 9, p. e92880, jan 2014.

[45] K. Briggs, H. Kwok, and V. Tabard-Cossa, "Automated Fabrication of 2-nm Solid-State Nanopores for Nucleic Acid Analysis," *Small*, vol. 10, no. 10, pp. 2077–2086, 2014.

[46] C. M. Frament and J. R. Dwyer, "Conductance-based determination of solid-state nanopore size and shape: An exploration of performance limits," *Journal of Physical Chemistry C*, vol. 116, no. 44, pp. 23315–23321, 2012.

[47] C. M. Frament, N. Bandara, and J. R. Dwyer, "Nanopore surface coating delivers nanopore size and shape through conductance-based sizing," *ACS Applied Materials and Interfaces*, vol. 5, no. 19, pp. 9330–9337, 2013.

[48] Y. M. D. Bandara, B. I. Karawdeniya, and J. R. Dwyer, "Real-Time Profiling of Solid-State Nanopores during Solution-Phase Nanofabrication," *ACS Applied Materials and Interfaces*, vol. 8, no. 44, pp. 30583–30589, 2016.

[49] Y. M. Bandara, J. W. Nichols, B. Iroshika Karawdeniya, and J. R. Dwyer, "Conductance-based profiling of nanopores: Accommodating fabrication irregularities," *Electrophoresis*, vol. 39, no. 4, pp. 626–634, 2018.

[50] V. Tabard-Cossa, "Instrumentation for Low-Noise High-Bandwidth Nanopore Recording," in *Engineered Nanopores for Bioanalytical Applications: A Volume in Micro and Nano Technologies*, ch. 3, pp. 59–93, Ottawa: Elsevier Inc., 2013.

[51] R. M. M. Smeets, U. F. Keyser, M. Y. Wu, N. H. Dekker, and C. Dekker, "Nanobubbles in solid-state nanopores," *Physical Review Letters*, vol. 97, no. 8, pp. 1–4, 2006.

[52] S. Shekar, D. J. Niedzwiecki, C. C. Chien, P. Ong, D. A. Fleischer, J. Lin, J. K. Rosenstein, M. Drndić, and K. L. Shepard, "Measurement of DNA translocation dynamics in a solid-state nanopore at 100 ns temporal resolution," *Nano Letters*, vol. 16, no. 7, pp. 4483–4489, 2016.

[53] J. K. Rosenstein, M. Wanunu, C. A. Merchant, M. Drndic, and K. L. Shepard, "Integrated nanopore sensing platform with sub-microsecond temporal resolution," *Nature Methods*, vol. 9, pp. 487–492, may 2012.

[54] M. Wanunu, W. Morrison, Y. Rabin, A. Y. Grosberg, and A. Meller, "Electrostatic focusing of unlabelled DNA into nanoscale pores using a salt gradient," *Nature Nanotechnology*, vol. 5, pp. 160–165, feb 2010.

[55] F. Farahpour, A. Maleknejad, F. Varnik, and M. R. Ejtehadi, "Chain deformation in translocation phenomena," *Soft Matter*, vol. 9, no. 9, pp. 2750–2759, 2013.

[56] P. Rowghanian and A. Y. Grosberg, "Electrophoretic capture of a DNA chain into a nanopore," *Physical Review E*, vol. 87, no. 4, pp. 1–8, 2013.

[57] M. Muthukumar, *Polymer Translocation*. CRC Press, 2011.

[58] M. Muthukumar, "Theory of capture rate in polymer translocation," *Journal of Chemical Physics*, vol. 132, no. 19, 2010.

[59] B. Lu, F. Albertorio, D. P. Hoogerheide, and J. A. Golovchenko, "Origins and Consequences of Velocity Fluctuations during DNA Passage through a Nanopore," *Biophysical Journal*, vol. 101, pp. 70–79, 2011.

[60] T. Sakaue, "Nonequilibrium dynamics of polymer translocation and straightening," *Physical Review E - Statistical, Nonlinear, and Soft Matter Physics*, vol. 76, no. 2, pp. 1–7, 2007.
[61] T. Sakaue, "Sucking genes into pores: Insight into driven translocation," *Physical Review E - Statistical, Nonlinear, and Soft Matter Physics*, vol. 81, no. 4, pp. 1–6, 2010.
[62] T. Saito and T. Sakaue, "Dynamical diagram and scaling in polymer driven translocation," *European Physical Journal E*, vol. 34, no. 12, 2011.
[63] T. Ikonen, A. Bhattacharya, T. Ala-Nissila, and W. Sung, "Unifying model of driven polymer translocation," *Physical Review E*, vol. 85, no. 5, pp. 1–7, 2012.
[64] P. Rowghanian and A. Y. Grosberg, "Force-driven polymer translocation through a nanopore: An old problem revisited," *Journal of Physical Chemistry B*, vol. 115, no. 48, pp. 14127–14135, 2011.
[65] J. L. A. Dubbeldam, V. G. Rostiashvili, A. Milchev, and T. A. Vilgis, "Forced translocation of a polymer: Dynamical scaling versus molecular dynamics simulation," *Physical Review E - Statistical, Nonlinear, and Soft Matter Physics*, vol. 85, no. 4, pp. 1–12, 2012.
[66] S. C. Vollmer and H. W. de Haan, "Translocation is a nonequilibrium process at all stages: Simulating the capture and translocation of a polymer by a nanopore," *The Journal of Chemical Physics*, vol. 145, no. 15, p. 154902, 2016.
[67] A. J. Storm, C. Storm, J. Chen, H. Zandbergen, J.-F. Joanny, and C. Dekker, "Fast DNA Translocation through a Solid-State Nanopore," *Nano letters*, pp. 1–5, 2005.
[68] M. Mihovilovic, N. Hagerty, and D. Stein, "Statistics of DNA Capture by a Solid-State Nanopore," *Physical Review Letters*, vol. 110, no. 2, pp. 1–5, 2013.
[69] K. Briggs, G. Madejski, M. Magill, K. Kastritis, H. W. De Haan, J. L. McGrath, and V. Tabard-Cossa, "DNA Translocations through Nanopores under Nanoscale Preconfinement," *Nano Letters*, vol. 18, no. 2, pp. 660–668, 2018.
[70] A. J. Storm, J. H. Chen, H. W. Zandbergen, and C. Dekker, "Translocation of double-strand DNA through a silicon oxide nanopore," *Physical Review E*, vol. 71, p. 051903, may 2005.
[71] M. Wanunu, J. Sutin, B. McNally, A. Chow, and A. Meller, "DNA translocation governed by interactions with solid-state nanopores.," *Biophysical Journal*, vol. 95, pp. 4716–25, nov 2008.
[72] A. T. Carlsen, O. K. Zahid, J. Ruzicka, E. W. Taylor, and A. R. Hall, "Interpreting the conductance blockades of DNA translocations through solid-state nanopores," *ACS Nano*, vol. 8, no. 5, pp. 4754–4760, 2014.
[73] C. Plesa, N. V. Loo, P. Ketterer, H. Dietz, and C. Dekker, "Velocity of DNA during translocation through a solid state nanopore," *Nano Letters*, vol. 15, no. 1, pp. 732–737, 2015.

[74] D. Sean, H. W. de Haan, and G. W. Slater, "Translocation of a polymer through a nanopore starting from a confining nanotube," *Electrophoresis*, vol. 36, no. 5, pp. 682–691, 2015.

[75] N. A. W. Bell, K. Chen, S. Ghosal, M. Ricci, and U. F. Keyser, "Asymmetric dynamics of DNA entering and exiting a strongly confining nanopore," *Nature Communications*, vol. 8, no. 1, p. 380, 2017.

[76] K. Briggs, M. Charron, H. Kwok, T. Le, S. Chahal, J. Bustamante, M. Waugh, and V. Tabard-Cossa, "Kinetics of nanopore fabrication during controlled breakdown of dielectric membranes in solution," *Nanotechnology*, vol. 26, no. 8, 2015.

[77] J. H. Forstater, K. Briggs, J. W. F. Robertson, J. Ettedgui, O. Marie-Rose, C. Vaz, J. J. Kasianowicz, V. Tabard-Cossa, and A. Balijepalli, "MOSAIC: A Modular Single Molecule Analysis Interface for Decoding Multi-state Nanopore Data," *Analytical Chemistry*, vol. 88, no. 23, pp. 11900–11907, 2016.

Chapter 2

Fabricating Solid-State Nanopores for Single-Molecule Sensing

Kyle Briggs and Vincent Tabard-Cossa

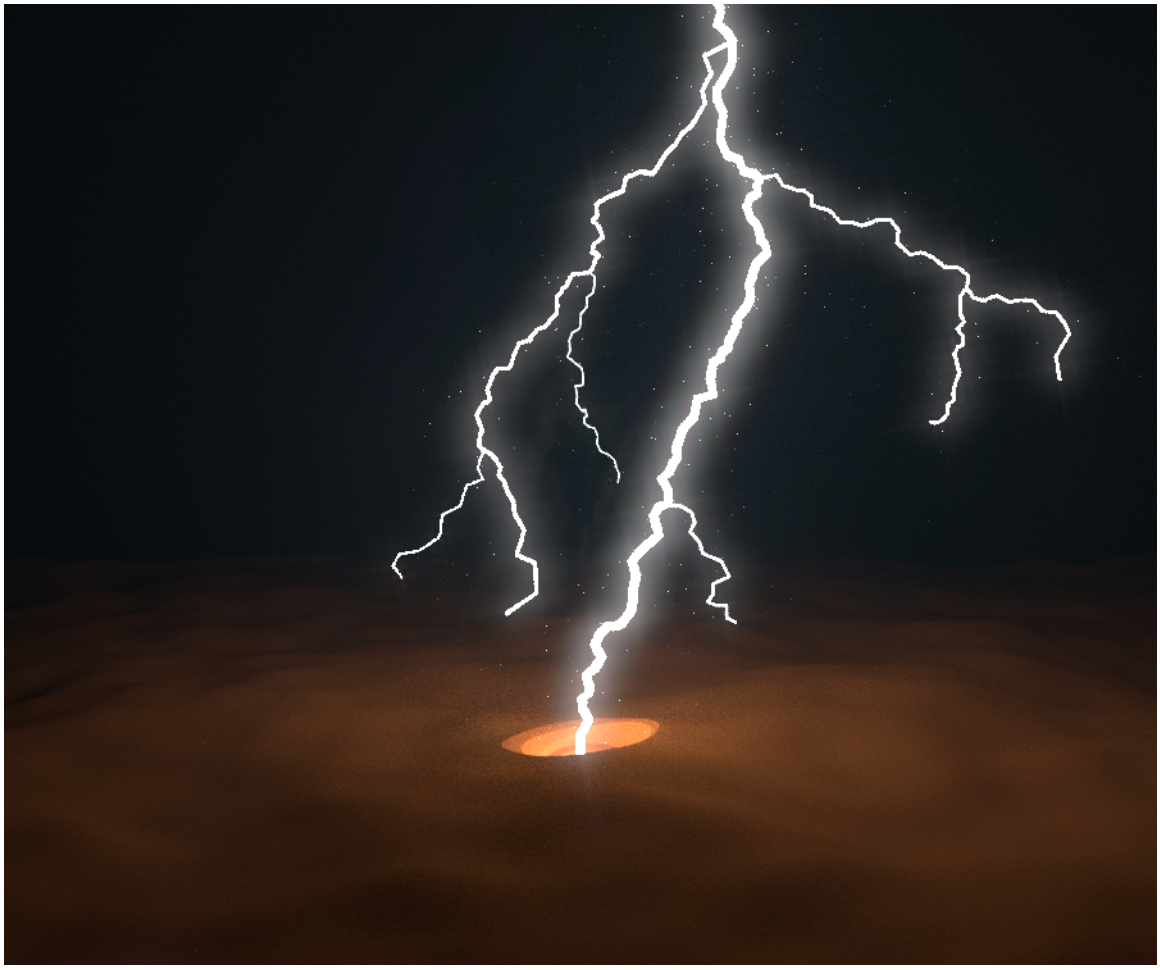

2.1 Introduction

The tremendous research efforts in nanopore-based sequencing over the last two decades have driven the emergence of a host of nanofabrication techniques geared toward the production of nanopores in thin solid-state membranes. The early 2000s saw the development of techniques with which to fabricate nanopores with dimensions in the 1 to 10 nm range in synthetic materials, in an effort to make biomimetic analogues of protein-based nanopores. In this chapter, the most used techniques will be reviewed, with a focus on tools or methods for fabricating nanopores in solid-state membranes that result in pores that can be used for single-molecule detection.

While there have been numerous worthy contributions to the growing list of nanopore fabrication techniques, including track-etching of polymeric membranes[1,2], stretchable polymeric membranes with tuneable pore sizes[3–5], and numerous wet-etching techniques[6–13], and more recent work using laser illumination to open single nanopores[14,15], we are unable to reasonably summarize them all here. We will focus instead on the handful of techniques that are currently most widely used to make sub-10 nm nanopores in inorganic, solid-state membranes or substrates. This restriction on the physical dimensions of the nanopore is particularly challenging, largely due to the fact that this size range is well below the limit of resolution of lithographic techniques, which has necessitated the development of alternative approaches. Other techniques also exist with which to fabricate arrays of nanopores[11,16–19], although these are generally are not capable of making very small or very thin pores, nor do they have the same level of precision as single-pore techniques.

The first two techniques to be discussed involve direct drilling of materials with tightly focused beams of ions or electrons. Prior to their development, it was known that beams of charged particles could induce controllable material changes, including

drilling holes, in dielectric membranes and heterostructures, knowledge that until that point had found application mainly in the production of metallic point contacts[20].

Early work with charged particle beams used a collimated Argon ion beam to open a nanopore by sputtering away SiN_x material leading to the tip of a cavity on the opposite side of the membrane[21]. It was then shown that one could use the same Argon ion beam at lower energies to controllably shrink existing nanopores by locally melting silicon dioxide membranes[22], followed by a demonstration of direct drilling of these nanopores using focused Argon beams prior to controlled shrinking[23]. Soon after, it was demonstrated that not only was an analogous controlled shrinking effect accessible using the electron beam from a transmission electron microscope (TEM), but that the electron beam could be used to directly drill nanopores below 10 nm in size[24] before controllably shrinking them even further. Beam-based pore fabrication was further refined to be able to directly drill small nanopores without requiring a post-drilling shrinking step, achieving sub-10 nm nanopore sizes using gallium ions[25,26], though the precision and reproducibility of such small pores is unclear. Sub-4 nm pores can be reliably achieved with Helium ions[27], while the current state of the art TEM-based drilling technique can make pores on the order of a single nanometer[28]. Various versions of both techniques are still used today, and despite its complexity and cost, electron beam drilling has been the workhorse of solid-state nanopore fabrication for the past 20 years, largely due to the fact that many nanopore labs have ready access to existing EM infrastructure.

A second class of nanopore is based on pipette pulling to define nanometer scale pipette tips. Nanopipettes were a natural extension of efforts to improve the spatial resolution of scanning probe microscopy techniques that employed micron-scale orifice pipettes to study ion activity in cells. By careful choice of pipette pulling parameters, it is possible to fabricate nanopipettes with openings on the order of 10 nm[29,30] quite

simply, which can applied to the detection of DNA and nanoparticle molecules[31]. It was later shown that like pores in flat membranes, nanopipette tip openings could be controllably shrunk under electron beam radiation, enabling nanopipettes to approach the single nm diameter limit[32], though in practice this shrinking technique is very rarely used due to the added complexity in fabrication.

More recently, nanopore fabrication based on dielectric breakdown of insulating membranes under high electric field stress was reported. It was first demonstrated that high electric fields could be used to controllably enlarge existing nanopores drilled by TEM[33], followed by the demonstration that this technique could be applied to pristine membranes to drive the formation of a single pore when the value of the sustained electric field approached that of the breakdown strength of the material. Controlled breakdown (CBD) fabricates pores directly in an electrolyte solution by applying high electric fields to an insulating membrane or membrane stack, resulting in localized breakdown of the insulating properties of the membrane, and the highly controllable formation of single nanopores[34,35] at a random position on the membrane. Sub-nm nanopores can be fabricated using this technique[36], with high yield reported for 2 nm nanopores[37]. Due to the inherent resolution, precision, simplicity, and near-zero cost of this technique, CBD is an attractive alternative to beam-based drilling techniques as the method of choice for nanopore research.

2.2 Electron Beam Drilling

2.2.1 Fabrication

Nanopore fabrication by electron beam is achieved by direct sputtering of membrane material by a tightly focused beam in a standard commercial transmission

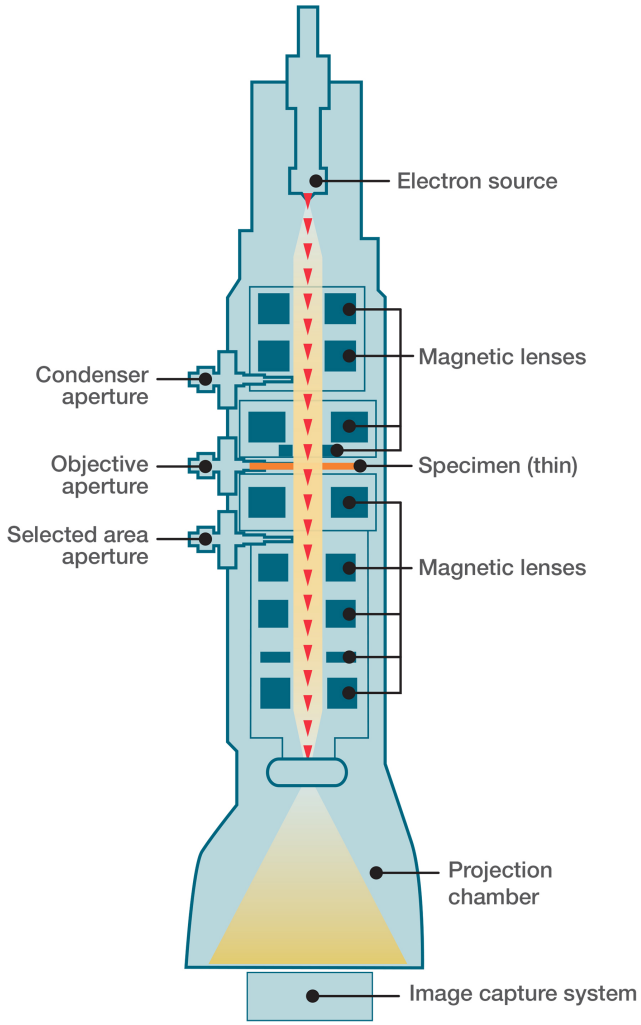

Figure 2.1: A schematic illustration of the electron optics used in a TEM. Image courtesy of Thermo Fisher Scientific.

electron microscope (TEM)[40], which is illustrated schematically in Figure 2.1. By focusing an electron beam down to a few nanometer spot size, it is possible to remove membrane material at the focus and thereby open a nanoscale hole in the membrane[41]. This method is generally applicable to a variety of materials, including SiN_x, SiO_2[42], Al_2O_3[43], HfO_2[44], graphene[45–47], MoS_2[48], WS_2[15], and ZnO_2[49]. The kinetics of material removal by the electron beam are complex, with different mem-

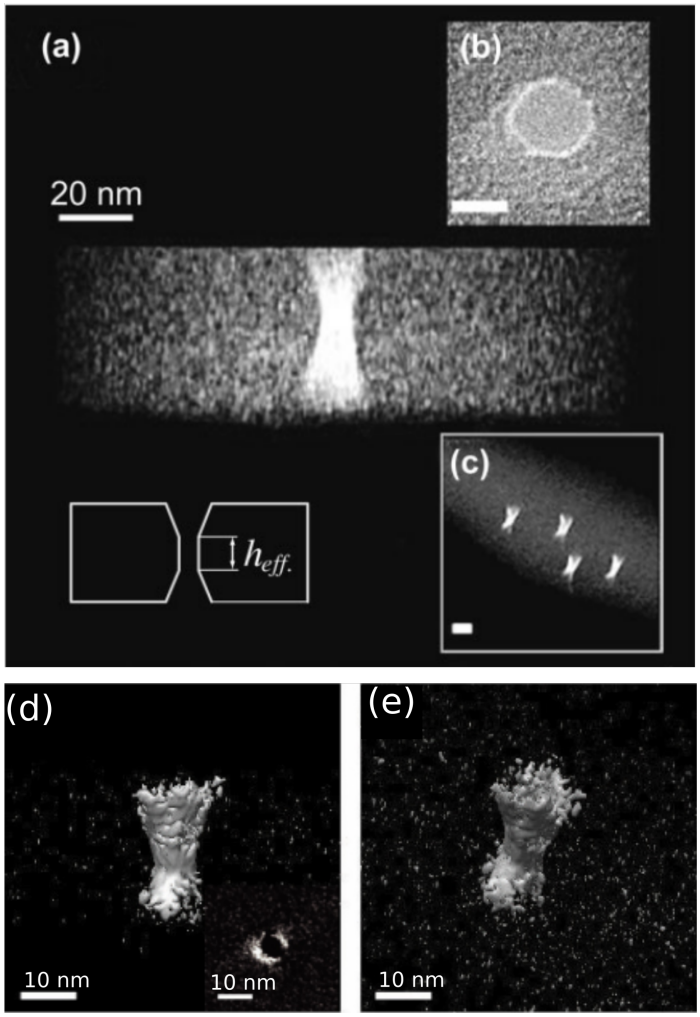

Figure 2.2: Electron beams from a TEM typically have a Gaussian intensity profile with hour-glass shaped contours, which leads to b) hour-glass shaped pores, as verified using TEM tomography to reconstruct the 3-dimensional nanopore profile[38,39].

brane elements being removed at different rates around the beam focus[50]. When SiN_x membranes are locally thinned using an electron beam down to their theoretical limit of stability, all that remains is amorphous silicon[51]. Only a handful of studies have reported the nanoscopic details of changes to the membrane material at the point of pore formation[40,52,53].

Due to the inherent divergence of a tightly focused electron beam, the pores that result from this technique are typically hourglass shaped, leading to a situation

wherein the effective thickness of the actual nanopore constriction is thinner than the nominal membrane thickness[38,39,50,54,55], somewhat improving spatial resolution and sensitivity. Some examples are show in Figure 2.2. In spite of this, electrical characterization of TEM-drilled nanopores typically assumes a cylindrical geometry with a reduced effective membrane thickness to account for the deviation from this assumption instead of using a model that accounts for curvature in the nanopore geometry. This is because the additional parameters needed for the fit are difficult to accurately fit with information about the nanopore conductance alone without somehow varying the pore size during measurement[56–60]. Most work with TEM pores models them as cylindrical pores with a reduced effective thickness of one third of the nominal membrane thickness[55].

2.2.2 Size Control

Electron beams can be used to controllably grow or shrink existing nanopores in solid-state membranes through local melting of the membrane material using a beam with a wider focus, depending on the initial nanopore size[61]. This behavior can be understood with a simple energetic argument. The free energy difference between in intact sheet with surface tension γ of thickness h and one containing a pore of radius r is

$$\Delta F \propto \gamma r h \left(1 - \frac{r}{h}\right), \tag{2.1}$$

which has a maximum at $r = h$, that indicates that the pore will grow if $r > h$, and shrink otherwise, a condition that agrees well with experimental evidence[24]. An example of this effect is shown in Figure 2.3.

Nanopore drilling by TEM has the advantage of providing a direct visual measurement of the resulting nanopore immediately after fabrication. However, care should

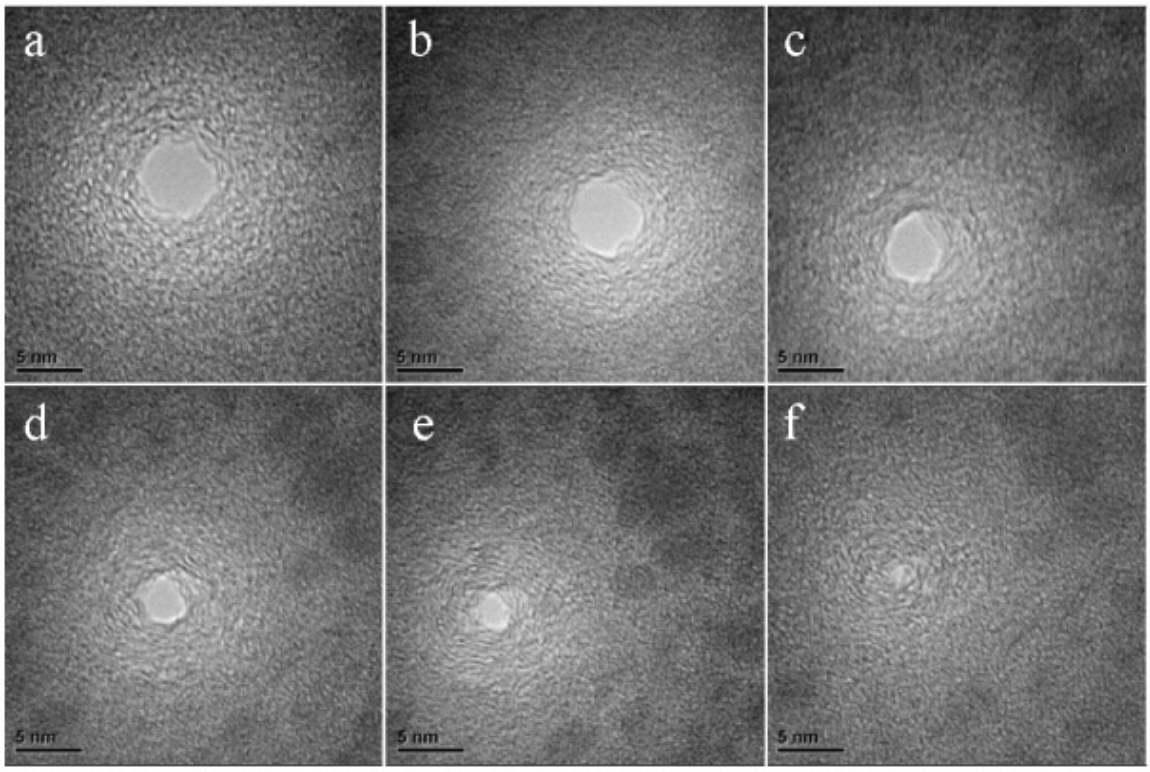

Figure 2.3: Continuous shrinking of an initially 5 nm nanopore down to 1 nm using 200kV electron beam radiation from a TEM over the course of 1 hour[61].

be taken when correlating images obtained this way to conductance measurements of the resulting nanopore in liquid, since imaging them for too long can also alter their size. Moreover, pores formed in TEM are formed in vacuum and typically require treatment in Piranha solution to make sufficiently hydrophilic for subsequent wetting in the solution used for molecular sensing. These additional processing steps and harsh etches can change the pore size from what was measured in the TEM, so the pore that is eventually wetted in solution no longer necessarily in retains its initial size.

2.2.3 Outlook

Despite its many shortcomings, nanopore drilling by TEM has been the main solid-state nanopore fabrication method used by a majority of nanopore research labs since its initial development, largely due to the fact that most major universities already have TEM infrastructure. It has been an enabling tool that took solid-state nanopores from an idea to a mainstream research field and demonstrated numerous exciting applications[62–65]. While the prohibitive equipment cost, extensive training required and inherently serial and manual nature of the technique will most likely not allow this technique to be used outside of research settings, TEM drilling of nanopores will likely continue to be used in many labs for applications requiring precisely located nanopores or visual feedback of the details of pore fabrication.

2.3 Ion Beam Drilling

2.3.1 Fabrication

Drilling of nanopores using ion beams is in principle identical to TEM drilling, except that an ion beam is used instead of an electron beam. Most realizations of this technique use noble gas ions, though other ions can be used and are discussed below.

Fabrication of pores using heavy noble gas ions generally proceeds in one of two ways. In the first method, a large tapered cavity is made in one side of the membrane, followed by exposure of the opposite side to a collimated ion beam that sputters material away until the very tip of the tapered cavity is broken through, producing a single pore[21]. This technique is shown schematically in Figure 2.4, and is generally termed ion-beam sculpting.

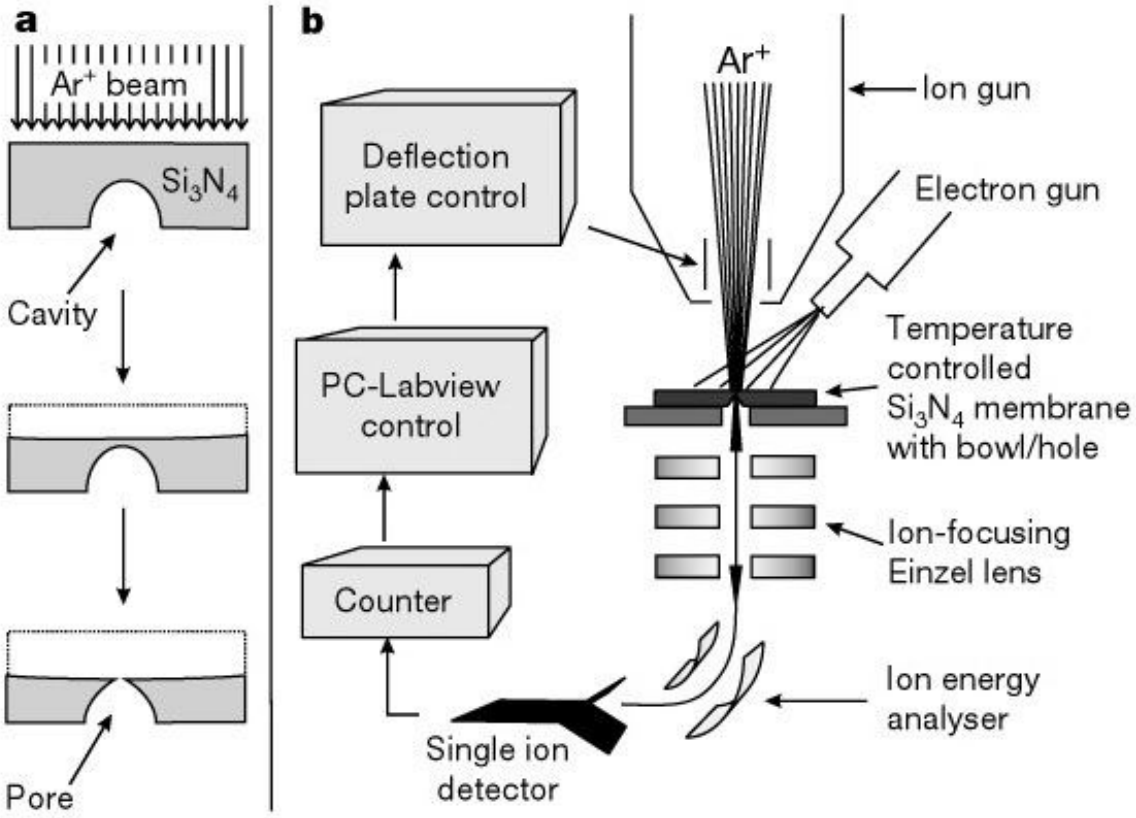

Figure 2.4: a) a collimated Ar^+ beam removes material from the surface of a membrane opposite a large cavity. The beam is terminated when ion transmission is detected, resulting in a nanopore at the tip of the cavity. b) A schematic diagram of the drilling setup[21].

Ion beam sculpting works with all noble gas ions up to xenon. While heavier ions have been shown to be more efficient at controlling the nanopore size by shrinking them, the mechanism of closure is a competition between mass flow of locally melted membrane material and sputtering of existing material by incident ions. Indeed, these competing effects can be tuned to either grow of shrink the pore through the choice of ion and beam characteristics[66].

In addition to patterning of bulk dielectric membranes, focused ion beam (FIB) techniques have been applied to metallized membranes and graphene[67,68]. Depending on the choice of drilling ion, metallization of the membrane may even be a requirement

for fabrication, since without a conductive layer, charge buildup due to implanted ions can defocus the beam.

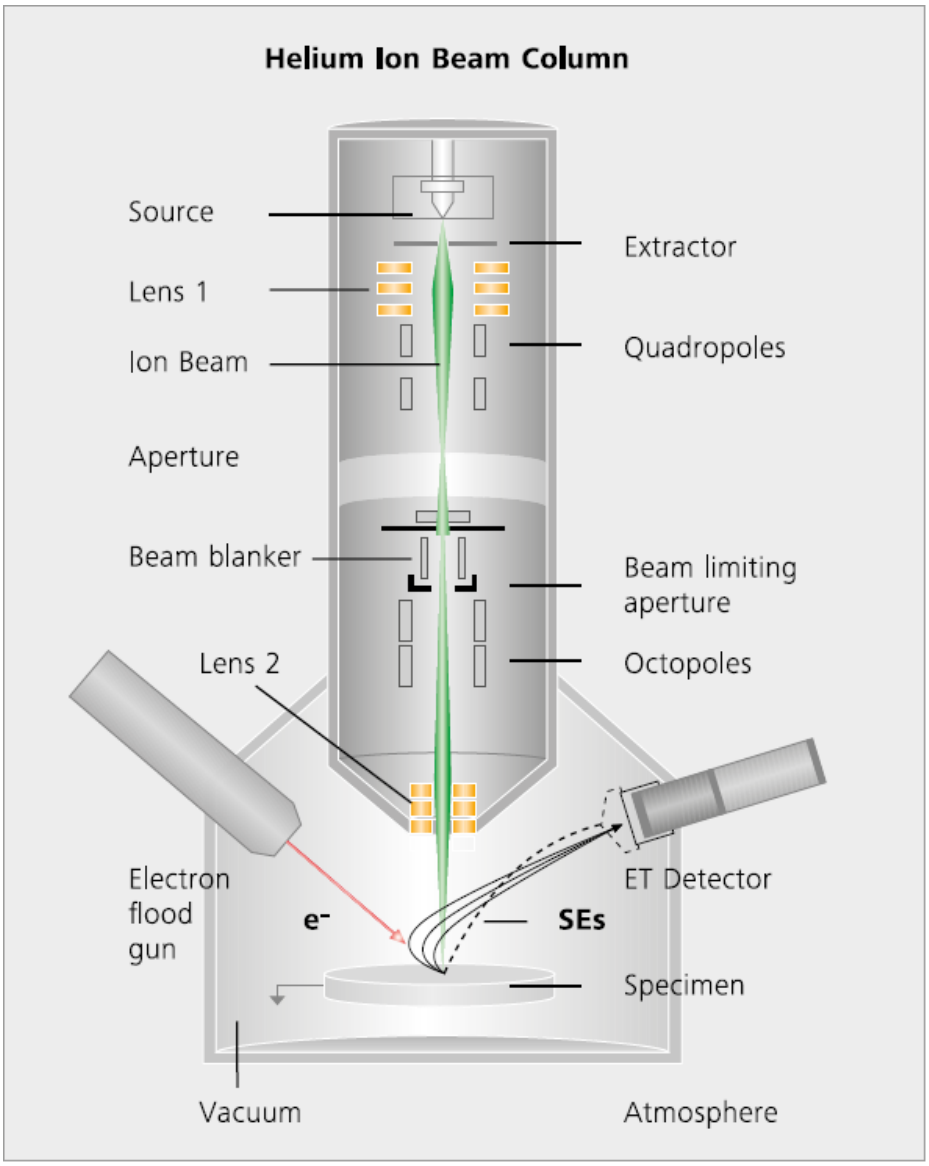

Figure 2.5: A schematic diagram of helium ion microscope components. With a sufficiently tight focus, such a system can drill sub-5 nm nanopores. Image used with permission from ZEISS Microscopy.

The second, and currently more widely used method, involves essentially the same process as TEM drilling and is achieved by direct focusing of the ion beam down to

a sufficiently small spot size to drill sub 10-nm nanopores through direct sputtering. Generally helium ion drilling[27,28,69] is preferred, for a number of reasons. Heavy ions do not penetrate very far into the material they are drilling, and tend to get embedded in the bulk material, resulting in buildup of charges that in turn defocus the incoming beam and reduce precision. While this effect can be mitigated by adding a conducting layer to the membrane to neutralize implanted charges, this is undesirable due to the added fabrication steps. Helium ions, being very light, have a large penetration depth, on the order of 100 nm[70], which often exceeds the thickness of the material being sputtered, limiting charge buildup and improving precision and simplifying the fabrication requirements[71–75]. A schematic of a helium ion microscope is shown in Figure 2.5.

The mechanism of material removal by ions is complex. At low ion flux, simulations indicate that direct sputtering dominates, while at high flux it is a more thermally-driven process that involves local melting and even boiling of membrane material[76]. Helium ions are particularly interesting, since depending on the membrane thickness, helium ions with sufficient energy can actually penetrate deeply in the membrane material and remove atoms on both sides of the membrane simultaneously[77], or create voids and nanobubbles inside the membrane bulk for membranes thicker than the helium ion penetration depth[72,73,75,78].

2.3.2 Size Control

Control of the initial pore size can be improved even to below the FWHM of the incident beam by monitoring the transmission intensity of ions through the membrane[79]. Of the various ion beams used for fabrication, helium has been shown to be most consistently able to make small pores. Once a pore is formed, its size can

be tuned using a technique similar to that used with TEM drilling, exposing the existing pore to a lower-intensity ion beam, or an electron beam from a TEM[21,22,66]. Pores can either grow or shrink using this method, depending on the beam intensity and the temperature[21]. Because of the focused nature of the ion beam, nanopores fabricated with ion beams are typically hour-glass shaped as well, depending on the desired aspect ratio.

2.3.3 Outlook

Because many FIB systems are usually dedicated pore fabrication systems, unlike TEM, ion beam drilling is more amenable to automation, allowing programmable fabrication of small nanopore arrays[80], or pre-patterning (for example, local thinning) of membrane surfaces prior to nanopore fabrication by other methods[78].

While helium ions in particular can achieve pore diameters in the 5-10 nm range, ion beam drilling is generally less widely used than electron beam drilling as a nanopore fabrication technique. This is mainly due to the fact that the equipment either needs to be home-built[81], such as for ion beam sculpting, or is still relatively less commonly found in nanofabrication facilities, such a helium ion microscope (ZEISS ORION NanoFab).

2.4 Nanopipettes

2.4.1 Fabrication

Unlike most other methods of solid-state nanopore production, nanopipettes do away with the membrane entirely in favor of a nanoscale opening at the end of a glass or quartz pipette, produced using standard pipette pulling techniques and in-

strumentation. Nanopipettes are fabricated using commercially available benchtop pipette pullers, which with careful choice of pulling parameters and starting pipette can produce inner tip diameters in the range of tens of nanometers[29–31,82–84]. Because of the tapered nature of the top of the pipette after pulling, the sensing region is potentially quite long compared to membrane-based nanopores, reducing spatial resolution in exchange for easy benchtop fabrication.

Electrically and fluidically nanopipettes behave quite differently from solid-state membrane-based nanopores, due to the differences in material used and form factor, which presents some unique fabrication opportunities. The conical and inherently asymmetric nature of the nanopipette opening leads to current rectification[29] and significant electroosmotic flow. The excellent dielectric properties of the glass used for nanopipettes leads to very low capacitance and reduced high-frequency noise compared to more conventional membrane-based nanopores[85].

Nanopipettes are amenable to functionalization with a variety of materials, including gold[86,87]. Unlike solid-state membranes wherein the entire membrane would be coated with a planar gold layer, the sharp tip of the nanopipettes can be leveraged to study effects such as dielectrophoresis, which require sharp electrodes and large potential gradients[87,88].

Nanopipettes can also serve as the substrate for various biomolecular layers, including antibodies[82], lipid bilayers[89] optionally containing biological pores[90] and synthetic pores produced using DNA origami techniques[91].

Nanopipette fabrication in double-barrelled pipettes has also been recently demonstrated using identical techniques to regular nanopipette pulling, allowing for the use of two pores in series, mediated by a meniscus of liquid at the tip[92], or functionalization into an electrically gated nanopore transistor[93].

2.4.2 Size Control

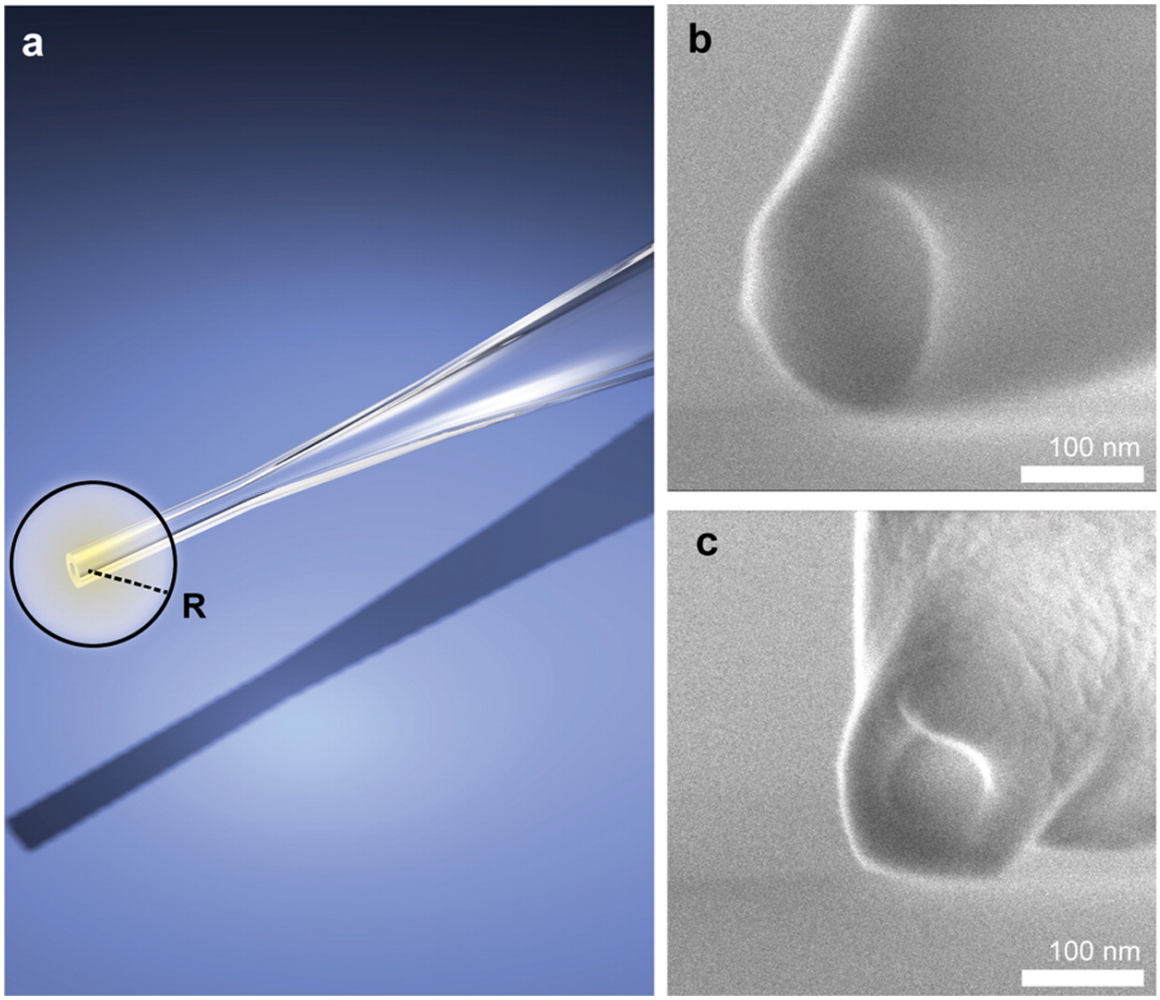

Figure 2.6: a) schematic diagram of the end of a nanopipette. b) A SEM micrograph of a nanopipette tip prior to electron beam irradiation. c) The same nanopipette tip after 14 minutes of electron beam exposure, showing partial shrinking and possible carbon deposition[32].

Without significant additional work to shrink pores, it is also not possible to reliably produce nanopipettes with openings much smaller than 10 nm. Once a nanopipette is formed, the size can be controllably reduced down to around 10 nm by irradiation in an electron beam[94], though having to do so mitigates the advantages of being able to actually make them with a benchtop instrument. An example is shown

in Figure 2.6. Since fabrication of a new nanopipette is fast and cheap, shrinking is generally eschewed in favor of simply making a new one until the desired dimensions are achieved.

2.4.3 Outlook

Compared to beam-based drilling techniques, nanopipettes offer significant advantages in terms of simplicity of fabrication, equipment cost, and noise properties, at the cost of larger minimum pore size and asymmetric electrical characteristics. Nanopipettes are versatile experimental tools that offer excellent noise performance at the cost of ionic current rectification and limited size control.

2.5 Controlled Breakdown

2.5.1 Introduction

Dielectric breakdown is a ubiquitous process in solid-state electronics, and is one of the most common causes of failure in most transistor-based electronics. It results when the electric field applied across an electrically insulating material exceeds its dielectric strength, making it conductive while causing physical damage to the material. For most applications this is an uncontrolled and detrimental event, resulting in failure of the device in question. In this context, it is a very well-studied problem, though most research efforts over the years have been applied toward ways to understand and avoid it. A review of the physics underlying dielectric breakdown phenomena in solid-state electronics is given by Lombardo *et al*[95].

When an electric field on the order of the dielectric strength of the membrane material is applied across a dielectric, it partially loses its insulating properties and

a leakage current flows through it. This current in generally attributed to tunnelling of electrons or holes, and causes localized damage to the bulk material (e.g. a broken chemical bond), which is assumed to take the form of neutral charge traps between which electrons can also tunnel if they are sufficiently close. The breakdown process then proceeds via a percolation effect, mediated by the fact that as these traps build up, they locally reinforce the tunnelling current at that location. Once a connected path of these traps exists that spans the material, a conductive path through is formed, and dielectric breakdown occurs, irreversibly damaging the material at that location.

Nanopore fabrication by controlled breakdown of membranes in solution harnesses this normally destructive and uncontrollable process to achieve precise nanofabrication of nanopores in solid-state membranes[34,96].

In the most basic realization of this approach, an insulating membrane or multilayered membrane stack is immersed between two fluidic reservoirs containing a conductive solution, usually an aqueous electrolyte, such that the only path for current flow between the reservoirs is through the nominally insulating membrane itself. A voltage is applied between the two reservoirs such that the electric field is smaller than, but on the order of the dielectric strength of the membrane material. Sustaining this electric field then drives tunnelling current through most likely a number of randomly distributed hot spots on the membrane. Eventually one such spot forms a localized path of conductive defects that spans the membrane before the others and breakdown occurs. The material at the damaged path is quickly washed away in the solution, leaving behind a nanoscale hole through the membrane[35]. The conductive solution fills the resulting nanopore and contributes an ionic current through the pore, which can be used as a feedback mechanism to terminate the voltage before further damage is done. This process, termed controlled breakdown (CBD) is shown

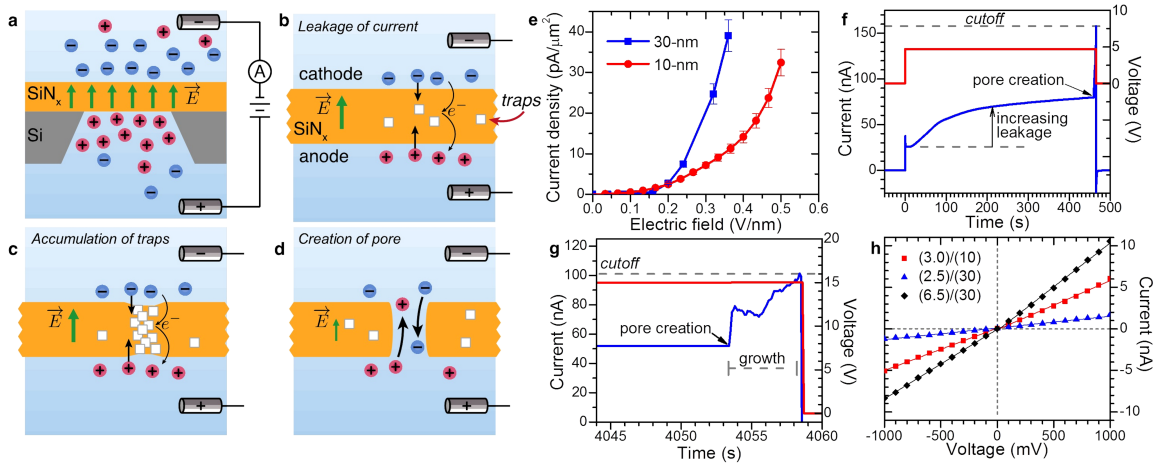

Figure 2.7: a) the mechanism of dielectric breakdown in solution, wherein an electric field applied across an insulating material drives tunnelling current through the material b) that in turn causes damage and reinforces the tunnelling current c). When a connected path of defects forms, high current causes material removal d). e) The charge density across the entire nanopore chip as a function of applied electric field, showing exponential dependence. f) A typical realization of DC CBD, showing slowly varying leakage current as damage accumulates, following by a spike indicating the opening of a pore. g) If the transmembrane voltage is not terminated immediately after pore fabrication, the pore will continue to grow as long as voltage is applied. h) Typical I-V characteristics of nanopores post-fabrication[34].

in Figure 2.7.

Because nanopores fabricated this way are made directly in the same solution and setup that is later used for single molecule sensing, this method of nanopore fabrication greatly increases the yield of precisely sized, low-noise nanopores compared to ex situ fabrication methods such as TEM and FIB. This is due to the fact that pores produced by CBD are immediately wetted as soon as they are fabricated, avoiding additional handling steps to subsequently facilitate wetting.

2.5.2 Fabrication

There are numerous ways to achieve control of dielectric breakdown. The first published realization of this scheme used active feedback and a DC bias voltage: by

monitoring the current through the membrane, one can detect an abrupt increase in the current when breakdown occurs that corresponds to the onset of ionic current passing through the newly opened pore. This can be used as a signal to terminate the voltage as soon as it is detected[34] (Figure 2.7). Feedback speed requirement are modest, needing only a response time on the order of 0.1s to reliably achieve pores as small as 2 nm[37].

Several other control approaches have been developed. In order to use a minimal voltage to open the nanopore, one can employ a slowly increasing voltage until the moment of breakdown[78]. More recently, a current clamp approach was employed, varying the voltage[98] to maintain a fixed tunnelling current, which naturally reduces the applied voltage when a pore is opened and the membrane resistance in consequently reduced. Alternatively, to avoid setting a feedback mechanism, others apply short voltage pulses interleaved with low voltage monitoring to check if a pore formed during the high voltage step[100]. One of the simplest options, which obviates the need for actives feedback entirely, is to use a resistor or otherwise passive resistive element (such as a long fluidic channel, for example) with resistance on the same order as the desired nanopore itself in series with the membrane. Immediately after pore fabrication, this resistive element would provide passive reduction in the voltage across the pore immediately after fabrication, since the resistive element then forms a voltage divider with the nanopore. As the pore grows, the voltage across it naturally drops and it transferred to the resistive element, limiting its size. Hybrid schemes also exist, wherein DC voltages are increased in steps until breakdown occurs[99]. While these schemes differ in their implementation and have been assigned a variety of acronyms, the mechanism by which the nanopore is formed appears to be the same in all cases. Several examples are shown in Figure 2.8.

When using active feedback and a DC bias it is particularly important to limit

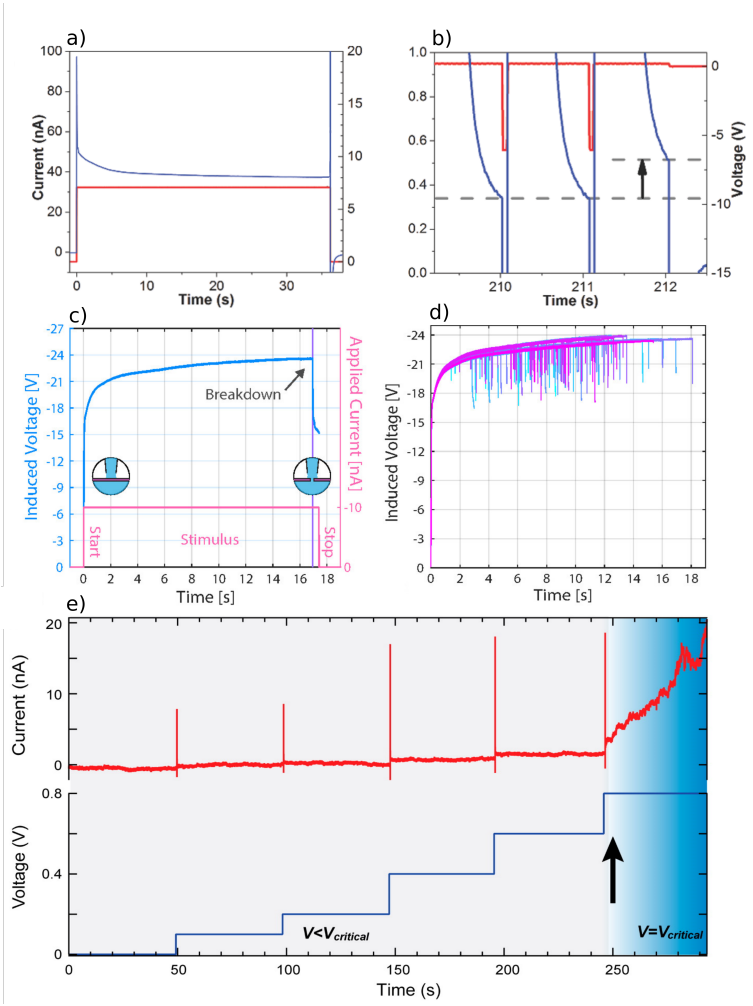

Figure 2.8: a) A typical realization of a simple DC bias control scheme, in which the voltage (red) terminates when the current (blue) spikes[97]. b) A realization of a constant pulsed voltage control scheme, in which high voltage pulses are following by low-voltage monitoring steps until the low-voltage current exceeds a threshold[97]. The high-voltage current response is not shown on this scale, since it is dominated by capacitive contributions and is not a useful quantity. c) A realization of a current-clamp fabrication scheme, in which the voltage is varied under fixed current until the opening of a pore is heralded by a sudden decrease in the voltage[98]. d) Typical voltage traces using the technique in c). e) A hybrid scheme in which the voltage across a MoS_2 membrane is periodically increased until pore formation is heralded by an increase in the current[99].

the voltage to biases such that the time to pore fabrication is much longer than the feedback time, since the time-to-breakdown is exponentially dependent on the

applied voltage. Because of the highly concentrated electrolyte and the fact that the membrane is not perfectly insulating at high voltage, the formation of the first pore only perturbs the electric field in its immediate vicinity, meaning that the generation of defects on the rest of the membrane continues unabated even after the pore is opened as long as a sufficiently high electric field continues to be applied. Since defects build up at different random locations over the membrane during electric field application, the time to fabrication of a second pore is much shorter than the time to the first pore, and using voltages too high for the feedback time of the system can lead to the formation of multiple pores before the voltage can be terminated[78,101].

Nanopore fabrication by CBD has been demonstrated on a variety of membrane materials and architectures. In addition to the usual nanopore staple of thin SiN_x, SiO_2[34], and HfO_2[102] films, it has been used to make pores in 2D materials, including graphene[100] and transition metal dichalcogenides such as MoS_2 and WsE_2[99]. In the 2D case the kinetics are qualitatively different, since there is no bulk materials in which to build up charge traps; rather, the first atom damaged by tunnelling current becomes the location of the pore. However, this is still a weakest-link problem governed by the kinetics underlying dielectric breakdown in the limit of membrane thickness approaching zero. To date, no studies have reported the details of time-to-breakdown distributions on 2D membranes.

CBD has also been used to realize pores through composite structures involving both dielectrics and metals (SiN_x/Au, SiN_x/Au/HfO_2, shown in Figure 2.9), as well as stacked layers of different dielectrics (SiN_x/HfO_2[103]). In the case of a membrane consisting of a gold layer on top of SiN_x, the breakdown process was shown to remove a circular of gold concentric with the fabricated nanopore[97], hinting at the enticing possibility of single-step and automated fabrication of a nanopore inside a zero-mode waveguide. Depositing a few atomic layers of HfO_2 on top of SiN_x has been shown

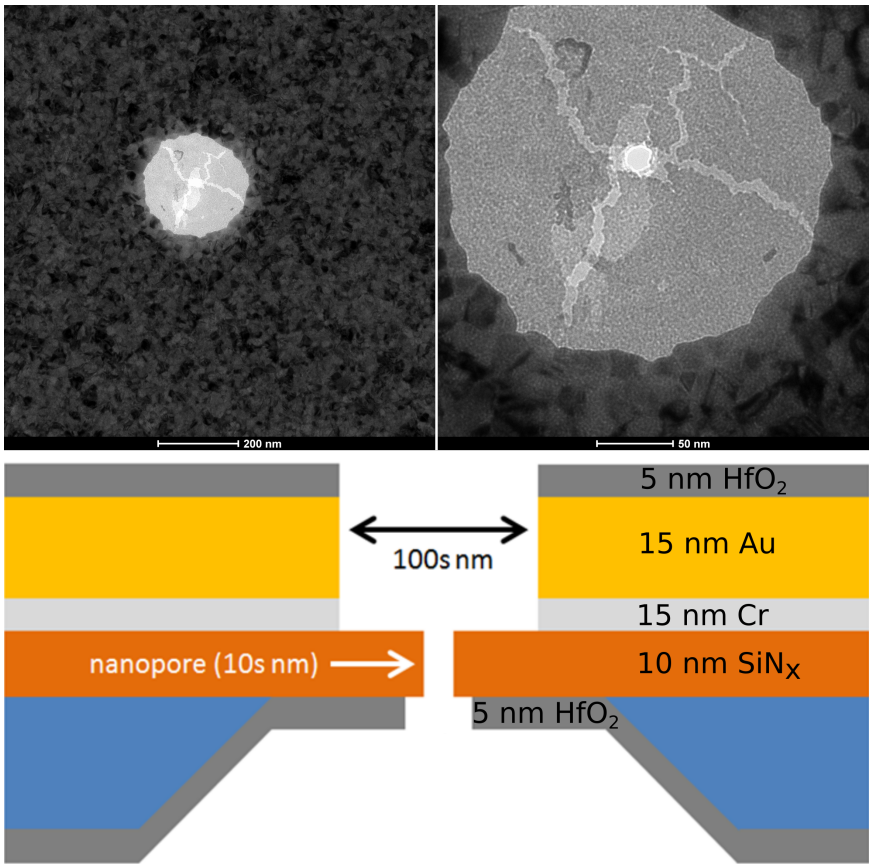

Figure 2.9: CBD can be used to fabricate pores through multilayers structures, even ones that include conductive layers like gold. Above, fabrication of a nanopore in a membrane stack consisting of SiN_x, Au, Cr, and HfO_2 is shown to produce a single nanopore concentric with a larger circular area in which the gold layer has been removed.

(unpublished data[104]) to stabilize solid-state nanopores, limiting pore growth to less than 0.1 nm over 6 days when stored in LiCl solution[103]. Moreover, CBD was used to fabricate a pore through a SiN_x membrane interfaced with a conductive gels[105]. As long as the membrane is in electrical contact with the voltage source, CBD can be used to fabricate a nanopore in any geometry and in almost any device architecture.

It should be noted that care needs to be taken when fabricating nanopores in membranes that have very low capacitance. While low capacitance is desirable as a way to suppress high-frequency noise in the nanopore ionic current signal, it can

also cause premature and unwanted breakdown if any small charge imbalance Q exists across the membrane prior to pore fabrication. Because the voltage across a capacitor with capacitance C is $V = \frac{Q}{C}$, even a small charge imbalance can induce voltages above the dielectric strength of the material in the low capacitance limit, causing the formation of multiple defects in the membrane. For typical SiN_x membranes the capacitance is high enough (greater than 10 pF) to limit this effect, but this can cause issues for capacitance-optimized membrane structures. Luckily this can easily be avoided by briefly shorting both sides of the membrane, with for example a Ag/AgCl electrode connecting the two opposing fluidic reservoirs, to balance any charges during the membrane wetting step[106].

Thus far, CBD has been able to fabricate a nanopore in every combination of membranes and membrane stacks that have been attempted, and has provided no reason to believe it will not continue to work as more complex structures are tested. This opens the possibility for simple fabrication of pores with embedded electrodes or plasmonic structures, which will likely find an important role in applications of nanopores moving forward.

2.5.3 Size Control

Unlike beam-based drilling techniques that tune pore sizes by starting with a large pore and shrinking it, CBD can be used to fabricate a small pore (typically around 2 nm when using 10 nm thick SiN_x, see Figure 2.10) and then enlarge it to the desired size with angstrom precision, or atomic precision in the case of 2D materials. Sub-1 nm openings have been fabricated, though the accuracy/precision in this size range is difficult to verify, since most biological polymers (proteins, DNA) are above this size.

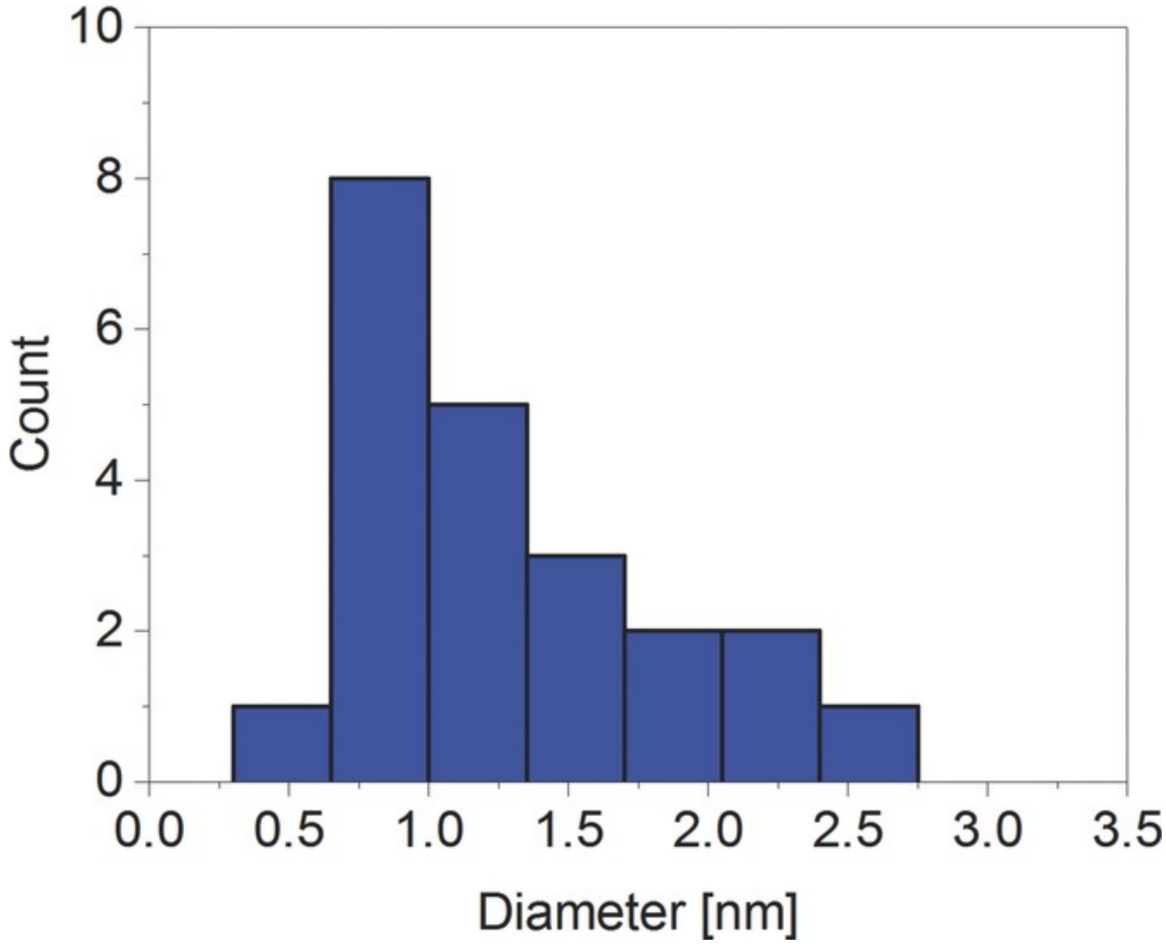

Figure 2.10: Nanopores fabricated by CBD can start out sub-nm in size, after which they can be controllably enlarged to any desired size. The distribution shown above represents the pore size for nanopores made in 10 nm thick SiN membranes fabricated in 1M KCl pH 10, after aging in 3.6M LiCl pH 8 for up to 24 hours[37].

Once a pore is formed, it can be controllably enlarged using moderate electric fields[33]. By applying pulses of enlarging voltage alternating with low-voltage monitoring of the nanopore, sub-nm precision can be achieved. It is generally more difficult to enlarge a pore reliably using continuous DC bias since the nanopore is past the Ohmic regime and no model exists to related conductance to pore geometry for such large voltages[107,108]. Even so, some groups do use DC bias to controllably enlarge pores as well[99]. Note that this scheme is similar to one of the presented alternatives

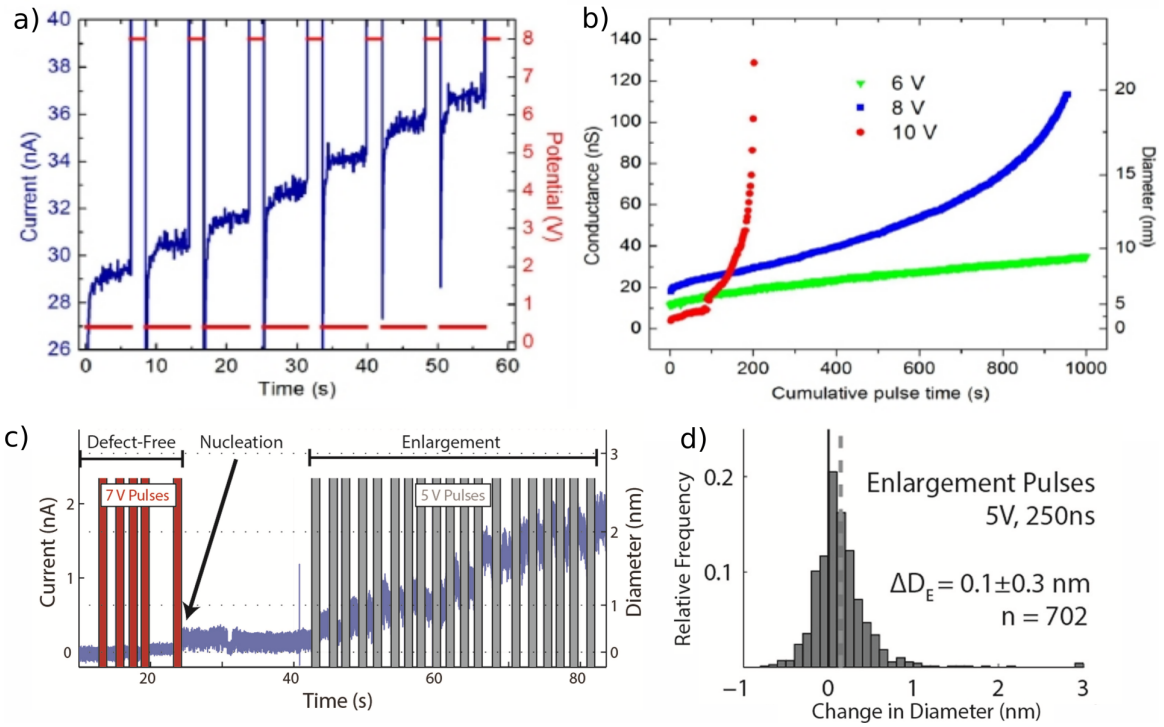

Figure 2.11: a) 8 V pulses are used to enlarge a pore in a 30 nm SiN_x membrane. b) Nanopores show a variety of enlargement profiles under pulsed DC bias, with most growing faster as they enlarge. c) 5 V pulses are used to enlarge a pore in graphene after pulsed fabrication. d) The change in graphene nanopore size per pulse indicates that the enlargement method can control pore size with atomic precision in 2D materials[100].

used for fabrication, but uses lower voltages to achieve more controllable pore growth to avoid overshooting the size, typically at most one third to one half of the dielectric strength of the membrane for bulk membrane materials.

Alternatively, a current clamp can be used to slowly reduce the voltage required to maintain a set value of the current as the pore grows[98]. Initially when the pore is small, this voltage is high enough to drive further enlargement of the pore, and as the pore approaches the desired size, the voltage is reduced below the threshold required for it to cause further growth (on the order of 0.1 $V\,nm^{-1}$ for SiN_x).

Moderate pulsed voltages have a variety of other positive side effects as well. As

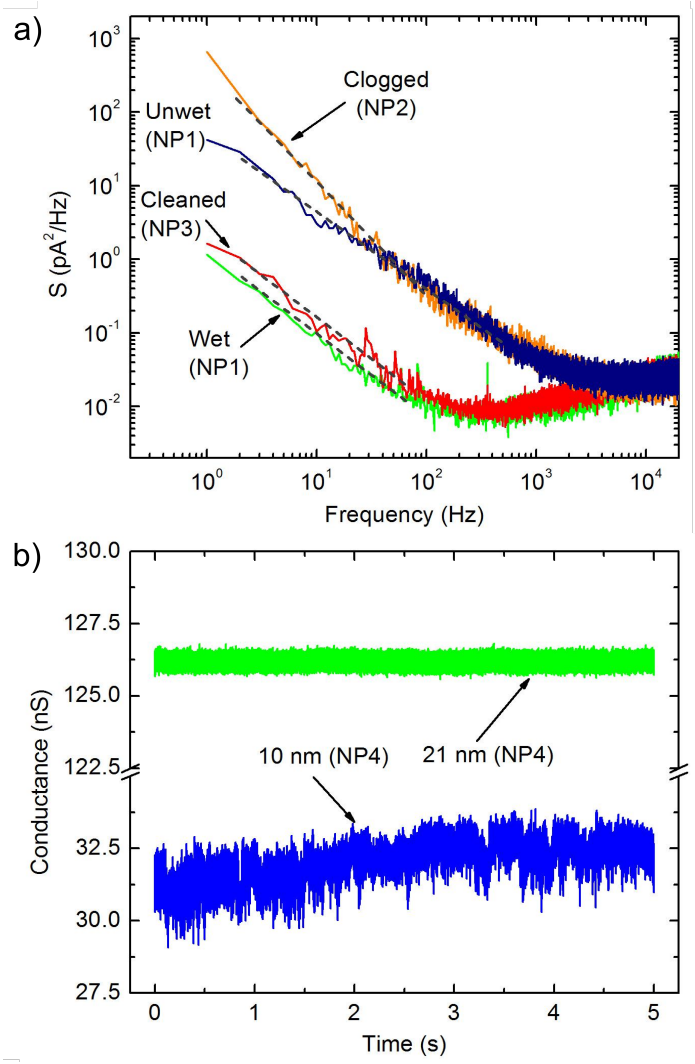

Figure 2.12: a) Power spectra for several nanopores, showing that a poorly wetted nanopore can be properly wetted after application of pulsed voltage. b) As a nanopore is enlarged, the noise characteristics can be improved significantly[33].

shown in Figure 2.12, low-frequency noise in solid-state nanopores can sometimes be improved during the enlargement step, and poorly wetted or clogged pores can be improved upon[33,109].

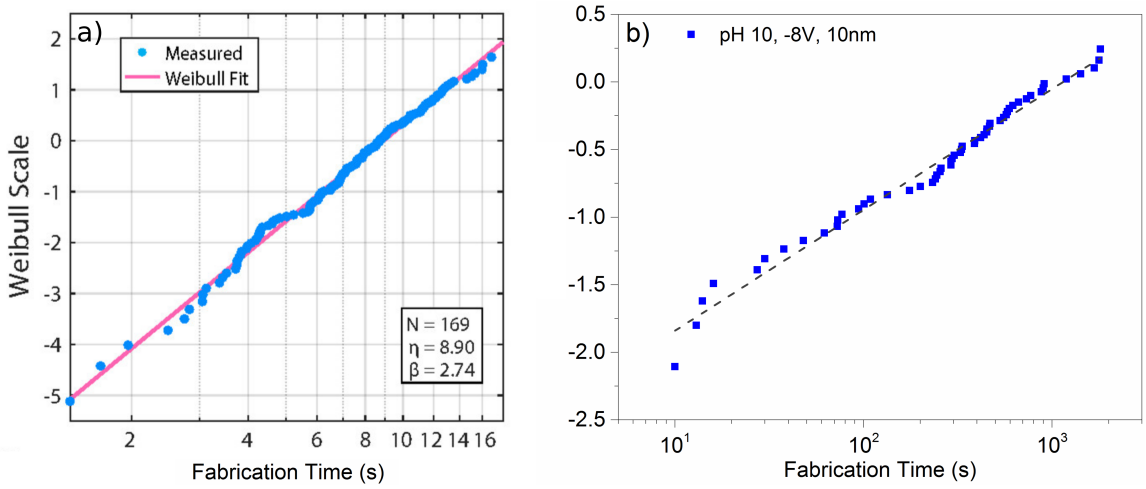

Figure 2.13: Time to breakdown follows a Weibull distribution for both a) a current clamp applying 10 nA in 1M LiCl pH 8[98] and b) a voltage clamp applying 8V in 1M KCl pH 10[35]. The Weibull scale is $\ln(-\ln(1-F(t)))$ where $F(t)$ is the cumulative fraction of membranes that have undergone CBD by time t. η and β are the Weibull timescale and slope, respectively.

2.5.4 Kinetics

The kinetics of pore formation and growth are complex, having numerous dependencies, not all of which are present in the case of breakdown in semiconductor devices, including dependencies on the membrane material, the electric field, and the composition of the electrolyte solution in which fabrication occurs. Additionally, breakdown kinetics have even been shown to vary between batches of nominally identical SiN_x membranes, pointing to the effects of variations in thickness or stoichiometry[35]. Due to the complexity of the physics involved in dielectric breakdown very few experimentally useful theoretical models exist, and so we instead discuss an empirical characterization of these dependencies.

Since dielectric breakdown occurs at the first location on the membrane that achieves a connected path of defects connecting the two membrane-electrolyte interfaces, the time required to open the first pore in the membrane is governed by the

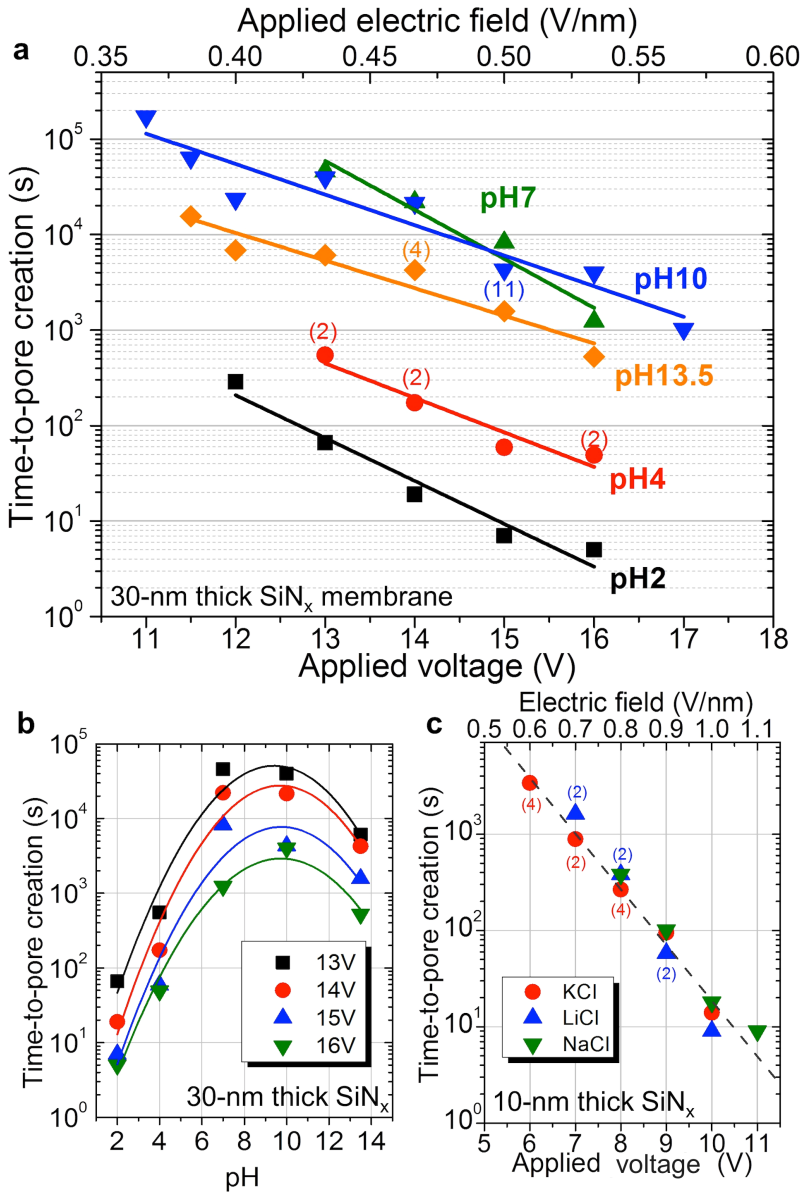

Figure 2.14: a) Time to breakdown is exponentially dependent on the applied voltage (or equivalently, the applied electric field). b) For a given electric field, fabrication times are highly sensitive to the pH of the electrolyte solution, while being insensitive to the choice of cation, as seen in c)[34].

kinetics of a weakest-link problem, which is described by a Weibull distribution of time-to-breakdown[35,98], which indicates that the probability that a membrane has

not undergone breakdown after time t is given by

$$F(t) = 1 - \exp\left(-\left(\frac{t}{\eta}\right)^{\beta}\right), \tag{2.2}$$

where η gives the breakdown timescale and β indicates the sharpness of the transition. This property has been demonstrated for both voltage clamp and current clamp fabrication schemes, as shown in Figure 2.13. It should be noted that the real quantity of interest in determining at what point the membrane will undergo breakdown is the total charge fluence that has passed the membrane[95], but it is difficult to isolate the contributions of current through the membrane from that which passes through the supporting structure, time serves as a reasonable alternative that exhibits the same statistics.

The mean time to breakdown depends exponentially on the applied electric field, as shown in Figure 2.14. This extreme electric field dependence can be used to change the mean time by many orders of magnitude for a given set of parameters using only a small variation in voltage. For this reason, care must be taken when choosing a voltage to ensure that the time it takes to fabricate the pore is much longer than the feedback time at which the pore can be detected and the voltage terminated, since as already notes, one otherwise risks opening several pores at the same time[78,101]. On the other hand, if the voltage is too low, the fabrication time will be prohibitively long.

Breakdown kinetics also depend on the nature of the electrolyte used to carry the current, a dependence that is obviously not present in the case of dry dielectric breakdown[35]. In particular, the time to breakdown was found to be very sensitive to pH for a given electric field strength, with time-to-breakdown being reduced by orders of magnitude at both extremes of the pH scale, while being largely insensitive

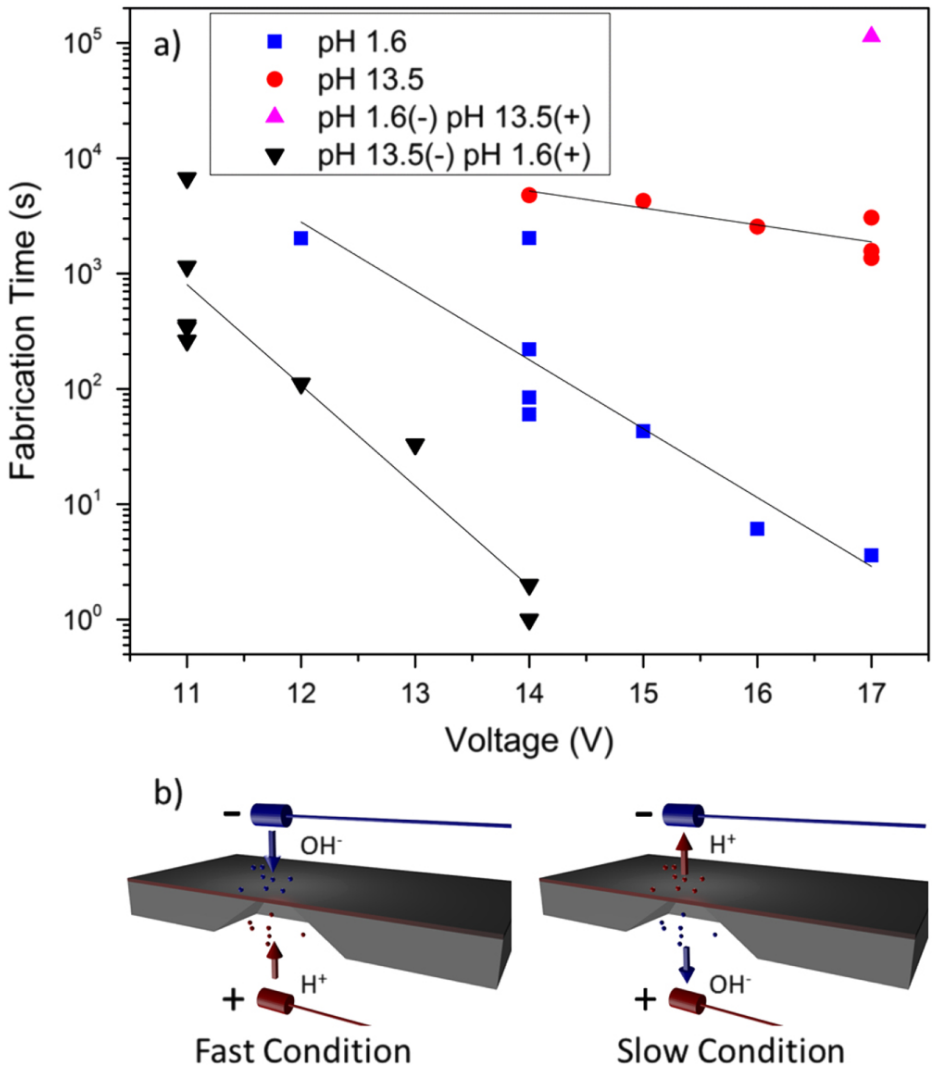

Figure 2.15: a) Time to breakdown is extremely sensitive to the local pH near the membrane. By modifying the local concentrations of OH- and H+ near the membrane, fabrication times can be modulated from seconds to days for a given electric field strength. b) A schematic representation of the effect of the electric field on the local charged species near the membrane[35].

to the nature of the cation used to carry the current through solution[34].

This sensitivity can be made even more extreme using different pH values on either side of the membrane, indicating that unsurprisingly, hydrogen and hydroxide ions likely both play a critical role in the redox reactions that generate tunnelling current at the membrane-solution interface[35], as shown in Figure 2.15. Simply changing the

direction of the pH asymmetry in the most extreme case changes the fabrication time from less than 1 second to more than 3 days. In principle nanopores could be fabricated in pure water, though the added electrolyte is required for active feedback control, since it is the ionic current signal that indicates that a pore has been formed. Care should be taken when attempting to use extreme pH values to speed up nanopore formation, since pore Ohmic behavior is often lost at both extremes, where pores formed in conditions of extreme pH often exhibit rectification. As a means to reduce fabrication time it is preferable to use a near-neutral pH and simply increase the voltage instead, though extreme pH values can still be used if diode-like behavior is desirable.

Membrane geometry is also important in breakdown kinetics. Membranes with larger active area achieve breakdown faster due to the fact that there is more area for defects to form[35], though the area dependence is logarithmic and therefore quite modestly affects time to breakdown[95]. Thinner membranes also have faster fabrication for a given voltage due to the higher electric field applied[35,110].

Dielectric breakdown is a universal process, and can be controlled with a large selection of possible conditions. The universality of the fabrication process, combined with the wide range of parameters that have a significant effect, provides a very large parameter space in which to optimize nanopore fabrication for a given application.

2.5.5 Localization

Since CBD is usually performed using purely electrical feedback, there is no *a priori* to know where on the membrane the nanopore was formed without additional monitoring steps. In the simplest form of CBD, because the electric field used to fabricate the nanopore is applied uniformly across the entire membrane, the actual

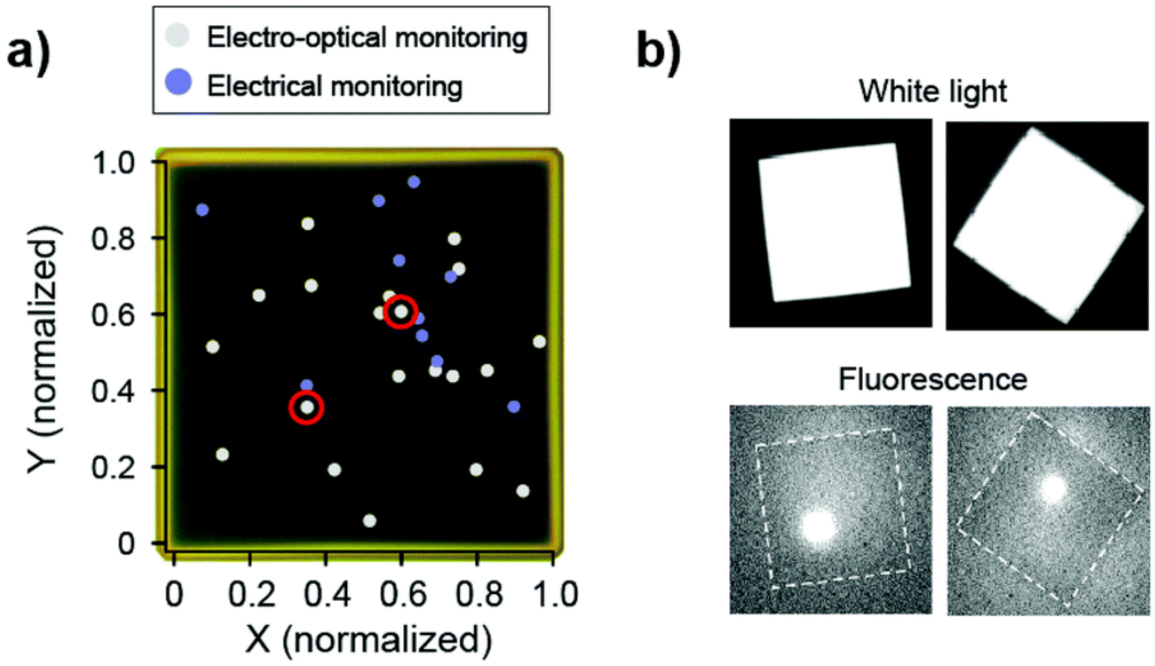

Figure 2.16: a) The locations of many nanopores fabricated on different membranes and overlaid, showing a roughly uniform distribution of pore locations on the membrane. Membrane locations are determined by Gaussian fitting of fluorescence spots produced by calcium dye. Circled points correspond to the two nanopores shown in b)[101].

location at which the pore is fabricated is random. Identifying the location of the pore has been achieved optically using a calcium-activated indicator dye on one side of the membrane, coupled with a calcium-based electrolyte on the other. Since the only place where the dye and calcium are both present in significant concentrations is the pore itself, the pore lights up and can be identified under a microscope[111] when a voltage is applied to drive calcium ions into the region with the dye. The random nature of pore formation has been confirmed with simultaneous electrical and calcium dye-based optical measurements of nanopores formed by CBD[101], as shown in Figure 2.16.

In spite of this randomness, it is possible to take advantage of the extreme electric-field dependence of the time to breakdown to deliberately position pores with varying

degrees of precision, either by locally increasing the electric field strength, or by limiting the membrane area that is exposed to electrolyte. Precisely positioned nanopore fabrication by controlled breakdown has been successfully demonstrated using various embodiments of both of these approaches.

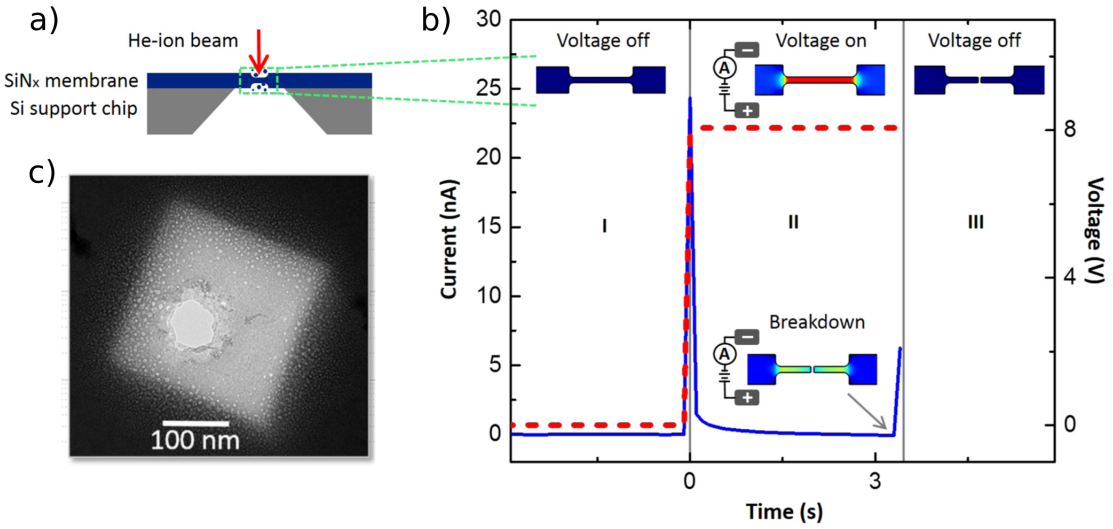

Figure 2.17: a) A schematic representation of the thinned membrane before nanopore fabrication (not to scale). b) A typical DC fabrication curve on thinned membranes, with insets showing simulations of the relative electric field strength on the various parts of the membrane at each step. c) A TEM image of the localized nanopore after fabrication by CBD, showing the pore confined to the locally thinned region[78].

Locally thinning a membrane has the effect of amplifying the electric field in the thinned regions for a given applied voltage[78,101], and can localize the nanopore to the same precision with which the membrane can be thinned by other means. The most precise localization by thinning demonstrated so far achieved accuracy on the order of 100 nm, using a helium ion microscope to perform partial milling down to 10 nm of 100×100 nm^2 regions in 100 nm thick membranes prior to CBD[78]. Of particular note in this approach is that while the probability per unit area of forming the pore at a given location is much higher on the thinned region, since the higher electric

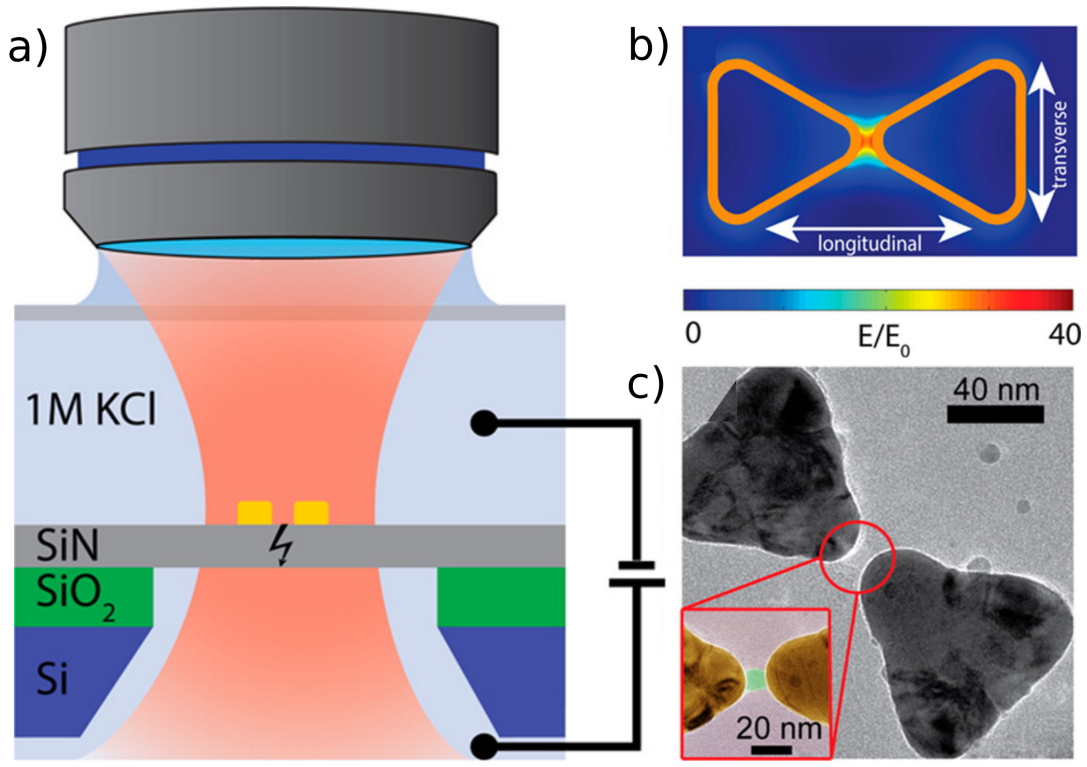

Figure 2.18: a) Schematic of the setup for nanopore localization by laser illumination of a nanopore membrane. b) The location of field enhancement can be made even more precise using plasmonic structures that locally enhance the field on a scale below the diffraction limit. c) TEM image of a pore formed in the junction of plasmonic structures with a precision on the order of 10 nm[112].

field there generates more defects per unit area per unit time, the thicker region is often orders of magnitude larger. While the area contribution breakdown in Weibull statistics is fairly modest, care must be taken to tune the electric field such that the time to breakdown on the thinned region is much faster than the time to breakdown in the thick region in cases where the degree of thinning is modest[78].

Another way to achieve local electric field enhancements is to use the optical field from a laser. This technique involves locally changing the electric field by shining a focused laser on the desired location of the nanopore[114]. The laser is hypothesized to increase the local conductivity by interacting with the photosensitive material, reduc-

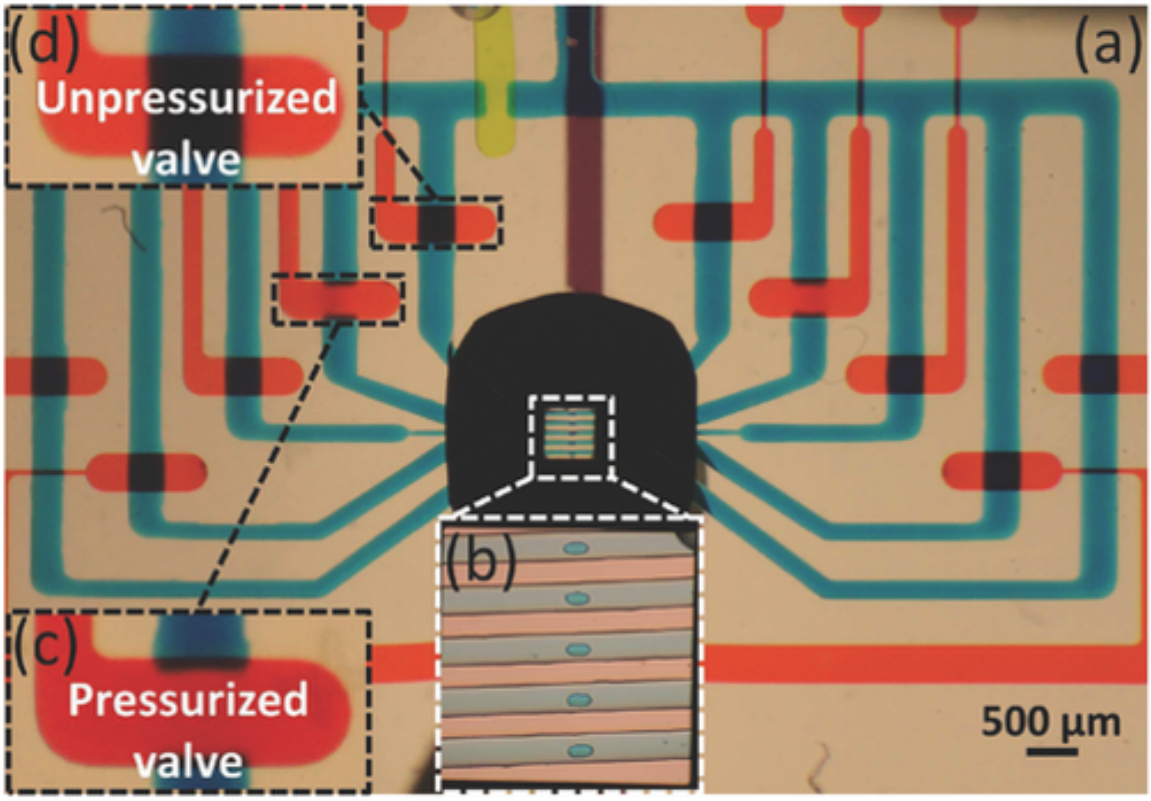

Figure 2.19: a) A realization of CBD in 5 independent channels on a single membrane[113]. b) 5 independent channels connect to the membrane using microvias in which a single nanopore can be fabricated. c,d) Fluidic channels (blue) can be accessed and addressed independently one at a time by compressing air valves (red) to cut off the electrical and fluidic contact to the unwanted channels.

ing the band gap for conduction in the membrane material near the laser focus and promoting controlled breakdown at that spot, a method that achieves diffraction-limited localization. The diffraction limit can be overcome for even more precise localization when the laser field is further modulated by plasmonic structures, a technique that permits reliable fabrication of solid-state nanopores within nanometer distances of existing nanostructures on a membrane[112], as shown in Figure 2.18, though this comes at the cost of complexity in nanofabricating the plasmonic structures and aligning the laser spot.

It is also possible to limit the area of application of the electric field using mi-

crofluidics to confine the electrically active areas to pre-specified parts of an intact membrane. One realization of this approach has been demonstrated by partitioning the membrane into various microfluidic channels[113,115,116], as shown in Figure 2.19. Due to the exponential dependence of fabrication time on local electric field, care must be taken to ensure that the applied electric field is uniform across the target area.

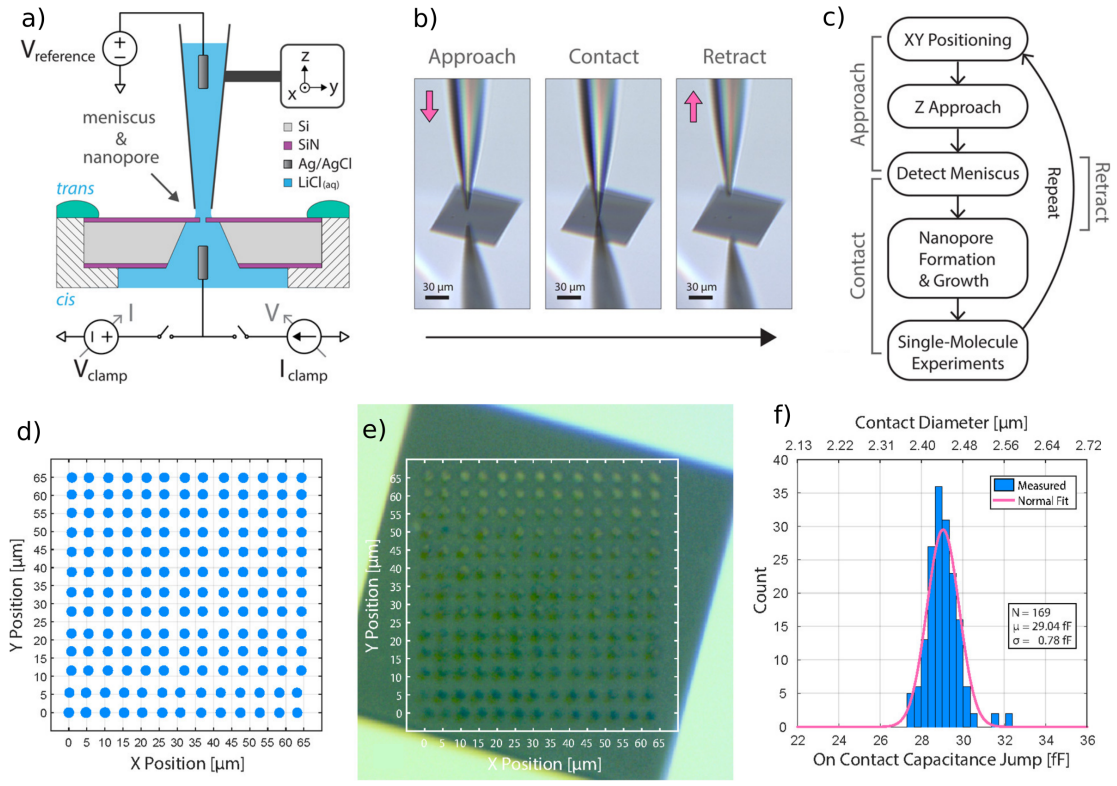

Figure 2.20: a) Schematic diagram of the nanopipette localization strategy. b) Microscopy images of the pipette tip during the positioning and approach steps. c) Flow chart showing the operation sequence for serial fabrication of multiple nanopores in a single membrane. d) A schematic diagram showing the maximal pore density for the given pipette tip. e) accounting for membrane rotation limits the useful membrane area of the scanner. f) Membrane contact is detected as an increase in the capacitance, which can also be used to infer the size of the contact area[98].

Localization of the pore has also been achieved by limiting the area over which

liquid contacts the membrane using the meniscus at the tip of a micropipette[98]. Using a micropositioner to scan the pipette tip across the membrane permits serial fabrication of hundreds of nanopores on a single microscale membrane. Localization is achievable with precision equal to the diameter of the liquid meniscus at the tip of the pipette. While micrometer precision has been demonstrated, it could in principle be improved with smaller pipette tips. The basic setup is shown in Figure 2.20.

2.5.6 Outlook

CBD is a simple, rapid, and cost-effective method for fabricating individual solid-state nanopores directly in the buffer conditions and electronics setup later used for single-molecule sensing. The fact that pores are formed wet translates into high yield of usable nanopores, while the *in situ* pore size control using only low-bandwidth electric field application allows for precise control of nanopore size using entirely automated feedback control. Compared to beam-based drilling the cost of equipment is essentially null, since a circuit capable of reliable nanopore fabrication can be constructed using hobby store electrical, components, 9 V batteries, and a simplistic feedback controller. This technique is also amenable to automation.

One of the major breakthroughs provided by CBD is that line-of-sight access to the eventual location of the pore is no longer required, as long as there is a liquid contact connecting the electrodes to either side of the membrane to be perforated. This permits pores to be fabricated deep inside complex geometries after they are fully assembled, greatly increasing yield and putting mass-manufacturing of devices with embedded nanopores within reach. The first such integrated device was recently demonstrated, which shows the possibility of fabricating a single nanopore through an existing porous structure in order to produce two solid-state nanopores in series

within nanoscale distances of one another[117].

2.6 Outlook

With growing industry interest in the state of the art in solid-state nanopore biosensing, the push for novel methods with which to realize precisely sized synthetic single-molecule sensors with high-yield in a scalable, low-cost way continues unabated. To that end, the ubiquitous carbon nanotube (CNT) has also found its way into the solid-state nanopore space. Though much less widely used for biosensing than membrane-based pores, CNTs have been employed as solid-state nanopores in a variety of different ways. Early methods generally involved embedding a CNT in a polymer matrix or epoxy block and slicing away thin sections to form the sensor membrane containing a pore made up of a CNT that was used to detect nanoparticles[119,121]. Lui *et al* improved on the resolution of this general approach by embedding 2 nm diameter single-walled CNTs (SWCNTs) in a PMMA coating and performing e-beam lithography to open channels connecting to either end of SWCNTs deposited at low density on a silicon wafer for the detection of single ssDNA molecules[118]. Aside from embedding in solid supports, CNTs can also be inserted into the opening of a glass nanopipette using a manipulator operating inside an SEM, such that the CNT forms the new nanopipette tip, though single-molecule detection was not demonstrated with this method[122].

Single-molecule detection with CNTs has been successfully demonstrated by embedding CNTs in a lipid bilayer membrane. In this technique, the natural hydrophobicity of CNTs promotes perpendicular insertion of CNTs into existing lipid bilayers, forming biomimetic nanotube channels through the lipid membrane that were shown to be able to pass ssDNA[120]. CNTs have also been successfully embedded in SiN_x

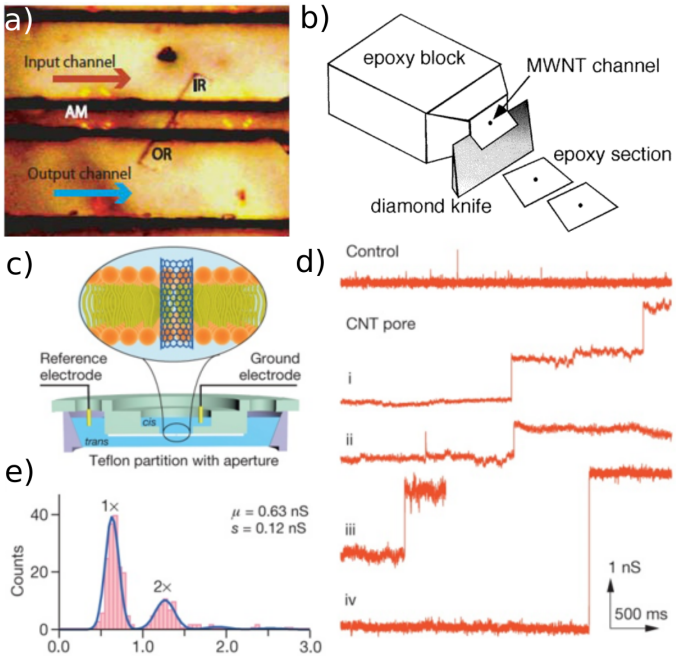

Figure 2.21: a) A CNT is embedded in spin-coated PMMA before channels are opened to give access to both the inlet (IR) and outlet (QR) ends[118]. b) A CNT is embedded in the bulk of a block of epoxy and thin sections are sliced away with a diamond knife to produce thin membranes containing a single CNT[119]. c) the natural hydrophobicity of CNTs causes them to embed readily in lipid bilayers, producing biomimetic pores in lipid substrates. d) Current traces showing incorporation of one or more CNTs in the lipid bilayer. e) clearly quantized levels corresponds to incorporation of additional CNTs[120].

membranes using a process of catalyzed growth, though this method produces large arrays of nanotubes as opposed to single molecular sensors[125]. While CNTs have yet to match more mature pore technologies in terms of sensing performance, their tunable physical and electrical properties make them interesting candidates as highly sensitive biomolecular sensors, and they certainly bear watching as an emerging class of solid-state nanopore. Several examples of nanopore devices made from CNTs are shown in Figure 2.21.

Since precise nanofabrication techniques exist, and viable industrial-scale nanopore fabrication processes are within reach, the focus of future nanopore and single-molecule

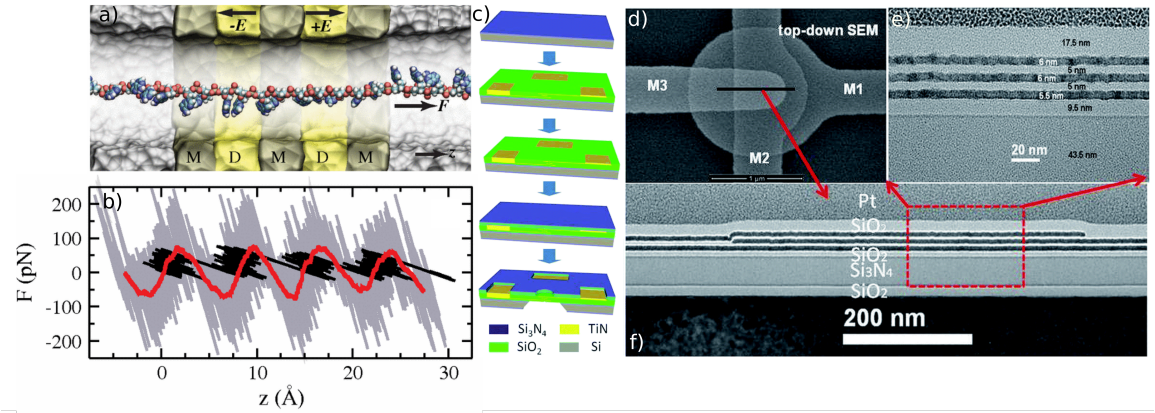

Figure 2.22: a) Simulation of ssDNA ratchetting through a system with 3 embedded electrodes marked M separating dielectric regions marked D. b) The force profile experienced by the ssDNA in such a system for stiff (grey) and weak (black) spring forces exerted by the electrodes. Red denotes the time-average of the forces, showing the ratchetting nature of the motion[123]. c) Fabrication steps required to realize this structure experimentally on a wafer scale using standard lithographic techniques. d) SEM images of the resulting structure showing 3 layered embedded electrodes prior to pore formation. e,f) side views of slices of the structure showing the various components[124].

nanosensor fabrication efforts is shifting toward the development of novel structures with which to control the motion of biomolecules as they translocate the sensor[126]. Oxford Nanopore recently demonstrated that using a ratcheting enzyme to control ssDNA motion through a biological nanopore enables direct-read sequencing[127] . This has provided impetus for research into fabrication techniques with which to produce heterostructure membranes incorporating multiple metallic and/or dielectric layers with the purpose of either improving motion control during biomolecular translocation through a solid-state nanopore[123], or increasing the speed of the temporal response of the pore to resistive pulses[128]. In many proposed schemes, motion control is achieved using precise electric fields in and around the pore[124], with proof of concept simulations demonstrating ratchet-like motion of ssDNA through a solid-state nanopore comprising multiple internal gate electrodes[123,129,130]. While nanopores have been

fabricated in composite membranes structures including embedded electrodes in a variety of configurations on both membrane-based pores[124,131–133] and nanopipettes[93], the requisite level of motion control for sequencing has not yet been demonstrated experimentally. A few examples of embedded electrode schemes are shown in Figure 2.22.

There is also interest in proposed devices with nanoscale electrodes or graphene ribbons that conduct transverse to the direction of molecular motion through the pore. Such a structure could in principle identify bases as they pass the pore with better spatial resolution than the full pore itself by measuring current tunnelling through the bases as they pass between the transverse electrodes. Several attempts at fabricating such structures have been made[134,135,137–140], and while individual DNA bases can be identified by their tunnelling current signature[136,141], single-base resolution and continuous base-reading have not yet been achieved, again largely due to the low residence time of each base in the recognition region and the difficulties in producing a number of viable nanodevices to experimentally explore and optimize operation conditions. Fabrication techniques that combine DNA motion control with base-recognition tunnelling will be of great interest in the coming decade as solid-state nanopores strive to catch up to their biological counterparts in the sequencing space. A few examples are shown in Figure 2.23.

While nanopore fabrication techniques in general are rapidly maturing, there are still segments of the parameter space of fabrication variables that have not yet been explored. Most nanopore research is conducted using SiN_x membranes, which is largely due to familiarity and convenience, since robust thin membrane fabrication protocols exist for this material. There are a few groups exploring alternative membranes, however. HfO_2 shows promise as a more stable and robust membrane material that could be made much thinner than SiN_x while retaining long term stability[44]. The

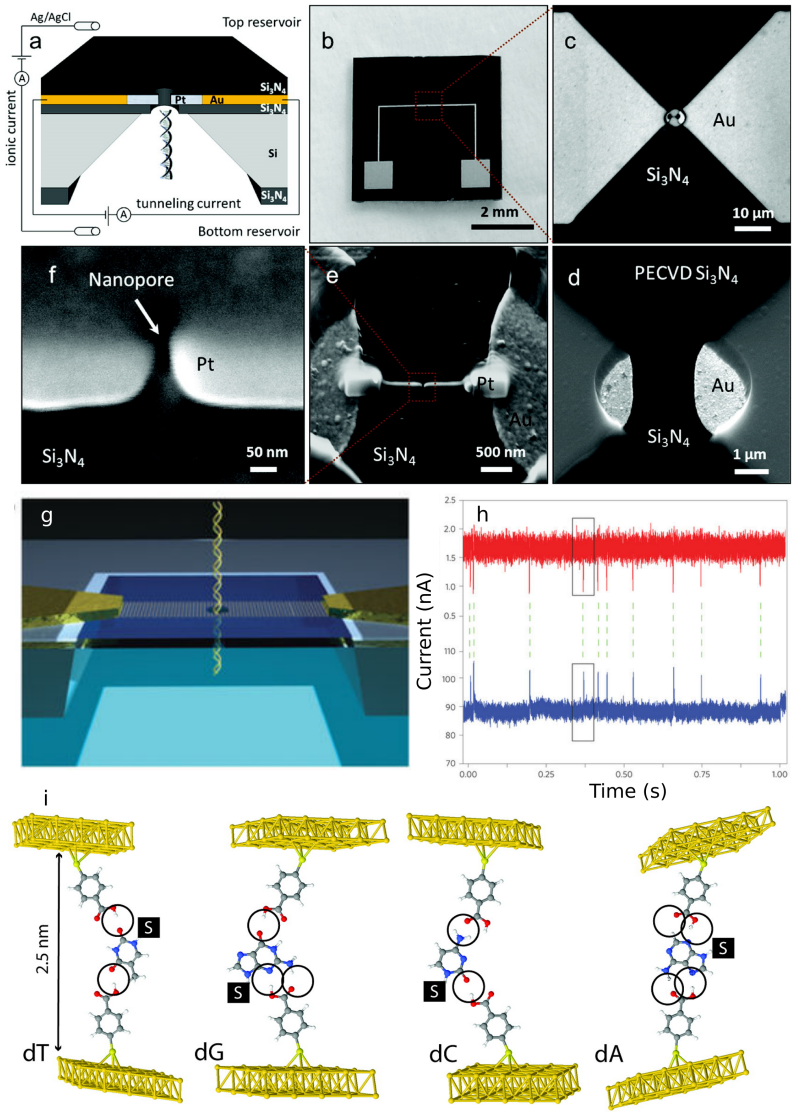

Figure 2.23: a) Platinum nanoelectrodes can be interfaced with gold microelectrodes near a nanopore to provide a transverse current signal as DNA passes between the electrodes. b-f) Successive magnification of the experimental realization of this structure[134]. g) A schematic of a nanopore in a graphene nanoribbon, which also allowed measurement of transverse current at the same time as the usual nanopore signal. Examples of the simultaneous signals are shown in h)[135]. i) Individual bases can be recognized by functionalizing the transverse electrodes with molecules that interact differently with each base[136].

unique and infinitely tunable electrical properties of transition metal dichalcogenides make them attractive as membrane materials, especially as components of multilayer

devices for more precise control of local electric fields in and around the pore, but so far only a few have been explored[48,99,142]. In short, while considerable strides have been made in fabrication techniques for solid-state nanopores over the past two decades, there can be no doubt that the pace of discovery will continue unabated for the foreseeable future.

Acknowledgements

The authors would like to thank all publishers referenced in this chapter, as well as ZEISS Microscopy and Thermo Fisher Scientific, for permission to reuse images from published works.

Bibliography

[1] P. Y. Apel, I. V. Blonskaya, N. E. Lizunov, K. Olejniczak, O. L. Orelovitch, B. A. Sartowska, and S. N. Dmitriev, "Asymmetrical nanopores in track membranes: Fabrication, the effect of nanopore shape and electric charge of pore walls, promising applications," *Russian Journal of Electrochemistry*, vol. 53, no. 1, pp. 58–69, 2017.

[2] Z. Siwy, P. Apel, D. Dobrev, R. Neumann, R. Spohr, C. Trautmann, and K. Voss, "Ion transport through asymmetric nanopores prepared by ion track etching," *Nuclear Instruments and Methods in Physics Research, Section B: Beam Interactions with Materials and Atoms*, vol. 208, no. 1-4, pp. 143–148, 2003.

[3] G. R. Willmott and P. W. Moore, "Reversible mechanical actuation of elastomeric nanopores," *Nanotechnology*, vol. 19, no. 47, p. 475504, 2008.

[4] G. S. Roberts, D. Kozak, W. Anderson, M. F. Broom, R. Vogel, and M. Trau, "Tunable nano/micropores for particle detection and discrimination: Scanning ion occlusion spectroscopy," *Small*, vol. 6, no. 23, pp. 2653–2658, 2010.

[5] S. J. Sowerby, M. F. Broom, and G. B. Petersen, "Dynamically resizable nanometre-scale apertures for molecular sensing," *Sensors and Actuators, B: Chemical*, vol. 123, no. 1, pp. 325–330, 2007.

[6] B. Zhang, J. Galusha, P. G. Shiozawa, G. Wang, A. J. Bergren, R. M. Jones, R. J. White, E. N. Ervin, C. C. Cauley, and H. S. White, "Bench-top method for fabricating glass-sealed nanodisk electrodes, glass nanopore electrodes, and

glass nanopore membranes of controlled size," *Analytical Chemistry*, vol. 79, no. 13, pp. 4778–4787, 2007.

[7] B. Zhang, Y. Zhang, and H. S. White, "The nanopore electrode," *Analytical Chemistry*, vol. 76, no. 21, pp. 6229–6238, 2004.

[8] W. J. Lan, D. A. Holden, and H. S. White, "Pressure-dependent ion current rectification in conical-shaped glass nanopores," *Journal of the American Chemical Society*, vol. 133, no. 34, pp. 13300–13303, 2011.

[9] R. J. White, E. N. Ervin, T. Yang, X. Chen, S. Daniel, P. S. Cremer, and H. S. White, "Single Ion-Channel Recordings Using Glass Nanopore Membranes Single Ion-Channel Recordings Using Glass Nanopore Membranes," *Journal of the American Chemical Society*, vol. 129, no. 15, pp. 11766–11775, 2007.

[10] A. E. P. Schibel, T. Edwards, R. Kawano, W. Lan, and H. S. White, "Quartz nanopore membranes for suspended bilayer ion channel recordings," *Analytical Chemistry*, vol. 82, no. 17, pp. 7259–7266, 2010.

[11] T. Deng, J. Chen, W. Si, M. Yin, W. Ma, and Z. Liu, "Fabrication of silicon nanopore arrays using a combination of dry and wet etching," *Journal of Vacuum Science & Technology B, Nanotechnology and Microelectronics: Materials, Processing, Measurement, and Phenomena*, vol. 30, no. 6, p. 061804, 2012.

[12] S. R. Park, H. Peng, and X. S. Ling, "Fabrication of nanopores in silicon chips using feedback chemical etching," *Small*, vol. 3, no. 1, pp. 116–119, 2007.

[13] T. Deng, J. Chen, C. N. Wu, and Z. W. Liu, "Fabrication of Inverted-Pyramid Silicon Nanopore Arrays with Three-Step Wet Etching," *Ecs Journal of Solid State Science and Technology*, vol. 2, no. 11, pp. P419–P422, 2013.

[14] T. Gilboa, A. Zrehen, A. Girsault, and A. Meller, "Optically-Monitored Nanopore Fabrication Using a Focused Laser Beam," *Scientific Reports*, vol. 8, no. 1, p. 9765, 2018.

[15] G. Danda, P. Masih Das, Y. C. Chou, J. T. Mlack, W. M. Parkin, C. H. Naylor, K. Fujisawa, T. Zhang, L. B. Fulton, M. Terrones, A. T. Johnson, and M. Drndić, "Monolayer WS2 Nanopores for DNA Translocation with Light-Adjustable Sizes," *ACS Nano*, vol. 11, no. 2, pp. 1937–1945, 2017.

[16] C. Qi, C. C. Striemer, T. R. Gaborski, J. L. McGrath, and P. M. Fauchet, "Highly porous silicon membranes fabricated from silicon nitride/silicon stacks," *Small*, vol. 10, no. 14, pp. 2946–2953, 2014.

[17] C. C. Streimer, T. R. Gaborski, J. L. McGrath, and P. M. Fauchet, "Charge- and size-based separation of maeromolecules using novel ultrathin silicon membranes," *Nature*, vol. 445, no. February, p. 177, 2006.

[18] J. P. S. DesOrmeaux, J. D. Winans, S. E. Wayson, T. R. Gaborski, T. S. Khire, C. C. Striemer, and J. L. McGrath, "Nanoporous silicon nitride membranes fabricated from porous nanocrystalline silicon templates," *Nanoscale*, vol. 6, no. 18, p. 10798, 2014.

[19] H. D. Tong, H. V. Jansen, V. J. Gadgil, C. G. Bostan, E. Berenschot, C. J. Van Rijn, and M. Elwenspoek, "Silicon Nitride Nanosieve Membrane," *Nano Letters*, vol. 4, no. 2, pp. 283–287, 2004.

[20] N. N. Gribov, S. J. C. H. Theeuwen, J. Caro, and S. Radelaar, "A new fabrication process for metallic point contacts," *Microelectronic Engineering*, vol. 35, pp. 317–320, 1997.

[21] J. Li, D. Stein, C. Mcmullan, D. Branton, M. J. Aziz, and J. a. Golovchenko, "Ion-beam sculpting at nanometre length scales," *Nature*, vol. 412, no. 6843, pp. 166–169, 2001.

[22] D. Stein, J. Li, and J. A. Golovchenko, "Ion Beam Sculpting Time Scales," *Phys. Rev. Lett.*, vol. 89, p. 276106, 2002.

[23] J. Li, M. Gershow, D. Stein, E. Brandin, and J. a. Golovchenko, "DNA molecules and configurations in a solid-state nanopore microscope.," *Nature materials*, vol. 2, no. 9, pp. 611–5, 2003.

[24] A. J. Storm, J. H. Chen, X. S. Ling, H. W. Zandbergen, and C. Dekker, "Fabrication of solid-state nanopores with single-nanometre precision," *Nature Materials*, vol. 2, p. 537, jul 2003.

[25] J. Gierak, A. Madouri, A. L. Biance, E. Bourhis, G. Patriarche, C. Ulysse, D. Lucot, X. Lafosse, L. Auvray, L. Bruchhaus, and R. Jede, "Sub-5 nm FIB direct patterning of nanodevices," *Microelectronic Engineering*, vol. 84, no. 5-8, pp. 779–783, 2007.

[26] P. Chen, M.-Y. Wu, H. W. M. Salemink, and P. F. a. Alkemade, "Fast single-step fabrication of nanopores.," *Nanotechnology*, vol. 20, no. 1, p. 015302, 2009.

[27] J. Yang, D. C. Ferranti, L. a. Stern, C. a. Sanford, J. Huang, Z. Ren, L.-C. Qin, and A. R. Hall, "Rapid and precise scanning helium ion microscope milling of solid-state nanopores for biomolecule detection.," *Nanotechnology*, vol. 22, no. 28, p. 285310, 2011.

[28] D. Emmrich, A. Beyer, A. Nadzeyka, S. Bauerdick, J. C. Meyer, J. Kotakoski, and A. Gölzhäuser, "Nanopore fabrication and characterization by helium ion microscopy," *Applied Physics Letters*, vol. 108, no. 16, 2016.

[29] C. Wei, A. J. Bard, and S. W. Feldberg, "Current Rectification at Quartz Nanopipet Electrodes," *Analytical Chemistry*, vol. 69, no. 22, pp. 4627–4633, 1997.

[30] Y. Shao and M. V. Mirkin, "Fast kinetic measurements with nanometer-sized pipets. Transfer of potassium ion from water into dichloroethane facilitated by dibenzo-18-crown-6," *Journal of the American Chemical Society*, vol. 119, no. 34, pp. 8103–8104, 1997.

[31] M. Karhanek, J. T. Kemp, N. Pourmand, R. W. Davis, and C. D. Webb, "Single DNA molecule detection using nanopipettes and nanoparticles," *Nano Letters*, vol. 5, no. 2, pp. 403–407, 2005.

[32] L. J. Steinbock, J. F. Steinbock, and A. Radenovic, "Controllable shrinking and shaping of glass nanocapillaries under electron irradiation," *Nano Letters*, vol. 13, no. 4, pp. 1717–1723, 2013.

[33] E. Beamish, H. Kwok, V. Tabard-Cossa, and M. Godin, "Precise control of the size and noise of solid-state nanopores using high electric fields.," *Nanotechnology*, vol. 23, p. 405301, oct 2012.

[34] H. Kwok, K. Briggs, and V. Tabard-Cossa, "Nanopore fabrication by controlled dielectric breakdown.," *PLoS One*, vol. 9, p. e92880, jan 2014.

[35] K. Briggs, M. Charron, H. Kwok, T. Le, S. Chahal, J. Bustamante, M. Waugh, and V. Tabard-Cossa, "Kinetics of nanopore fabrication during controlled breakdown of dielectric membranes in solution," *Nanotechnology*, vol. 26, no. 8, 2015.

[36] I. Yanagi, R. Akahori, T. Hatano, and K.-i. Takeda, "Fabricating nanopores with diameters of sub-1 nm to 3 nm using multilevel pulse-voltage injection.," *Scientific reports*, vol. 4, p. 5000, 2014.

[37] K. Briggs, H. Kwok, and V. Tabard-Cossa, "Automated Fabrication of 2-nm Solid-State Nanopores for Nucleic Acid Analysis," *Small*, vol. 10, no. 10, pp. 2077–2086, 2014.

[38] M. J. Kim, B. McNally, K. Murata, and A. Meller, "Characteristics of solid-state nanometre pores fabricated using a transmission electron microscope," *Nanotechnology*, vol. 18, no. 20, p. 205302, 2007.

[39] M. J. Kim, M. Wanunu, D. C. Bell, and A. Meller, "Rapid fabrication of uniformly sized nanopores and nanopore arrays for parallel DNA analysis," *Advanced Materials*, vol. 18, no. 23, pp. 3149–3153, 2006.

[40] M. Y. Wu, D. Krapf, M. Zandbergen, H. Zandbergen, and P. E. Batson, "Formation of nanopores in a SiN/SiO2 membrane with an electron beam," *Applied Physics Letters*, vol. 87, no. 11, pp. 1–4, 2005.

[41] H.-M. Kim, M.-H. Lee, and K.-B. Kim, "Theoretical and experimental study of nanopore drilling by a focused electron beam in transmission electron microscopy.," *Nanotechnology*, vol. 22, no. 27, p. 275303, 2011.

[42] A. J. Storm, J. H. Chen, X. S. Ling, H. W. Zandbergen, and C. Dekker, "Electron-beam-induced deformations of SiO 2 nanostructures," *Journal of Applied Physics*, vol. 98, no. 1, 2005.

[43] B. M. Venkatesan, B. Dorvel, S. Yemenicioglu, N. Watkins, I. Petrov, and R. Bashir, "Highly sensitive, mechanically stable nanopore sensors for DNA analysis," *Advanced Materials*, vol. 21, no. 27, pp. 2771–2776, 2009.

[44] J. Larkin, R. Henley, D. C. Bell, T. Cohen-Karni, J. K. Rosenstein, and M. Wanunu, "Slow DNA transport through nanopores in hafnium oxide membranes.," *ACS Nano*, vol. 7, pp. 10121–8, nov 2013.

[45] C. J. Russo and J. A. Golovchenko, "Atom-by-atom nucleation and growth of graphene nanopores," *Proceedings of the National Academy of Sciences*, vol. 109, no. 16, pp. 5953–5957, 2012.

[46] S. Liu, Q. Zhao, J. Xu, K. Yan, H. Peng, F. Yang, L. You, and D. Yu, "Fast and controllable fabrication of suspended graphene nanopore devices," *Nanotechnology*, vol. 23, no. 8, p. 085301, 2012.

[47] G. Goyal, Y. B. Lee, A. Darvish, C. W. Ahn, and M. J. Kim, "Hydrophilic and size-controlled graphene nanopores for protein detection," *Nanotechnology*, vol. 27, pp. 1–30, 2016.

[48] K. Liu, J. Feng, A. Kis, and A. Radenovic, "Atomically Thin Molybdenum Disulfide Nanopores with High Sensitivity for DNA Translocation," *ACS Nano*, vol. 8, no. Xx, pp. 2504–2511, 2014.

[49] K. B. Park, H. J. Kim, Y. H. Kang, J. S. Yu, H. Chae, K. Lee, H. M. Kim, and K. B. Kim, "Highly reliable and low-noise solid-state nanopores with an atomic layer deposited ZnO membrane on a quartz substrate," *Nanoscale*, vol. 9, no. 47, pp. 18772–18780, 2017.

[50] M. Wu, R. Smeets, M. Zandbergen, U. Zlese, D. Krapf, P. E. Batson, N. H. Dekker, C. Dekker, and H. Zandbergen, "Control of shape and material composition of solid-state nanopores," *Nano Letters*, vol. 9, no. 1, 2009.

[51] J. A. Rodriguez-Manzo, M. Puster, A. Nicolai, V. Meunier, and M. Drndic, "DNA Translocation in Nanometer Thick Silicon Nanopores," *ACS Nano*, vol. 9, no. 6, pp. 6555–6564, 2015.

[52] R. F. Egerton, P. Li, and M. Malac, "Radiation damage in the TEM and SEM," *Micron*, vol. 35, no. 6, pp. 399–409, 2004.

[53] D. G. Howitt, S. J. Chen, B. C. Gierhart, R. L. Smith, and S. D. Collins, "The electron beam hole drilling of silicon nitride thin films," *Journal of Applied Physics*, vol. 103, no. 2, 2008.

[54] M. van den Hout, A. R. Hall, M. Y. Wu, H. W. Zandbergen, C. Dekker, and N. H. Dekker, "Controlling nanopore size, shape and stability.," *Nanotechnology*, vol. 21, no. 11, p. 115304, 2010.

[55] S. W. Kowalczyk, A. Y. Grosberg, Y. Rabin, and C. Dekker, "Modeling the conductance and DNA blockade of solid-state nanopores.," *Nanotechnology*, vol. 22, no. 31, p. 315101, 2011.

[56] C. M. Frament and J. R. Dwyer, "Conductance-based determination of solid-state nanopore size and shape: An exploration of performance limits," *Journal of Physical Chemistry C*, vol. 116, no. 44, pp. 23315–23321, 2012.

[57] C. M. Frament, N. Bandara, and J. R. Dwyer, "Nanopore surface coating delivers nanopore size and shape through conductance-based sizing," *ACS Applied Materials and Interfaces*, vol. 5, no. 19, pp. 9330–9337, 2013.

[58] C. M. Frament, N. Bandara, and J. R. Dwyer, "Nanopore surface coating delivers nanopore size and shape through conductance-based sizing.," *ACS applied materials & interfaces*, vol. 5, pp. 9330–7, oct 2013.

[59] Y. M. D. Bandara, B. I. Karawdeniya, and J. R. Dwyer, "Real-Time Profiling of Solid-State Nanopores during Solution-Phase Nanofabrication," *ACS Applied Materials and Interfaces*, vol. 8, no. 44, pp. 30583–30589, 2016.

[60] Y. M. Bandara, J. W. Nichols, B. Iroshika Karawdeniya, and J. R. Dwyer, "Conductance-based profiling of nanopores: Accommodating fabrication irregularities," *Electrophoresis*, vol. 39, no. 4, pp. 626–634, 2018.

[61] C. J. Lo, T. Aref, and A. Bezryadin, "Fabrication of symmetric sub-5 nm nanopores using focused ion and electron beams," *Nanotechnology*, vol. 17, no. 13, p. 3264, 2006.

[62] C. Dekker, R. Article, and C. Dekker, "Solid-state nanopores," *Nature Nanotechnology*, vol. 2, no. 4, pp. 209–215, 2007.

[63] M. Wanunu, "Nanopores: A journey towards DNA sequencing," *Physics of Life Reviews*, vol. 9, no. 2, pp. 125–158, 2012.

[64] D. Branton, D. W. Deamer, A. Marziali, H. Bayley, S. A. Benner, T. Butler, M. Di Ventra, S. Garaj, A. Hibbs, X. Huang, S. B. Jovanovich, P. S. Krstic, S. Lindsay, X. S. Ling, C. H. Mastrangelo, A. Meller, J. S. Oliver, Y. V. Pershin, J. M. Ramsey, R. Riehn, G. V. Soni, V. Tabard-Cossa, M. Wanunu, M. Wiggin, and J. A. Schloss, "The potential and challenges of nanopore sequencing," *Nature Biotechnology*, vol. 26, no. 10, pp. 1146–1153, 2008.

[65] E. Atas, A. Singer, and A. Meller, "DNA sequencing and bar-coding using solid-state nanopores," *Electrophoresis*, vol. 33, no. 23, pp. 3437–3447, 2012.

[66] Q. Cai, B. Ledden, E. Krueger, J. A. Golovchenko, and J. Li, "Nanopore sculpting with noble gas ions," *Journal of Applied Physics*, vol. 100, no. 2, 2006.

[67] Y. Deng, Q. Huang, Y. Zhao, D. Zhou, C. Ying, and D. Wang, "Precise fabrication of a 5 nm graphene nanopore with a helium ion microscope for biomolecule detection," *Nanotechnology*, vol. 28, no. 4, p. 045302, 2017.

[68] A. Hemamouche, A. Morin, E. Bourhis, B. Toury, E. Tarnaud, J. Mathé, P. Guégan, A. Madouri, X. Lafosse, C. Ulysse, S. Guilet, G. Patriarche, L. Auvray, F. Montel, Q. Wilmart, B. Plaçais, J. Yates, and J. Gierak, "FIB patterning of dielectric, metallized and graphene membranes: A comparative study," *Microelectronic Engineering*, vol. 121, pp. 87–91, 2014.

[69] O. K. Zahid and A. R. Hall, *Helium Ion Microscope Fabrication of Solid-State Nanopore Devices for Biomolecule Analysis*, pp. 447–470. Cham: Springer International Publishing, 2016.

[70] J. Ziegler, "Stopping and Range of Ions in Matter (SRIM) Computer Software." http://www.srim.org/, 2013.

[71] S. Tan, K. Klein, D. Shima, R. Livengood, E. Mutunga, and A. Vladár, "Mechanism and applications of helium transmission milling in thin membranes," *Journal of Vacuum Science & Technology B, Nanotechnology and Microelectronics: Materials, Processing, Measurement, and Phenomena*, vol. 32, no. 6, p. 06FA01, 2014.

[72] R. Livengood, S. Tan, Y. Greenzweig, J. Notte, and S. McVey, "Subsurface damage from helium ions as a function of dose, beam energy, and dose rate," *Journal of Vacuum Science & Technology B: Microelectronics and Nanometer Structures*, vol. 27, no. 6, p. 3244, 2009.

[73] M. G. Stanford, B. B. Lewis, V. Iberi, J. D. Fowlkes, S. Tan, R. Livengood, and P. D. Rack, "In Situ Mitigation of Subsurface and Peripheral Focused Ion Beam Damage via Simultaneous Pulsed Laser Heating," *Small*, vol. 12, no. 13, pp. 1779–1787, 2016.

[74] M. A. Nguyen, M. O. Ruault, and F. Fortuna, "Formation and growth of nanocavities and cavities induced by He+ implantation in silicon," *Advances in Natural Sciences: Nanoscience and Nanotechnology*, vol. 3, no. 1, 2012.

[75] R. Siegele, G. C. Weatherly, H. K. Haugen, D. J. Lockwood, and L. M. Howe, "Helium bubbles in silicon: Structure and optical properties," *Applied Physics Letters*, vol. 66, no. 11, pp. 1319–1321, 1995.

[76] K. Das, J. B. Freund, and H. T. Johnson, "Mechanisms of material removal and mass transport in focused ion beam nanopore formation," *Journal of Applied Physics*, vol. 117, no. 8, 2015.

[77] M. M. Marshall, J. Yang, and A. R. Hall, "Direct and transmission milling of suspended silicon nitride membranes with a focused helium ion beam," *Scanning*, vol. 34, no. 2, pp. 101–106, 2012.

[78] A. T. Carlsen, K. Briggs, A. R. A. A. R. Hall, and V. Tabard-Cossa, "Solid-state nanopore localization by controlled breakdown of selectively thinned membranes," *Nanotechnology*, vol. 28, no. 8, 2017.

[79] N. Patterson, D. P. Adams, V. C. Hodges, M. J. Vasile, J. R. Michael, and P. G. Kotula, "Controlled fabrication of nanopores using a direct focused ion beam approach with back face particle detection.," *Nanotechnology*, vol. 19, no. 23, p. 235304, 2008.

[80] F. Sawafta, B. Clancy, A. T. Carlsen, M. Huber, and A. R. Hall, "Solid-state nanopores and nanopore arrays optimized for optical detection.," *Nanoscale*, pp. 6991–6996, 2014.

[81] J. Li, D. Stein, C. McMullan, D. Branton, M. J. Aziz, and J. A. Golovchenko, "Ion-beam sculpting at nanometre length scales," *Nature*, vol. 412, no. 6843, pp. 166–169, 2001.

[82] S. Umehara, M. Karhanek, R. W. Davis, and N. Pourmand, "Label-free biosensing with functionalized nanopipette probes.," *Proceedings of the National Academy of Sciences of the United States of America*, vol. 106, no. 12, pp. 4611–6, 2009.

[83] P. Actis, A. C. Mak, and N. Pourmand, "Functionalized nanopipettes: Toward label-free, single cell biosensors," *Bioanalytical Reviews*, vol. 1, no. 2, pp. 177–185, 2010.

[84] T. R. Gibb, A. P. Ivanov, J. B. Edel, and T. Albrecht, "Single Molecule Ionic Current Sensing in Segmented Flow Microfluidics," *Analytical Chemisry*, vol. 86, pp. 1864–1871, 2014.

[85] L. J. Steinbock, R. D. Bulushev, S. Krishnan, C. Raillon, and A. Radenovic, "DNA translocation through low-noise glass nanopores," *ACS Nano*, vol. 7, no. 12, pp. 11255–11262, 2013.

[86] X. Xu, H. He, and Y. Jin, "Facile One-Step Photochemical Fabrication and Characterization of an Ultrathin Gold-Decorated Single Glass Nanopipette," *Analytical Chemistry*, vol. 87, no. 6, pp. 3216–3221, 2015.

[87] K. J. Freedman, L. M. Otto, A. P. Ivanov, A. Barik, S.-H. Oh, and J. B. Edel, "Nanopore sensing at ultra-low concentrations using single-molecule dielectrophoretic trapping.," *Nature communications*, vol. 7, p. 10217, 2016.

[88] L. Ying, S. S. White, A. Bruckbauer, L. Meadows, Y. E. Korchev, and D. Klenerman, "Frequency and voltage dependence of the dielectrophoretic trapping of short lengths of DNA and dCTP in a nanopipette.," *Biophysical journal*, vol. 86, no. 2, pp. 1018–27, 2004.

[89] S. Hernández-Ainsa, C. Muus, N. a. W. Bell, L. J. Steinbock, V. V. Thacker, and U. F. Keyser, "Lipid-coated nanocapillaries for DNA sensing.," *The Analyst*, vol. 138, no. 1, pp. 104–6, 2013.

[90] J. L. Gornall, K. R. Mahendran, O. J. Pambos, L. J. Steinbock, O. Otto, C. Chimerel, M. Winterhalter, and U. F. Keyser, "Simple reconstitution of protein pores in nano lipid bilayers," *Nano Letters*, vol. 11, no. 8, pp. 3334–3340, 2011.

[91] S. Hernández-Ainsa, N. A. W. Bell, V. V. Thacker, K. Göpfrich, K. Misiunas, M. E. Fuentes-Perez, F. Moreno-Herrero, and U. F. Keyser, "DNA origami nanopores for controlling DNA translocation," *ACS Nano*, vol. 7, no. 7, pp. 6024–6030, 2013.

[92] P. Cadinu, B. Paulose Nadappuram, D. Lee, J. Y. Y. Sze, G. Campolo, Y. Zhang, A. Shevchuk, S. Ladame, T. Albrecht, Y. E. Korchev, A. P. Ivanov, and J. B. Edel, "Single Molecule Trapping and Sensing using Dual Nanopores separated by a Zeptolitre Nanobridge," *Nano Letters*, vol. 17, no. 10, pp. 6376–6384, 2017.

[93] R. Ren, Y. Zhang, B. P. Nadappuram, B. Akpinar, D. Klenerman, A. P. Ivanov, J. B. Edel, and Y. Korchev, "Nanopore extended field-effect transistor for selective single-molecule biosensing," *Nature Communications*, vol. 8, no. 1, p. 586, 2017.

[94] W. M. Zhang, Y. G. Wang, J. Li, J. M. Xue, H. Ji, Q. Ouyang, J. Xu, and Y. Zhang, "Controllable shrinking and shaping of silicon nitride nanopores under electron irradiation," *Applied Physics Letters*, vol. 90, no. 16, pp. 88–91, 2007.

[95] S. Lombardo, J. H. Stathis, B. P. Linder, K. L. Pey, F. Palumbo, and C. H. Tung, "Dielectric breakdown mechanisms in gate oxides," *Journal of Applied Physics*, vol. 98, no. 12, p. 121301, 2005.

[96] W. Hei, H. Kwok, and P. Studies, *New Approach in Fabrication of Solid-State Nanopore for Bio-Sensing Applications*. PhD thesis, University of Ottawa, 2015.

[97] H. Kwok, M. Waugh, J. Bustamante, K. Briggs, and V. Tabard-Cossa, "Long passage times of short ssDNA molecules through metallized nanopores fabri-

cated by controlled breakdown," *Advanced Functional Materials*, vol. 24, no. 48, pp. 7745–7753, 2014.

[98] C. E. Arcadia, C. C. Reyes, and J. K. Rosenstein, "In Situ Nanopore Fabrication and Single-Molecule Sensing with Microscale Liquid Contacts," *ACS Nano*, vol. 11, no. 5, pp. 4907–4915, 2017.

[99] J. Feng, K. Liu, M. Graf, M. Lihter, R. D. Bulushev, D. Dumcenco, D. T. L. Alexander, D. Krasnozhon, T. Vuletic, A. Kis, and A. Radenovic, "Electrochemical reaction in single layer MoS2: Nanopores opened atom by atom," *Nano Letters*, vol. 15, no. 5, pp. 3431–3438, 2015.

[100] A. T. Kuan, B. Lu, P. Xie, T. Szalay, and J. A. Golovchenko, "Electrical pulse fabrication of graphene nanopores in electrolyte solution," *Applied Physics Letters*, vol. 106, no. May, p. 203109, 2015.

[101] A. Zrehen, T. Gilboa, and A. Meller, "Real-Time Visualization and Sub-Diffraction Limit Localization of Nanometer-Scale Pore Formation by Dielectric Breakdown," *Nanoscale*, 2017.

[102] Y. Wang, Q. Chen, T. Deng, and Z. Liu, "Nanopore fabricated in pyramidal HfO ₂ film by dielectric breakdown method," *Applied Physics Letters*, vol. 111, no. 14, p. 143103, 2017.

[103] A. Carlsen and V. Tabard-Cossa, "Enhanced Stability of 2-nm Nanopores Fabricated by Controlled Breakdown," in *Biophysical Society of Canada 1st Annual Meeting*, Biophysical Society of Canada, 2015.

[104] K. Briggs, "Applications of Nanopore Fabrication by Controlled Breakdown." 2015.

[105] M. Waugh, A. Carlsen, D. Sean, G. W. G. Slater, K. Briggs, H. Kwok, and V. Tabard-Cossa, "Interfacing solid-state nanopores with gel media to slow DNA translocations," *Electrophoresis*, vol. 36, no. 15, pp. 1759–1767, 2015.

[106] K. Matsui, I. Yanagi, Y. Goto, and K. I. Takeda, "Prevention of dielectric breakdown of nanopore membranes by charge neutralization," *Scientific Reports*, vol. 5, pp. 1–9, 2015.

[107] Y. Liu, D. E. Huber, and R. W. Dutton, "Limiting and overlimiting conductance in field-effect gated nanopores," *Applied Physics Letters*, vol. 96, no. 25, pp. 2010–2013, 2010.

[108] A. Höltzel and U. Tallarek, "Ionic conductance of nanopores in microscale analysis systems: Where microfluidics meets nanofluidics," *Journal of Separation Science*, vol. 30, no. 10, pp. 1398–1419, 2007.

[109] M. Wanunu and A. Meller, *Single-Molecule Techniques: A Laboratory Manual*. New York: Cold Spring Harbor Laboratory, 2008.

[110] I. Yanagi, K. Fujisaki, H. Hamamura, and K. I. Takeda, "Thickness-dependent dielectric breakdown and nanopore creation on sub-10-nm-thick SiN membranes in solution," *Journal of Applied Physics*, vol. 121, no. 4, 2017.

[111] A. Ivankin, R. Y. Henley, J. Larkin, S. Carson, M. L. Toscano, and M. Wanunu, "Label-free optical detection of biomolecular translocation through nanopore arrays," *ACS Nano*, vol. 8, no. 10, pp. 10774–10781, 2014.

[112] S. Pud, D. Verschueren, N. Vukovic, C. Plesa, M. P. Jonsson, and C. Dekker, "Self-Aligned Plasmonic Nanopores by Optically Controlled Dielectric Breakdown," *Nano Letters*, vol. 15, no. 10, pp. 7112–7117, 2015.

[113] R. Tahvildari, E. Beamish, V. Tabard-Cossa, and M. Godin, "Integrating nanopore sensors within microfluidic channel arrays using controlled breakdown," *Lab Chip*, vol. 15, no. 6, pp. 1407–1411, 2015.

[114] J. Bustamante, *Synchronous Optical and Electrical Measurements of Single DNA Molecules Translocating Through a Solid-State Nanopore*. M.sc., University of Ottawa, 2014.

[115] R. Tahvildari, E. Beamish, K. Briggs, S. Chagnon-Lessard, A. N. Sohi, S. Han, B. Watts, V. Tabard-Cossa, and M. Godin, "Manipulating Electrical and Fluidic Access in Integrated Nanopore-Microfluidic Arrays Using Microvalves," *Small*, vol. 13, no. 10, pp. 1–7, 2017.

[116] T. Jain, B. C. Rasera, R. J. S. Guerrero, J. M. Lim, and R. Karnik, "Microfluidic multiplexing of solid-state nanopores," *Journal of Physics Condensed Matter*, vol. 29, no. 48, 2017.

[117] K. Briggs, G. Madejski, M. Magill, K. Kastritis, H. W. De Haan, J. L. McGrath, and V. Tabard-Cossa, "DNA Translocations through Nanopores under Nanoscale Preconfinement," *Nano Letters*, vol. 18, no. 2, pp. 660–668, 2018.

[118] H. Liu, J. He, J. Tang, H. Liu, P. Pang, D. Cao, P. Krstic, S. Joseph, S. Lindsay, and C. Nuckolls, "Translocation of Single-Stranded DNA Through Single-Walled Carbon Nanotubes," *Science (New York, N.Y.)*, vol. 327, no. 5961, pp. 64–68, 2010.

[119] T. Ito, L. Sun, and R. M. Crooks, "Simultaneous Determination of the Size and Surface Charge of Individual Nanoparticles Using a Carbon Nanotube-Based Coulter Counter," *Analytical Chemistry*, vol. 75, no. 10, pp. 2399–2406, 2003.

[120] J. Geng, K. Kim, J. Zhang, A. Escalada, R. Tunuguntla, L. R. Comolli, F. I. Allen, A. V. Shnyrova, K. R. Cho, D. Munoz, Y. M. Wang, C. P. Grigoropoulos, C. M. Ajo-Franklin, V. A. Frolov, and A. Noy, "Stochastic transport through carbon nanotubes in lipid bilayers and live cell membranes," *Nature*, vol. 514, no. 7524, pp. 612–615, 2014.

[121] L. Sun and R. M. Crooks, "Single carbon nanotube membranes: A well-defined model for studying mass transport through nanoporous materials," *Journal of the American Chemical Society*, vol. 122, no. 49, pp. 12340–12345, 2000.

[122] E. Secchi, S. Marbach, A. Niguès, D. Stein, A. Siria, and L. Bocquet, "Massive radius-dependent flow slippage in single carbon nanotubes," *Nature*, vol. 537, no. 7619, pp. 210–213, 2016.

[123] B. Luan, H. Peng, S. Polonsky, S. Rossnagel, G. Stolovitzky, and G. Martyna, "Base-By-Base Ratcheting of Single Stranded DNA through a Solid-State Nanopore," *Physical Review Letters*, vol. 104, p. 238103, jun 2010.

[124] J. Bai, D. Wang, S.-w. Nam, H. Peng, R. Bruce, L. Gignac, M. Brink, E. Kratschmer, S. Rossnagel, P. Waggoner, K. Reuter, C. Wang, Y. Astier, V. Balagurusamy, B. Luan, Y. Kwark, E. Joseph, M. Guillorn, S. Polonsky, A. Royyuru, S. Papa Rao, and G. Stolovitzky, "Fabrication of sub-20 nm nanopore arrays in membranes with embedded metal electrodes at wafer scales," *Nanoscale*, vol. 6, no. 15, pp. 8900–8906, 2014.

[125] J. K. Holt, A. Noy, T. Huser, D. Eaglesham, and O. Bakajin, "Fabrication of a carbon nanotube-embedded silicon nitride membrane for studies of nanometer-scale mass transport," *Nano Letters*, vol. 4, no. 11, pp. 2245–2250, 2004.

[126] B. Luan, G. Stolovitzky, and G. Martyna, "Slowing and controlling the translocation of DNA in a solid-state nanopore," *Nanoscale*, vol. 4, no. 4, pp. 1068–1077, 2012.

[127] N. J. Loman and M. Watson, "Successful test launch for nanopore sequencing," *Nature Methods*, vol. 12, no. 4, pp. 303–304, 2015.

[128] P. S. Waggoner, A. T. Kuan, S. Polonsky, H. Peng, and S. M. Rossnagel, "Increasing the speed of solid-state nanopores," *Journal of Vacuum Science & Technology B, Nanotechnology and Microelectronics: Materials, Processing, Measurement, and Phenomena*, vol. 29, no. 3, p. 032206, 2011.

[129] B. Luan, C. Wang, A. Royyuru, and G. Stolovitzky, "Controlling the motion of DNA in a nanochannel with transversal alternating electric voltages.," *Nanotechnology*, vol. 25, no. 26, p. 265101, 2014.

[130] B. Luan, G. Martyna, and G. Stolovitzky, "Characterizing and controlling the motion of ssDNA in a solid-state nanopore," *Biophysical Journal*, vol. 101, no. 9, pp. 2214–2222, 2011.

[131] J. Shim, J. A. Rivera, and R. Bashir, "Electron beam induced local crystallization of HfO2 nanopores for biosensing applications," *Nanoscale*, vol. 5, no. 22, p. 10887, 2013.

[132] Z. Jiang, M. Mihovilovic, J. Chan, and D. Stein, "Fabrication of nanopores with embedded annular electrodes and transverse carbon nanotube electrodes.," *Journal of physics. Condensed matter : an Institute of Physics journal*, vol. 22, no. 45, p. 454114, 2010.

[133] S. Harrer, P. S. Waggoner, B. Luan, A. Afzali-Ardakani, D. L. Goldfarb, H. Peng, G. Martyna, S. M. Rossnagel, and G. A. Stolovitzky, "Electrochemical protection of thin film electrodes in solid state nanopores," *Nanotechnology*, vol. 22, no. 27, p. 275304, 2011.

[134] A. P. Ivanov, E. Instuli, C. M. McGilvery, G. Baldwin, D. W. McComb, T. Albrecht, and J. B. Edel, "DNA tunneling detector embedded in a nanopore," *Nano Letters*, vol. 11, no. 1, pp. 279–285, 2011.

[135] F. Traversi, C. Raillon, S. M. Benameur, K. Liu, S. Khlybov, M. Tosun, D. Krasnozhon, A. Kis, and A. Radenovic, "Detecting the translocation of DNA through a nanopore using graphene nanoribbons," *Nature Nanotechnology*, vol. 8, no. 12, pp. 939–945, 2013.

[136] S. Chang, S. Huang, J. He, F. Liang, P. Zhang, S. Li, X. Chen, O. Sankey, and S. Lindsay, "Electronic signatures of all four DNA nucleosides in a tunneling gap," *Nano Letters*, vol. 10, no. 3, pp. 1070–1075, 2010.

[137] P. S. Spinney, S. D. Collins, D. G. Howitt, and R. L. Smith, "Fabrication and characterization of a solid-state nanopore with self-aligned carbon nanoelectrodes for molecular detection," *Nanotechnology*, vol. 23, no. 13, p. 135501, 2012.

[138] P. Xie, Q. Xiong, Y. Fang, Q. Qing, and C. M. Lieber, "Local electrical potential detection of DNA by nanowire–nanopore sensors," *Nature Nanotechnology*, vol. 7, no. 2, pp. 119–125, 2011.

[139] A. P. Ivanov, K. J. Freedman, M. J. Kim, T. Albrecht, and J. B. Edel, "High precision fabrication and positioning of nanoelectrodes in a nanopore," *ACS Nano*, vol. 8, no. 2, pp. 1940–1948, 2014.

[140] T. Nelson, B. Zhang, and O. V. Prezhdo, "Detection of nucleic acids with graphene nanopores: Ab initio characterization of a novel sequencing device," *Nano Letters*, vol. 10, no. 9, pp. 3237–3242, 2010.

[141] M. Tsutsui, M. Taniguchi, K. Yokota, and T. Kawai, "Identifying single nucleotides by tunnelling current," *Nature Nanotechnology*, vol. 5, no. 4, pp. 286–290, 2010.

[142] J. Feng, K. Liu, R. D. Bulushev, S. Khlybov, D. Dumcenco, A. Kis, and A. Radenovic, "Identification of single nucleotides in MoS2 nanopores," *Nature Nanotechnology*, vol. 10, no. 12, pp. 1070–1076, 2015.

Chapter 3

Automated Fabrication of 2 nm Solid-State Nanopores for Nucleic Acid Analysis

Kyle Briggs, Harold Kwok, and Vincent Tabard-Cossa

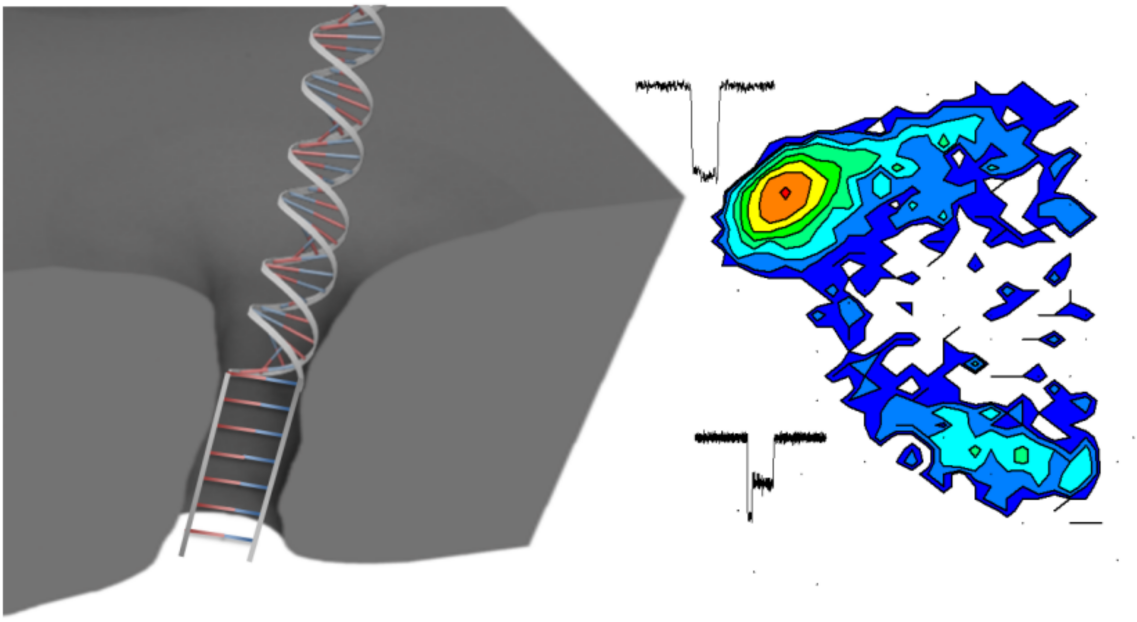

Adapted with permission from [K. Briggs, H. Kwok, and V. Tabard-Cossa, "Automated Fabrication of 2-nm Solid-State Nanopores for Nucleic Acid Analysis," *Small*, vol. 10, no. 10, pp. 2077–2086, 2014]

Abstract

We demonstrate the automated and reproducible fabrication of sub-2 nm nanopores in 10 nm thick silicon nitride membranes, through controlled dielectric breakdown in solution. Our results reveal that under the appropriate conditions, nanopores can be fabricated with a size no larger than 2.0 ± 0.5 nm in diameter for a sample of $N = 23$ nanopores, with an average and standard deviation of 1.3 ± 0.6 nm. The dimensions of these nanopores are confi rmed by using individual translocating DNA molecules as molecular rulers. We show that a 2.0 nm and a 2.1 nm diameter nanopore are capable of distinguishing single-stranded DNA versus double-stranded DNA, and that a 2.4 nm diameter nanopore can be used to investigate the overstretching transition in short dsDNA fragments. These results highlight the reliability and precision of the automated fabrication of nanopores via controlled dielectric breakdown, showing great promise for the manufacturing of future nanopore-based technologies.

3.1 Introduction

The utility of nanopores as single-molecule sensors is well-established, and relies on electrokinetically driving a charged analyte through the nanopore in an electrolyte solution while monitoring changes in the ionic current[2–5]. For nucleic acid analysis, it is often essential for the DNA molecule to pass through the pore in a single-file, sequential, manner. For this reason, nanopores with diameter comparable to that of DNA are crucial. At the same time, the sensitivity of the sensor also improves as its size approaches that of the analyte of interest.

The atomically precise structure of biological pores, such as α-hemolysin and MspA, has, in part, contributed to their success in sequencing DNA strands, and at least in the short-term makes them more attractive for the commercialization of

nanopore-based technologies[6–8]. Yet, compared to their organic counterparts, solid-state nanopore devices possess many attributes advantageous for the development of clinical diagnostic tools for personalized medicine applications. Solid-state nanopores offer: a tunable pore size; increased stability over a wide range of operating conditions (pH, voltage, temperature); mechanical robustness; and a natural propensity for integration with semiconductor and microfluidics technologies.

However, reliable fabrication of nanopores in thin solid-state membranes which are small enough to ensure single-file passage of double stranded DNA (dsDNA) and single-stranded DNA (ssDNA) has been challenging. While techniques for fabricating nanopores in the sub-5 nm range exist, either based on transmission electron microscope (TEM)[9,10] or ion-beam sculpting machine[11], they are time-consuming, labor intensive, and have low yield. Typically, beams of high-energy particles cannot be focused tightly enough to reliably achieve 2 nm nanopores. Larger pores must therefore be shrunk through localized melting of the membrane in order to achieve the desired pore size[9], though at the cost of locally modifying the membrane material composition[12,13]. In addition, for the case of the widely used TEM-based drilling, the nanopore creation is detected by eye, monitoring flickering on a fluorescent screen, confounding automation.

In spite of these difficulties, small nanopores with dimensions ranging from 1.5 nm to 5 nm are being fabricated and used by a few research groups. Sub-2 nm nanopores are capable of directly affecting DNA structure and probing unzipping mechanics[14]. Another interesting observation was that the kinetics of DNA translocation were found to be qualitatively different as the nanopore size decreases, revealing much longer dwell times, highlighting the importance of DNA-pore interactions (e.g. friction) in the translocation dynamics[15,16]. The ability of small nanopores to detect DNA substructure also makes possible numerous medical diagnostic applications, includ-

ing analytic drug screening through spatially resolved detection of DNA-biomolecule bound complexes[17]. More recently, it has been shown that small nanopores are capable of distinguishing short homopolymers from one another[18] and detecting DNA substructure[19], moving one step closer to the goal of solid-state nanopore-based technologies for health related applications. Another study has demonstrated the utility of hafnium oxide as a robust membrane material for sub-2 nm nanopores which can be used to slow DNA translocations through interactions with the substrate[20]. Despite these impressive demonstrations, the pace of scientific discoveries employing small solid-state nanopores remains very limited by the low yield and complexity of the fabrication methods, which require extensive manual control from a highly trained user and numerous handling steps to prepare the nanopores, any part of which can damage the membrane. Consequently, commercially available 50×50 μm^2, 10 nm thick membranes are rarely used as they are far more likely to break, thus limiting fabrication to thicker membranes at the expense of a lower signal-to-noise ratio. Some groups overcome this difficulty by locally thinning part of a membrane[21], though this adds multiple steps to the fabrication process, unavoidably affecting yield and increasing the time invested in fabrication.

Here, we show that fabrication by controlled dielectric breakdown can be used to reliably produce, in a simple and automated fashion, individual 2 nm nanopores in a 10 nm thick silicon nitride (SiN_x) membrane. We demonstrate a yield greater than 95% by optimizing the fabrication conditions for the controlled breakdown of a dielectric membrane in an electrolyte solution[22]. The method relies on application of a sustained electric field across an insulating membrane in solution near its dielectric breakdown strength, which induces a localized leakage current through the membrane. By monitoring the resulting sustained tunneling current, the creation of a single nanopore is detected as an abrupt increase in the leakage current, which we

attribute to the onset of ionic current. Small nanopores in thin membranes are obtained through feedback control at low to moderate voltages ($5 - 10$ V) to limit the damage to the membrane after the dielectric breakdown event. The current-voltage (I-V) characteristics of these nanopores over a ± 1 V range are measured in high salt concentration in order to minimize surface effects, which can cause current rectification, particularly for pores with diameters on the scale of the Debye length[23,24]. We employ the commonly used method of inferring nanopore size from conductance measurements, following Wanunu *et al.*[21,25].

$$G = \sigma \left(\frac{4L}{\pi d^2} + \frac{1}{d} \right)^{-1}, \tag{3.1}$$

where σ is the solution conductivity, L the membrane thickness, d the pore diameter, and G the nanopore conductance, the validity of which has previously been demonstrated for nanopores fabricated by dielectric breakdown[22]. We demonstrate that nanopores produced in this way are excellent single-molecule detectors, capable of distinguishing ssDNA from dsDNA or probing tertiary structure in dsDNA. These results also serve to validate the accuracy of the nanopore size extracted from the conductance-based model.

3.2 Results and Discussion

3.2.1 Fabrication of sub-2 nm Nanopores

While our previous work with nanopores established the possibility of creating a single sub-2 nm nanopore in a thin silicon nitride membrane, parameters were not optimized for their reproducible and automated fabrication. To demonstrate that nanofabrication by dielectric breakdown can consistently achieve nanopores smaller

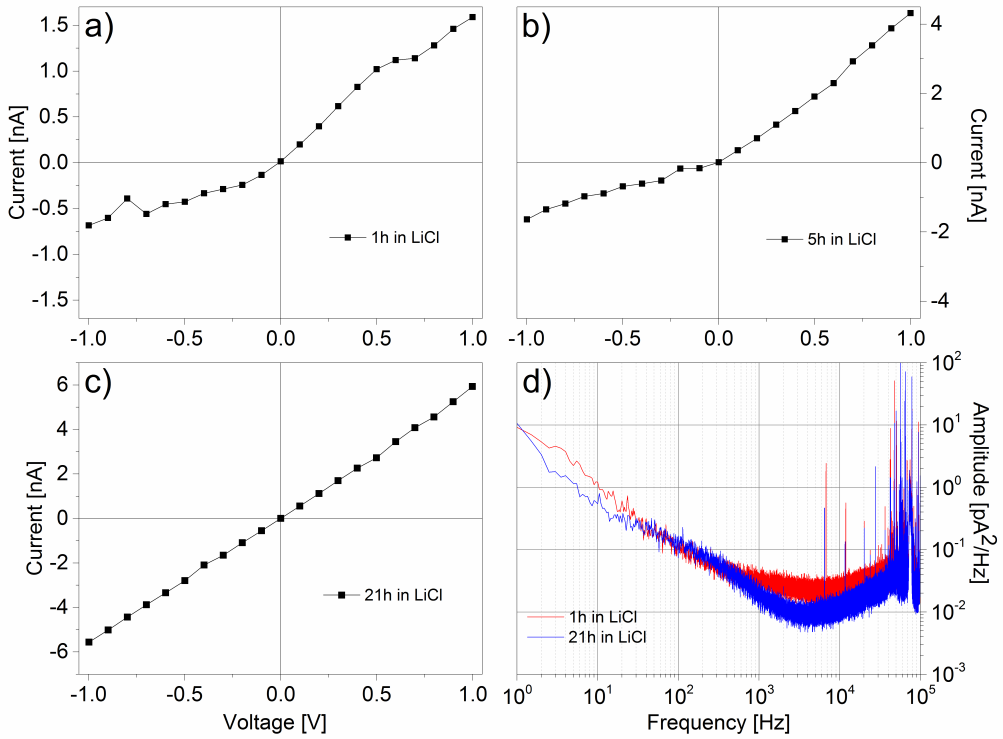

Figure 3.1: Time evolution of I-V characteristics for a nanopore immersed in 3.6 M LiCl pH 8. No other action was performed except for the periodic I-V curve measurements ramped from –1V and +1V. a) After 1 hour, $G_+ = 1.54$ nS, $G_- = 0.59$ nS, rectification ratio of 2.6; b) after 5 hours, $G_+ = 4.4$ nS, $G_- = 1.57$ nS, rectification ratio of 2.8; c) after 21 hours, $G_{pore} = 5.68$ nS, pore is Ohmic. Estimated final size from conductance model is 2.3 nm. Note that vertical scales differ on all three graphs. d) Power spectrum density for the ionic current signal captured at +200 mV, showing marginal improvement to noise despite increased current passage over the duration of nanopore equilibration.

than 2 nm in diameter, we performed a systematic study under a specific set of fabrication conditions.

Prior to pore fabrication, 10 nm thick SiN_x membranes are cleaned in O_2 plasma for 30 s at 30 W to ensure a uniformly clean surface and to facilitate wetting of the membrane. We fabricate nanopores in 1M KCl or NaCl solution buffered at pH

10 with a trans-membrane potential difference of -8 V. Once the leakage current, $I_{leakage}$, exceeds a preset threshold, I_{cutoff}, defined as $\frac{I_{cutoff}}{I_{leakage}} = 1.2 \pm 0.1$ and updated as needed during the fabrication process to maintain this ratio, the applied voltage is terminated at a response rate of 10 Hz. These conditions are generally sufficient to limit the time between pore creation and voltage termination to less than 0.5 s. The typical time-to-pore creation in these conditions is approximately 10 minutes.

Immediately after creation, nanopores fabricated in this way typically exhibit some degree of rectification, self-gating, or significant levels of low-frequency ($\frac{1}{f}$-type) noise. As described in work by Beamish *et al.*[26], a moderate electric field strength in the range of $\pm 0.2 - 0.3$ V/m can be used rapidly mitigate these issues. However, we have found that this approach generally results in significant enlargement of the pore diameter. For this study, to ensure the fabrication of nanopores of the smallest diameter with low $\frac{1}{f}$-type noise and Ohmic behavior, we simply switched the solution to 3.6 M LiCl buffered at pH 8 and allowed the nanopore to equilibrate for a few hours after fabrication. We have found this to be an effective way to improve electrical characteristics of our nanopores. All I-V curves improve steadily in these conditions, showing an Ohmic response within a few hours. Figure 3.1 presents the time evolution of the I-V characteristics of a nanopore as a function of immersion time in 3.6 M LiCl pH 8, showing progressive improvement from a rectifying and self-gating pore to a well-behaved, Ohmic nanopore. Nanopores left in 3.6 M LiCl pH 8 overnight usually grow less than 1 nm. Note that nanopores drilled with a TEM also generally show conductance increasing over time, at a rate which can be significantly higher than observed here[12]. Figure 3.2a shows I-V curves of 5 independent nanopores fabricated via controlled dielectric breakdown once their I-V characteristics showed an Ohmic response, within the first 4 hours after creation. We have found that all pores fabricated for this study showed similar electrical behaviors. These nanopores

are also relatively stable over time, showing on average a growth rate of 0.4 nm/day ($N = 4$, for a period of 4 days) at room temperature in 3.6 M LiCl pH 8, with most of the growth concentrated in the first day. Remarkably, our results show that under the conditions described above we can fabricate nanopores no larger than 2.0 ± 0.5 nm in diameter for a sample of $N = 23$ nanopores ($N = 19$ in KCl, $N = 4$ in NaCl), with an average and standard deviation of 1.3 ± 0.6 nm. The distribution of initial nanopore sizes is shown in Figure 3.2b.

To achieve these results, we have identified two key conditions to reproducibly create small nanopores. First, the applied voltage must be rapidly reduced or turned off upon detection of the first discrete breakdown event, to avoid significant nanopore growth[26]. Secondly, the use of thinner membranes (e.g. 10 nm thick SiN_x) should be favored to minimize the variability in the damage size as a result of the dielectric breakdown event. Indeed, we have observed that although the fabrication of sub-2 nm nanopores is possible on 30 nm thick SiN_x membranes, the width of the distribution of fabricated size is larger. Once these conditions have been met, the choice of electrolyte solution used for fabrication plays a secondary role in the overall nanopore characteristics. We have found that using 1 M KCl pH 10 as the fabrication solution gives reliable results, showing a clearer indication of a nanopore creation event and less initial ionic current rectification than other experimental conditions.

Under these fabrication conditions, pore enlargement after the discrete breakdown event is slow enough that a tighter cutoff or faster response time is not necessary to achieve 2 nm diameter nanopores. In principle, more rapid (10^{-3} vs. 10^{-1} s) response time and finer control could be achieved if it were necessary. The slightly extended tail toward larger pore sizes in Figure 2b is a direct consequence of the loose cutoff conditions used ($\frac{I_{cutoff}}{I_{leakage}} = 1.2 \pm 0.1$ and 0.1 s response time), and the distribution could be made even narrower if an application demanded it.

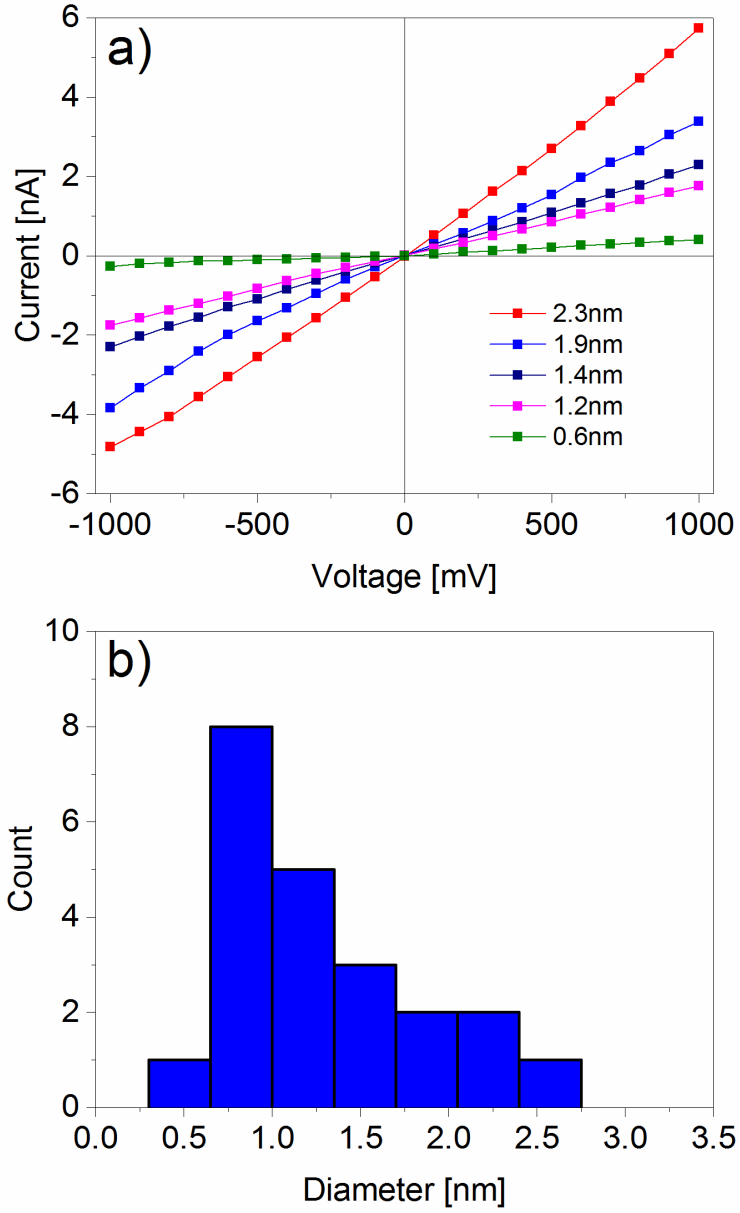

Figure 3.2: a) I-V curves of fabricated nanopores ranging in size from 0.6 nm to 2.3 nm, after aging for up to 24 h in 3.6 M LiCl pH 8. Based on 3.1 1, a 1.5 nm nanopore has a conductance of 2.54 nS, a 2 nm nanopore has a conductance of 4.4 nS, while a 2.5 nm pore has a conductance of 6.60 nS. b) A histogram of the initial size of the fabricated nanopores, measured after allowing 1 hour of equilibration in 3.6 M LiCl pH 8, as determined from a conductance-based model[25], which assumes a cylindrical geometry. In the case of rectification, size is inferred from the polarity of highest conductance.

3.2.2 dsDNA and ssDNA as Molecular Rulers

In order to establish the accuracy of the effective nanopore size extracted from the conductance-based model (Equation 3.1), we demonstrate the translocation of 50 nt fragments of single-stranded DNA (ssDNA) and 50 bp fragments of double-stranded DNA (dsDNA) through nanopores which were measured at only slightly larger than the nominal diameter of the type of DNA in solution. In particular, we demonstrate successful translocation of ssDNA ($d_{ss} \approx 1.4$ nm) through nanopores measured at 2.0 ± 0.2 nm and 2.1 ± 0.2 nm, which should not be able to pass dsDNA ($d_{ds} \approx 2.2$ nm), and successful dsDNA translocation through a nanopore measured at 2.4 ± 0.2 nm. All translocation experiments are carried out in 3.6 M LiCl pH 8 in order to maximize passage times[27] and to suppress surface effects. We first investigate the translocation kinetics of DNA through a 2.0 nm nanopore as inferred from Equation 3.1. In order to avoid contamination or ambiguity between which species is being translocated, dsDNA and ssDNA are added to opposite sides of the membrane, and the fluid reservoirs are biased appropriately to drive negatively charged DNA though the nanopore. Since the diameter of this particular nanopore should be too small to allow dsDNA to pass, the attempt is first made to translocate dsDNA at -100 mV and -200 mV. Figures 3.3a and 3.3b show current traces before and after addition of both types of DNA on opposite sides of the membrane at a concentration of 50 nM. The baseline current is stable before addition of any DNA, showing no transient fluctuations during a control lasting 180 seconds. Upon addition of 50 bp dsDNA, very long (on the order of seconds) single-molecule events are observed, which fully block the nanopore (greater than 95% blockage). In the reverse voltage polarity, 50 nt ssDNA is observed to translocate readily, with an average of 70% blockade level, as shown in Figure 3.3c and 3.3d. The scatter plot of the conductance block-

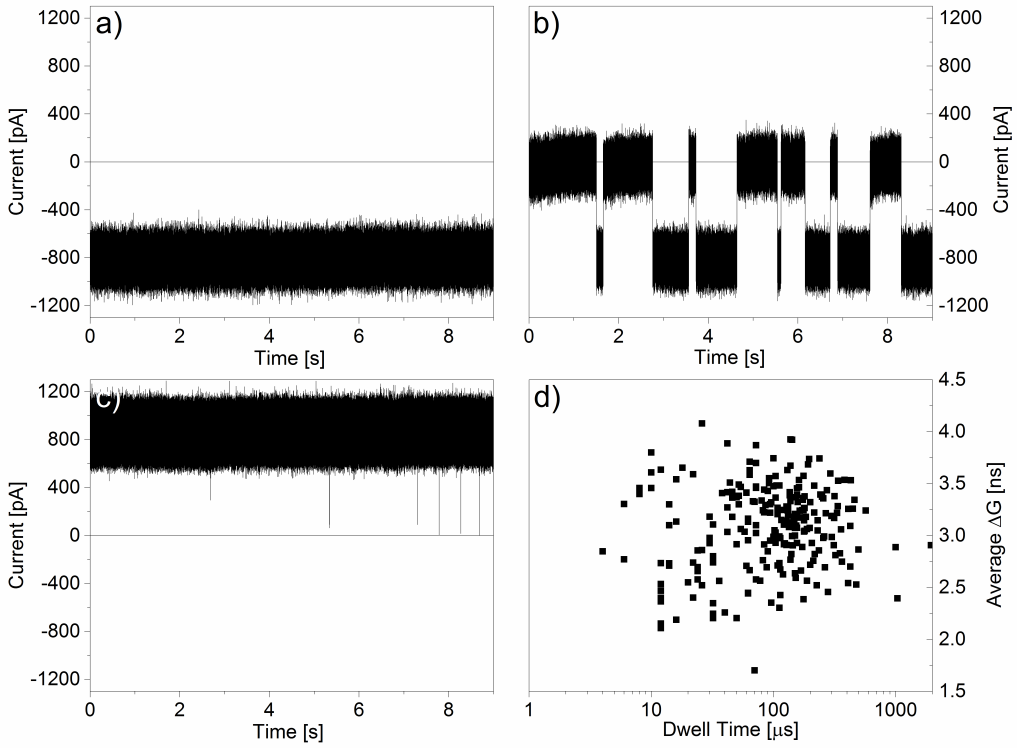

Figure 3.3: Current traces of a 2.0 nm diameter nanopore in 3.6 M LiCl pH 8 (nanopore conductance, $G_{pore} = 4.5$ nS) with a) no DNA at -200 mV, showing a clean baseline; b) 50 nM 50 bp dsDNA at -200 mV showing very long lasting events, which fully blocks the pore (residual current is less than 30 pA, within the noise), and c) 50 nM 50 nt ssDNA at +200 mV showing fast DNA translocation events with deep nanopore conductance blockades (70% blockage); d) Scatter plot of conductance blockades versus dwell times for ssDNA translocation events ($N = 245$ events). Data was sampled at 500 kHz and low-pass filtered at 100 kHz.

ages as a function of the translocation times, shown in Figure 3.3d, shows a slightly higher blockade than expected from a bulk excluded area argument in a solution of conductivity σ through a membrane of length L given by[28,29]:

$$\Delta G = \sigma \frac{\pi d_{DNA}^2}{4L} \tag{3.2}$$

which predicts a blockage of 2.5 nS, whereas the average blockage level observed is 3.1 nS for 245 single-molecule translocation events. We discuss this small discrepancy below.

In the dsDNA experiment shown in Figure 3.3, while it is clear from the presence of fully blocked events that dsDNA molecules are indeed interacting with the nanopore, the events are so long (seconds to minutes, in some cases) that it is unlikely that they represent full translocations. Moreover, if dsDNA translocated on that timescale, one might expect that reversing the voltage polarity during an event would result in a roughly comparable length of time before the nanopore returned to its open conductance state. This is not observed, and reversing the polarity immediately unblocks the pore, suggesting that dsDNA intercalates at the entrance of the pore, but is most probably not fully threaded at the voltages attempted (-100 mV and -200 mV). On the other hand, ssDNA translocates readily once the voltage reaches $+200$ mV. The dwell times in Figure 3.3d are nevertheless surprisingly long given the short length of the ssDNA strands (25 nm), and corresponds to an exponential distribution with a characteristic time of 170 μs. Whereas for unhindered translocations through a nanopore one expects that the total amount of charge blocked by the biomolecule during translocation, called the equivalent charge deficit (ECD), will be constant and independent of the conformation in which the molecule translocates, this does not apply to friction-dominated translocation. Instead, the general trend is for increasing dwell time with increasing conductance blockade, which correspondingly increases the ECD linearly with dwell time. This behaviour has been observed by several other groups working with solid-state nanopores of similar diameter, and is generally attributed to friction and other short-range pore-analyte interactions[15,16]. A control experiment (data not shown), translocating ssDNA through a nanopore fabricated in the same conditions but enlarged to 4.5 nm in diameter, showed passage times

which were much faster, nearing the resolution of our instrument, limited in bandwidth with a maximum low-pass filter of 100 kHz, thus confirming that the reduced translocation times in small nanopores is a size effect, as in previous studies[16,20,30]. Analysis of ssDNA translocation data at +200 mV, presented in Figure 3.3d, reveals

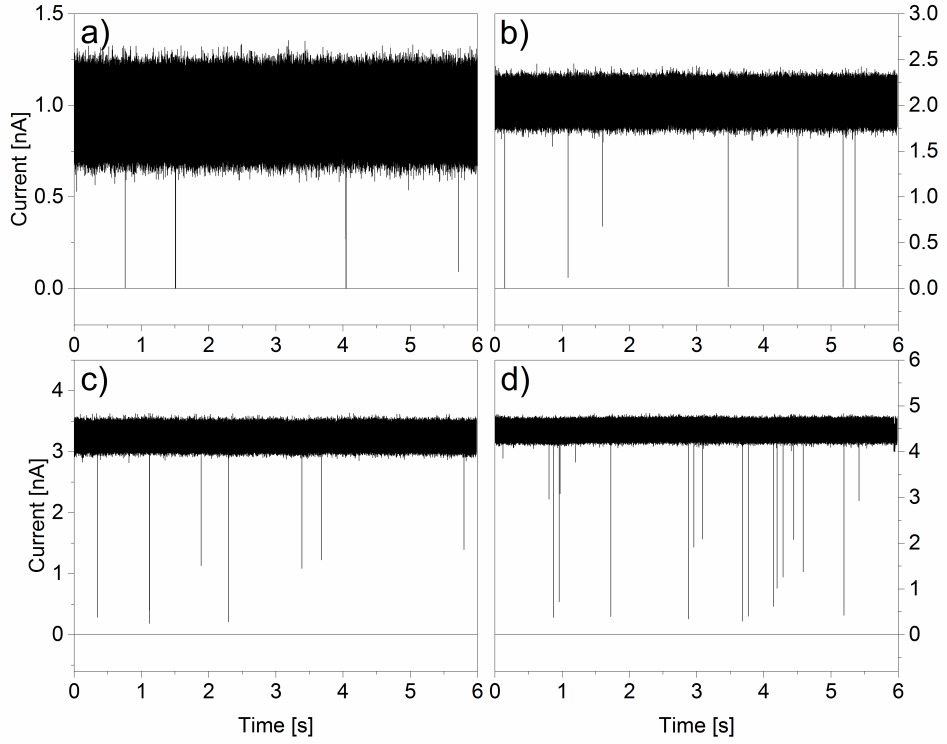

Figure 3.4: Current traces of ssDNA translocating a 2.1 nm nanopore (nanopore conductance 4.88 nS) in 3.6M LiCl pH 8 at a) −200 mV, showing only single-level blockages with approximately 73% blockage b) -400mV, showing two-level events with around 80% blockage and single-level events with around 60% blockage. c) −600 mV, showing two-level events with approximately 80% blockage and single-level events with approximately 50% blockage and d)−800mV, showing mainly single-level events with approximately 45% blockage. Current traces are multiplied by −1 for clarity. Data was acquired at 500 kHz and low-pass filtered at 100 kHz.

no current levels associated with molecules threading in folded configurations, despite the fact that the persistence length of ssDNA in high molarity electrolyte is less than

1 nm[31]. The absence of folded events is another strong indication that this particular nanopore, estimated at 2.0 nm by the conductance model, has a highly circular opening, with axes ranging between 1.5 nm (to allow passage of ssDNA at all) and 2.2 nm (to disallow folded ssDNA), indicating a measurement error in the conductance model used to extract an effective size of ± 0.5 nm. This is further supported by the fact that dsDNA can fully block the nanopore, which would not be possible if the minor axis of the nanopore diameter was less than 2.0 nm. The conductance blockade observed is on average slightly larger than the 2.5 nS predicted by the bulk model. We attribute this small discrepancy to uncertainties in the actual membrane thickness (nominally 10 ± 1 nm) and in the conductivity of the electrolyte inside the nanopore at this length scale. In addition, since electroosmotic flow opposes DNA motion at this pH[32], any interaction of the DNA with the electric double layer, which is unavoidable given the size of the nanopore, would tend to block more current than the bulk prediction. In order to properly include the surface contribution to the ionic current requires an accurate estimate of the surface charge of the nanopore, which is as yet unknown for this fabrication process. However, accounting for the surface charge contribution to equation 3.1 would only reduce the extracted pore size, and the error incurred by ignoring it remains smaller than 0.5 nm[33] for these particular conditions over the typical range of surface charge values for silicon nitride[34].

Next, we performed another set of experiments, under identical condition, on a different nanopore estimated at 2.1 nm in diameter by Equation 3.1. Figure 3.4 displays ionic current traces showing individual 50 nt ssDNA translocation events for voltages between -200 mV and -800 mV. We observed thousands of single-molecule translocation events at each voltage. Note that, contrary to the previous study, no dsDNA translocations were observed at +200 mV. At +600 mV, some transient, very small conductance blockages were observed, showing ca. 10% blockage, suggesting

dsDNA collisions with the nanopore, but no threading.

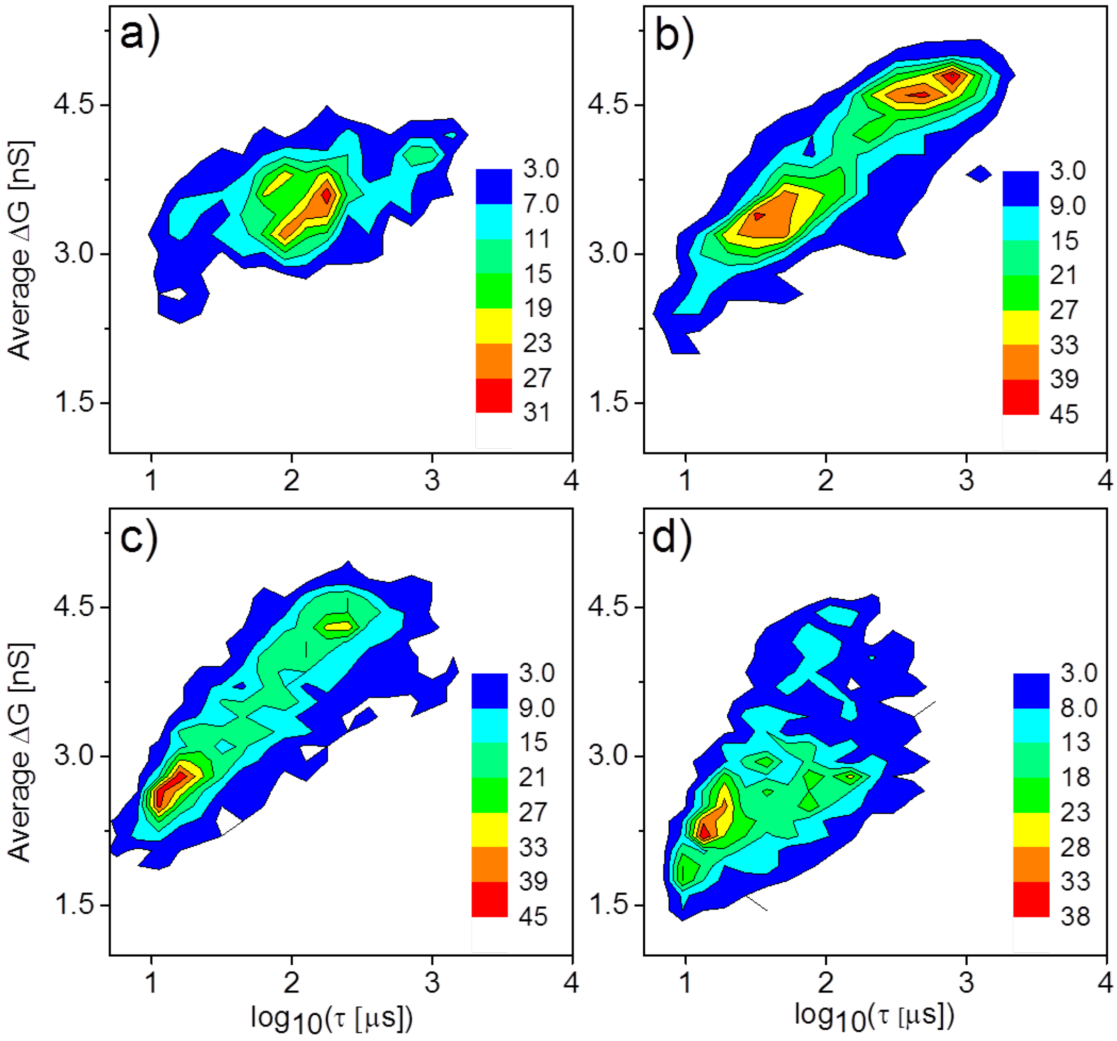

Figure 3.5: Semi-log event density plots of 50 nt ssDNA translocation events through a nanopore with an area equivalent to a 2.1 nm nanopore, with open pore conductance of 4.9 nS. a) Data acquired at −200 mV showing only one conductance blockade level ($N = 877$ events); b) Data acquired at −400 mV showing a second conductance blockade levels ($N = 1290$ events); c) Data acquired at −600 mV showing two conductance blockade levels ($N = 1823$ events); d) Data acquired at −800 mV showing two conductance blockade levels ($N = 1685$ events). Color scale indicates number of events. Data was digitized at 500 kHz and low-pass filtered at 100 kHz.

Figure 3.5 presents analysis of the data acquired at various voltages in the form of

semi-log density plots of conductance blockade versus dwell times for ssDNA translocation events. Similarly to the data acquired on the 2.0 nm nanopore, the relationship between dwell time and conductance blockage is not what one would expect for electrophoretically dominated translocation (the e.c.d is not conserved), showing weaker voltage dependence on the translocation time than the $t \propto V^{-1}$ observed for larger nanopores created in solution[22], strong friction effects, and significantly weaker dwell time dependence than the exponential dependence of dsDNA dwell time on voltage observed in small nanopores[16,20]. We attribute this difference to increased interactions between ssDNA and the nanopore than would be observed for dsDNA, which would lead to increased dwell times with a weaker voltage dependence. At -200 mV, we only observe single-level events with a distribution of blockade amplitudes and dwell times equivalent to the data shown in Figure 3.3d. Recall that the predicted blockage is 2.5 nS, whereas the average blockage level observed for this pore is 3.5 nS for $N = 877$ single-molecule translocation events. This compares well with the previous 2.0 nm nanopore studied. However, at higher voltages, another type of event is present, exhibiting a second deeper blockage level. These events, for which the ionic current trace resembles folded events, take much longer to translocate than their single-level counterparts. This is consistent with the notion of friction-dominated translocations, since folded events in such a small pore would force ssDNA to be squeezed inside the nanopore and cause much stronger interactions with the nanopore. These folded events could indicate the possibility of a slightly more elliptically shaped opening for this particular pore, which could be as much as much as 1.4×2.8 nm^2 while presenting the same cross-sectional area, and still preventing dsDNA passage. However, data at -200 mV suggests that the cylindrical model is valid and some previous TEM images of nanopores created via dielectric breakdown showed circular cross-sections[22]. Therefore, it may be more likely that we are simply able to force ssDNA though an

opening smaller than its nominal diameter in solution by applying such high voltage. From Figure 3.5, it is clear that despite having a sub-linear voltage dependence, the dwell time of both the low and high conductance blockage states decreases with increasing voltage, consistent with full translocation events as opposed to intercalation. Also of note is the fact that the single level conductance blockage is voltage dependent, showing lower blockages with increasing voltage, consistent with previous studies showing ssDNA stretching with increasing voltages[35].

Finally, we investigate the translocations of dsDNA ($d_{ds} \approx 2.2$ nm) molecules through a nanopore measured at 2.4 nm in diameter to further ascertain the accuracy of the nanopore size extracted from the conductance-based model. At this size, dsDNA should barely thread through the nanopore, while maintaining its hybridized form. The experimental conditions are identical as those used for the ssDNA experiments described above. Ionic current traces exhibiting transient current blockades from individual translocating dsDNA molecules are presented in Figure 3.6. At all voltages we observe two types of events. Most events display a single deep conductance blockade level (ca. 98% blocked), while some exhibit two conductance levels, having first the same deep conductance level followed by a lower and longer blockage level, as shown in Figure 3.6e.

At -200 mV, the observed conductance blockage of the single-level events is 5.6 ± 0.4 nS, which is roughly consistent with the expected value of $\Delta G = 6.1$ nS for single file translocations of dsDNA, according to Equation 3.2. As the voltage is increased to -800 mV in 200 mV increments, the conductance blockage of the single-level events is gradually reduced. This is clearly observed in Figure 3.7, which shows a density plot of the observed conductance blockages versus dwell times at various voltages. Again, we observe the departure of translocation events from the line of conserved e.c.d and a dramatic increase in the translocation time for nanopores larger than 5

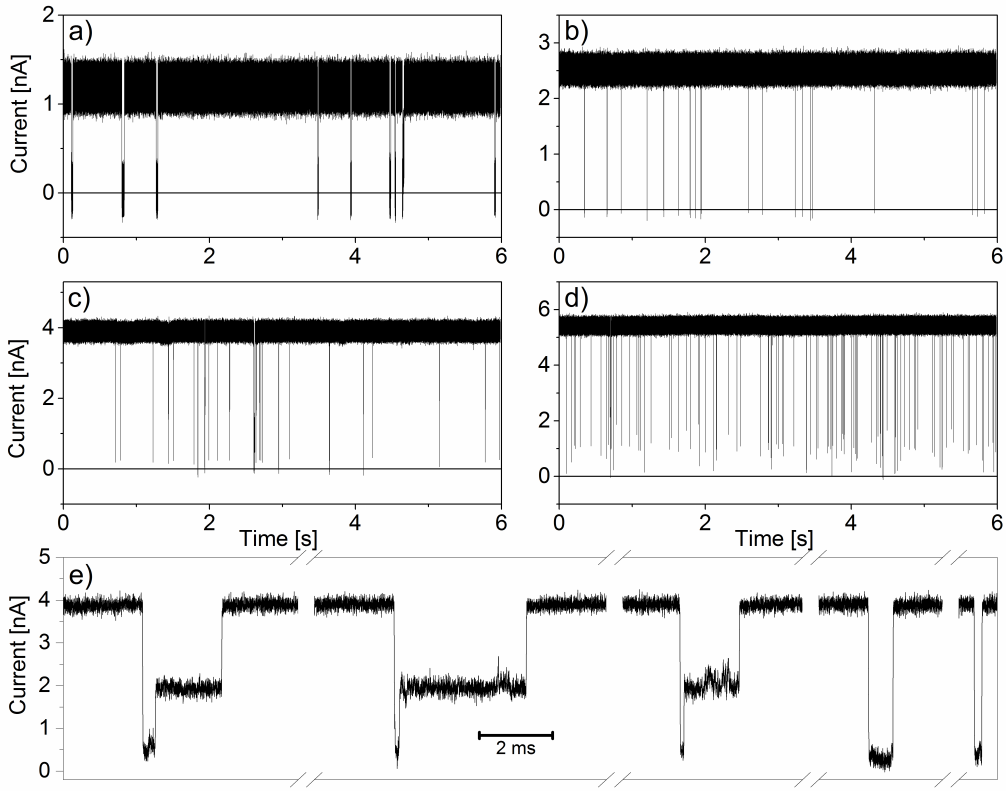

Figure 3.6: Current traces for dsDNA translocating a 2.4 nm nanopore at a) −200 mV, showing mainly single-level events with complete pore blockage (residual current less than noise level) b) −400 mV, where stretched events begin to appear c) −600 mV, with the highest population of stretched events, and d) −800 mV, with a reduced stretched population. e) Examples of typical overstretched (two-level events) and unstretched (single-level events) dsDNA translocation events at −600 mV. Data was acquired at 500 kHz and low-pass filtered at 100 kHz. The recorded current is multiplied by −1 for clarity.

nm diameter made in similar conditions[22]. As seen in figure 3.7e, the dwell time of dsDNA molecules follows an exponential dependence on voltage, consistent with previous work[16,20]. Dwell times are roughly log-normally distributed at each voltage, shown in Figure 3.7f, though there is a slightly heavy tail toward longer translocation times, indicative of DNA-nanopore interactions.

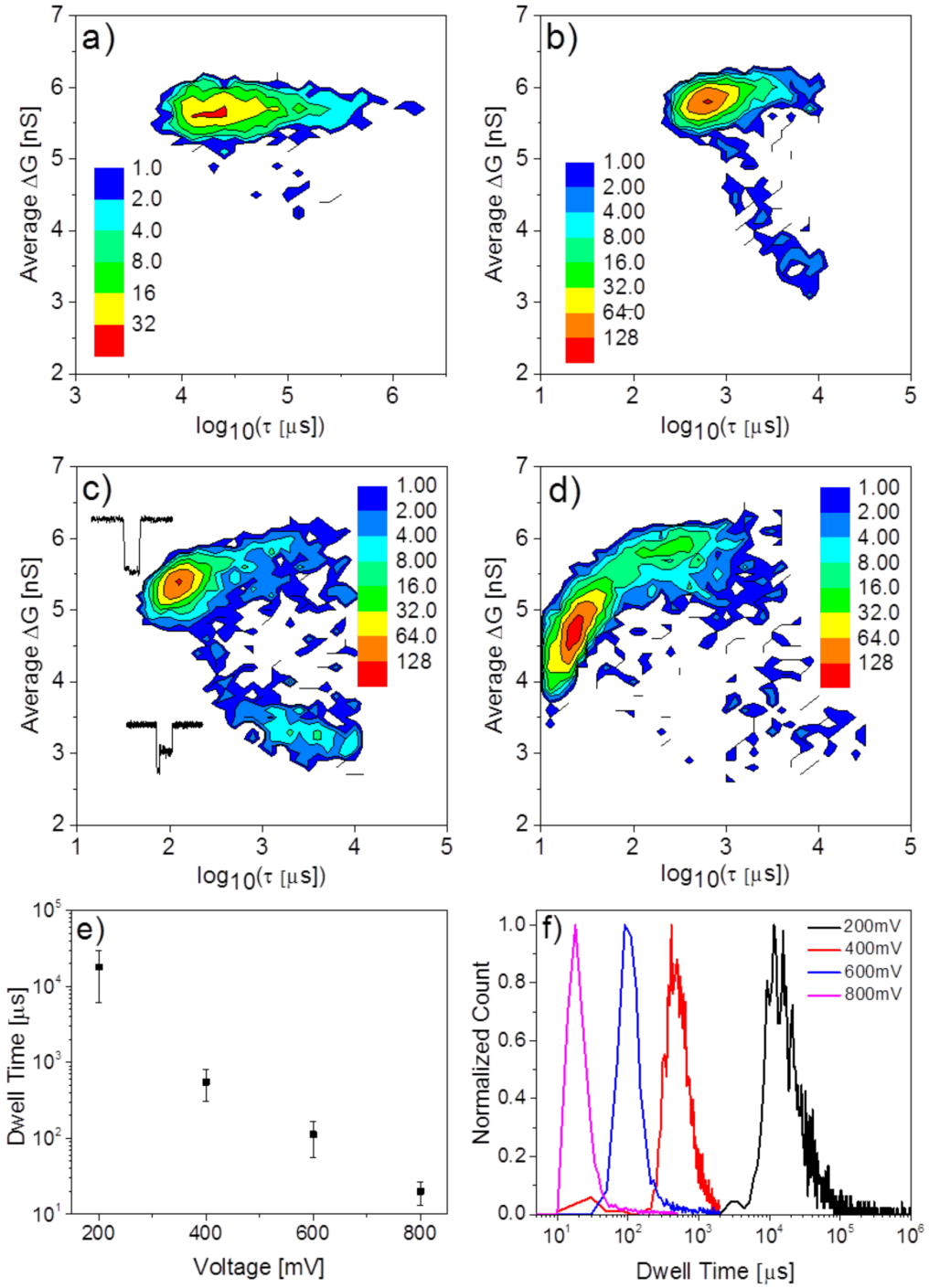

Figure 3.7: Scatter plot of 50 bp dsDNA translocation events through a 2.4 nm pore, with open pore conductance 6.3 nS. The expected conductance blockage for dsDNA is 6.1 nS, which is approached at low voltage. Reduced blockage levels with long dwell

times are attributed to overstretched dsDNA. a) Data acquired at −200 mV (N = 1370 events, less than 1% show two-level events; b) Data acquired −400 mV (N = 2565 events, 5% show two-level events); c) Data acquired −600 mV (N = 2834 events, 14% show two-level events) Inset shows typical events from each population; d) Data acquired −800 mV (N = 5055 events, 2% show two-level events). Note the scale chance change between plots a) and b). Color scale indicates number of events. The dwell time dependence on voltage is shown in e), and the log-normal distribution of dwell time for each voltage is shown in f). Data was sampled at 500 kHz and low-pass filtered at 100 kHz.

Although events consisting of two discrete conductance levels are reminiscent of folded DNA translocations, these cannot be folded events. Considering that the initial level is the expected conductance blockage for dsDNA entering the pore in a single file manner, the second blockage level, which is significantly smaller, must therefore be indicative of a narrower molecular state. Moreover, since the persistence length of 50 bp dsDNA is longer than the fragment size (50 nm vs. 18 nm), the molecule should essentially be rod-like, thus avoiding folded molecular conformations. Consequently, to explain our results, we propose that the nanopore is accessing the B-S stretching transition in dsDNA, in which a stretching force of 65 pN is sufficient to uncoil the double helix, resulting in a factor of 1.7× increase in DNA strand length[36–39]. We argue that since the force is applied to both strands, the unzipping of the double helix is unlikely. First-order constant volume estimates suggest that an increase in DNA length should result in an equal decrease in cross-sectional area, and therefore conductance blockage, and predicts a conductance blockage of 3.6 nS for overstretched DNA. This is consistent with the most probable conductance level of these events, measured at 3.3 ± 0.4 nS at −600 mV (Figure 3.7c). We propose the following mechanism for the observed electrical signals: one end of the short dsDNA fragment is fully threaded inside the 2.4 nm nanopore but does not completely translocate, resulting in the deep blockade seen at the beginning of the two-level

events. The dsDNA molecule is then temporarily trapped by the nanopore, resulting in the exceptionally long translocation time observed in all of the stretched DNA events. To first order, considering the nanopore is cylindrical, we expect a uniform electric field across its length. At 400 mV, we estimate the stall force experienced by a 10 nm segment of dsDNA, using

$$f(V) = ze\frac{n}{L}V, \tag{3.3}$$

where $ze = -0.49e$ (inferred from figure 3.4a in[40]) is the DNA effective charge in the nanopore per base pair, nL^{-1} is the inverse of the base-pair spacing of 0.34 nm for the B form of dsDNA. The calculated force is 92 pN, slightly above the range required to access the full extent of the B-S stretching transition, which is expected to occur above 65 pN[36]. However, note that not all the electrostatic pulling force is necessarily translated to a stretching force. For a translocating molecule the opposing force is provided by friction in the nanopore, which will always be less than the pulling force, unless the molecule is completely stalled. Moreover, there is a certain level of uncertainty with the value of the effective charge of DNA inside a nanopore[41,42], which will affect the accuracy of the calculated pulling force, and as DNA is stretched, the linear charge density is reduced proportionately, reducing the stretching force. Thus, we would expect that the pulling force experienced by the DNA molecule must be somewhat higher than the required stretching force to access the stretching transition. The fact that the nanopore frequently shows deep and long lasting blockages which need to be cleared by reversing the voltage polarity attests to the strong likelihood that DNA can be temporarily trapped and stretched during translocation.

Of particular interest is the voltage dependence of the blockade events, which decreases with increasing applied voltage. The single-level conductance blockages

approach the predicted 6.1 nS at low voltage as seen in Figure 3.7. We attribute this voltage-dependent behavior to stretching of the dsDNA segment inside the pore, but below the B-S overstretching transitio[36]n. We argue that considering the increased translocation times, the significant DNA-pore interactions present will contribute to generate a substantial stretching force on the molecule, which can result in its elongation even if it does not reach the full stretching transition. The decreasing conductance blockage at higher voltages for the stretched events indicates stretching past the B-S plateau. We propose a similar explanation for the decreased conductance blockage with higher voltage observed for ssDNA as well (Figure 3.5). One would only expect to be able to see this behavior in pores small enough to cause appreciable friction to provide the opposing force for stretching to occur. Such behavior has also been indirectly observed in nanopores slightly smaller than the diameter of dsDNA under higher voltage, consistent with this interpretation[30].

In the absence of TEM images of every fabricated nanopore, the accuracy of the nanopore size inferred from the measured conductance can be questioned. The model relies on the assumption of no appreciable thinning of the membrane in the vicinity of the pore and a cylindrical geometry[25]. While in previous work we were able to confirm the first condition using simple excluded area arguments for DNA translocation, and the second condition through TEM images in the case of slightly larger nanopores[22], it is not necessarily obvious that this conductance model of the nanopore would extend to such a small size regime, while maintaining its accuracy. Remarkably, the results presented here strongly support these assumptions and the validity of the model. Using -200mV, we are able to pass dsDNA through nanopores, which we measured to be 2.4 ± 0.2 nm in diameter, but not through pores we measured to be 2.0 ± 0.2 nm and 2.1 ± 0.2 nm, showing that the accuracy of our extracted pore size can be in the angstrom range for the small nanopores fabricated for this work. However, we

note one caveat. Due to the importance of electric double layer effects in sub-5 nm nanopores, the model is only accurate in the limit of high electrolyte concentration. For pores on the order of 2 nm, we have observed a systematic increase in measured nanopore size by as much as 30% when measured in 1 M KCl as opposed to 3.6 M LiCl (data not shown). Given the close match between the measured pore diameters and the range of possible diameters predicted for passage of ss- and dsDNA, it is clear that the more accurate estimate comes from the higher salt concentration[24,33].

3.3 Conclusion

We have demonstrated that systematic fabrication of solid-state nanopores in 10 nm thick silicon nitride membranes is possible using controlled dielectric breakdown in solution, achieving an average diameter of 1.3 ± 0.6 nm for a sample of $N = 23$ nanopores through careful feedback control and automation of the fabrication process. Given that the fabrication conditions required are very general and non-specific to SiN_x, we expect this method to be readily applicable to other dielectric substrates, such as Al_2O_3 or HfO_2. The small nanopores created in this manner are excellent single-molecule sensors, showing clear, high signal-to-noise electrical signals and long, friction-dominated DNA translocation times. These translocation characteristics are consistent with that observed for nanopores of similar size fabricated with traditional TEM-drilling approach, though with a fraction of the effort and cost.

Given the intriguing dynamics accessible to sub-2 nm nanopores, we hope this work will spark further investigations of the transport of nucleic acids and proteins through small solid-state nanopores by a wider range of researchers. We envision that the low-cost automated fabrication by dielectric breakdown of sub-2 nm nanopores with sub-nm precision will enable a more rapid development of solid-state nanopore-

based technologies for personalized genomics.

3.4 Materials and Methods

We fabricate nanopores in 10 nm low-stress SiN_x transmission electron microscope (TEM) windows purchased commercially from Norcada Inc. Membranes consist of SiN_x desposited on a Si substrate by low-pressure chemical vapor deposition (LPCVD). A 50×50 μm^2 window is opened through the Si substrate with an anisotropic KOH etch to expose a free-standing area of SiN_x. To ensure the structural integrity of the membrane, voltage below 1 V is applied to the membrane prior to nanopore creation to ensure no ionic current can pass. Fabrication is carried out following the method outlined in our previous work[22]. The salt used for fabrication is 1 M KCl or NaCl pH 10 buffered with 10 mM $NaHCO_3$, while the salt used in translocation experiments and for measuring nanopore size is 3.6 M LiCl pH 8 buffered with 10 mM HEPES. The etch pit side of the membrane is grounded and all voltages in this paper are referred from this ground.

Data is acquired using custom LabVIEW software interfacing with a National Instruments USB-6351 DAQ card. During nanopore fabrication, data is acquired at 250kHz and software-averaged to 10 Hz. During DNA translocation experiments, data is acquired at 500 kHz using an Axopatch 200B and hardware low-pass filtered at 100 kHz using a 4 pole Bessel filter. All data analysis was done using custom LabVIEW software and Origin.

50 bp dsDNA samples were purchased from Fermentas (NoLimits Thermo Scientific product # SM1421), and 50 nt ssDNA samples were purchased from Integrated DNA Technologies, Inc. The sequence of the ssDNA strands was $(A_9C)_5$.

Acknowledgements

This work was supported by the Natural Sciences and Engineering Research Council of Canada (NSERC), and the Canada Foundation for Innovation. K. Briggs acknowledges the financial support provided by NSERC (Postgraduate Fellowship). The authors would like to thank L. Andrzejewski for valuable technical support.

Bibliography

[1] K. Briggs, H. Kwok, and V. Tabard-Cossa, "Automated Fabrication of 2-nm Solid-State Nanopores for Nucleic Acid Analysis," *Small*, vol. 10, no. 10, pp. 2077–2086, 2014.

[2] D. Branton, D. W. Deamer, A. Marziali, H. Bayley, S. A. Benner, T. Butler, M. Di Ventra, S. Garaj, A. Hibbs, X. Huang, S. B. Jovanovich, P. S. Krstic, S. Lindsay, X. S. Ling, C. H. Mastrangelo, A. Meller, J. S. Oliver, Y. V. Pershin, J. M. Ramsey, R. Riehn, G. V. Soni, V. Tabard-Cossa, M. Wanunu, M. Wiggin, and J. A. Schloss, "The potential and challenges of nanopore sequencing," *Nature Biotechnology*, vol. 26, no. 10, pp. 1146–1153, 2008.

[3] B. M. Venkatesan and R. Bashir, "Nanopore sensors for nucleic acid analysis," *Nature Nanotechnology*, vol. 6, pp. 615–624, 2011.

[4] J. J. Kasianowicz, J. W. Robertson, E. R. Chan, J. E. Reiner, and V. M. Stanford, "Nanoscopic Porous Sensors," *Annual Review of Analytical Chemistry*, vol. 1, no. 1, pp. 737–766, 2008.

[5] M. Wanunu, "Nanopores: A journey towards DNA sequencing," *Physics of Life Reviews*, vol. 9, no. 2, pp. 125–158, 2012.

[6] J. Clarke, H.-C. Wu, L. Jayasinghe, A. Patel, S. Reid, and H. Bayley, "Continuous base identification for single-molecule nanopore DNA sequencing," *Nature Nanotechnology*, vol. 4, no. 4, pp. 265–270, 2009.

[7] E. A. Manrao, I. M. Derrington, A. H. Laszlo, K. W. Langford, M. K. Hopper, N. Gillgren, M. Pavlenok, M. Niederweis, and J. H. Gundlach, "Reading DNA at single-nucleotide resolution with a mutant MspA nanopore and phi29 DNA polymerase.," *Nature Biotechnology*, vol. 30, pp. 349–53, apr 2012.

[8] I. M. Derrington, T. Z. Butler, M. D. Collins, E. Manrao, M. Pavlenok, M. Niederweis, and J. H. Gundlach, "Nanopore DNA sequencing with MspA.," *Proceedings of the National Academy of Sciences of the United States of America*, vol. 107, pp. 16060–5, sep 2010.

[9] A. J. Storm, J. H. Chen, X. S. Ling, H. W. Zandbergen, and C. Dekker, "Fabrication of solid-state nanopores with single-nanometre precision.," *Nature Materials*, vol. 2, pp. 537–540, jul 2003.

[10] A. J. Storm, J. H. Chen, X. S. Ling, H. W. Zandbergen, and C. Dekker, "Electron-beam-induced deformations of SiO 2 nanostructures," *Journal of Applied Physics*, vol. 98, no. 1, 2005.

[11] J. Li, D. Stein, C. McMullan, D. Branton, M. J. Aziz, and J. A. Golovchenko, "Ion-beam sculpting at nanometre length scales," *Nature*, vol. 412, no. 6843, pp. 166–169, 2001.

[12] M. van den Hout, A. R. Hall, M. Y. Wu, H. W. Zandbergen, C. Dekker, and N. H. Dekker, "Controlling nanopore size, shape and stability.," *Nanotechnology*, vol. 21, no. 11, p. 115304, 2010.

[13] A. S. Prabhu, K. J. Freedman, J. W. F. Robertson, Z. Nikolov, J. J. Kasianowicz, and M. J. Kim, "SEM-induced shrinking of solid-state nanopores for single molecule detection," *Nanotechnology*, vol. 22, no. 42, p. 425302, 2011.

[14] B. McNally, M. Wanunu, and A. Meller, "Electromechanical unzipping of individual DNA molecules using synthetic sub-2 nm pores," *Nano Letters*, vol. 8, no. 10, pp. 3418–3422, 2008.

[15] V. Kurz, E. M. Nelson, J. Shim, and G. Timp, "Direct visualization of single-molecule translocations through synthetic nanopores comparable in size to a molecule," *ACS Nano*, vol. 7, no. 5, pp. 4057–4069, 2013.

[16] M. Wanunu, J. Sutin, B. McNally, A. Chow, and A. Meller, "DNA translocation governed by interactions with solid-state nanopores.," *Biophysical Journal*, vol. 95, pp. 4716–25, nov 2008.

[17] M. Wanunu, J. Sutin, and A. Meller, "DNA Profiling Using Solid-State Nanopores: Detection of DNA binding Molecules," *Nano Letters*, vol. 9, no. 10, pp. 3498–3502, 2009.

[18] K. Venta, G. Shemer, M. Puster, J. A. Rodríguez-Manzo, A. Balan, J. K. Rosenstein, K. Shepard, and M. Drndić, "Differentiation of short, single-stranded DNA homopolymers in solid-state nanopores," *ACS Nano*, vol. 7, no. 5, pp. 4629–4636, 2013.

[19] A. Singer, H. Kuhn, M. Frank-Kamenetskii, and A. Meller, "Detection of urea-induced internal denaturation of dsDNA using solid-state nanopores," *Journal of Physics: Condensed Matter*, vol. 22, no. 45, p. 454111, 2010.

[20] J. Larkin, R. Henley, D. C. Bell, T. Cohen-Karni, J. K. Rosenstein, and M. Wanunu, "Slow DNA transport through nanopores in hafnium oxide membranes.," *ACS Nano*, vol. 7, pp. 10121–8, nov 2013.

[21] M. Wanunu, T. Dadosh, V. Ray, J. Jin, L. McReynolds, and M. Drndić, "Rapid electronic detection of probe-specific microRNAs using thin nanopore sensors," *Nature Nanotechnology*, vol. 5, no. 11, pp. 807–814, 2010.

[22] H. Kwok, K. Briggs, and V. Tabard-Cossa, "Nanopore fabrication by controlled dielectric breakdown.," *PLoS One*, vol. 9, p. e92880, jan 2014.

[23] E. C. Yusko, R. An, and M. Mayer, "Electroosmotic Flow Can Generate Ion Current Rectification in Nano- and Micropores," *ACS Nano*, vol. 4, no. 1, pp. 477–487, 2010.

[24] Y. Liu, D. E. Huber, V. Tabard-Cossa, and R. W. Dutton, "Descreening of field effect in electrically gated nanopores," *Applied Physics Letters*, vol. 97, no. 14, pp. 2010–2013, 2010.
[25] S. W. Kowalczyk, A. Y. Grosberg, Y. Rabin, and C. Dekker, "Modeling the conductance and DNA blockade of solid-state nanopores.," *Nanotechnology*, vol. 22, no. 31, p. 315101, 2011.
[26] E. Beamish, H. Kwok, V. Tabard-Cossa, and M. Godin, "Precise control of the size and noise of solid-state nanopores using high electric fields.," *Nanotechnology*, vol. 23, p. 405301, oct 2012.
[27] S. W. Kowalczyk, D. B. Wells, A. Aksimentiev, and C. Dekker, "Slowing down DNA translocation through a nanopore in lithium chloride.," *Nano Letters*, vol. 12, pp. 1038–44, feb 2012.
[28] D. Fologea, J. Uplinger, B. Thomas, D. S. McNabb, and J. Li, "Slowing DNA Translocation in a Solid-State Nanopore," *Nano Letters*, vol. 5, pp. 1734–1737, sep 2005.
[29] A. J. Storm, J. H. Chen, H. W. Zandbergen, and C. Dekker, "Translocation of double-strand DNA through a silicon oxide nanopore," *Physical Review E*, vol. 71, p. 051903, may 2005.
[30] U. Mirsaidov, J. Comer, V. Dimitrov, A. Aksimentiev, and G. Timp, "Slowing the translocation of double-stranded DNA using a nanopore smaller than the double helix," *Nanotechnology*, vol. 21, no. 39, p. 395501, 2010.
[31] H. Chen, S. P. Meisburger, S. A. Pabit, J. L. Sutton, W. W. Webb, and L. Pollack, "Ionic strength-dependent persistence lengths of single-stranded RNA and DNA," *Proceedings of the National Academy of Sciences*, vol. 109, no. 3, pp. 799–804, 2012.
[32] B. Luan and A. Aksimentiev, "Control and reversal of the electrophoretic force on DNA in a charged nanopore," *Journal of Physics: Condensed Matter*, vol. 22, no. 45, p. 454123, 2010.
[33] R. M. M. Smeets, U. F. Keyser, D. Krapf, M.-Y. Wu, H. Nynke, C. Dekker, N. H. Dekker, and C. Dekker, "Salt-dependence of ion transport and DNA translocation through solid-state nanopores," *Nano Letters*, vol. 6, no. 1, pp. 89–95, 2006.
[34] M. Firnkes, D. Pedone, J. Knezevic, M. Döblinger, and U. Rant, "Electrically facilitated translocations of proteins through silicon nitride nanopores: Conjoint and competitive action of diffusion, electrophoresis, and electroosmosis," *Nano Letters*, vol. 10, no. 6, pp. 2162–2167, 2010.
[35] G. M. Skinner, M. van den Hout, O. Broekmans, C. Dekker, and N. H. Dekker, "Distinguishing single- and double-stranded nucleic acid molecules using solid-state nanopores.," *Nano letters*, vol. 9, pp. 2953–60, aug 2009.
[36] S. B. Smith, Y. Cui, and C. Bustamante, "B-DNA : The Elastic Response of Overstretching Individual Double-Stranded and Single-Stranded," *Science*, vol. 271, no. 5250, pp. 795–799, 1996.

[37] M. C. Williams, J. R. Wenner, I. Rouzina, and V. A. Bloomfield, "Effect of pH on the overstretching transition of double-stranded DNA: Evidence of force-induced DNA melting," *Biophysical Journal*, vol. 80, no. 2, pp. 874–881, 2001.

[38] X. Zhang, H. Chen, H. Fu, P. S. Doyle, and J. Yan, "Two distinct overstretched DNA structures revealed by single-molecule thermodynamics measurements," *Proceedings of the National Academy of Sciences*, vol. 109, no. 21, pp. 8103–8108, 2012.

[39] H. Fu, H. Chen, X. Zhang, Y. Qu, J. F. Marko, and J. Yan, "Transition dynamics and selection of the distinct S-DNA and strand unpeeling modes of double helix overstretching.," *Nucleic Acids Research*, vol. 39, pp. 3473–81, apr 2011.

[40] S. van Dorp, U. F. Keyser, N. H. Dekker, C. Dekker, and S. G. Lemay, "Origin of the electrophoretic force on DNA in solid-state nanopores," *Nature Physics*, vol. 5, pp. 347–351, mar 2009.

[41] J. Zhang and B. I. Shklovskii, "Effective charge and free energy of DNA inside an ion channel," *Physical Review E*, vol. 75, no. 2, pp. 1–10, 2007.

[42] B. Luan and A. Aksimentiev, "Electro-osmotic screening of the DNA charge in a nanopore," *Physical Review E*, vol. 78, no. 2, pp. 1–4, 2008.

Chapter 4

Kinetics of Nanopore Fabrication During Controlled Breakdown of Dielectric Membranes in Solution

Kyle Briggs, Martin Charron, Harold Kwok, Timothea Le, Sanmeet Chahal, José Bustamante, Matthew Waugh, and Vincent Tabard-Cossa

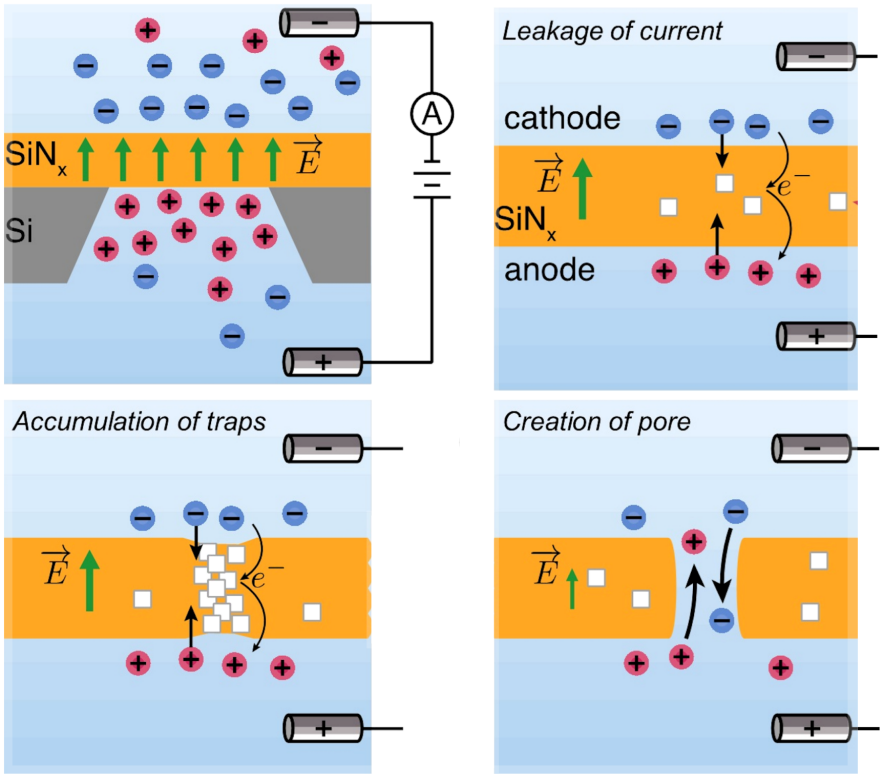

Adapted with permission from [K. Briggs, M. Charron, H. Kwok, T. Le, S. Chahal, J. Bustamante, M. Waugh, and V. Tabard-Cossa, "Kinetics of nanopore fabrication during controlled breakdown of dielectric membranes in solution," *Nanotechnology*, vol. 26, no. 8, 2015]

Abstract

Nanopore fabrication by controlled breakdown (CBD) overcomes many of the challenges of traditional nanofabrication techniques, by reliably forming solid-state nanopores sub-2 nm in size in a low-cost and scalable way for nucleic acid analysis applications. Herein, the breakdown kinetics of thin dielectric membranes immersed in a liquid environment are investigated in order to gain deeper insights into the mechanism of solid-state nanopore formation by high electric fields. For various fabrication conditions, we demonstrate that nanopore fabrication time is Weibull-distributed, in support of the hypothesis that the fabrication mechanism is a stochastic process governed by the probability of forming a connected path across the membrane (i.e. a weakest-link problem). Additionally, we explore the roles that various ions and solvents play in breakdown kinetics, revealing that asymmetric pH conditions across the membrane can significantly affect nanopore fabrication time for a given voltage polarity. These results, characterizing the stochasticity of the nanopore fabrication process and highlighting the parameters affecting it, should assist researchers interested in exploiting the potential of CBD for nanofluidic channel fabrication, while also offering guidance towards the conceivable manufacturing of solid-state nanopore-based technologies for DNA sequencing applications.

4.1 Introduction

Biological and solid-state nanopores have now established themselves as versatile single-molecule detectors of biomolecules in aqueous environments, and are considered leading candidates for the next generation of low-cost, rapid DNA sequencing technologies[2]. Since the initial discovery that a beam of energetic particles can create nanometer-sized holes in dielectric materials[3,4], solid-state nanopores have been

at the forefront of single-molecule research, although their use has been limited to well-equipped research settings. Current state-of-the-art fabrication methods involve the use of a focused beam of electrons or ions to create a nanopore, but these methods are costly, both in terms of the infrastructure required and time invested by qualified personnel in producing each nanopore. Moreover, while nanopores sub-5 nm in diameter can be fabricated, it is very difficult and time consuming to precisely control their size below these dimensions. Techniques to achieve these nanopore sizes, using diffused beams of energetic particles to locally melt the membrane around the pore[4], are slow, typically have poor yield, and modify the membrane composition in the vicinity of the pore[5,6].

Recently, we reported an alternative nanopore fabrication technique that permits low-cost, scalable fabrication of precisely sized solid-state nanopores by controlled breakdown (CBD) of a dielectric membrane in aqueous solution. This innovative nanofabrication strategy significantly reduces the complexity and cost of nanopore fabrication and provides a clear path towards the manufacturing of solid-state nanopore devices[7]. The method achieves near perfect yield with minimal user intervention and can be used to reliably fabricate nanopores 1 nm in diameter or greater, with sub nm precision[8]. While the effectiveness of the method has been thoroughly demonstrated[7–10], some details of the kinetics of nanopore formation by CBD remain unclear. In particular, the relative importance of the various electrolytic species in solution, and the role of the solvent itself, needs to be further investigated.

Dielectric breakdown of solid-state devices in the dry state has been extensively studied both theoretically and experimentally, with Lombardo *et al.* providing a particularly thorough review[11]. Studies also exist on breakdown in cases where liquid is present on one side of the membrane, an area of importance for electrolytic capacitor systems[12–15]. However, to the best of our knowledge, breakdown of thin membranes in

a wet environment remains largely unexplored, particularly for insulating materials in contact with liquids on both sides[15]. There are a number of theories behind dry dielectric breakdown, along with an ongoing debate about the precise physical mechanisms which underlie the process. Fortunately, most models follow a similar basic outline: (i) a large electric field leads, directly or indirectly, to probabilistic production of charge traps (defects) in the material between which electrons can tunnel if they are within a tunneling cross-section of one another, typically on the order of a few nanometers[16,17]; (ii) if a connected path of such traps exists which spans the insulating material, increased localized current can flow through it[11]. As current leaks through the material, it leads to a runaway process that very rapidly results in the damage of the material around the breakdown path, possibly through Joule heating[18]. The precise origin of trap generation remains the subject of debate, as does the nature of the traps which are responsible for the eventual breakdown[19]; impact ionization, hole injection, and trap creation involving atomic hydrogen are all possibilities[20].

Because dielectric breakdown is caused by random trap generation in the material[19], the time-to-breakdown is a stochastic process governed by the probability of forming a connected path across the membrane. Such a weakest-link problem is defined in semiconductor physics as a Weibull-distributed process[11,21], following a distribution of the form

$$F(t) = 1 - \exp\left(-\left(\frac{t}{\lambda}\right)^{\beta}\right), \tag{4.1}$$

where $F(t)$ is the cumulative breakdown probability after the electric field has been applied for a time t, λ is the time at which 63% of membranes have experienced breakdown, and β is the Weibull slope, a parameter which characterizes the steepness

of the breakdown transition. This parameter relates to process memory. Note that for $\beta = 1$ one recovers a simple exponential distribution, which is what is expected for a process with no memory. Physically, this corresponds to the limit of thin membranes, where all that is required for breakdown to occur is a single defect. For thicker membranes, where many defects must coincide spatially, the process has memory and the probability of breakdown at any particular spot builds over time as more defects are introduced, which can be interpreted as a memory effect. Processes with large β show much steeper breakdown transitions, since the breakdown event must thoroughly sample the distribution of defect placements, as compared to the thin membrane case where outliers are more likely since a single defect is sufficient. Note that the average value of a Weibull distribution takes the form $\lambda\Gamma\left(1+\beta^{-1}\right)$, which is equal to λ within $\pm 10\%$ for values of β typically seen in dielectric breakdown experiments. We calculate $F(t)$ as

$$F(t) = \frac{n(t)}{N} \tag{4.2}$$

where $n(t)$ denotes the number of devices that have undergone pore formation by time t, and N is the total number of devices tested.

From our previous work we know that the average time to breakdown is an exponential function of the applied voltage or electric field used to fabricate the nanopore[7], which corresponds within $\pm 10\%$ to λ in the case of the Weibull distribution. In the case of dry breakdown, β is an increasing function of dielectric thickness, while λ depends on the thickness and area of the material, and the applied voltage[21]. A large value of β represents a very sharp breakdown transition, with only a small range of times separating the extremes of $F(t)$, whereas a small value of β (near unity) is obtained when the defect tunneling cross-section approaches the thickness of the

membrane.

In the case of wet breakdown, the underlying details of the process are qualitatively similar, with additional dependencies not present in the dry state[7,12,13,22]. In this work, we will compare and contrast the kinetics of dielectric breakdown in aqueous environments of 10 nm and 30 nm thick low-stress silicon nitride membranes to the case of oxide breakdown in semiconductor devices in integrated circuits in order to gain some further understanding of the underlying mechanisms of nanopore formation. In particular, in our previous work[7] we found that the nature of the solution (e.g. pH) played an active role in the breakdown kinetics, particularly in the distribution of time-to-nanopore fabrication. In this work, we demonstrate that nanopore fabrication time is Weibull-distributed for a variety of fabrication conditions, supporting the notion that the nanopore formation process is primarily governed by dielectric breakdown as opposed to chemical etching. Additionally, we investigate the roles that various species in solution play in breakdown kinetics, demonstrating that while a judicious choice of pH on each side of the membrane can have an enormous effect on the fabrication time distribution parameters discussed above, the presence of water as a solvent is not essential for a nanopore to form.

4.2 Results and Discussion

4.2.1 Dielectric Breakdown Statistics

To study the distribution of fabrication times of nanopores by dielectric breakdown in an aqueous environment, we fabricated at least 10 nanopores in 10 nm and 30 nm thick SiN_x membranes under a given set of pH and voltage conditions. A typical nanopore fabrication experiment is shown in Figure 4.1. The fabrication time

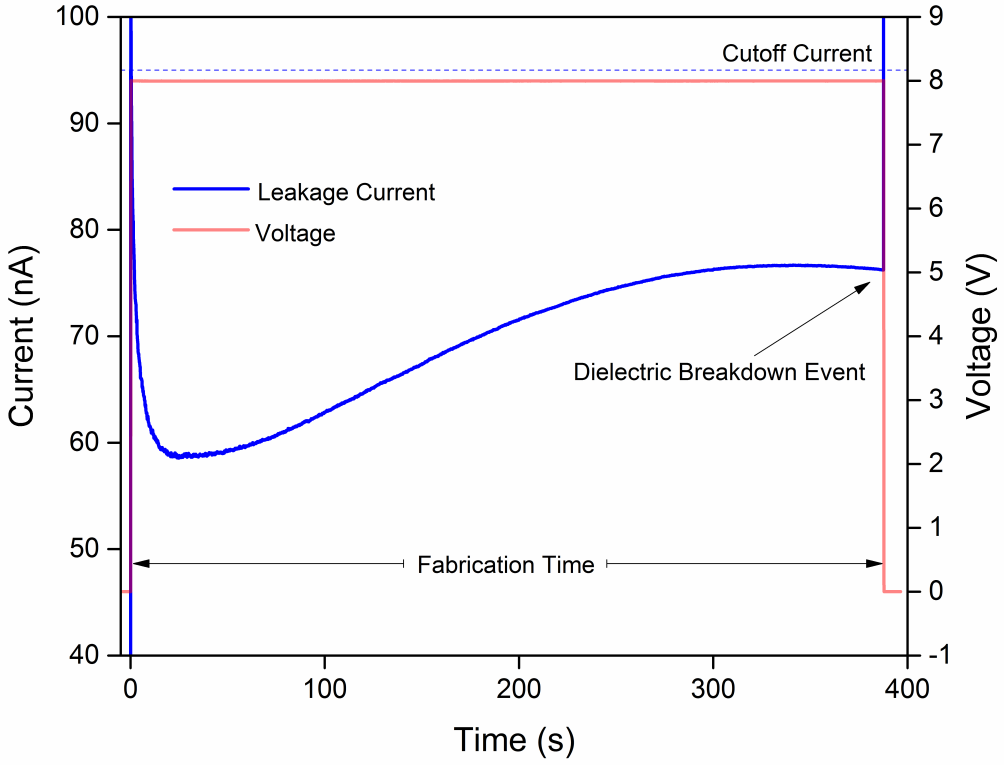

Figure 4.1: A typical nanopore fabrication experiment by CBD, showing leakage current for -8 V applied across a 10 nm thick SiN_x membrane in 1 M KCl pH 8. The time to nanopore fabrication is determined by detection of a current spike passing the preset cutoff current, signaling a breakdown event and the onset of ionic current. The measured leakage current during fabrication contains contributions from both the SiN_x membrane and the silicon support chip, to which ionic current is added once breakdown occurs. The data are multiplied by -1 for display clarity.

distribution parameters λ and β of the cumulative distribution function for dielectric breakdown $F(t)$ can be extracted by fitting $\ln(-\ln(1-F(t)))$ as a function of $\ln(t)$, which yields a linear relationship with slope β and intercept $\beta \ln \lambda$. Such a scale is called a Weibull plot[11]. A distinguishing characteristic of the Weibull distribution is that it retains linearity at the extremes of low and high total failure probability when plotted on this scale.

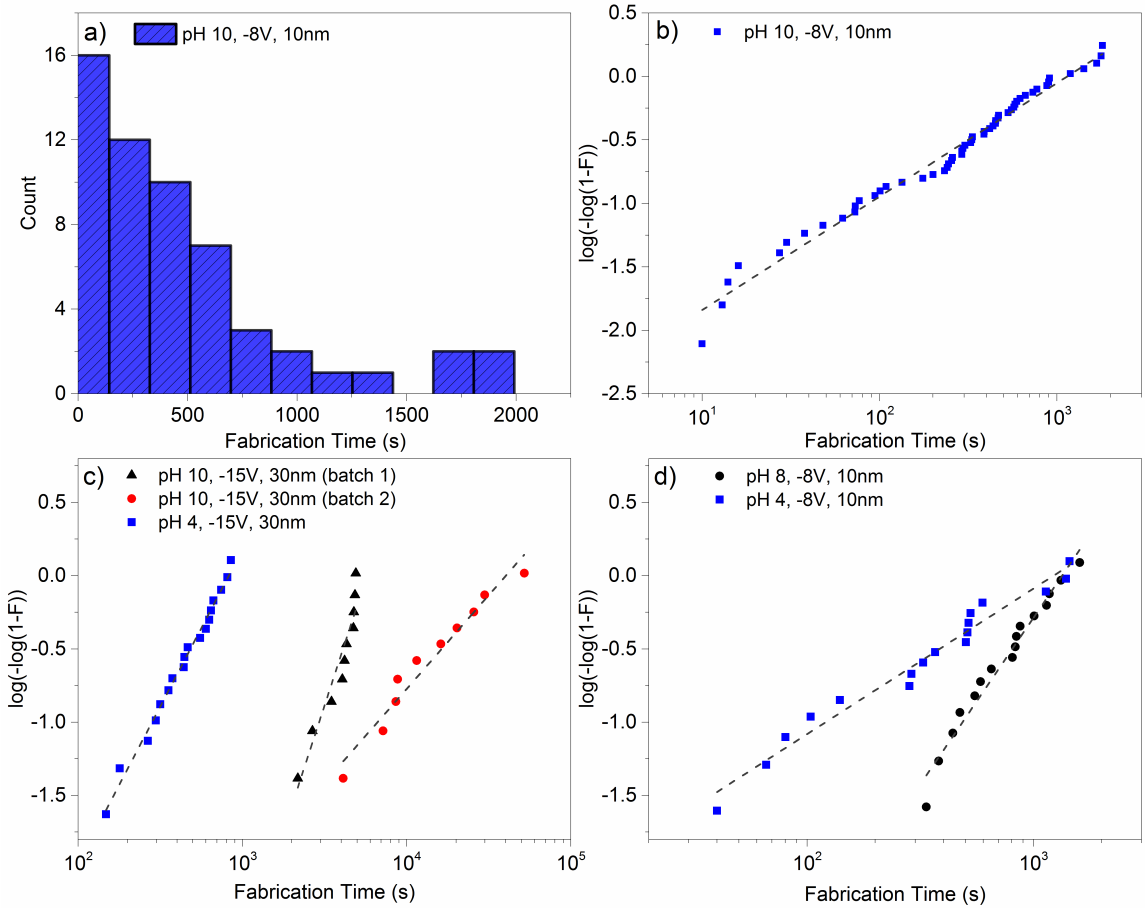

Figure 4.2: a) Distribution of fabrication times for 56 nanopores formed in 10 nm membranes in pH 10 at −8 V. b-d) Weibull plots of fabrication statistics show that nanopore fabrication is caused by dielectric breakdown in the membrane material. The vertical axis reflects cumulative breakdown probability as calculated according to Equation 4.2. Dashed lines are a fit to Equation 4.1, from which the Weibull parameters are extracted. b) 56 nanopores are formed in 10 nm membranes in pH 10 and −8 V. c) 19 nanopores are formed in 30 nm membranes in pH 4, and 11 nanopores are formed in each of two different batches of 30 nm membranes at pH 10 at −15 V, highlighting batch differences. d) 17 nanopores are formed in 10 nm membranes in pH 8 at −8 V and 18 nanopores are formed in 10 nm membranes in pH 4 and −8 V. Note that the final data point in each case is not plotted since a probability of 1 is undefined in a Weibull scale.

When describing dielectric breakdown, it is common in the semiconductor field to use the total charge passed through the dielectric or the charge fluence, i.e. the amount of charge passed per unit area, during the experiment instead of the time-to-

pore formation[11]. However, leakage current measured from our devices also includes the leakage current through the SiN_x film over the Si support chip, as the area of SiN_x exposed to liquid is larger than the free-standing membrane and extends to the edge of the silicone elastomer gasket. For this reason, for most of the data presented herein, we cannot extract a value for charge fluence through solely the SiN_x membrane, making time a more reliable metric. Results for such fittings are shown in Figure 4.2. Each plot is generated from at least 11, and up to 56, independent nanopore fabrication experiments at a given combination of pH and voltage, and as such, we will limit our discussion to a few sets of fabrication conditions.

In our previous work[7], we found that the average time-to-pore formation was exponentially related to applied voltage for a given value of pH. The fabrication time for 30 nm thick SiN_x membranes was also observed to have a maximum somewhere between pH 7 and 10, with faster fabrication in both highly acidic and highly alkaline conditions. pH was shown to play a much less prominent role in reducing fabrication time in thinner 10 nm thick membranes. By contrast, in this work we will use the Weibull parameter λ as our measure of fabrication time as opposed to the average time, but the scaling will remain unchanged. The data displayed as Weibull plots in Figure 4.2 collapse to a linear form. Because of the time and cost associated with getting a high-resolution fit in this case, we have performed detailed statistics (56 pores, Figure 4.2a) only for one pH and voltage combination (i.e. 8V, pH 10, 10 nm SiN_x) in order to demonstrate that the relationship retains its Weibull-linear form at low values of cumulative breakdown probability, shown in Figure 4.2b. We fitted from 11 to 19 pores for the extraction of Weibull parameters under other experimental conditions. Analysis of the data plotted in Figure 4.2c, on 30 nm thick membranes, reveals a breakdown time of 4500 ± 150 s and a slope β of 3.4 ± 0.4 for the first batch of membranes at pH 10 versus 560 ± 8 s and a slope of 2.14 ± 0.06 at pH 4. Comparing

the values of the slope indicates that pH has a large effect on both fabrication time and the breakdown kinetics, with a tighter time distribution (larger slope) at higher pH values. In contrast, Figure 4.2b and 4.2d show that the effect of pH is reduced on 10 nm thick membranes, for which at both extremes of pH 4 and 10 the breakdown distributions are very similar, with values of the intercept of 530 ± 30 s and 450 ± 10 s and slopes 0.99 ± 0.05 and 0.89 ± 0.02 respectively. These results indicate that thinner membranes have a wider distribution of breakdown times and that pH has less of an impact on the time-to-pore formation for the set of voltages studied here. The wider distribution for thin membranes lies in the fact that it is more likely to have fast fabrication outliers by getting lucky and lining up the smaller number of defects needed to span a thinner membrane. There is a maximum in creation time near pH 8, with a breakdown time of 930 ± 20 s and a tighter breakdown distribution with a slope of 2.3 ± 0.1, as summarized in tables 1 and 2. Note that as in the dry dielectric breakdown case[21], our data from[7] suggest that the Weibull slope is independent of electric field.

This new data is in agreement with our previous work[7], demonstrating that pH has a larger effect on the time distribution for pore formation on thicker membranes, with λ changing by a full order of magnitude when going from pH 10 to 4 on 30 nm membranes, and, within our measurement uncertainty, only changing by about 10% on 10 nm membranes. Similarly to what is observed in the case of dry breakdown[21], we see an increase in β for thicker membranes and an electric field dependence in λ, indicating that the distribution of fabrication times becomes tighter for thicker membranes, as would be expected for a model based on a partially randomly generated path of defects. A larger value of β is of practical value to any manufacturing process based on this technique, since it means a more consistent time to breakdown (i.e. predictable fabrication time). It should be noted that we have seen significant

variation in Weibull parameters between batches of membranes. This is likely due to systematic differences in membrane thickness, which can be as large as 10% according to the manufacturer, or to differences in stoichiometry of the low-stress silicon nitride films. Pretreatment of the membrane, for example by plasma cleaning, has also been observed to affect kinetics to some extent, highlighting the importance of the nature of the membrane-liquid interface. In spite of this, the effect of pH on the Weibull parameters is clearly greater in the case of thicker membranes. This fits the understanding in the dry breakdown case: in thin membranes, where the defect cross-section approaches the membrane thickness, the breakdown process can happen with only a few defects lined up, leading to a large variance in breakdown times ($\beta \sim 1$) but much less sensitivity to the efficiency of defect formation. This observation may have significant importance for the fabrication of nanopores in increasingly thinner membranes[23,24].

The fact that the Weibull distribution fits the cumulative distribution of fabrication times well for a given set of experimental parameters suggests that material removal during nanopore formation by CBD is not rate-limiting. In support of this, we occasionally observe a sudden sharp increase in leakage current, without actual nanopore formation (i.e. complete fluidic path), as verified by low-voltage impedance measurements. Restarting the voltage immediately results in proper nanopore fabrication soon after. We attribute these events to cases where a conductive path is formed but the material is not yet fully removed (termed soft breakdown in the semiconductor community[11,18]). Considering that the LabView software used to control the custom fabrication circuit employs a response rate of 10 Hz for the feedback loop to terminate the applied voltage when the current exceeds a threshold, this puts a rough upper bound on the time to remove material after breakdown at on the order of 0.1 s, compared to the breakdown transient time, which is typically measured in tens

Table 4.1: Extracted Weibull parameters for the fits in Figure 4.2c for 30 nm thick membranes at −15 V. Error bars denote standard errors for nonlinear fit parameters in Equation 4.1.

30 nm −15 V	pH 10 Batch 1 $N = 11$	pH 10 Batch 2 $N = 11$	pH 4 $N = 19$
β	3.4 ± 0.4	1.3 ± 0.1	2.14 ± 0.06
λ	4500 ± 150 s	21000 ± 1300 s	560 ± 8 s

Table 4.2: Extracted Weibull parameters for the fits in Figure 4.2b and 4.2d for 10 nm thick membranes at −8 V. Error bars denote standard errors for nonlinear fit parameters in Equation 4.1.

10 nm −8 V	pH 10 $N = 56$	pH 8 $N = 17$	pH 4 $N = 18$
β	0.89 ± 0.02	2.3 ± 0.1	0.99 ± 0.05
λ	450 ± 10 s	930 ± 20 s	530 ± 30 s

of nanoseconds[18]. This indicates that the by-products of the breakdown process are easily removed once breakdown occurs and that the timescale for material removal must be much less than the timescale for dielectric breakdown in these conditions.

4.2.2 pH Asymmetry

Besides the dominant effect of the electric field strength, the pH of the solution impacts the time-to-pore formation for the thicker 30 nm membranes. As discussed in our previous work[7], nanopore fabrication time can be decreased by 3 orders of magnitude when going from pH 7 to pH 2, or by a full order of magnitude when going from pH 7 to 13, suggesting that protons (H^+) and hydroxide ions (OH^-) also play key roles in the fabrication mechanism. In that work, we argued that in 30 nm thick membranes, the breakdown at low pH is amplified by impact ionization-induced

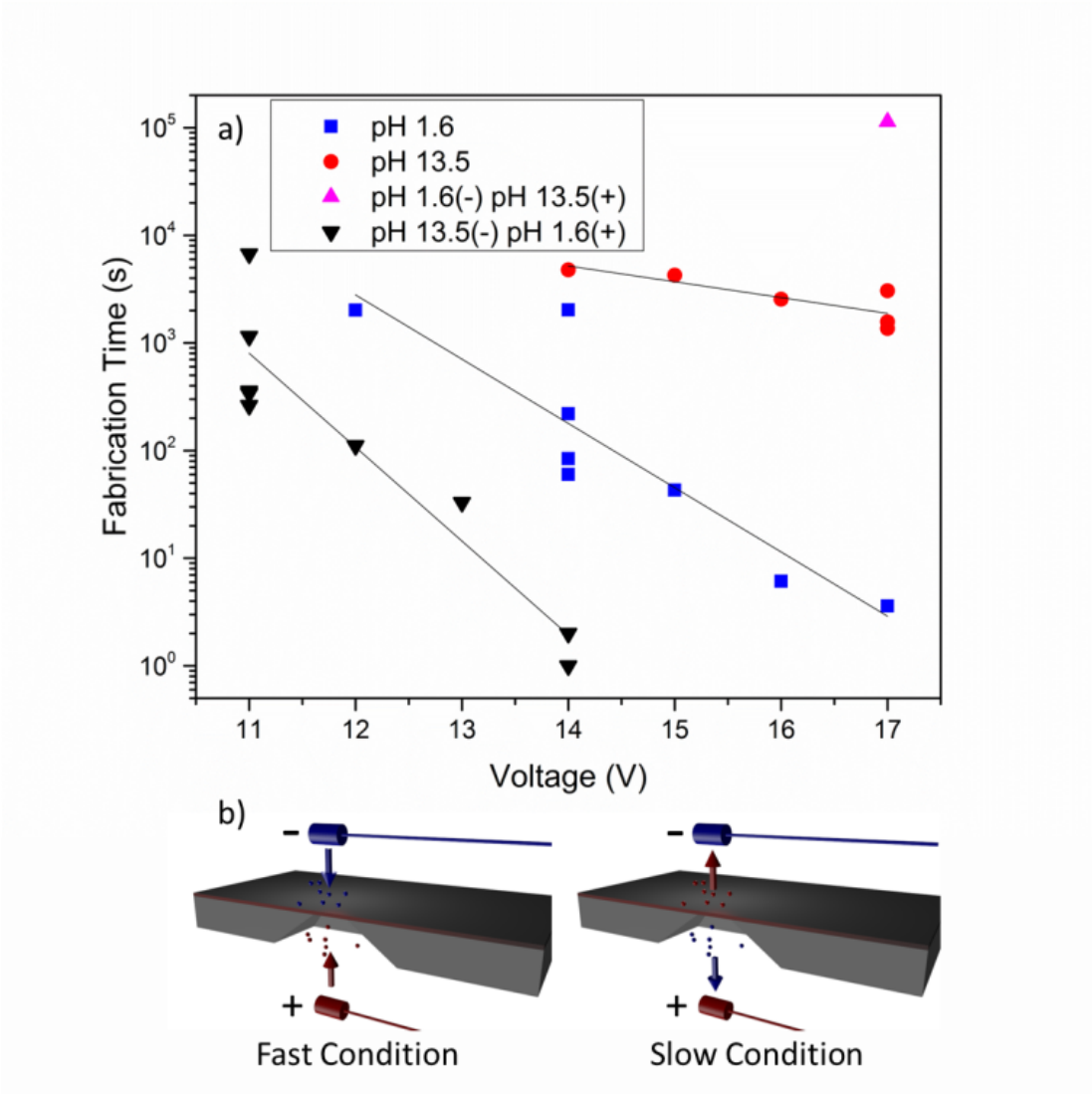

Figure 4.3: a) Semi-log plot of fabrication time of individual nanopores fabricated in 30 nm thick SiN_x membranes in 1 M KCl buffered as indicated versus the applied voltage. The symbol "+" and "-" refer to the polarity in the respective pH solution, as depicted in b) Schematic representation of the nanopore chip in asymmetric conditions. Hydrogen and hydroxide ions, denoted in red (positive) and blue (negative) respectively, are driven toward (fast fabrication) or away (slow fabrication) from the membrane depending on the voltage polarity of the electrodes, as indicated by the arrows. Note that inverting the voltage polarity is equivalent to inverting the solutions.

avalanche, due to the increased likelihood of H^+ incorporation or hole injection from the anode side of the membrane[14]. To investigate this effect in more detail, we

fabricated nanopores under a pH imbalance across the membrane as a function of the strength and polarity of the applied voltage.

Nanopores were fabricated in 30 nm thick SiN_x membranes in 1 M KCl with pH 1.6 in one reservoir and pH 13.5 in the other. Fabrication experiments, on the same batch of membranes, under symmetric pH conditions were also performed as controls. The results as a function of the applied voltage are illustrated in Figure 4.3. Depending on the voltage polarity, an asymmetry in the value of the pH across the membrane can either decrease or increase the fabrication time compared to the symmetric case. In these experiments, the fast asymmetric fabrication condition is characterized by having the acidic solution on the side of the membrane that is grounded, while negatively biasing the other side of the membrane that contains the alkaline solution. The slow asymmetric fabrication condition is achieved by inverting the solutions. We have also observed that, while the exponential dependence of the fabrication time on voltage (or electric field) is retained for all conditions, the sensitivity (i.e. slope of the semi-log plot) differs. The effect is striking: when making a pore in asymmetric conditions, the fabrication time can vary by more than 10^6-fold for a given voltage. In fact, in the slow fabrication condition, we were unable to make a nanopore below 17 V despite leaving the voltage applied for several days. Breakdown times were so unreasonably long that only a few data points were attempted, most of which were stopped after they exceeded two days without a breakdown event.

These intriguing results highlight the role of the nature and distribution of ions in the electrostatic double layer (EDL) surrounding the membrane. In the fast fabrication condition, the higher concentrations of protons and hydroxide ions on each side are being driven toward the membrane, changing the pH in the EDL and reinforcing the asymmetry. The opposite effect would be taking place for the slow fabrication condition. Since redox reactions at the membrane-liquid interface are required to

inject charge carriers into the dielectric in order to sustain a leakage current through the membrane, by locally increasing or decreasing the availability of a specific species required for these reactions, the rate of charge injection, and hence that of defect formation, can be controlled indirectly. In this framework, one would then expect a higher current density in the faster fabrication condition.

In order to test this hypothesis, the leakage current through the membrane must be measured accurately, without the contribution from the rest of the support chip exposed to solution, which contributes a parallel path for the leakage current. For this purpose, chips with 30 nm thick SiN_x membranes were painted with PDMS so that only a small measured area (approximately 10^3 μm^2) of SiN_x membrane remained exposed to the solution. The rest of the support chip and membrane edges were entirely insulated from the solution by the PDMS. Figures 4.4a and 4.4b show the measured leakage current passing through the membrane as a function of voltage and normalized by the exposed membrane area for both the fast and slow fabrication conditions, while Figures 4.4c and 4.4d show the ratios of current in the two conditions. Current is acquired at each voltage for 60 s and averaged over the final 30 s. At high voltage the current rarely attains a steady state for longer than a few minutes, but this provides a reasonable estimate of the current density upon initial voltage application (see Figure 4.1). Consistent with expectations, in the fast fabrication condition we observe a full order of magnitude more tunneling current than in the slow fabrication condition.

Interestingly, the difference in current density between slow and fast conditions is only 1 to 2 orders of magnitude, which is insufficient to explain the enormous fabrication time differences that we observe between the two conditions (more than 6 orders of magnitude). Moreover, while the current density measured for symmetric pH conditions does fall between the two extremes of slow and fast fabrication, we see

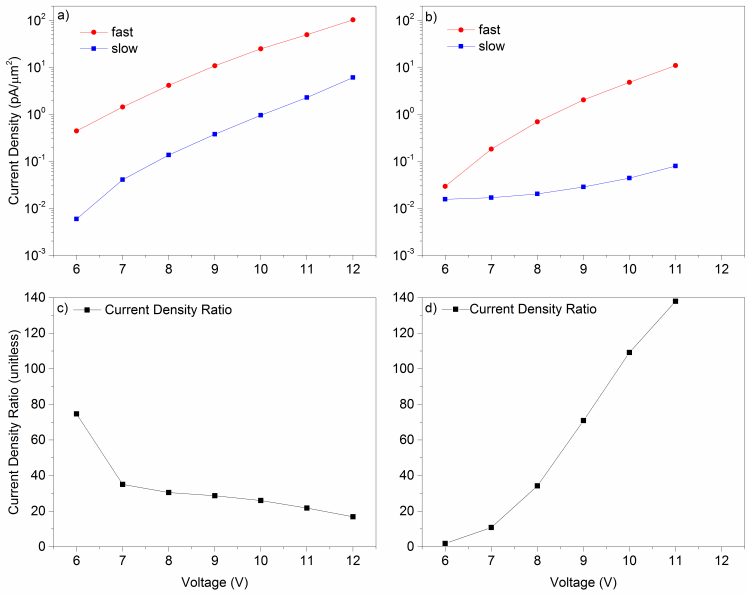

Figure 4.4: a) I-V curves for a single 30 nm membrane chip painted with PDMS. The slow fabrication condition was sampled first, after which the solutions on both sides of the membranes were inverted to test the fast fabrication condition. We observed some hysteresis when more than 10 V was applied in either condition, but the differences here are much larger than what is accounted for by the hysteresis. In the faster fabrication condition, current levels are at least a full order of magnitude higher than in the slow condition. Note that the slow condition was swept four times before the fast condition, with the the data displayed being the fourth iteration. b) The same experiments, performed on a different device without any prior application of voltage above 1 V (i.e. voltage stressing). It can be seen that the slow condition always results in lower current density than the fast fabrication experiment that preceded it, in agreement with the results from part a). The system shows hysteresis, with voltage stress resulting in higher current in experiments that follow. Data is acquired at 10 Hz at each voltage for 60 s and each point is averaged over the last 30 s. c-d) Ratios of current densities in the two conditions for the graphs directly above.

more current density in the alkaline case than in the acidic case. The latter actually roughly overlaps the slow conditions, despite the fabrication time being significantly shorter.

In light of this, it is clear that neither the electric field nor the current density

provide a complete story in understanding the kinetics of dielectric breakdown of SiN_x membranes in solution. The fact that pH asymmetry has such an enormous effect suggests that the nature of the membrane-liquid interface is important in controlling the efficiency at which defects are generated in the material and thus of the breakdown mechanism. The asymmetric pH results are likely explained by a cooperative effect of both protons and hydroxide ions, which are only both in abundance in the fast fabrication condition. We note that nanopores fabricated in asymmetric conditions are highly rectifying and generally only conduct appreciably in one voltage polarity, even after replacing both sides with identical buffer solutions. This observed asymmetric electrostatic nanopore profile could point towards a conical geometry or an asymmetric surface charge density[25–27]. While such diode-like devices could potentially be useful in nanofluidic circuits[26], asymmetric pH conditions during fabrication could also be employed to achieve the formation of long nanopores in an acceptable time through membranes that would otherwise be too thick to sustain a sufficiently high electric field, while keeping voltages relatively low.

4.2.3 Breakdown in Organic Solvents

While it is clear from the previous section that in an aqueous solution of 1M KCl, protons and hydroxide ions play an active role in the breakdown kinetics, water is not an essential ingredient for nanopore formation to occur. As expected from a breakdown model, as long as a redox reaction can take place at the membrane-liquid interface to inject charge carriers into the membrane such that a current is allowed to pass, breakdown can occur and lead to the formation of a nanopore. The details of the membrane-liquid interface and field strength will control the breakdown mechanism and the likelihood/efficiency of defect formation varying the kinetics of nanopore

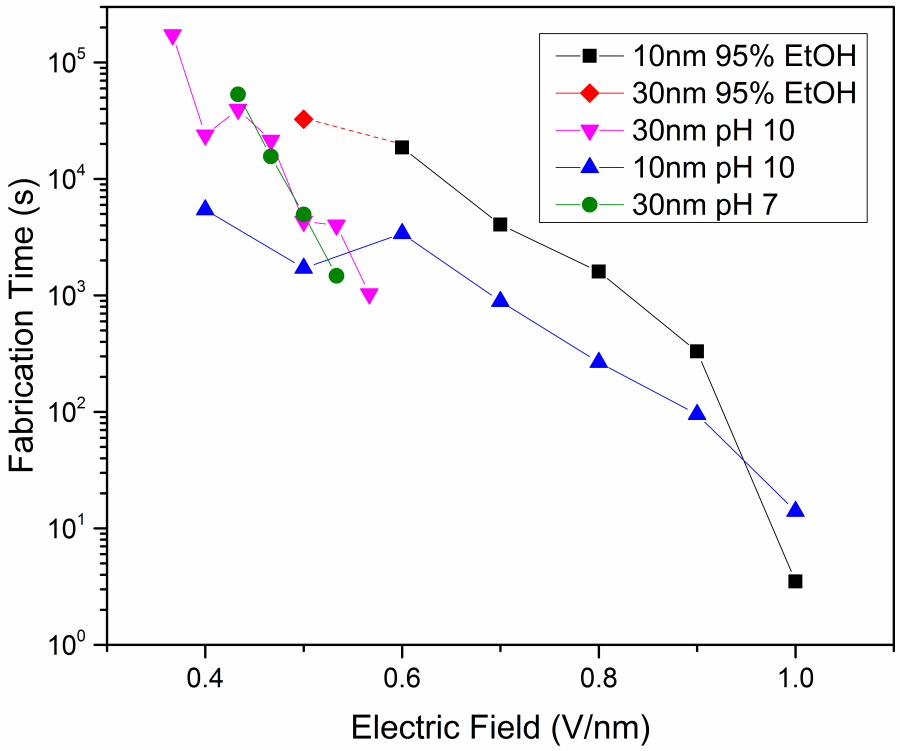

Figure 4.5: Semi-log plot of the time-to-pore fabrication as a function of the electric field strength for nanopores fabricated in 1 M LiCl in ethanol on 10 nm and 30 nm thick SiN_x membranes. For the sake of comparison, the data is overlaid with time-to-pore fabrication in aqueous environment from[7].

fabrication. In principle however, past a certain voltage threshold most ionic species in a given electrolyte solution will undergo redox reactions at the membrane surface, generating a current, which should generalize the fabrication of nanopores by CBD to various solvents. In this section, to support the general character of nanopore fabrication by CBD, we demonstrate nanopore formation in 1 M LiCl dissolved in 95% ethanol. The results for the time-to-pore fabrication on 10 nm and 30 nm SiN_x membranes, as compared to the aqueous pH 10 1 M KCl case, are shown in Figure 4.5. As in the aqueous case, the data follows an exponential dependence with

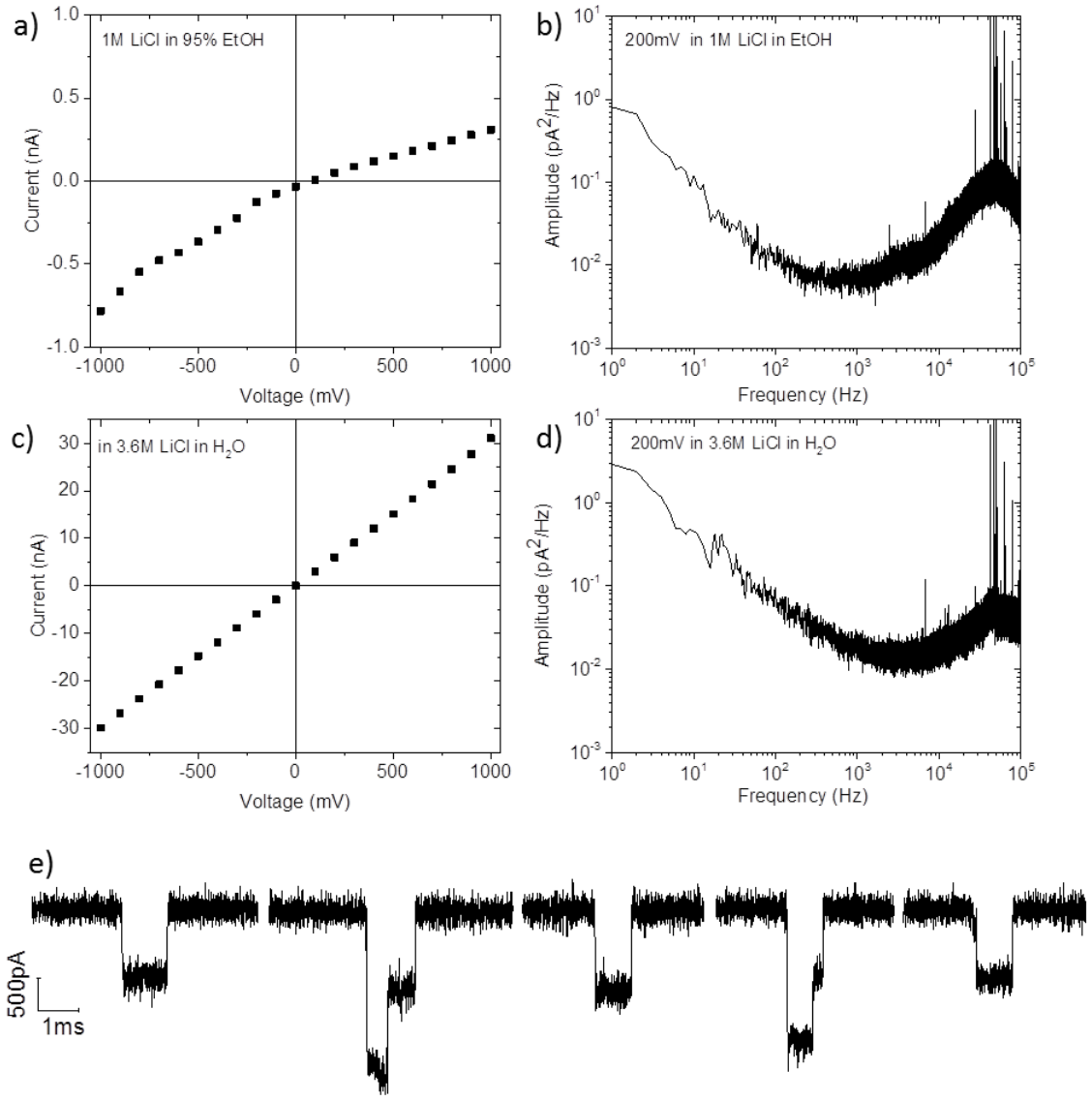

Figure 4.6: a-b) I-V and noise characteristics at 200 mV for a nanopore fabricated in 1 M LiCl in 95% ethanol at −9 V. c-d) I-V characteristics and noise performance at 200 mV of the same pore after changing to 3.6 M LiCl in water. e) 1.5 nM 10 kbp DNA translocation traces at −200 mV through the pore, demonstrating the presence of a single channel of the appropriate size.

applied voltage (and electric field). Interestingly, the data roughly follows the pH 10 fabrication times from 1 M KCl aqueous environments as a function of electric field. This may indicate that the primary underlying mechanism of pore formation (i.e.

defect generation) is the same in these conditions, and predominantly relies on redox-mediated injection of electrons into the membrane to supply current. In addition, these results support the argument that no particular solvents nor electrolyte species are participating in a specific chemical reaction to etch the pore, as one would not expect a chemical etching process to generalize so easily across both solvents and substrates[7].

To confirm that nanopores fabricated in 1 M LiCl in ethanol could also be leveraged for the detection of individual molecules, we switched from an organic to an aqueous solvent to solubilize DNA after pore fabrication. Following switching of the solution, we systematically observed an increase in the measured effective pore size (by a factor of $1.5-2\times$) when going from low conductivity ethanol-based salts ($\sigma = 5-8$ mS/cm) to higher conductivity water-based salts when using Equation 3 from Kowalczyk *et al.*[28]. We believe the size extracted from conductance measurements in high concentration aqueous salt solutions (above 1 M), provides more reliable estimates of the actual physical size, since surface and edge effects are attenuated[8]. The results for a nanopore fabricated in a 10 nm thick SiN_x membrane in 1 M LiCl in ethanol are shown in Figure 4.6. DNA translocation data are consistent with the I-V-based estimate of the pore size of 5.9 nm, validating the fabrication process in ethanol. Our DNA data shows a measured $\Delta G = 5.2 \pm 1.3$ nS for the first blockade level (unfolded molecules), which leads to an effective membrane thickness of 12 nm, and a calculated effective nanopore diameter of 6.3 nm.

4.3 Conclusion

We have investigated the dielectric breakdown of silicon nitride membranes in aqueous and organic environments and determined that the mechanisms for break-

down are qualitatively similar to semiconductor devices operated in the dry state, following a Weibull distribution of time-to-breakdown. Studying the kinetics of nanopore fabrication by varying the concentration of ionic species in solution on either side of the membrane, we have determined that the nature of the membrane-liquid interface is important in regulating charge injection into the membrane. Charge carriers are injected by redox reactions or proton incorporation, enabling breakdown kinetics to be tuned by controlling the efficiency or the mechanism by which particular charges generate defects in the material. The fact that nanopore fabrication is sensitive to changes in the proton and hydroxide concentration, despite both species being two orders of magnitude less concentrated than the background potassium and chloride ions even in the most extreme conditions, strongly suggests that protons and hydroxide ions are both directly participating in the redox reactions leading to charge injection into the membrane. In support of this, the asymmetric pH results indicate that there are multiple different redox reactions leading to charge injection, one or more of which become rate-limiting depending on the particular conditions used. The differences in current density between opposite asymmetric pH conditions point to the importance of the membrane-liquid interface and suggest that depending on the redox reaction that is dominant, defect generation is accomplished with different efficiency by the injected charge carriers. Moreover, measurements of the current density passing through the membrane in asymmetric pH conditions showed that the leakage current should not be regarded as an etching current, since not all of the charges actually contribute to the nanopore formation. Depending on the strength of the electric field and the nature of the membrane-liquid interface, only a fraction of the tunnelling charge carriers leads to defect generations, and ultimately dielectric breakdown and nanopore formation. Lastly, nanopore fabrication in an ethanol-based electrolyte provided further evidence of the anticipated generality CBD. Fabrication in differ-

ent solvents could be useful in maintaining the integrity of more complex membrane architectures during nanopore formation. This work characterizing the parameters affecting the stochasticity of the nanopore fabrication process by CBD should provide guidelines for the fabrication of solid-state nanopore devices for future generation of nucleic acid analysis platforms and DNA sequencing systems.

4.4 Materials and Methods

We fabricate individual nanopores in custom PEEK or Teflon fluidic cells which consist of two fluidic reservoirs separated by a silicon TEM window support chip through which a 10 nm or 30 nm thick, low-stress SiN_x membrane has been exposed on a $50 \times 50\ \mu m^2$ area by anisotropic KOH etching. These membranes are purchased from Norcada Inc. Nanopores are fabricated directly in electrolytic solution by the CBD method, using a custom current amplifier as described in previous work[7]. The membrane integrity is verified prior to nanopore fabrication through a series of low-voltage (below 0.3 V/nm) pulses, which do not result in appreciable levels of current if the membrane is intact. 1 M KCl pH 1.6 (σ = 114.7 mS/cm), pH 2 (σ = 109.6 mS/cm) and pH 13.5 (σ = 137.4 mS/cm) are unbuffered, with the pH verified before and after the experiment to ensure that no drift occurred. 1 M KCl pH 4 (σ = 113.3 mS/cm) is buffered with 20 mM acetic acid and 4 mM sodium acetate, 1 M KCl pH 10 (σ = 107.2 mS/cm) is buffered with 10 mM $NaHCO_3$, and 1 M KCl pH 8 (σ = 111.1 mS/cm) is buffered with 10 mM HEPES. The pH of all solutions is fine-tuned using small amounts of KOH or HCl. All solutions are filtered and degassed prior to use. The side of the chip with the etch pit is grounded and all voltages used in this work are applied to the membrane side of the chip and are negative in reference to this ground.

When conducting asymmetry experiments, asymmetry is inverted by changing the solutions on each side of the membrane rather than simply inverting the bias voltage, which one would expect to be physically equivalent processes. By maintaining the bias with respect to the geometry of the chip, we control for the effects of chip geometry which were seen to have an effect on the current level[7] on unpainted chips. Analysis of asymmetric current density data is slightly complicated by the fact that the system exhibits some hysteresis as current is passed through the membrane. In particular, when the membrane has been stressed by obtaining an I-V characteristic, the next time the same I-V curve is obtained, the current density is usually higher. Our data shows that the slow fabrication condition generally results in less hysteresis, and so experiments on a single device are conducted in order of slowest to fastest conditions to control for this effect. Differences between chips preclude direct comparison of any condition between individual devices without considerable statistics.

Acknowledgements

This work was supported by the Natural Sciences and Engineering Research Council of Canada (NSERC), and the Canada Foundation for Innovation. J. Bustamanté, K. Briggs, and M. Waugh acknowledge the financial support provided by SENESCYT, NSERC, and OGS respectively, for postgraduate fellowships. T. Le and S. Chahal acknowledge the financial support of NSERC for undergraduate research awards.

Bibliography

[1] K. Briggs, M. Charron, H. Kwok, T. Le, S. Chahal, J. Bustamante, M. Waugh, and V. Tabard-Cossa, "Kinetics of nanopore fabrication during controlled breakdown of dielectric membranes in solution," *Nanotechnology*, vol. 26, no. 8, 2015.

[2] M. Wanunu, "Nanopores: A journey towards DNA sequencing," *Physics of Life Reviews*, vol. 9, no. 2, pp. 125–158, 2012.

[3] J. Li, D. Stein, C. McMullan, D. Branton, M. J. Aziz, and J. A. Golovchenko, "Ion-beam sculpting at nanometre length scales," *Nature*, vol. 412, no. 6843, pp. 166–169, 2001.

[4] A. J. Storm, J. H. Chen, X. S. Ling, H. W. Zandbergen, and C. Dekker, "Fabrication of solid-state nanopores with single-nanometre precision.," *Nature Materials*, vol. 2, pp. 537–540, jul 2003.

[5] M. van den Hout, A. R. Hall, M. Y. Wu, H. W. Zandbergen, C. Dekker, and N. H. Dekker, "Controlling nanopore size, shape and stability.," *Nanotechnology*, vol. 21, no. 11, p. 115304, 2010.

[6] A. S. Prabhu, K. J. Freedman, J. W. F. Robertson, Z. Nikolov, J. J. Kasianowicz, and M. J. Kim, "SEM-induced shrinking of solid-state nanopores for single molecule detection," *Nanotechnology*, vol. 22, no. 42, p. 425302, 2011.

[7] H. Kwok, K. Briggs, and V. Tabard-Cossa, "Nanopore fabrication by controlled dielectric breakdown.," *PLoS One*, vol. 9, p. e92880, jan 2014.

[8] K. Briggs, H. Kwok, and V. Tabard-Cossa, "Automated Fabrication of 2-nm Solid-State Nanopores for Nucleic Acid Analysis," *Small*, vol. 10, no. 10, pp. 2077–2086, 2014.

[9] I. Yanagi, R. Akahori, T. Hatano, and K.-i. Takeda, "Fabricating nanopores with diameters of sub-1 nm to 3 nm using multilevel pulse-voltage injection.," *Scientific reports*, vol. 4, p. 5000, 2014.

[10] H. Kwok, M. Waugh, J. Bustamante, K. Briggs, and V. Tabard-Cossa, "Long passage times of short ssDNA molecules through metallized nanopores fabricated by controlled breakdown," *Advanced Functional Materials*, vol. 24, no. 48, pp. 7745–7753, 2014.

[11] S. Lombardo, J. H. Stathis, B. P. Linder, K. L. Pey, F. Palumbo, and C. H. Tung, "Dielectric breakdown mechanisms in gate oxides," *Journal of Applied Physics*, vol. 98, no. 12, p. 121301, 2005.

[12] S. Ikonopisov and N. Elenkov, "Field and temperature dependence of the electronic conduction from electrolytes through the barrier anodic film on niobium," *J. Electroanal. Chem*, vol. 88, pp. 417–420, 1978.

[13] K. C. Kalra, K. C. Singh, and M. Singh, "Electrical breakdown of anodic films on titanium in aqueous electrolytes," *Journal of Electroanalytical Chemistry*, vol. 371, no. 1-2, pp. 73–78, 1994.

[14] J. M. Albella and I. Montero, "A Theory Of Avalanche Breakdown Oxidation during anodic oxidation," *Electrochimica Acta*, vol. 32, no. 2, pp. 255–258, 1987.

[15] S. Lee, R. An, and A. J. Hunt, "Liquid glass electrodes for nanofluidics.," *Nature Nanotechnology*, vol. 5, no. 6, pp. 412–6, 2010.

[16] J. H. Stathis, "Percolation models for gate oxide breakdown," *Journal of Applied Physics*, vol. 86, no. 10, p. 5757, 1999.

[17] D. J. DiMaria and J. H. Stathis, "Explanation for the oxide thickness dependence of breakdown characteristics of metal-oxide-semiconductor structures," *Applied Physics Letters*, vol. 70, no. 20, p. 2708, 1997.

[18] S. Lombardo, A. La Magna, C. Spinella, C. Gerardi, and F. Crupi, "Degradation and hard breakdown transient of thin gate oxides in metal–SiO2–Si capacitors: Dependence on oxide thickness," *Journal of Applied Physics*, vol. 86, no. 11, p. 6382, 1999.

[19] W. D. Zhang, J. F. Zhang, C. Z. Zhao, M. H. Chang, G. Groeseneken, and R. Degraeve, "Electrical signature of the defect associated with gate oxide breakdown," *IEEE Electron Device Letters*, vol. 27, no. 5, pp. 393–395, 2006.

[20] D. J. DiMaria, E. Cartier, and D. Arnold, "Impact ionization, trap creation, degradation, and breakdown in silicon dioxide films on silicon," *Journal of Applied Physics*, vol. 73, no. 7, pp. 3367–3384, 1993.

[21] R. Degraeve, G. Groeseneken, R. Bellens, J. L. Ogier, M. Depas, P. J. Roussel, and H. E. Maes, "New insights in the relation between electron trap generation and the statistical properties of oxide breakdown," *IEEE Transactions on Electron Devices*, vol. 45, no. 4, pp. 904–911, 1998.

[22] J. M. Albella, I. Montero, J. M. Martínez-Duart, and V. Parkhutik, "Dielectric breakdown processes in anodic Ta2O5 and related oxides - A review," *Journal of Materials Science*, vol. 26, no. 13, pp. 3422–3432, 1991.

[23] J. Larkin, R. Henley, D. C. Bell, T. Cohen-Karni, J. K. Rosenstein, and M. Wanunu, "Slow DNA transport through nanopores in hafnium oxide membranes.," *ACS Nano*, vol. 7, pp. 10121–8, nov 2013.

[24] A. T. Carlsen, O. K. Zahid, J. Ruzicka, E. W. Taylor, and A. R. Hall, "Interpreting the conductance blockades of DNA translocations through solid-state nanopores," *ACS Nano*, vol. 8, no. 5, pp. 4754–4760, 2014.

[25] E. C. Yusko, R. An, and M. Mayer, "Electroosmotic Flow Can Generate Ion Current Rectification in Nano- and Micropores," *ACS Nano*, vol. 4, no. 1, pp. 477–487, 2010.

[26] K. Zhou, J. M. Perry, and S. C. Jacobson, "Transport and Sensing in Nanofluidic Devices," *Annual Review of Analytical Chemistry*, vol. 4, no. 1, pp. 321–341, 2011.

[27] Z. S. Siwy, "Ion-current rectification in nanopores and nanotubes with broken symmetry," *Advanced Functional Materials*, vol. 16, no. 6, pp. 735–746, 2006.

[28] S. W. Kowalczyk, A. Y. Grosberg, Y. Rabin, and C. Dekker, "Modeling the conductance and DNA blockade of solid-state nanopores.," *Nanotechnology*, vol. 22, no. 31, p. 315101, 2011.

Chapter 5

Solid-State Nanopore Localization by Controlled Breakdown of Selectively Thinned Membranes

Autumn T. Carlsen[1,*], Kyle Briggs[1,*], Adam R. Hall[2], and Vincent Tabard-Cossa[1]

1 – Department of Physics, University of Ottawa, Ottawa, Ontario K1N 6N5
2 – Virginia Tech-Wake Forest School of Biomedical Engineering and Sciences, Wake Forest University School of Medicine, Winston Salem, North Carolina 27101
* – These authors contributed equally to this work

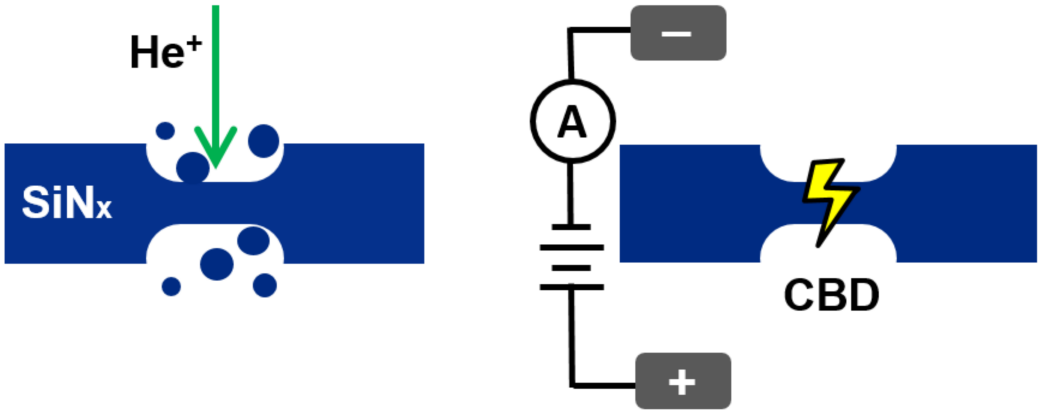

Adapted with permission from [A. T. Carlsen, K. Briggs, A. R. A. A. R. Hall, and V. Tabard-Cossa, "Solid-state nanopore localization by controlled breakdown of selectively thinned membranes," *Nanotechnology*, vol. 28, no. 8, 2017]

Abstract

We demonstrate precise positioning of nanopores fabricated by controlled breakdown (CBD) on solid-state membranes by spatially varying the electric field strength with localized membrane thinning. We show 100×100 nm^2 precision in standard SiN_x membranes ($30 - 100$ nm thick) after selective thinning by as little as 25% with a helium ion beam. Control over nanopore position is achieved through the strong dependence of the electric field-driven CBD mechanism on membrane thickness. Confinement of pore formation to the thinned region of the membrane is confirmed by TEM imaging and by analysis of DNA translocations. These results enhance the functionality of CBD as a fabrication approach and enable the production of advanced nanopore devices for single-molecule sensing applications.

5.1 Introduction

Solid-state nanopore-based devices have emerged as leading candidates among single-molecule detection technologies for life and health science applications[2–6], including next-generation DNA sequencing[7,8]. At present, solid-state nanopores are fabricated exclusively for research purposes, typically using expensive and/or low-throughput methods such as transmission electron microscopy (TEM) or focused ion beam (FIB) drilling. In order for nanopore-based devices to make the transition to mainstream applications, including medical diagnostics, an alternative fabrication technique has been needed that could produce nanopores of the desired size at low cost. With that goal in view, we recently introduced a technique called controlled breakdown (CBD) as a means to fabricate pores rapidly, reliably, economically, and with high precision[9–12]. Since then, we have been exploring methods to enhance the functionality of this transformative new approach.

One avenue for enhancing CBD functionality is the implementation of strategies for precise localization of nanopores, since CBD normally produces a pore at a random location on the membrane through a stochastic process[9,11]. Most standard nanopore-based sensors do not require pore positioning, but a number of specialized applications – including nanofluidic transistors, electrode-embedded devices[13–24], and plasmonic nanopores[25–28] – necessitate formation of the pore within a short distance of an existing structure on the membrane. Other applications require pore fabrication in a region of the membrane that has been locally thinned to maximize the signal amplitude of translocating biomolecules[5,29]. Positioning efforts typically employ a focused beam of electrons or ions to mill the pore, calling for line-of-sight access to the desired pore location under vacuum conditions.

The electric-field-driven CBD technique can be implemented in pore localization strategies using one of two approaches: 1) defining the path of the electric field produced when voltage is applied across the membrane or 2) increasing the local electric field strength in a predefined region of the membrane. With regard to the first approach, we recently reported the successful fabrication of a five-nanopore array using CBD in concert with a microfluidic device[30]. The patterning of five fluidically- and electrically-independent PDMS channels on a single SiN_x membrane allowed the confinement of the electric field employed in the CBD process to five individually addressable regions, resulting in the localization of pores on a 10 μm length scale. In terms of the second approach, we noted in our initial paper on the CBD technique that nanopore fabrication time is exponentially dependent on local electric field strength in the membrane[9]. Pud *et al.* exploited this property by combining the CBD process with laser excitation of gold nanostructures deposited on a membrane to locally enhance current density and promote pore formation in the plasmonic hotspot between two metallic nanostructures[31]. Another strategy for enhancement of electric field

strength is to exploit local thickness changes, which could be leveraged to localize pore formation through patterning of the membrane[9]. Indeed, we initially reported in Kwok *et al.*[9] that bottom-up patterning of a membrane with a thick oxide layer (on the order of 1 μm) could be used to spatially restrict pore fabrication.

In this work, we introduce a new, top-down methodology to support the latter approach by reducing the thickness of a defined region in an otherwise featureless membrane prior to CBD nanopore production. The resulting increase in local electric field strength in the thinned region yields a greatly increased probability of nanopore formation compared to the surrounding membrane, while maintaining full control over pore diameter. Here, we employ helium ion microscope (HIM) thinning to demonstrate the viability of selective membrane thinning for pore localization, due to its rapid, flexible nature[32]. However, we note that in future iterations, wafer-scale approaches could easily be incorporated, including soft, photo-, or beam-based lithographic techniques. The use of the CBD technique also enables in situ fabrication of stable, precisely sized pores in fully assembled, fluid-filled devices containing pre-positioned thinned areas, with no line-of-sight access or vacuum required. Therefore, the research described in this paper represents a significant advancement in the ease of use and precision of localized pore fabrication, opening the door to a cost-effective, high-throughput pore positioning strategy.

5.2 Results and Discussion

5.2.1 Selective HIM-Thinning and CBD Pore Formation

HIM milling is used to reduce membrane thickness as previously described[29,33], wherein a SiN_x membrane supported by a Si chip is exposed with a coherent beam

of He ions over a pre-defined area. In this work, we use square patterns measuring 100×100, 250×250, or 300×300 nm^2, as noted in the text. The ion dosage necessary to achieve a specific reduction in thickness within the pattern is determined by calibrated transmission ion brightness assessment, as detailed elsewhere[34]. In order to minimize redeposition and other undesirable effects (e.g. swelling or deformation of the surrounding material[33]), the focused HIM beam is rastered repeatedly over the square pattern, exposing each (1 nm^2) point in the pattern for roughly 0.1 μs until the desired total dose is achieved. After thinning (Figure 5.1a), the standard CBD workflow is employed. First, the Si chip bearing the locally thinned SiN_x membrane is sealed between two halves of a fluidic cell, and then the cell's reservoirs are filled with electrolyte solution for pore fabrication by CBD, followed by analyte detection (Figure 5.1)).

5.2.2 Effect of Membrane Properties on CBD

The CBD method is based on dielectric breakdown, which is a stochastic process, dependent on the probability of random defect (trap) generation and subsequent formation of a highly localized conductive path through the membrane. However, certain factors – including applied voltage, pH, membrane thickness and area – play a vital role in determining the most probable time to breakdown[9,11]. Given the exponential dependence of pore fabrication time on electric field strength, for a given applied voltage, locally thinning the membrane will produce a region where the electric field is proportionally stronger (Figure 5.1c, inset diagrams), thus increasing the rate of defect generation per unit area in the thinned region compared to the rest of the membrane. In essence, the thinned region would offer a more favorable path toward pore formation than the thicker surrounding membrane for a given voltage. Increasing the

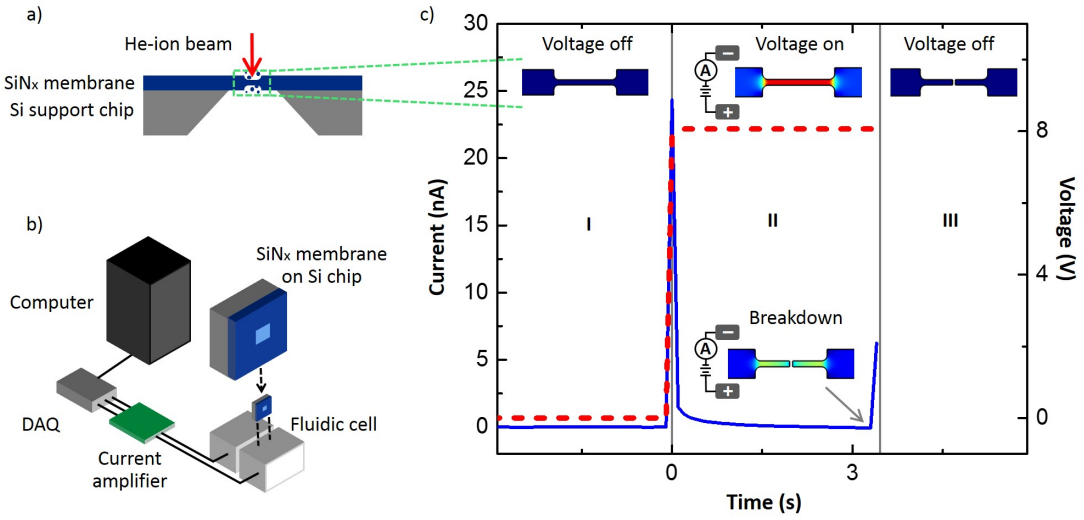

Figure 5.1: Selective thinning by HIM followed by localized CBD pore fabrication. Schematic representation of (a) helium-ion beam thinning a region of a SiN_x membrane supported by a Si chip and (b) insertion of the membrane-bearing support chip into a CBD fabrication setup. (c) Measured pore formation data, displaying the monitored current (blue solid line) as a function of time for a DC voltage (red dashed line) of 8 V applied from 0 seconds to 3.4 seconds on a 100 nm thick membrane thinned by 90% in a 250×250 nm^2 area. Inset schematic diagrams show cross-sectional view of the electric field produced in the membrane by the following events: I) Immersion of the intact SiN_x membrane in electrolyte solution (3.6M LiCl, pH 8); II) Application of 8 V to the membrane, initially resulting in leakage current below the resolution of our custom electronics (on the order of 0.1 nA). Breakdown corresponds to nanopore formation in the membrane, producing the sudden onset of ionic current indicated by a large, easily-detected current spike; III) Removal of fabrication voltage from the wetted nanopore terminates fabrication.

surface area of the thinned region would further reduce the time to formation, since a greater area offers a significant increase in the number of potential damage sites, as predicted by the Weibull distribution that governs the time to pore formation[11], which predicts a logarithmic dependence on membrane area in the characteristic time to breakdown. In addition, ion beam exposure is known to induce defects[35], which may further contribute to pore formation efficiency[36].

5.2.3 CBD Pore Formation in Membranes HIM-Thinned by at Least 90%

With the goal of achieving relatively short fabrication times while maintaining a much higher probability of pore formation in the thinned region, we locally reduced thickness of a 250×250 nm^2 region in eight SiN_x membranes (100×100 μm^2, 100 nm thick) by HIM. Based on calibrated brightness measurements from transmission ion imaging[34] on a chip from the same wafer, we selected dosage values of 537 pC for four membranes and 586 pC for four others to target final thicknesses in the vicinity of 10 nm. After mounting the lower-dose membranes in fluidic cells with electrolyte solution (3.6 M LiCl, pH 8), we applied 5 to 8 V of potential bias, which produced small, relatively stable leakage currents. The small magnitude of the leakage currents was not surprising given that the 100 nm thick portion of the membrane experiences a maximum electric field on the order of 0.08 V/nm, while only a minute fraction of its surface area (less than 0.001%) has been reduced to a thickness such that the applied voltage approaches the dielectric strength (approximately 1 V/nm) that would result in significant leakage current. Fabrication and DNA translocation kinetics are shown in Figure 5.2. The pores formed in all four membranes exhibited low $\frac{1}{f}$ noise and linear IV curves, as shown in Figure 5.3. For the four membranes thinned with the higher dose (586 pC), we observed some anomalous behavior, including pores that seemingly opened then shrank, requiring additional voltage treatment to re-open. We attribute this behavior to the generation of temporary percolation paths[37–39] or to possible restructuring of membrane material in the thinned region, likely resulting from increased ion exposure[40].

For membranes exposed with either dose, we found that the presence of the thinned region dramatically reduced pore formation times for a given applied voltage.

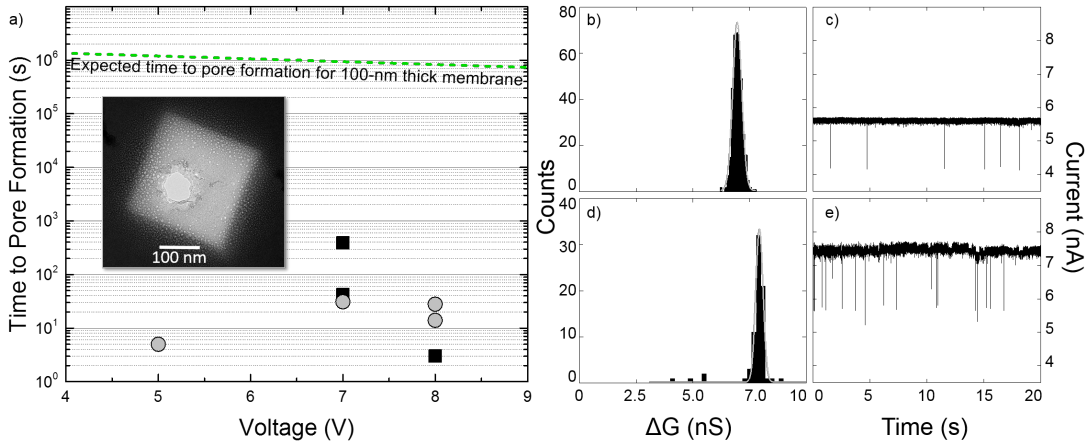

Figure 5.2: Results obtained from 100 nm thick SiN_x membranes thinned by HIM. (a) Graph showing time to pore formation vs. voltage for membranes thinned by $80-90\%$ from 100 nm original thickness. Black squares represent membranes thinned with a 537 pC He-ion dose; gray circles correspond to membranes thinned with a 586 pC He-ion dose. Green dotted line represents estimated time to pore formation in an unthinned 100 nm thick membrane. Inset: TEM image of 100 nm thick SiNx membrane showing large pore formed in 250×250 nm^2 region thinned to 10 nm by HIM. (b-e) Conductance blockage histograms with example current traces for translocations of 0.3 nM solution of 2 kb dsDNA (b,c) and 6 nM solution of 5 kb dsDNA (d,e) at 200 mV through two different pores in 3.6 M LiCl (pH 8).

Compared to an expected pore fabrication time of over 10^6 s (more than 10 days) at 8 V for a 100 nm thick membrane (extrapolated from published data[11]), membranes with a region of reduced thickness underwent pore formation within hundreds of seconds or less (Figure 5.2a), representing a decrease in fabrication time by at least 4 orders of magnitude. Following formation, these pores were subsequently treated with $1-4$ s voltage pulses of alternating polarity ($\pm 2-8$ V) to precisely and controllably bring their diameters within the range of 4 to 50 nm[12].

To confirm localization of the pore in the thinned region, we employed DNA molecules as molecular rulers to measure membrane thickness. A 3.6 M LiCl (pH 8) solution containing double-stranded (ds-) DNA was loaded into the reservoir on the

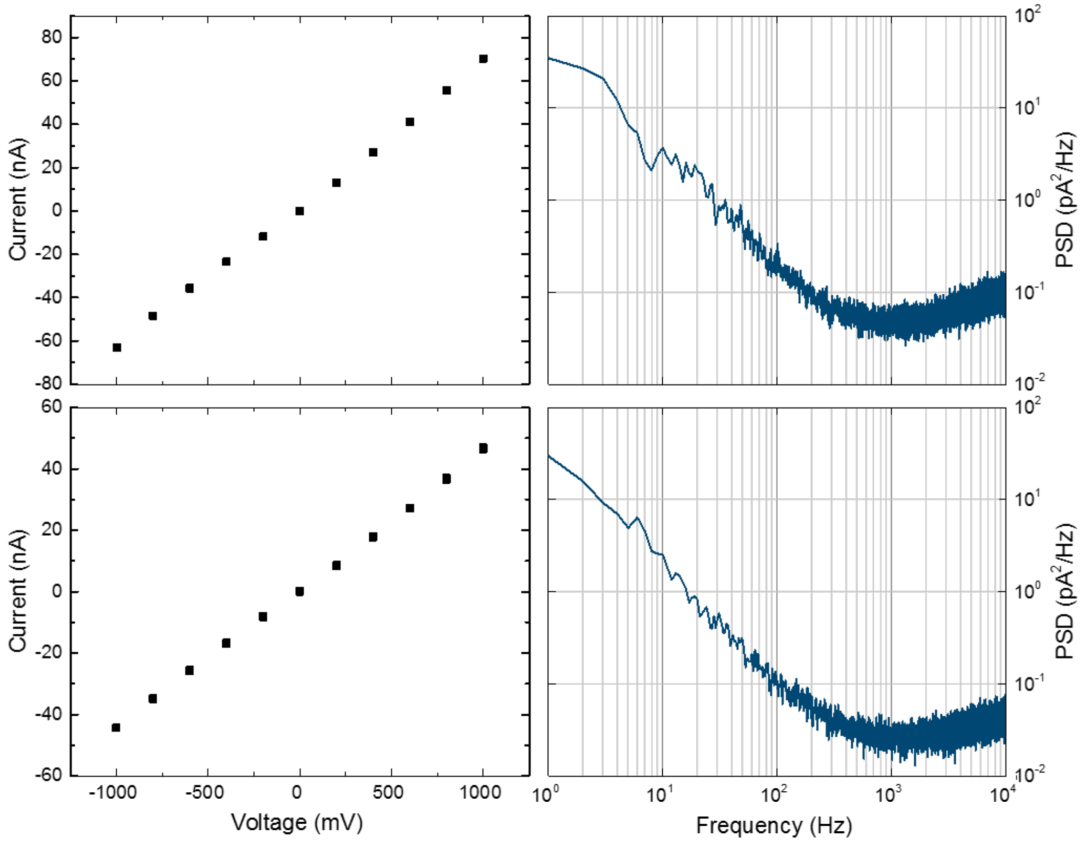

Figure 5.3: IV characteristics and power spectrum densities captured at 200 mV for two different nanopores formed in 100 nm thick membranes thinned to roughly 7 to 8 nm by a He-ion dose of 537 pC on a 250×250 nm^2 region. Measurement performed in 3.6 M LiCl (pH 8) using an Axopatch 200B. Pores were formed within a few hundred seconds with the application of 6 to 8 V.

membrane side of the chip and subjected to 200 mV electric potential difference. As seen in Figure 5.2b-e, we observed clear conductance blockage events with average first-level depths of 7.0 ± 0.5 nS and 7.9 ± 0.4 nS for two different membranes thinned to approximately 10 nm. Values for membrane thickness L were calculated using the simplest conductance model for a cylindrical pore[41,42]:

$$\Delta G_{DNA} = \sigma \frac{\pi d_{DNA}^2}{4L} \tag{5.1}$$

by substituting the diameter of dsDNA as $d_{DNA} = 2.2$ nm, along with the measured solution conductivity ($\sigma = 155.6$ mS/cm) and first-level blockage depth (ΔG_{DNA}). According to this approach, the measured conductance blockages of roughly 7 and 8 nS correspond to effective membrane thicknesses of 8 ± 1 nm and 7.4 ± 0.8 nm, in close agreement with the targeted membrane thickness, considering possible deviations from an exact cylindrical geometry. Since the original membrane thickness of 100 nm would produce conductance blockage depths on the order of 0.6 nS, these significantly deeper blockages provide strong evidence of pore formation in the thinned region of the membranes.

While the large contrast difference of the thinned region compared to the surrounding (unthinned) membrane was expected to make direct imaging of the pore much easier, obtaining conclusive TEM confirmation of pore formation in the thinned region proved challenging, except in the case of the largest pore (Figure 5.2a, inset). This is because we observed that extensive thinning appeared to produce circular features that rendered the identification of a single, small (sub-10 nm) nanopore difficult.

In order to isolate the source of these circular features, TEM was performed on membranes after HIM-thinning, but before CBD pore fabrication and liquid immersion. In these membranes, we observed the same spurious bright features, shown in Figure 5.4. Prior work on the effect of He-ion irradiation on surfaces reveals a potential explanation for the observation. The formation of voids in both crystalline and amorphous silicon through helium ion beam exposure has been previously reported[40,43–47]. Indeed, TEM imaging of samples exposed to He-ion doses of 1017 ions/cm^2 or higher has revealed a dense band of helium-filled nano bubbles[40,44,46], with the band's width and depth beneath the bombarded surface dependent on the ion beam energy and dose[40,48]. It has been shown that peak helium implantation

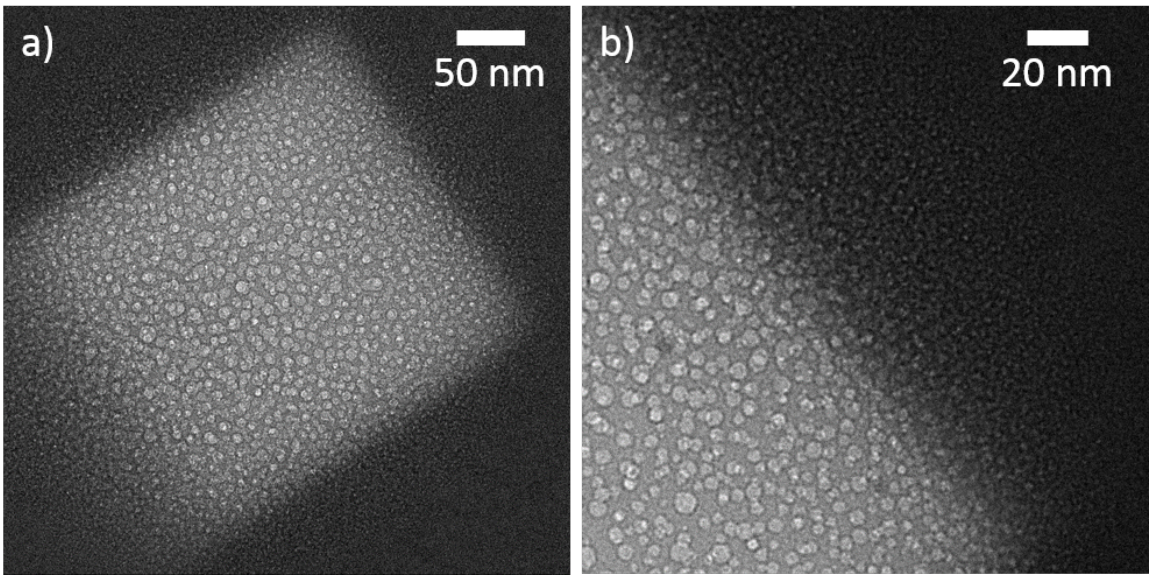

Figure 5.4: TEM images of helium bubbles trapped in 100 nm thick SiN_x membranes thinned by HIM using doses of a) 537 pC and b) 500 pC.

occurs at roughly the nuclear stopping range of the sample, while maximum bubble concentration may occur at a slightly shallower depth[40,47]. Here, we are working with He-ion doses on the order of 1018 ions/cm^2 on SiN_x, which exhibits a stopping range of roughly 130 nm with a spread (straggle) of 50 nm for a 20 keV He-ion beam[49]. For an initial film thickness approaching the stopping range value, subsurface helium implantation and bubble formation will likely occur. However, for films significantly thinner than the stopping range, there should be almost no helium implantation; instead, impinging ions will remove material, effectively milling the sample[50]. This explains why bubbles have not been observed in previous HIM thinning experiments despite similar He-ion beam energy and dose, since those that incorporated TEM imaging[29] utilized a starting membrane thickness of roughly 20 nm.

5.2.4 CBD Pore Formation in Membranes HIM-Thinned by 25-60%

Having demonstrated successful pore localization for membranes thinned from 100 nm to 10 nm (i.e. 90% thinned) in a 250×250 nm^2 area, we sought to push the boundaries of this CBD-based approach in two ways: 1) by confining pores to an even smaller region and 2) by using a less drastic thickness reduction. To achieve the former, we introduced a six-fold reduction in the area of the thinned region, going from 250×250 nm^2 to 100×100 nm^2. For the latter, we targeted a final membrane thickness of 10 nm from a starting membrane thickness of 30 nm, as opposed to 100 nm. Besides determining if pore formation would still be limited to the thinned region, the less drastic thickness reduction allowed for a starting membrane thickness well below the material's nuclear stopping range, thereby strongly favoring milling over the implantation that produced voids in experiments with HIM-thinning from 100 nm.

For the reasons just described, we HIM-thinned 100×100 nm^2 regions in 30 nm thick membranes, targeting a final thickness of 10 nm. Subsequent transmembrane application of 8 V via the CBD process in an aqueous solution of 1 M KCl (pH 10) produced pores, but fabrication times were prohibitively long, sometimes lasting several days. In fact, we observed an average time of around $290,000$ s (80 hours) for three such devices. By comparison, membranes thinned from 100 nm to the same target thickness of 10 nm formed within hundreds of seconds. Some increase in pore fabrication time was expected, concurrent with the six-fold reduction in the area of the thinned region; strong area dependence of fabrication time by CBD is consistent with the Weibull distribution of nanopore fabrication time developed in previous work[11]. However, the six-fold reduction in area cannot account for the three orders

of magnitude increase in pore fabrication time.

The explanation for the precipitous rise in pore fabrication time lies in the pore length (equivalent to membrane thickness for a cylindrical pore model), obtained using DNA as a molecular ruler. We observed DNA translocations in three separate devices, which produced conductance blockage values corresponding to respective membrane thicknesses of 12±1 nm, 13±4 nm, and 23±8 nm, compared to the original membrane thickness of 30 nm (Table 5.1). These thickness values are $2-3\times$ larger than those obtained for the membranes thinned from 100 nm. Thus, the pore fabrication times were significantly longer at the same voltage, since pore fabrication time depends exponentially on electric field[9] which is inversely proportional to thickness for a given voltage.

Table 5.1: Summary of data collected from 5 different nanopores which were HIM-thinned from either 30 nm or 100 nm as-purchased membrane thickness. Translocation of dsDNA (1 to 20 kbp) was collected at 200 mV in 3.6 M LiCl (pH 8) and analysed for conductance blockage depths. Where peaks corresponding to single and folded events appeared, the single-level peak was selected.

Number of Events	Nominal Length (nm)	Open-Pore Conductance (nS)	Blockage Depth (nS)	Pore Length (nm)	Pore Diameter (nm)	Electric Field (V/nm)
2546	30	162 ± 1	2.6 ± 0.9	23 ± 8	23 ± 8	0.35
615	30	39.5 ± 0.6	4.97 ± 0.08	12 ± 1	7.6 ± 0.6	0.67
5755	30	61 ± 6	4 ± 1	13 ± 4	10 ± 1	0.62
82	100	37.3 ± 0.6	7.9 ± 0.4	7.4 ± 0.8	6.1 ± 0.5	1.08
372	100	25.7 ± 0.7	7.0 ± 0.5	8 ± 1	5.2 ± 0.4	1.00

Subsequent experimental analysis by TEM clearly showed the pores in the thinned regions, providing definitive confirmation of the effectiveness of thinning the membrane by just 25 to 60% in order to localize pores. Further, the lack of visible bubbles or voids in the thinned regions confirmed that the 30 nm starting thickness of SiN_x

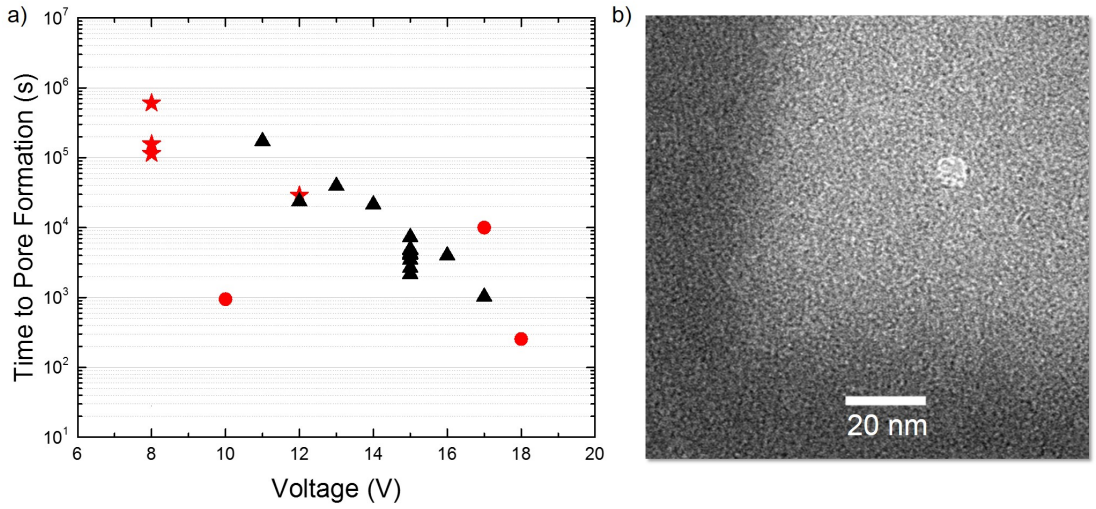

Figure 5.5: Pore formation in thinned vs. unthinned 30 nm thick membranes. (a) Graph of pore formation time vs. voltage for a series of membranes with an original thickness of 30 nm. Red stars represent 100×100 nm^2 thinned regions, while red circles represent 300×300 nm^2 thinned regions. Black triangles correspond to unthinned membranes, for the purpose of comparison. (b) TEM image of pore in thinned (bright) region.

membranes is insufficient to trap helium as in the much thicker 100 nm membranes.

In an effort to decrease the pore formation time, we next investigated the application of higher voltages to the 30 nm thick membranes thinned in a slightly larger area (300×300 nm^2). Indeed, the use of voltages in excess of 15 V did produce pores much more rapidly (e.g., 2.8 hours at 17 V, 255 s at 18 V). We found that the average time to pore formation for these thinned membranes (Figure 5.5a) was not dramatically shorter than that of unprocessed 30 nm membranes at 15V (estimated at roughly 1.25 hours by reference[11]). Taken alone, these times to breakdown suggest possible pore fabrication in the thicker region of the membrane. Nevertheless, TEM visualization revealed that the pores were still confined to the thinned region, even for higher-voltage pore formation (Figure 5.5b). In some cases, contamination on the membrane itself interfered with imaging, as shown in Figure 5.6.

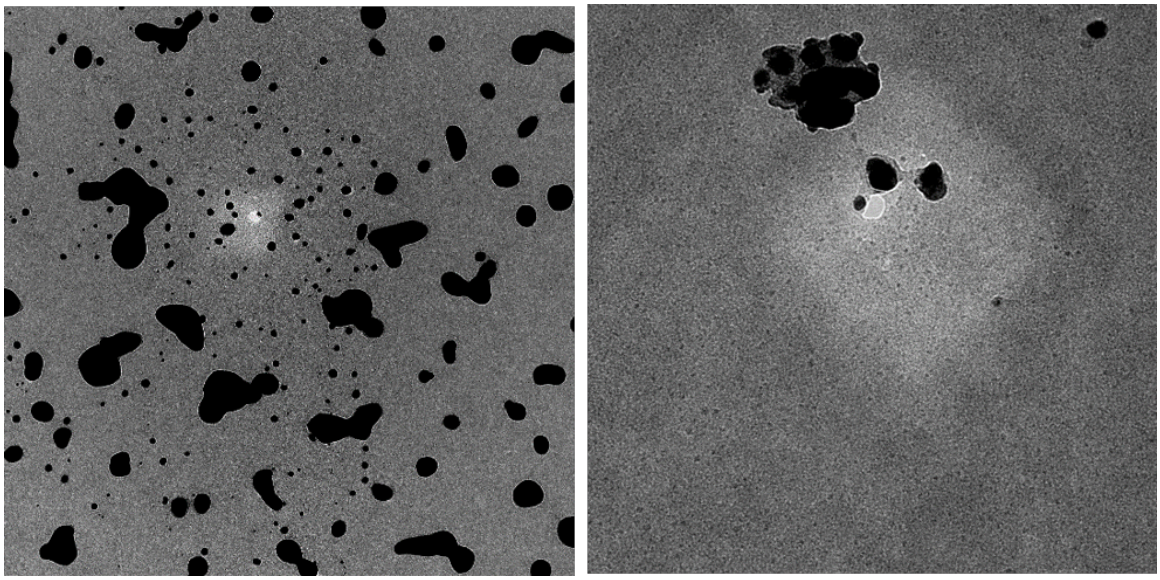

Figure 5.6: TEM images show a pore appearing in the 100×100 nm^2 regions thinned to 23 nm (pore 9) and 13 nm (pore 11) from an original 30 nm SiN_x thickness.

In some cases where higher fabrication voltages (greater than 15 V) or conditioning voltages (greater than 4 V) were employed, multiple pores were observed. For example, in the case of a membrane exposed to 17 V, TEM visualization (Figure 5.7a) revealed two pores in the thinned region (300×300 nm^2). Close inspection of the leakage current trace (Figure 5.7b) showed an initial, transient current spike occurring roughly 3000 seconds prior to a much larger spike which surpassed the user-set current threshold in our software to trigger removal of the applied voltage. That initial, brief spike likely corresponded to pore formation, but was not correctly identified. This approach is not well-suited to fabrication of multiple similarly sized pores on the same membrane, since the continued presence of a high electric field will drive growth of the initial pore[12] even as additional pores are forming.

Preventing fabrication of multiple pores hinges on careful consideration of key parameters at two junctures in the CBD process: fabrication and conditioning. First, fabrication voltages must be selected to ensure that median fabrication time is sub-

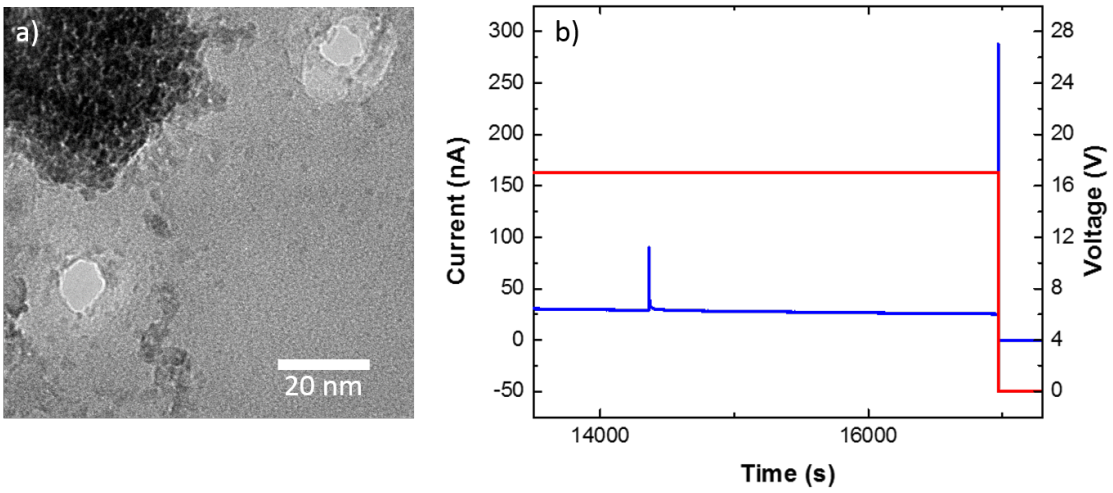

Figure 5.7: Multiple pore formation at high voltage. (a) TEM image of two pores formed in a 30 nm thick SiN_x membrane after HIM-thinning to 10 nm in a 300 × 300 nm^2 area. (b) Measured pore formation data for the same pore, displaying the monitored current (blue) as a function of time for a constant applied voltage of 17 V (red) in 3.6 M LiCl (pH 8).

stantially longer than the time it takes for the software to recognize initial pore formation and cut off the voltage, determined here by the threshold used to trigger detection of a breakdown event and the capacitive timescales on which the current responds to voltage changes. Secondly, if an existing pore requires conditioning (to reduce noise, remove rectification or increase diameter)[12], the value of the applied conditioning voltage must lie well below the voltage necessary to produce a pore within the conditioning time frame (usually on the order of $10^2 - 10^3$ s for 10 nm SiN_x at ca. ±3 V). For these thinned membranes, it appears that multiple pores were formed at the fabrication level: selection of an overly aggressive electric field strength during fabrication, well above 1 V/nm (greater than 15 V on membranes approximately 10 nm thick), interfered with our software's ability to identify a newly formed pore and remove the applied voltage before additional pores could form.

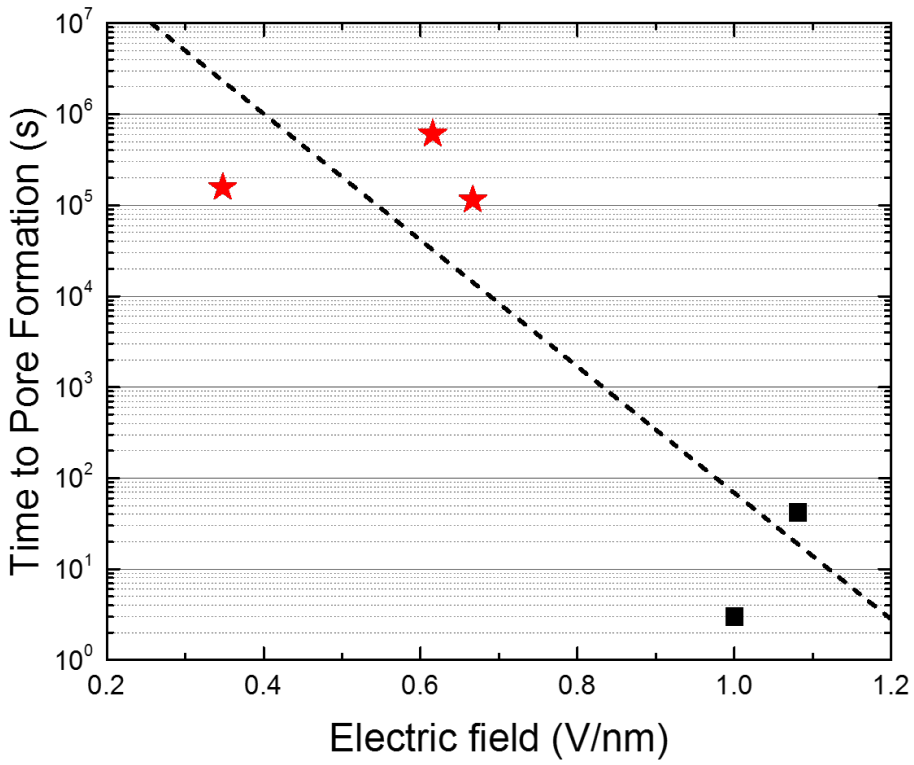

Figure 5.8: Graph showing the relationship between time-to-formation for a pore and electric field strength for a series of membranes thinned from 30 nm (red stars) or 100 nm (black squares) original thickness down to 10 nm (actual membrane thickness used to calculate electric field strength was extracted from DNA translocation data). Dashed black line serves to guide the eye.

Finally, an overview of all the data presented in this paper reveals pore fabrication times ranging from seconds to days. For those membranes on which we performed the DNA translocation experiments described earlier, we used the fabrication voltages and corresponding membrane thickness values to identify the electric field strength across each membrane in the thinned region (see Table 1). We then compared the electric field strength to the time-to-formation, as seen in Figure 5. Consistent with the exponential relation between time to breakdown and electric field strength, we see

that higher electric fields tend to produce pores in shorter times. Although there could be effects due to material differences between membranes (e.g. the presence of helium bubbles), these results support the validity of our DNA-based thickness measurements and highlight the possibility of reducing fabrication times with selective membrane thinning.

5.3 Conclusion

We have demonstrated localization of nanopores fabricated by CBD in membranes thinned by $25 - 90\%$ in 100×100 nm^2 to 300×300 nm^2 regions. Upon voltage application during CBD, the enhanced electric field strength in the thinned region strongly promotes pore formation. Confinement of the pore to the desired area has been confirmed by the conductance blockage depths of translocating DNA molecules and by direct TEM imaging. With the demonstrated capacity of a Helium-ion beam to reduce SiN_x membrane thickness down to 1 nm and to produce features with sub-10 nm precision[29], this pore localization strategy shows great promise for applications requiring the enhanced signal-to-noise ratio afforded by thinner membranes while leveraging the stability offered by thicker membranes, or for applications requiring pore formation near a pre-existing feature and/or within a pre-assembled device. Future endeavors integrating the CBD process with wafer-scale thinning techniques could pave the way for the rapid, automated manufacture of precisely sized and positioned nanopores.

5.4 Materials and Methods

Silicon TEM chips, each supporting either a 100×100 μm^2 window of low-stress SiN_x membrane with 100 nm thickness or a 50×50 μm^2 window with 30 nm thickness, were obtained commercially (Norcada NT010C and NT005X, respectively). After chips were loaded into the antechamber of a commercial HIM (Orion PLUS, Carl Zeiss), they were subjected to a brief air-plasma clean (10 W, 3 min) before being moved into the main chamber. Using beam conditions of $5 - 6$ pA current, 25 kV accelerating voltage, and a 20 μm aperture, the helium-ion beam shape and focus were optimized on the SiN_x membrane near the window where the membrane was suspended. Next, a single region of the membrane (100×100 nm^2, 250×250 nm^2, or 300×300 nm^2) was thinned by rastering the beam over a lithographically-defined square pattern, repeatedly exposing each 1 nm^2 point in the pattern for 0.1 μs until the desired total dose of 32 pC (for 30 nm thick membranes) or 537/586 pC (for 100 nm thick membranes) was achieved. In each case, ion dose was selected by referencing a transmission ion imaging brightness calibration[34] performed with a membrane from the same wafer.

Pore fabrication was performed in a 1 M KCl (pH 10, $\sigma = 100$ mS/cm) aqueous solution buffered with 10 mM $NaHCO_3$ or in a 3.6 M LiCl (pH 8, $\sigma = 154.8$ mS/cm) solution buffered with 10 mM HEPES, using similar custom electronics and software to those previously described[9].

Translocation of dsDNA (NoLimits, ThermoFisher) with lengths of 1 kbp, 5 kbp, or 20 kbp took place in 3.6 M LiCl (pH 8) solutions. Translocation data was acquired using custom Labview software, a National Instruments USB-6351 DAQ card, with a 250 or 500 kHz sampling rate and an Axopatch 200B with a 4-pole Bessel low-pass filter set at 10 or 100 kHz. Data analysis was performed using custom Labview

software and Origin.

Acknowledgements

This work was supported in part by the Natural Sciences and Engineering Research Council of Canada (NSERC), and by NIH grant 1R21CA193067. K.B. acknowledges the financial support provided by the NSERC Vanier program for postgraduate fellowships. We gratefully acknowledge Dr. Yun Liu for her help in TEM imaging.

Bibliography

[1] A. T. Carlsen, K. Briggs, A. R. A. A. R. Hall, and V. Tabard-Cossa, "Solid-state nanopore localization by controlled breakdown of selectively thinned membranes," *Nanotechnology*, vol. 28, no. 8, 2017.

[2] A. T. Carlsen, O. K. Zahid, J. A. Ruzicka, E. W. Taylor, and A. R. Hall, "Selective detection and quantification of modified DNA with solid-state nanopores," *Nano Letters*, vol. 14, no. 10, pp. 5488–5492, 2014.

[3] D. Fologea, B. Ledden, D. S. McNabb, and J. Li, "Electrical characterization of protein molecules by a solid-state nanopore," *Applied Physics Letters*, vol. 91, no. 5, pp. 5–8, 2007.

[4] J. Shim, G. I. Humphreys, B. M. Venkatesan, J. M. Munz, X. Zou, C. Sathe, K. Schulten, F. Kosari, A. M. Nardulli, G. Vasmatzis, and R. Bashir, "Detection and Quantification of Methylation in DNA using Solid-State Nanopores," *Scientific Reports*, vol. 3, no. 1, p. 1389, 2013.

[5] M. Wanunu, T. Dadosh, V. Ray, J. Jin, L. McReynolds, and M. Drndić, "Rapid electronic detection of probe-specific microRNAs using thin nanopore sensors," *Nature Nanotechnology*, vol. 5, no. 11, pp. 807–814, 2010.

[6] O. K. Zahid, B. S. Zhao, C. He, and A. R. Hall, "Quantifying mammalian genomic DNA hydroxymethylcytosine content using solid-state nanopores," *Scientific Reports*, vol. 6, no. June, pp. 1–6, 2016.

[7] M. Wanunu, "Nanopores: A journey towards DNA sequencing," *Physics of Life Reviews*, vol. 9, no. 2, pp. 125–158, 2012.

[8] D. Branton, D. W. Deamer, A. Marziali, H. Bayley, S. A. Benner, T. Butler, M. Di Ventra, S. Garaj, A. Hibbs, X. Huang, S. B. Jovanovich, P. S. Krstic, S. Lindsay, X. S. Ling, C. H. Mastrangelo, A. Meller, J. S. Oliver, Y. V. Pershin, J. M. Ramsey, R. Riehn, G. V. Soni, V. Tabard-Cossa, M. Wanunu, M. Wiggin,

and J. A. Schloss, "The potential and challenges of nanopore sequencing," *Nature Biotechnology*, vol. 26, no. 10, pp. 1146–1153, 2008.

[9] H. Kwok, K. Briggs, and V. Tabard-Cossa, "Nanopore fabrication by controlled dielectric breakdown.," *PLoS One*, vol. 9, p. e92880, jan 2014.

[10] K. Briggs, H. Kwok, and V. Tabard-Cossa, "Automated Fabrication of 2-nm Solid-State Nanopores for Nucleic Acid Analysis," *Small*, vol. 10, no. 10, pp. 2077–2086, 2014.

[11] K. Briggs, M. Charron, H. Kwok, T. Le, S. Chahal, J. Bustamante, M. Waugh, and V. Tabard-Cossa, "Kinetics of nanopore fabrication during controlled breakdown of dielectric membranes in solution," *Nanotechnology*, vol. 26, no. 8, 2015.

[12] E. Beamish, H. Kwok, V. Tabard-Cossa, and M. Godin, "Precise control of the size and noise of solid-state nanopores using high electric fields.," *Nanotechnology*, vol. 23, p. 405301, oct 2012.

[13] S. Harrer, S. Ahmed, A. Afzali-Ardakani, B. Luan, P. S. Waggoner, X. Shao, H. Peng, D. L. Goldfarb, G. J. Martyna, S. M. Rossnagel, L. Deligianni, and G. A. Stolovitzky, "Electrochemical characterization of thin film electrodes toward developing a DNA transistor," *Langmuir*, vol. 26, no. 24, pp. 19191–19198, 2010.

[14] K. Healy, V. Ray, L. J. Willis, N. Peterman, J. Bartel, and M. Drndic, "Fabrication and characterization of nanopores with insulated transverse nanoelectrodes for DNA sensing in salt solution," *Electrophoresis*, vol. 33, no. 23, pp. 3488–3496, 2012.

[15] P. Pang, B. A. Ashcroft, W. Song, P. Zhang, S. Biswas, Q. Qing, J. Yang, R. J. Nemanich, J. Bai, J. T. Smith, K. Reuter, V. S. Balagurusamy, Y. Astier, G. Stolovitzky, and S. Lindsay, "Fixed-gap tunnel junction for reading DNA nucleotides," *ACS Nano*, vol. 8, no. 12, pp. 11994–12003, 2014.

[16] A. P. Ivanov, K. J. Freedman, M. J. Kim, T. Albrecht, and J. B. Edel, "High precision fabrication and positioning of nanoelectrodes in a nanopore," *ACS Nano*, vol. 8, no. 2, pp. 1940–1948, 2014.

[17] E. S. Sadki, S. Garaj, D. Vlassarev, J. A. Golovchenko, and D. Branton, "Embedding a carbon nanotube across the diameter of a solid state nanopore," *Journal of Vacuum Science & Technology B, Nanotechnology and Microelectronics: Materials, Processing, Measurement, and Phenomena*, vol. 29, no. 5, p. 053001, 2011.

[18] K. H. Paik, Y. Liu, V. Tabard-Cossa, M. J. Waugh, D. E. Huber, J. Provine, R. T. Howe, R. W. Dutton, and R. W. Davis, "Control of DNA capture by nanofluidic transistors," *ACS Nano*, vol. 6, no. 8, pp. 6767–6775, 2012.

[19] Y. Zhao, B. Ashcroft, P. Zhang, H. Liu, S. Sen, W. Song, J. Im, B. Gyarfas, S. Manna, S. Biswas, C. Borges, and S. Lindsay, "Single-molecule spectroscopy of amino acids and peptides by recognition tunnelling," *Nature Nanotechnology*, vol. 9, no. 6, pp. 466–473, 2014.

[20] S. Chang, S. Huang, H. Liu, P. Zhang, F. Liang, R. Akahori, S. Li, B. Gyarfas, J. Shumway, B. Ashcroft, J. He, and S. Lindsay, "Chemical recognition and binding kinetics in a functionalized tunnel junction," *Nanotechnology*, vol. 23, no. 23, 2012.

[21] P. Krishnakumar, B. Gyarfas, W. Song, S. Sen, P. Zhang, P. Krstić, and S. Lindsay, "Slowing DNA translocation through a nanopore using a functionalized electrode.," *ACS nano*, vol. 7, pp. 10319–26, nov 2013.

[22] H. Kwok, M. Waugh, J. Bustamante, K. Briggs, and V. Tabard-Cossa, "Long passage times of short ssDNA molecules through metallized nanopores fabricated by controlled breakdown," *Advanced Functional Materials*, vol. 24, no. 48, pp. 7745–7753, 2014.

[23] J. A. Rodríguez-Manzo, Z. J. Qi, A. Crook, J.-H. Ahn, A. T. C. Johnson, and M. Drndić, "In Situ Transmission Electron Microscopy Modulation of Transport in Graphene Nanoribbons," *ACS Nano*, vol. 10, no. 4, pp. 4004–4010, 2016.

[24] A. P. Ivanov, E. Instuli, C. M. McGilvery, G. Baldwin, D. W. McComb, T. Albrecht, and J. B. Edel, "DNA tunneling detector embedded in a nanopore," *Nano Letters*, vol. 11, no. 1, pp. 279–285, 2011.

[25] F. Nicoli, D. Verschueren, M. Klein, C. Dekker, and M. P. Jonsson, "DNA translocations through solid-state plasmonic nanopores," *Nano Letters*, vol. 14, no. 12, pp. 6917–6925, 2014.

[26] C. R. Crick, P. Albella, B. Ng, A. P. Ivanov, T. Roschuk, M. P. Cecchini, F. Bresme, S. A. Maier, and J. B. Edel, "Precise attoliter temperature control of nanopore sensors using a nanoplasmonic bullseye," *Nano Letters*, vol. 15, no. 1, pp. 553–559, 2015.

[27] M. P. Cecchini, A. Wiener, V. A. Turek, H. Chon, S. Lee, A. P. Ivanov, D. W. McComb, J. Choo, T. Albrecht, S. A. Maier, and J. B. Edel, "Rapid ultrasensitive single particle surface-enhanced raman spectroscopy using metallic nanopores," *Nano Letters*, vol. 13, no. 10, pp. 4602–4609, 2013.

[28] M. Belkin, S. H. Chao, M. P. Jonsson, C. Dekker, and A. Aksimentiev, "Plasmonic Nanopores for Trapping, Controlling Displacement, and Sequencing of DNA," *ACS Nano*, vol. 9, no. 11, pp. 10598–10611, 2015.

[29] F. Sawafta, A. T. Carlsen, and A. R. Hall, "Membrane thickness dependence of Nanopore formation with a focused helium ion beam," *Sensors*, vol. 14, no. 5, pp. 8150–8161, 2014.

[30] R. Tahvildari, E. Beamish, V. Tabard-Cossa, and M. Godin, "Integrating nanopore sensors within microfluidic channel arrays using controlled breakdown," *Lab Chip*, vol. 15, no. 6, pp. 1407–1411, 2015.

[31] S. Pud, D. Verschueren, N. Vukovic, C. Plesa, M. P. Jonsson, and C. Dekker, "Self-Aligned Plasmonic Nanopores by Optically Controlled Dielectric Breakdown," *Nano Letters*, vol. 15, no. 10, pp. 7112–7117, 2015.

[32] J. Yang, D. C. Ferranti, L. a. Stern, C. a. Sanford, J. Huang, Z. Ren, L.-C. Qin, and A. R. Hall, "Rapid and precise scanning helium ion microscope milling of

solid-state nanopores for biomolecule detection.," *Nanotechnology*, vol. 22, no. 28, p. 285310, 2011.

[33] M. M. Marshall, J. Yang, and A. R. Hall, "Direct and transmission milling of suspended silicon nitride membranes with a focused helium ion beam," *Scanning*, vol. 34, no. 2, pp. 101–106, 2012.

[34] A. R. Hall, "In situ thickness assessment during ion milling of a free-standing membrane using transmission helium ion microscopy," *Microscopy and Microanalysis*, vol. 19, no. 3, pp. 740–744, 2013.

[35] S. Nakaharai, T. Iijima, S. Ogawa, S. Suzuki, S. L. Li, K. Tsukagoshi, S. Sato, and N. Yokoyama, "Conduction tuning of graphene based on defect-induced localization," *ACS Nano*, vol. 7, no. 7, pp. 5694–5700, 2013.

[36] J. Scarpulla, E. Ahlers, D. Eng, D. Leung, S. Olson, and Chan-Shin Wu, "Dielectric breakdown, defects and reliability in SiN MIMCAPs," *1998 GaAs Reliability Workshop. Proceedings (Cat. No.98EX219)*, pp. 92–105, 1998.

[37] V. L. Lo, K. L. Pey, C. H. Tung, and X. Li, "Multiple Digital Breakdowns and Its Consequence on Ultrathin Gate Dielectrics Reliability Prediction," in *IEEE International Electron Devices Meeting*, pp. 497–500, 2007.

[38] P. Roussel, R. Degraeve, B. Kaczer, and G. Groeseneken, "Accurate and Robust Noise-based Trigger Algorithm for Soft Breakdown Detection in Ultra Thin Oxides," in *IIEEE International Reliability Physics Symposium Proceedings. 39th Annual*, pp. 386–392, 2001.

[39] J. Schmilz, H. P. Tuinhout, H. J. Kretschmann, and P. H. Woerlee, "Comparison of soft-breakdown triggers for large-area capacitors under constant voltage stress," *IEEE Transactions on Device and Materials Reliability*, vol. 1, no. 3, pp. 150–157, 2001.

[40] R. Livengood, S. Tan, Y. Greenzweig, J. Notte, and S. McVey, "Subsurface damage from helium ions as a function of dose, beam energy, and dose rate," *Journal of Vacuum Science & Technology B: Microelectronics and Nanometer Structures*, vol. 27, no. 6, p. 3244, 2009.

[41] R. M. M. Smeets, U. F. Keyser, D. Krapf, M.-Y. Wu, H. Nynke, C. Dekker, N. H. Dekker, and C. Dekker, "Salt-dependence of ion transport and DNA translocation through solid-state nanopores," *Nano Letters*, vol. 6, no. 1, pp. 89–95, 2006.

[42] S. W. Kowalczyk, A. Y. Grosberg, Y. Rabin, and C. Dekker, "Modeling the conductance and DNA blockade of solid-state nanopores.," *Nanotechnology*, vol. 22, no. 31, p. 315101, 2011.

[43] V. F. Reutov and A. S. Sokhatskii, "Formation of ordered helium pores in amorphous silicon subjected to low-energy helium ion irradiation," *Technical Physics*, vol. 48, no. 1, pp. 68–72, 2003.

[44] R. Siegele, G. C. Weatherly, H. K. Haugen, D. J. Lockwood, and L. M. Howe, "Helium bubbles in silicon: Structure and optical properties," *Applied Physics Letters*, vol. 66, no. 11, pp. 1319–1321, 1995.

[45] C. C. Griffioen, J. H. Evans, P. C. De Jong, and A. Van Veen, "Helium desorption/permeation from bubbles in silicon: A novel method of void production," *Nuclear Inst. and Methods in Physics Research, B*, vol. 27, no. 3, pp. 417–420, 1987.

[46] M. G. Stanford, B. B. Lewis, V. Iberi, J. D. Fowlkes, S. Tan, R. Livengood, and P. D. Rack, "In Situ Mitigation of Subsurface and Peripheral Focused Ion Beam Damage via Simultaneous Pulsed Laser Heating," *Small*, vol. 12, no. 13, pp. 1779–1787, 2016.

[47] M. A. Nguyen, M. O. Ruault, and F. Fortuna, "Formation and growth of nanocavities and cavities induced by He+ implantation in silicon," *Advances in Natural Sciences: Nanoscience and Nanotechnology*, vol. 3, no. 1, 2012.

[48] V. Raineri, P. G. Fallica, G. Percolla, A. Battaglia, M. Barbagallo, and S. U. Campisano, "Gettering of metals by voids in silicon," *Journal of Applied Physics*, vol. 78, no. 6, pp. 3727–3735, 1995.

[49] J. Ziegler, "Stopping and Range of Ions in Matter (SRIM) Computer Software." http://www.srim.org/, 2013.

[50] S. Tan, K. Klein, D. Shima, R. Livengood, E. Mutunga, and A. Vladár, "Mechanism and applications of helium transmission milling in thin membranes," *Journal of Vacuum Science & Technology B, Nanotechnology and Microelectronics: Materials, Processing, Measurement, and Phenomena*, vol. 32, no. 6, p. 06FA01, 2014.

Chapter 6

DNA Translocations through Nanopores under Nanoscale Preconfinement

Kyle Briggs[1], Gregory Madejski[2], Martin Magill[3], Konstantinos Kastritis[3], Hendrick W. de Haan[3], James L. McGrath[2], and Vincent Tabard-Cossa[1]

1 – Department of Physics, University of Ottawa, Ottawa, Ontario K1N 6N5
2 – Department of Biomedical Engineering, University of Rochester, Rochester, New York 14627
3 – Faculty of Science, University of Ontario Institute of Technology, Oshawa, Ontario L1H 7K4

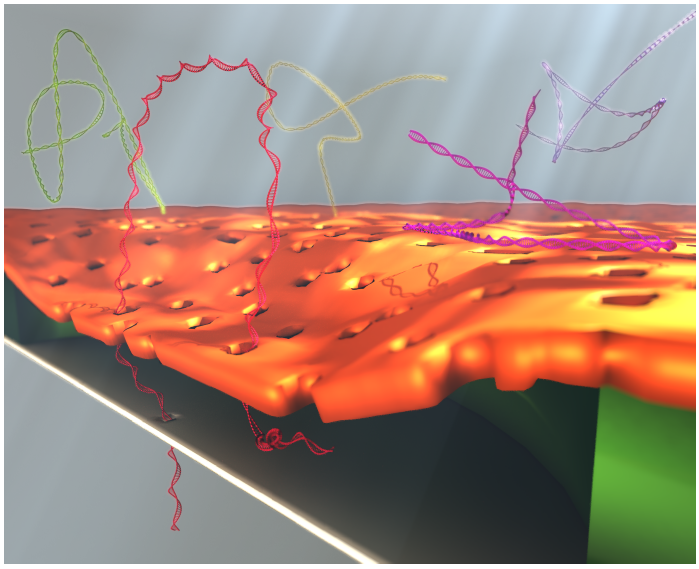

Adapted with permission from [K. Briggs, G. Madejski, M. Magill, K. Kastritis, H. W. de Haan, J. L. McGrath, and V. Tabard-Cossa, "DNA Translocations Through Nanopores Under Nanoscale Preconfinement," *Nano Letters*, vol. 18, no. 2, pp. 660–668, 2017]

Abstract

To reduce unwanted variation in the passage speed of DNA through solid-state nanopores, we demonstrate nanoscale pre-confinement of translocating molecules using an ultra-thin nanoporous silicon nitride membrane separated from a single sensing nanopore by a nanoscale cavity. We present comprehensive experimental and simulation results demonstrating that the presence of an integrated nanofilter within nanoscale distances of the sensing pore eliminates the dependence of molecular passage time distributions on pore size, revealing a global minimum in the coefficient of variation of the passage time. These results provide experimental verification that the inter- and intra-molecular passage time variation depends on the conformational entropy of each molecule prior to translocation. Furthermore, we show that the observed consistently narrower passage time distributions enables a more reliable DNA length separation independent of pore size and stability. We also demonstrate that the composite nanofilter/nanopore devices can be configured to suppress the frequency of folded translocations, ensuring single-file passage of captured DNA molecules. By greatly increasing the rate at which usable data can be collected, these unique attributes will offer significant practical advantages to many solid-state nanopore-based sensing schemes, including sequencing, genomic mapping, and barcoded target detection.

6.1 Introduction

When a single biopolymer such as DNA translocates a nanopore, the dynamics of molecular transport are complex[2–6]. The speed during passage is thought to be dependent on the fraction and conformation of the molecule outside the pore[7], as well as being subject to thermal fluctuations and transient interactions with the pore

walls and membrane materials[8–10]. The net effect is for the molecular motion to be afflicted by a wide distribution of passage speeds, both due to inter- and intra-molecular velocity fluctuations[2]. Such spread in passage times confounds simple translation of time to molecular position, complicating mapping applications, and greatly limits the ability of the nanopore to distinguish charged molecules by size compared to traditional gel-based electrophoresis techniques.

Most experimental efforts aimed at controlling the speed of molecular translocation through a solid-state nanopore have focused on slowing DNA by various means, including interfacing the pore with a gel[11,12]; by judicious choice of electrolyte, both aqueous[13] and ionic-liquid[14]; by laser-modulating the surface charge density[15] by adjustment of the viscosity[16]; or by using different membrane materials[17,18]. While these methods are able to slow DNA translocations to varying degrees, they generally do so at the cost of wider passage time distributions.

Few studies have considered the factors that contribute to the wide distributions of passage times. Experimentally, the choice of salt solution has been shown to have a significant effect on the width of passage time distributions[13], while a pore with diameter matched to the size of DNA limited DNA self-interaction and reduced the variation in passage time.[19]. Barcoded molecules have also been used to explore intra-molecular variation in passage times, revealing speed up toward the end of the translocation[20], and it was found that Brownian motion alone is insufficient to explain the observed variations[21,22]. Simulation work, on the other hand, has demonstrated that polymers are perturbed from equilibrium by the extended electric field gradient during the capture process[23], changing the passage time distribution compared to equilibrium predictions. In addition, molecules which are extended prior to translocation have longer passage times due to increased drag forces[7].

Unfortunately, while the dominant mechanism responsible for high variability in

passage time is thought to be the large conformational entropy available to DNA molecules prior to translocation through the nanopore[24], experimental verification has remained difficult due to the complexity of fabricating devices with sufficiently confining geometries in the vicinity of a nanopore[25–28]. Recent work, employing the confining geometry of nanopipette-based conical nanopores, has provided evidence that polymer entropy prior to translocation is related to mean passage time, but did not consider the standard deviation[29]. In this work, we present the first experimental verification that entropy reduction through pre-confinement of DNA reduces the passage time variation inherent in nanopore transport processes. Confinement is achieved by taking advantage of the extreme flexibility and permeability of ultra-thin (50 nm) nanoporous silicon nitride (NPN) membranes[30,31] to place them within nanoscale distances of a solid-state nanopore sensor while still allowing fluidic contact in an innovative single-molecule biosensor configuration.

6.2 Setup

6.2.1 Experimental

The nanofiltered nanopore device architecture realizes a two-membrane system, comprised of an ultra-thin, nanoporous layer of 50 nm thick NPN membrane, separated by a 200 nm gap from a 20 nm thick silicon nitride (SiN_x) membrane. This essentially creates an architecture comprising two pores in series. NPN is a recently developed highly porous nanomembrane technology with tunable pore sizes (20-80 nm) and porosities $(1 - 40\%)$[30]m where porosity is defined as the ratio of the sum of the open areas formed by pores to the total available membrane area. The gap between the nanofilter and SiN_x membranes is achieved through the lithographic

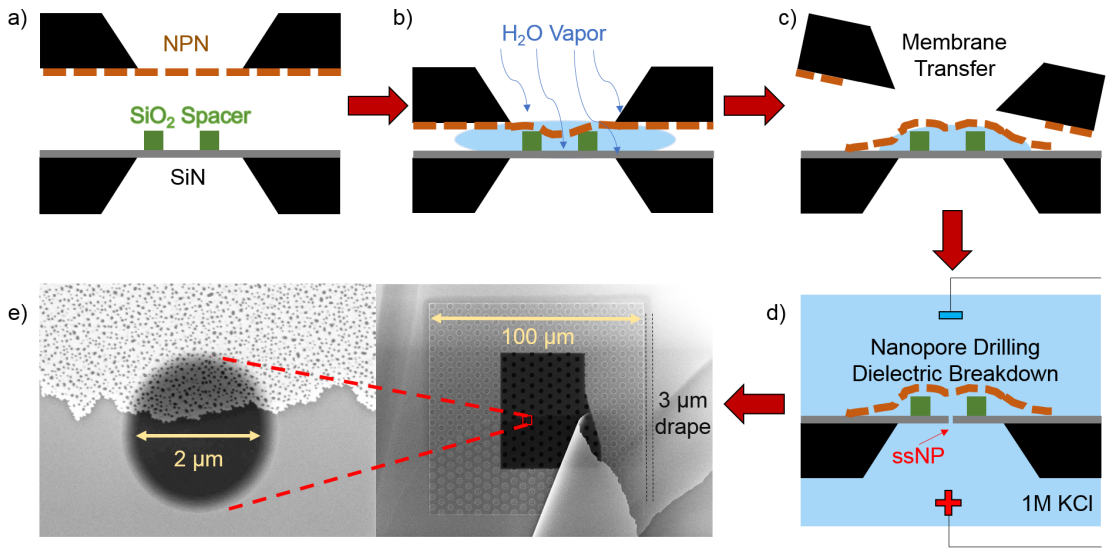

Figure 6.1: a) 50 nm NPN membrane is aligned to a 20 nm SiN_x membrane, patterned with a 200 nm SiO_2 spacer. b) Condensation of water vapor penetrates the NPN membrane, inundates the nanocavity, and draws the NPN membrane to the SiO_2 spacer. c) The NPN membrane is torn away from the carrier chip by surface tension, and remains attached to the SiO_2 spacer and SiN_x surface. d) Nanopore fabrication by controlled breakdown with the nanofilter already in place. e) SEM image of a device after step c. A section of NPN membrane is torn away, revealing the SiO_2 spacer underneath. The pore may be formed in any oxide microwell in the darker central region, which corresponds to the free-standing SiN_x membrane. The device shown in this SEM image has a 2 μm microwell, whereas the devices used in the rest of the paper use 1 μm microwells.

patterning of a hexagonal grid of 1 μm diameter holes in a 200 nm thick SiO_2 layer deposited on top of SiN_x. A backside etch then creates a freestanding SiN_x membrane beneath cylindrical SiO_2 cavities spaced 5 μm apart. The nanofilter is passively held in place directly above these oxide wells, most likely by Van der Waal's forces. A schematic and electron microscopy images of the device assembly process are shown in Figure 6.1.

SEM and TEM imaging of sample sections of nanoporous nitride (NPN) material from the wafer used for this project reveal that not all of the visible features are

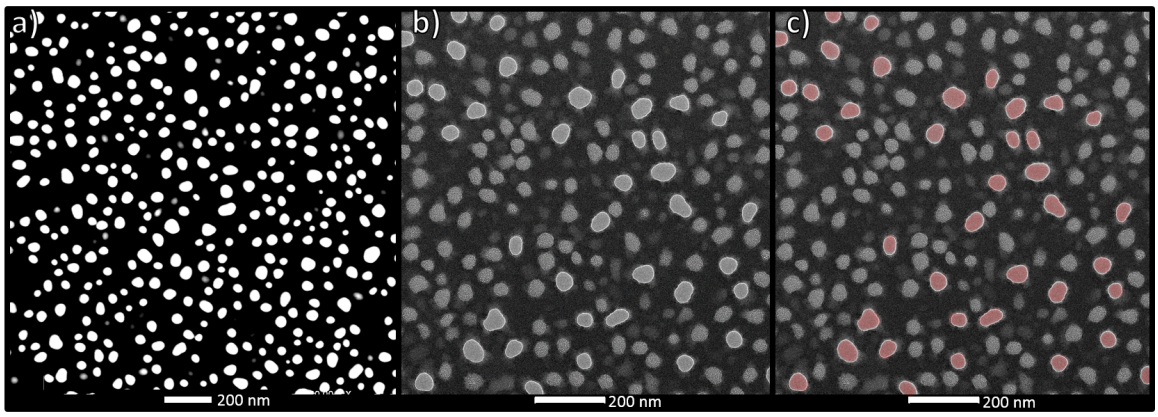

Figure 6.2: a) STEM micrograph of NPN with high contrast, showing an apparent 20% porosity. b) Closer and lower contrast view of a TEM image of 5% porous NPN, showing partially opened nanopores. c) The same image as b), with false color. Only nanopores highlighted in red contribute to the porosity of the wafer.

through-holes (Figure 6.2). While porosity is calculated to be as high as 20% if all features are taken into account (Figure 6.2a), TEM imaging of the pores reveals a porosity of 5% for this particular batch of NPN when considering only through-holes (Figure 6.2b-c).

The method by which the nanofilter is transferred to the device is illustrated schematically in Figure 6.1. Transferring the nanofilter structure using water vapor is a dynamic process, as the nanofilter rips and sticks to a target substrate. Applied here, this method provides a simple and effective way to fabricate a nanocavity while still allowing fluidic access to the interior space. Conformal contact is achieved due to the inherent flexibility of such a thin material, since the bending resistance for membranes scales with the third power of membrane thickness. Despite this flexibility, once the nanofilter is wetted and in close contact with the substrate, it is very resistant to meniscus stresses, surviving fluid shear stress from wetting and rewetting. However, if the membrane is not in close contact, the membrane can be torn apart on a meniscus of liquid.

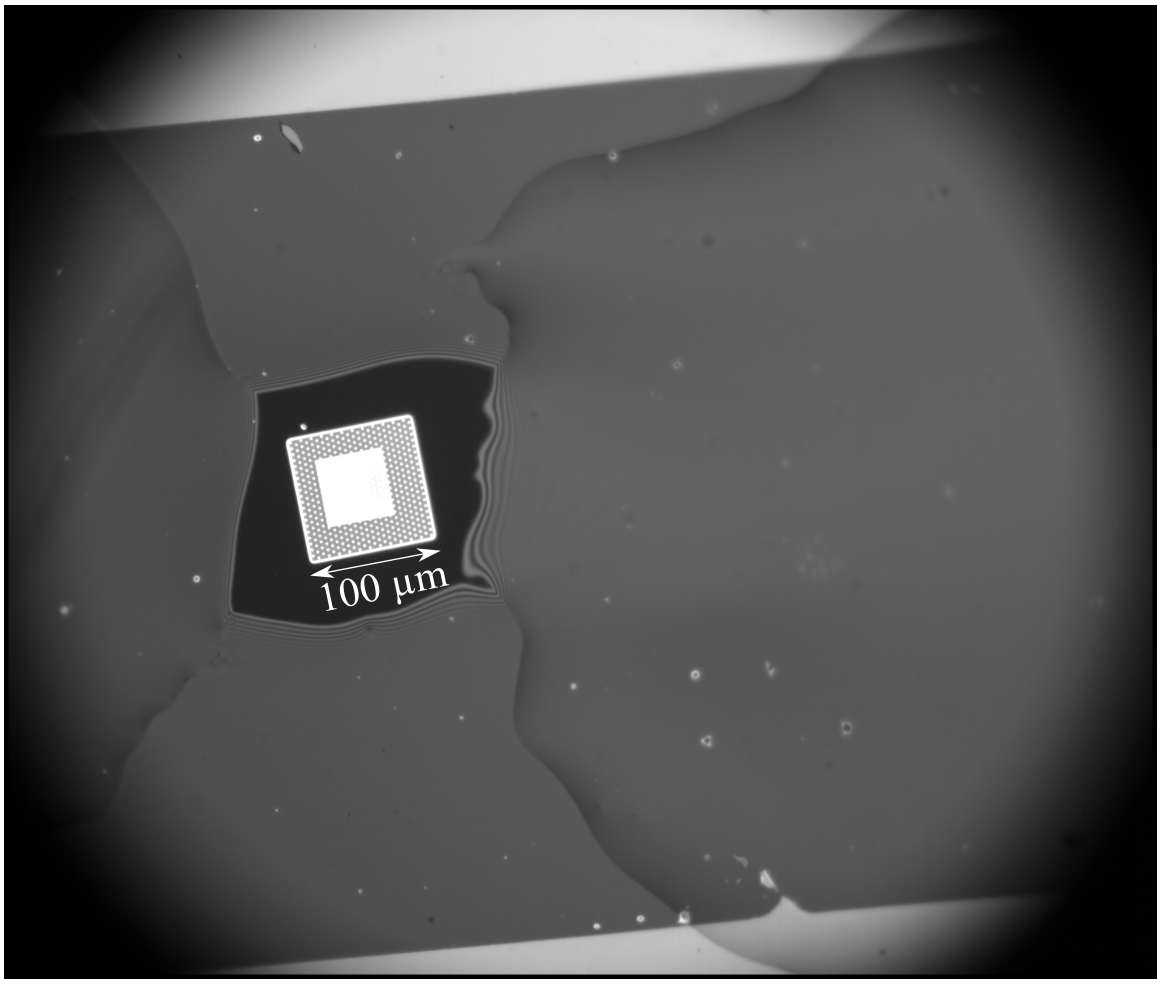

Figure 6.3: PDMS is painted over the nanofilter. The central white square is the free-standing silicon nitride membrane which will contain the sensing pore. The larger concentric square is the silicon dioxide spacer, containing a hexagonal grid of 1 μm microwells. The irregular black area defines the area, which is not covered by PDMS. The large dark grey rectangle comprising most of the figure is the nanofilter membrane.

If the nanofilter is unevenly wetted, wrinkles can form and the gap between the nanofilter and the sensing pore can vary. In order to avoid this defect, and to ensure that dsDNA cannot shunt the nanofilter by going around the edges, we seal the nanofilter in place by painting PDMS by hand around the silicon nitride membrane of the single sensing pore, an example of which is shown in Figure 6.3.

Even though only a single sensing pore is fabricated and consequently only a single microwell is active in each device, multiple microwells are necessary for several reasons. As discussed above, NPN is an extremely flexible material, able to mould itself around microscopic contours. Using 1 μm diameter microwells ensures that the maximal bending displacement of the nanofilter within a given microwell is insufficient to contact the sensing membrane, maintaining the cavity. Second, the CBD technique is sensitive to exposed area, taking a longer time to fabricate pores on small membrane areas[32]. Using a large number of microwells ensures a sufficiently large active membrane area that nanopore fabrication is limited to a few minutes. Finally, the use of multiple microwells ensures that at least one will be wetted easily, though in practice wetting is near 100%.

The electrical resistance of the nanofilter can be calculated simply by assuming each pore is a parallel resistor using Equation 3 from Kowalczyk *et al.*[13], giving approximately 10^2 kΩ per oxide microwell. During CBD fabrication, the current through the entire system is on the order of $10^1 - 10^2$ nA. Assuming that current is divided evenly among the microwells, this results in an electrical current per microwell on the order of $10^{-1} - 10^0$ nA, and a corresponding voltage drop across the nanofilter of only $10^0 - 10^1$ mV, far too little to have any effect on the nanofilter pore size distribution. After pore fabrication, the nanofilter remains electrically invisible. A typical sensing pore used in this study is between $3-14$ nm in diameter, corresponding to a resistance in 3.6 M LiCl of $10^1 - 10^2$ MΩ. With a voltage bias of $\Delta V = 200$ mV applied across the entire system, the voltage drop across the nanofilter is $10^{-3} - 10^{-2}\Delta V$, and has negligible effect on the electrical response of the single sensing pore. The sensing pore can even be conditioned at moderate to high voltages to increase its size or tune noise characteristics[33] without impacting the pore size distribution of the nanofilter.

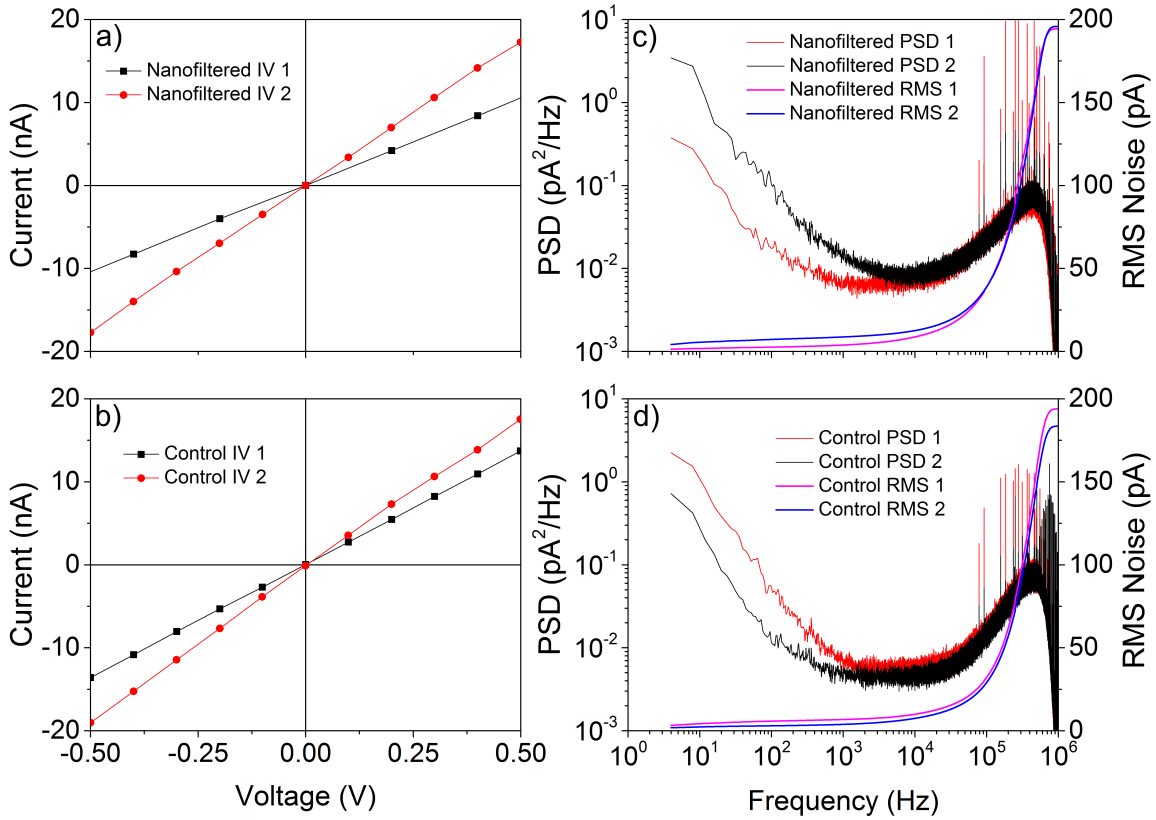

Figure 6.4: a,b) I-V response of nanofiltered (a) and control (b) pores, showing linear behavior in both cases. c,d) power spectral densities and RMS noise profiles in nanofiltered (c) and control (d) pores. PSDs are digitally low-pass Bessel filtered at 900 kHz. The high-frequency spikes (92.5 kHz + harmonics) were later identified to be due to a malfunctioning graphics card, but their contribution to the total RMS current noise is marginal and thus does not interfere with sensing.

Typical I-V responses and PSDs for pores with and without the nanofilter are shown in Figure 6.4, demonstrating that the nanofilter has an insignificant effect on the electrical properties of the sensing pore. The root-mean-square (RMS) noise at 900 kHz bandwidth ranges from $140-220$ pA. Double-stranded DNA (dsDNA) molecules of lengths varying from 100 bp to 4000 bp are introduced to the cis (nanofilter) side of the system and are driven through the system by a voltage bias of 200 mV in 3.6M LiCl pH 8 unless otherwise noted. Because the resistance of the sensing pore dominates that of the nanofilter, the current blockage that is sensed is due entirely to

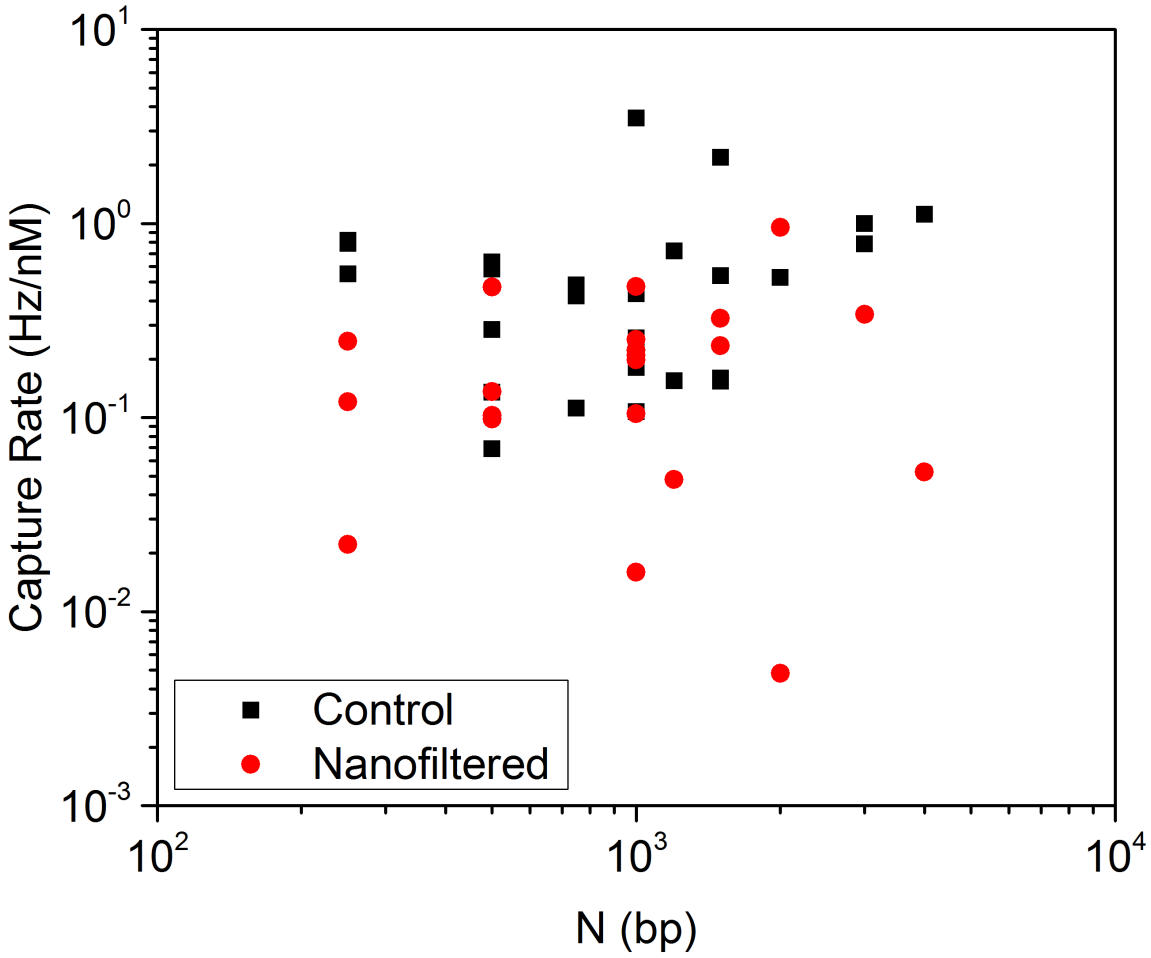

Figure 6.5: Normalized capture rates for all experiments conducted in both control (black squares) and nanofiltered (red circles) pores.

the interaction between dsDNA molecules and the sensing pore, while the nanofilter remains electrically invisible. Interestingly, the capture rate of nanofiltered devices is comparable to the capture rate of control devices in most cases, as shown in Figure 6.5. While it is to be expected that very long polymers might have reduced capture rates due to high entropic cost of passage through the nanofilter, this was not observed for the lengths of DNA studied here, though it is unclear why at this stage.

6.2.2 Simulation

Simulations were also conducted to better understand the behavior of nanofiltered pores. A standard coarse-grained polymer model was used to model the DNA chains[34]. The driving electric field was solved numerically between the nanofilter and the sensing pore, and approximated analytically elsewhere. Only a single pore in the nanofilter was explicitly represented in simulations, placed 150 nm off-axis from the sensing pore, which was located in the center of the microwell. Coarse-grained Langevin dynamics (LD) simulations were used to explore the physical mechanisms underlying the behavior witnessed in experiment. The ESPResSo molecular dynamics software package was used for this purpose[35]. The DNA molecules were modelled as linear polymers composed of N identical spherical monomers. Adjacent monomers along the chain were joined using the finitely-extensible nonlinear elastic (FENE) potential,

$$U_{FENE}(r) = -\frac{k_{FENE}}{2} r_{max}^2 \ln\left(1 - \frac{r^2}{r_{max}^2}\right), \tag{6.1}$$

where k_{FENE} and r_{max} are constants representing the stiffness of the bond and the maximum possible extension of the bond, respectively, and r is the center-to-center distance between the monomers[34]. Excluded volume interactions between monomers were modelled using the Weeks-Chandler-Andersen (WCA) potential, given by

$$U_{WCA}(r) = \begin{cases} 4\varepsilon\left[\left(\frac{\sigma}{r}\right)^{12} - \left(\frac{\sigma}{r}\right)^{6}\right] + \varepsilon & r \leq 2^{\frac{1}{6}}\sigma \\ 0 & r > 2^{\frac{1}{6}}\sigma \end{cases}, \tag{6.2}$$

where ε and σ are the energy and length scales of the interaction, respectively[34]. The first term is an approximation to a hard-sphere repulsion which has smooth derivatives for the sake of numerical stability, while the second term represents short-

ranged attractive interactions such as Van der Waals. By choosing the indicated cutoff, we are modelling only the repulsive part of the potential, and ignoring any short-range attraction between monomers. The FENE parameters were chosen in terms of the WCA parameters to be

$$k_{FENE} = 30\frac{\varepsilon}{\sigma^2}, \qquad r_{max} = 1.5\sigma, \tag{6.3}$$

in line with the seminal work by Kremer and Grest that demonstrated the robust numerical stability of this configuration[36]. The energy scale of the WCA potential was set equal to $\varepsilon = k_B T$, the thermal energy of the system set in the LD thermostat. All other energies were normalized to this value, and as such $k_B T$ was set to a numerical value of 1.0. With these choices of parameters, the average equilibrium bond length between adjacent monomers was roughly $b = 0.97\sigma$, so σ will be considered the effective monomer size. The friction coefficient γ of the LD thermostat was also set to 1.0 (except during equilibration, as discussed below).

In addition to the FENE and WCA pairwise interactions, a three-body angular potential was used to model polymer stiffness. This potential was chosen simply to be harmonic in the angle θ formed by any three consecutive monomers along the chain:

$$U_{angle}(\theta) = \left(\frac{k_{angle}}{2}\right)\theta^2. \tag{6.4}$$

Using this angular potential and the FENE and WCA potentials as specified above, the persistence length L_p of the simulated polymer satisfies

$$L_p \approx k_{angle}. \tag{6.5}$$

The remaining free parameters of the potentials were chosen to establish a cor-

respondence between the polymer in simulation and the DNA chains in experiment. The steric width of DNA is roughly 2.4 nm[37], but its effective width can be somewhat larger than this[37–40], depending on electrolytic conditions. For this reason, and for computational tractability, $\sigma = 5$ nm was chosen. The remaining length scales of the system were derived from this choice, so σ was set to a numerical value of 1. In particular, the persistence length of DNA is roughly 30 nm under relevant conditions[38,39], and so the simulated polymer should satisfy $L_p = 6\sigma$. Using Equation 6.5, this was implemented by setting the numerical value of $k_{angle} = 6.0$.

The geometry of the system was implemented in ESPResSo using pore constraint objects. These are planar boundaries of finite thickness through which a cylinder is removed. The same WCA interaction used to represent excluded volume interactions between monomers was defined between the monomers and these boundaries. For monomer-constraint interactions, the distance r was computed from the center of the monomer to the nearest point on the boundary. When the center of the monomer is a distance σ from the boundary, its interaction energy is equal to k_BT. This distance from the boundary determines the effective dimensions of the pore. The effective dimensions are mapped to the measured experimental lengths of the device using $\sigma = 5$ nm.

One pore constraint was used to define the sensing pore, which was given effective dimensions of $d_{eff} = 2.6\sigma$ and $t_{eff} = 4\sigma$, where d_{eff} is the effective radius of the pore and t_{eff} is its effective length. These parameters correspond to a sensing pore that is 13 nm in diameter and 20 nm in length. The sensing pore was placed in the center of the microwell. Although this was not necessarily the case in experiment, it was considered a natural first approximation.

By default, the pore constraints in ESPResSo only contain a single pore in each plane. As such, only a single pore of the nanofilter was represented, with $d_{eff} = 2.6\sigma$

and $t_{eff} = 10\sigma$. The postulated events wherein a single chain threads through two pores in the nanofilter simultaneously cannot be represented in these simulations. Future work will utilize modified pore constraints capable of capturing this phenomenon. Note that d_{eff} for the pore in the nanofilter was set to $2.6\sigma = 13$ nm, which is much smaller than the pore sizes seen in experiment. This choice was used to enforce single-file passage of the polymer through the nanofilter. In closer agreement with experimental values, the electric field in the pore of the nanofilter was set according to the correct filter porosity, and the field above the nanofilter pore was set as if the pore had a radius of $5.0\sigma = 25$ nm, in closer agreement with experimental values. The location of the pore in the nanofilter was set to 30σ off-axis from the sensing pore. Finally, the walls of the microwell were also represented by a pore constraint, with $d_{eff} = 200\sigma$ and $t_{eff} = 40\sigma$.

The final component of the simulation model is the electric field. In the experiments, a voltage drop of 200 mV was fixed from far above the nanofilter to far below the sensing pore. For the simulations, the electric field was solved in a piecewise fashion. Analytic forms were used on the cis side of the nanofilter and inside the pore in the nanofilter. In the gap between the two membranes, the field was solved numerically. The field on the trans side of the sensing pore was neglected. The numerical solution to the field inside the device was obtained using a second-order finite difference method to find the electric potential. The electric potential was assumed to satisfy Laplace's equation. The system was represented in cylindrical coordinates, with the $\rho = 0$ axis placed in the middle of the sensing pore and parallel to its axis. Homogeneous Neumann boundary conditions were applied orthogonal to the effective dimensions of the pore constraints inside the sensing pore, on the surface of the sensing pore membrane, and at the walls of the inter-membrane gap. These represent insulating boundaries. The trans opening of the sensing pore was modelled as

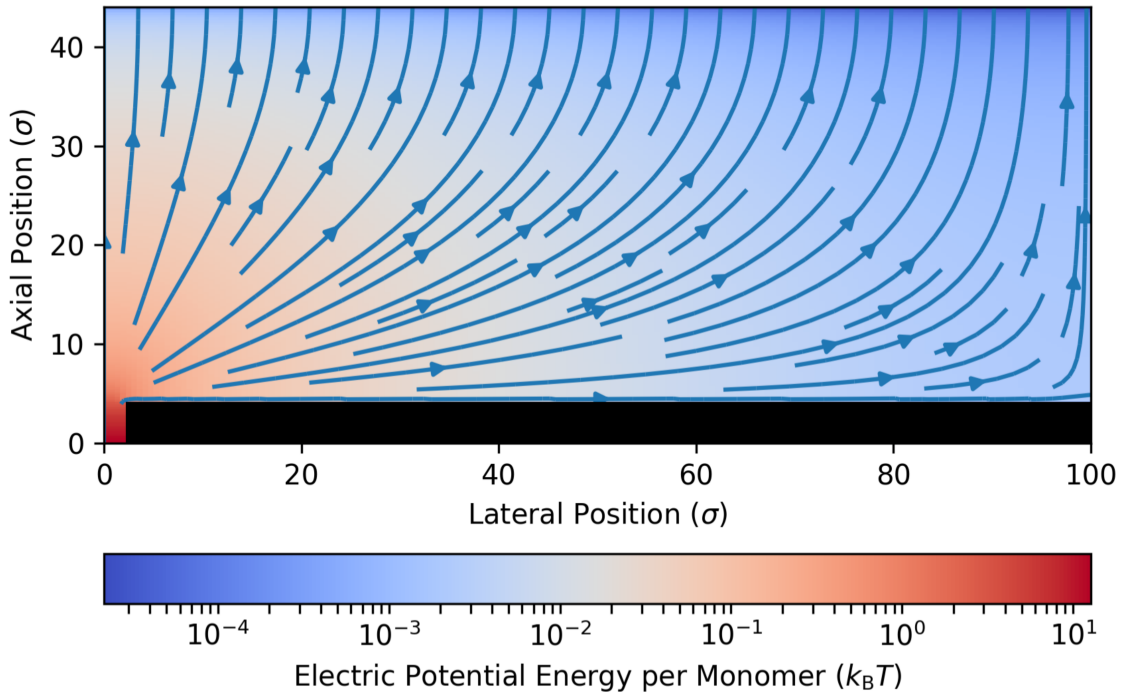

Figure 6.6: Numerical solution for the electric potential between the two membranes. The bottom of the nanofilter corresponds with the top of the figure. The electric potential is expressed in simulations in terms of the electric potential energy of a monomer at a given position in the system.

a Dirichlet boundary condition, representing a surface of constant electric potential. This is a good approximation, since the electric field must be approximately axial inside the sensing pore. Finally, the inner boundary of the nanofilter was approximated by a Dirichlet boundary condition. This approximation was made in light of the low electrical resistivity presented by the nanofilter in comparison to the sensing pore, and since the exact locations of the pores in the nanofilter in the membrane vary from device to device.

As a result of these choices for boundary conditions, the system for the electric potential is cylindrically symmetric. Laplace's equation was solved in (ρ, z) without angular dependence. The solver was implemented in C using LAPACK[41]. The solu-

tion for the electric potential energy per monomer is shown in Figure 6.6, expressed in units of k_BT.

The numerical field was only defined up to the inner boundary of the nanofilter. Inside the pore in the nanofilter the electric field was modelled as purely axial. The magnitude of this electric field was chosen by conservation of electric flux, as follows. The total axial electric flux of the system passes through the sensing pore, and the field is essentially axial therein. If the flux through the sensing pore and a given pore in the nanofilter are Φ_{sp} and Φ_{fp}, respectively, and there are N_{fp} pores in the active portion of the nanofilter, then the relation

$$N_{fp}\Phi_{fp} = \Phi_{sp} \tag{6.6}$$

must hold. Since the field is purely axial in the pores, this is equivalent to

$$N_{fp}E_{fp}\pi r_{fp}^2 = E_{sp}\pi r_{sp}^2. \tag{6.7}$$

Solving this for E_{fp} yields

$$E_{fp} = \left(\frac{1}{\phi}\right)\left(\frac{r_{sp}}{r_{fp}}\right)^2 E_{sp}. \tag{6.8}$$

The number of pores in the nanofilter was obtained from the porosity ϕ to be

$$N_{fp} = \left(\pi R_{gap}^2\right)\frac{\phi}{\pi r_{fp}^2}, \tag{6.9}$$

so that the field in the nanofilter pores can be expressed as

$$E_{fp} = \left(\frac{1}{\phi}\right)\left(\frac{r_{sp}}{R_{gap}}\right)^2 E_{sp}. \tag{6.10}$$

Above the nanofilter, the electric field was modelled by the sum of two terms. Near each pore in the nanofilter, the field should be well-represented by the analytic solution

$$E_{analytic} = \hat{\mu}\frac{V_0}{\pi r_{pore}\cosh(\mu)\sqrt{\sinh^2(\mu)+\sin^2(\nu)}}, \tag{6.11}$$

obtained in oblate spheroid coordinates for a single nanopore[42], with $r_{pore} = 5.0\sigma$. Farther above the nanofilter, the fields from all nanofilter pores will cancel all but their axial components, so the field should converge to an axial profile. The field above the nanofilter was therefore modelled as

$$E_{cis} = E_{analytic} + E_{par}, \tag{6.12}$$

where E_{par} represents the (axial) field a distance comparable to R_{gap} above the nanofilter, and $E_{analytic}$ is of the form given above. The magnitude of E_{par} was chosen to be

$$E_{par} = \phi E_{fp} = \left(\frac{r_{sp}}{R_{gap}}\right)^2 E_{sp}, \tag{6.13}$$

which is the field magnitude obtained if the electric flux passing through the sensing pore is redistributed into a cylinder of radius R_{gap}. This is an approximation to the field profile that would be present at the nanofilter location if the nanofilter were not present. The magnitude of V_0 for $E_{analytic}$ was chosen such that E_{cis} is equal to E_{fp} at the cis side of the nanofilter membrane.

The preceding paragraphs have established the shape of the electric field profile for the system. However, its absolute magnitude remains unspecified. This was chosen by increasing the field magnitude until the distributions of folded events seen in simulations were comparable to those in experiments. The total voltage drop across the simulation system was set to $12.7\frac{k_BT}{q}$, where q is the monomer charge. This

was approximately 40% stronger than the weakest field strength that enabled folded events to occur at all.

The units of simulation time were mapped to units of experimental time by equating the respective drift velocities. The experimental drift velocity was taken to be

$$v_{exp} = \mu \left(\frac{V_{exp}}{L_{exp}} \right) \left[\frac{m}{s} \right], \tag{6.14}$$

where the units of meters and seconds are shown explicitly, where[43] $\mu = 0.6 \times 10^{-8}$ $\mathrm{m^2V^{-1}s^{-1}}$, $V_{exp} = 200$ mV, and L_{exp} is a characteristic length scale. Similarly, in simulation the drift velocity is

$$v_{sim} = \left(\frac{1}{\gamma} \right) \left(\frac{V_{sim}}{L_{sim}} \right) \left[\frac{\sigma}{\tau} \right], \tag{6.15}$$

where σ is the monomer size, τ is the simulation time unit, and the remaining quantities are expressed in terms of simulation units. Here γ is the friction coefficient, V_{sim} is the voltage drop across the system, and L_{sim} is the same characteristic length scale as L_{exp}. Equating v_{sim} to v_{exp} and solving for τ yields

$$\tau = \left(\frac{1}{\mu\gamma} \right) \left(\frac{V_{sim}}{V_{exp}} \right) \left(\frac{L_{exp}}{L_{sim}} \right) \left[\frac{\sigma}{m} \right] [s], \tag{6.16}$$

where L_{exp} and L_{sim} are the same characteristic length expressed in SI units and simulation units, respectively. Choosing this length to be equal to $\sigma = 5$ nm yields $\tau = 265$ ns.

The simulations themselves were conducted as follows. The initialization modelled the polymers as being at equilibrium when they were captured by the nanofilter, and imposed that chains must thread through the nanofilter in single file. The first 5% of monomers in a chain (rounded up to the nearest monomer) were fixed in a straight line

through the pore in the nanofilter while the rest of the chain was evolved under the LD equations with the friction coefficient γ reduced to 0.1 from the value of 1.0 used in the main simulations. After an equilibration period of $100N\tau$, the fixed monomers were released and γ was returned to 1.0. Next, the polymer was allowed to evolve under the influence of the LD equations. If the polymer retracted entirely to the cis region above the nanofilter, the event was considered a failed threading attempt and the polymer was reset. Each simulation was terminated when the entire polymer was located in the trans region of the sensing pore. The entire process was repeated until 1000 successful translocations were recorded for several chain lengths N.

To study the influence of polymer dynamics between the nanofilter and the sensing pore, simulations were performed wherein the chain was initialized with its first monomer fixed in the sensing pore. Equilibration proceeded as in the main simulations, and events that retracted from the sensing pore were reset.

6.3 Results and Discussion

6.3.1 DNA Translocation Kinetics

Following Mihovilovic *et al.*[44], we define type 1 events to be single-file passage of dsDNA, type 21 events to be partially folded events in which the event begins in the folded state. More complex event shapes are indicated by longer strings of integers, which correspond to integer multiples of the single-file dsDNA blockage in the order in which they appear. Events containing levels which do not correspond to an integer multiple of the level 1 blockage are labelled anomalous and are excluded from subsequent analysis. These comprise less than 5% of events overall, and are typically attributed to interactions of DNA with the access regions of nanopores[45], or to fitting

artefacts. A full list of DNA event counts and relavant details of pore geometry are shown in Tables 6.1 and 6.2. The pore size is corrected for local deviations from a cylindrical pore shape following the method used in previous work[46]. Briefly, the effective membrane thickness L_{eff} and pore diameter d are calculated from the conductance blockage ΔG of dsDNA assuming $d_{DNA} = 2.2$ nm, using

$$L_{eff} = \sigma \frac{\pi d_{DNA}^2}{4\Delta G}, \qquad d = \frac{G}{2\sigma}\left(1 + \sqrt{1 + \frac{16\sigma L_{eff}}{\pi G}}\right), \tag{6.17}$$

where σ is the solution conductivity and G is the open-pore conductance.

Table 6.1: Event counts for every nanofiltered pore that contributed data to the paper. Run time varied between experiments, so total event numbers do not necessarily reflect differences in capture rate. For a given device, the order in which DNA lengths were studied corresponds to the order of increasing pore size. Where "mix" is indicated for the DNA length, it refers to a mixture of all other sizes used with that same pore. Note that K478 used a different nanofilter membrane with higher porosity and smaller average pore size and consequently required higher voltage to translocate dsDNA. It was therefore not included in the following passage time analysis.

Pore	Length (bp)	Events	Type 1	L_{eff} (nm)	d_i (nm)	d_f (nm)
K417	250	24164	21162	12.8	7.0	7.1
	1000	6084	3392	12.6	7.2	7.2
K423	1000	3802	3587	15.2	7.0	7.5
	2000	160	158	16.8	9.1	9.1
K434	100	9483	9483	12.1	8.5	9.0
	250	3760	3594	10.6	4.7	4.8
	500	10362	8603	11.4	5.5	5.6
	1000	23691	12780	12.7	6.7	6.7
	2000	25686	12675	13.0	7.3	7.3
	3000	16040	6265	13.0	8.0	8.1
K435	100	754	754	8.4	4.1	4.2
	250	15781	1529	8.9	4.5	4.5
	500	6668	6323	8.7	4.3	4.3
	1000	15214	13143	8.9	4.6	4.6
K439	750	3885	3169	15.5	7.6	8.0
	1200	6550	2786	17.2	9.4	9.9
	4000	1181	315	17.4	9.9	10.7
K454	1000	5565	3003	12.6	6.1	7.3
K462	500	6294	5011	9.5	5.2	5.7
	1000	3933	2645	10.1	6.4	6.8
	1500	2385	1231	11.7	8.3	8.7
	Mix	38029	20363	12.3	9.3	9.5
K465	500	13748	9219	13.1	10.1	10.4
	1000	5802	2880	12.8	9.4	9.6
	1500	4932	2010	11.9	7.7	8.5
	Mix	13409	8261	12.3	6.1	6.9
K478	2000	890	740	11.8	5.4	5.6

Table 6.2: Event counts for every control pore that contributed data to the paper. Run time varied between experiments, so total event numbers do not necessarily reflect differences in capture rate. For a given device, the order in which DNA lengths were studied corresponds to the order of increasing pore size. Where "mix" is indicated for the DNA length, it refers to a mixture of all other sizes used with that same pore.

Pore	Length (bp)	Events	Type 1	L_{eff} (nm)	d_i (nm)	d_f (nm)
K443	1500	3170	1842	11.4	7.0	7.1
K444	250	38256	32851	13.7	12.4	12.6
	500	35358	24531	11.9	9.2	9.6
	1000	4801	2411	11.4	7.5	8.0
	2000	18497	6406	12.2	10.4	10.6
K445	250	308149	256688	11.5	11.7	11.7
	500	141302	91819	11.5	11.4	11.4
	750	8242	6352	9.2	5.4	5.6
	1000	26728	13044	11.7	11.1	11.2
	1200	4403	2540	10.4	7.1	7.5
	1500	12636	5038	11.0	8.7	8.7
	3000	13776	3979	10.9	8.9	9.0
K446	100	3836	3836	6.0	3.2	3.2
	500	18729	14950	9.0	5.8	6.3
	750	41215	22670	9.9	8.5	8.6
	1200	31582	13869	9.6	8.9	9.1
	3000	15776	4464	9.8	9.6	9.7
K446	100	14876	14876	8.2	8.4	8.6
	250	222942	152133	8.9	7.7	8.1
	750	30397	15026	8.7	7.1	7.3
	1000	19487	8186	8.4	6.2	6.6
	4000	27062	7075	8.9	9.5	9.6
K466	500	14847	10387	9.4	7.0	7.1
	1000	4861	2962	10.3	6.3	6.6
	1500	3745	15026	9.5	4.9	5.2
	Mix	5237	4693	8.9	9.5	9.6
K467	500	6599	5127	8.5	4.9	4.9
	1000	2817	2006	8.4	4.9	4.9
	1500	5733	3341	8.3	4.9	4.9
	Mix	37417	23643	8.3	4.9	5.1

6.3.2 DNA Passage Time Analysis

We first consider the kinetics of passage of molecules which pass the sensing pore in an unfolded type 1 configuration. The distribution of unfolded passage times t is well characterized by a log-normal distribution, having the form

$$p\left(\ln\left(t\right)\right) = A\exp\left(-\frac{\left(\ln\left(t\right)-M\right)^2}{2s^2}\right), \tag{6.18}$$

where A, M, and s are variable parameters for the non-linear fit. This form is purely for mathematical convenience rather than being physically motivated. Other groups have used a simple first-passage time distribution model which produces good fits[19] but which was originally intended for use with featureless nanoparticles. More complex models exist which take into account the polymer nature of the analyte as well as pore-analyte interactions[47], but these depend on parameters which are unavailable experimentally. Here, we use a simple form, which allows us to easily extract metrics of interest. In cases where long polymers lead to an extended tail of events which thread through two different nanofilter pores, only the log-normal part of the passage time distribution, representing unhindered translocations, is considered when calculating mean and standard deviation passage times. Only single-file, unfolded events are used for passage time distribution fitting.

The mean τ and standard deviation σ of the passage times are related to the fit parameters M and s by

$$\tau = \exp\left(M+\frac{1}{2}s^2\right), \qquad \sigma = \tau\sqrt{\exp\left(s^2\right)-1}. \tag{6.19}$$

The coefficient of variation is then

$$\frac{\sigma}{\tau} = \sqrt{\exp\left(s^2\right)-1}. \tag{6.20}$$

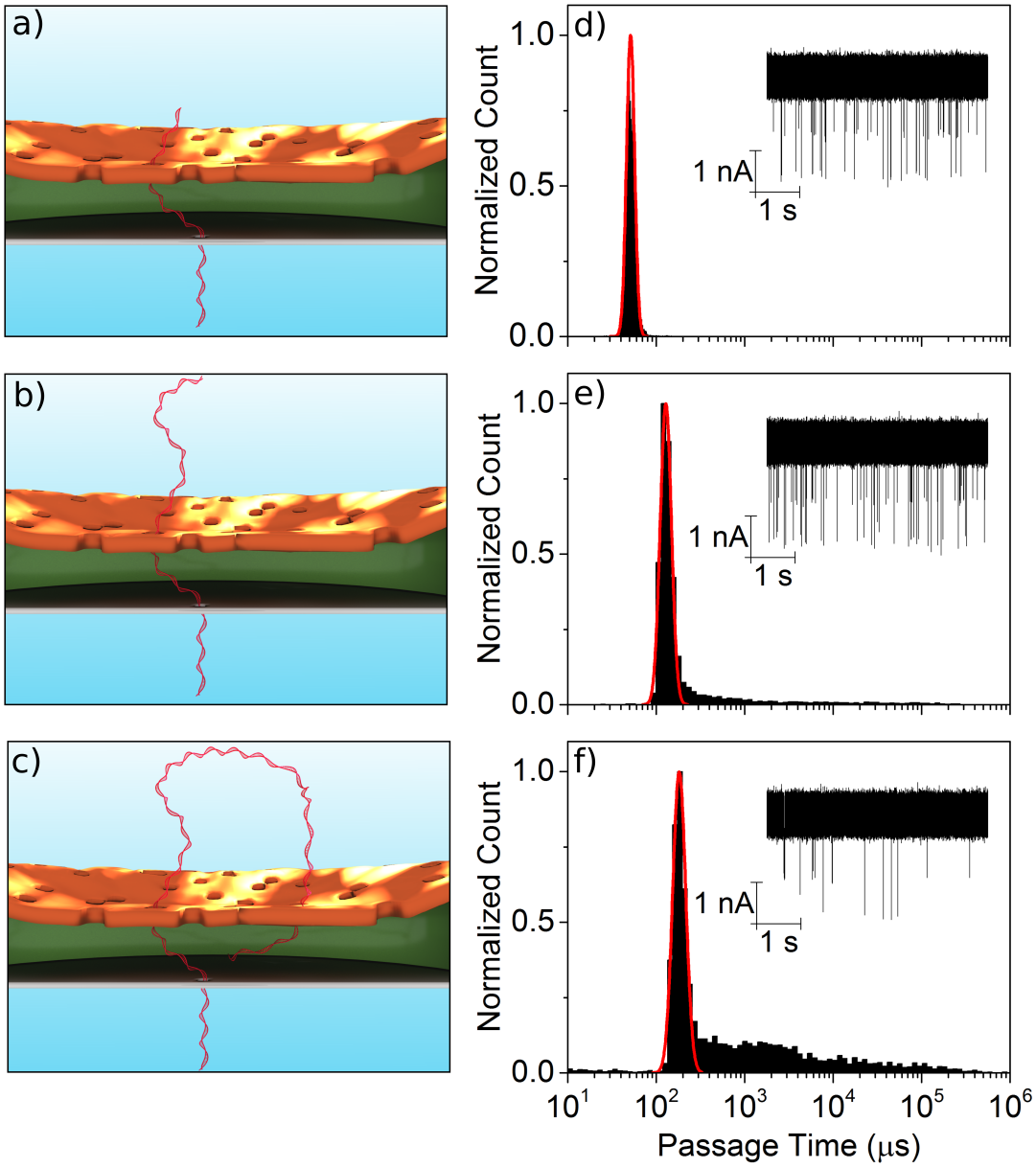

Figure 6.7: a, b, c) Schematic representations of 1000, 2000, and 3000 bp dsDNA traversing the nanofiltered pore device, respectively. Vertical distance and DNA length is to scale. d, e, f) Passage time histograms of unfolded type 1 events for the corresponding lengths of dsDNA. All three histograms are obtained using the same pore, while the pore grew during the course of the experiment (4.3h), from top to bottom, from 6.7 nm, to 7.3 nm, and finally to 8.0 nm, respectively. Insets: time series of dsDNA translocations (including folded events) for the corresponding histogram. Data recorded at 4.166 MHz sampling rate, digitally filtered with a low-pass Bessel filter at 900 kHz, and down-sampled to 2.5 MHz for plotting.

Figures 6.7a-6.7c show schematic representations of possible conformations of ds-DNA prior to translocation through the sensing pore. As can be seen in Figure 6.7d, when $N \leq 1300$ bp, there is a single population of passage times for single-file passage which is well characterized by a log-normal distribution. For $N \geq 1300$ bp (Figures 6.7e and 6.7f), a one-sided tail appears in addition to the log-normal component, comprising events with very long passage times. We attribute the log-normal portion of the passage time distributions to unhindered passage through the two serial membranes.

Figure 6.8 shows properties of unhindered dsDNA passage time distributions as a function of the number of base pairs N, representing fits to data extracted from a total of 1.3 million individual DNA translocations through 8 nanofiltered pores and 7 control pores.

The mean passage time τ for nanofiltered pores is fitted well by a single power law,

$$\tau(N) = \tau_0 N^p, \tag{6.21}$$

which yields an exponent of $p_{exp} = 1.19 \pm 0.06$, as shown in Figure 6.8a. This exponent is in reasonable agreement with previous studies on regular solid-state nanopores[44,48]. Error bars define the 95% confidence interval for the fit parameters. Control devices without the nanofilter (Figure 6.8b) behave similarly, but with slightly larger spread in mean passage times. Simulations (Figure 6.8c) also show power law scaling, though the exponent, $p_{sim} = 1.61 \pm 0.02$, is larger than in the experimental case. This is consistent with previous work, since simulations typically find scaling exponents which are larger than those extracted from experiments[49,50].

The effect of the nanofilter becomes more apparent when considering the standard deviation σ of the passage time (Figures 6.8d-6.8f), where the nanofilter usually

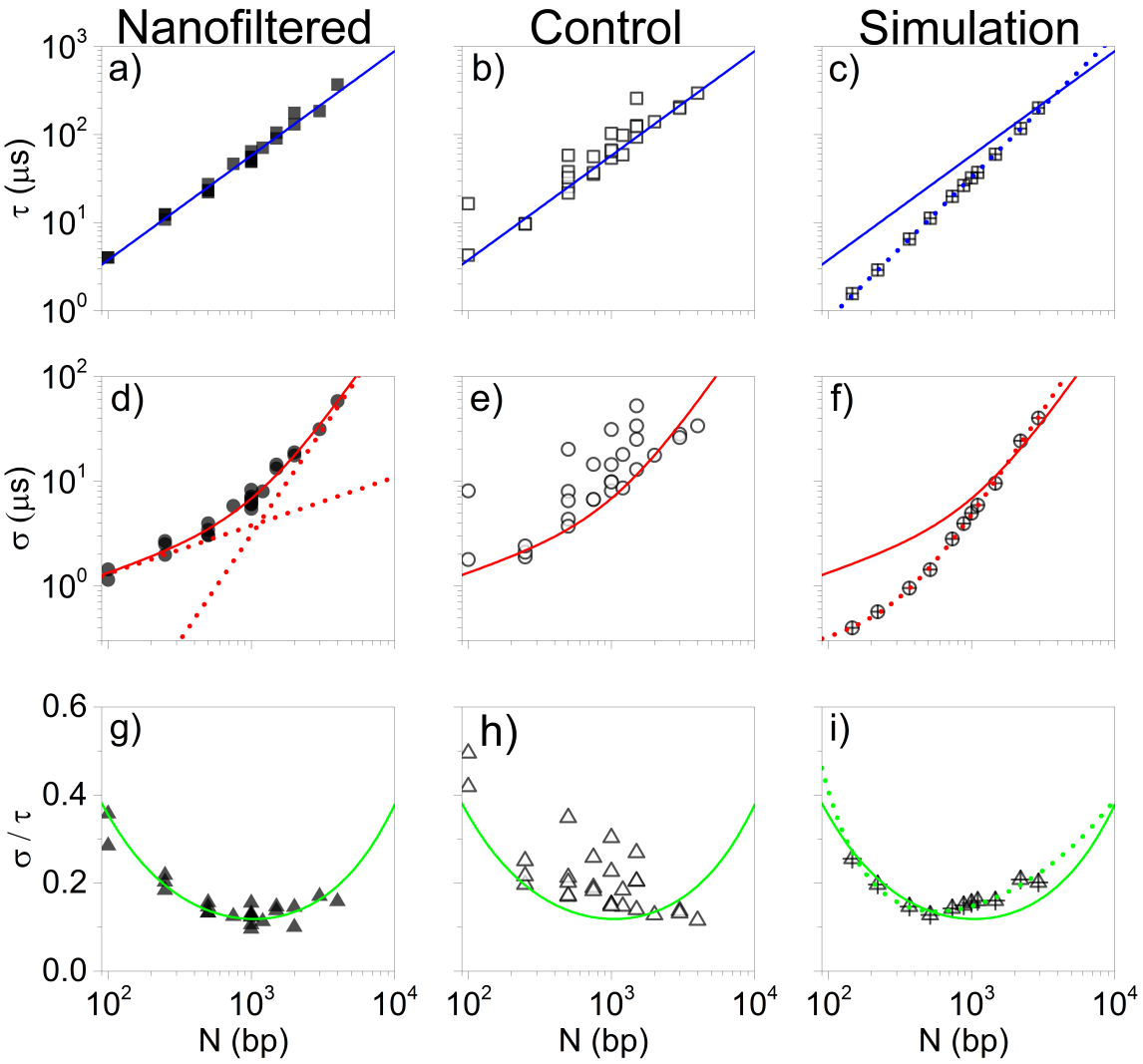

Figure 6.8: Mean passage times for a) nanofiltered, b) control, and c) simulated nanofiltered pores as a function of DNA length. The solid blue lines are a fit of Equation 6.21 to the data in a), while the dashed line in c) is a fit to the simulated data. Standard deviation of passage times for d) nanofiltered, e) control, and f) simulated nanofiltered pores. The solid red lines are a fit of Equation 6.22 to the data in d). The dotted lines in d) show the two power laws separately, while the dotted line in f) shows the two-power fit to the simulated results. Coefficient of variation for g) nanofiltered, h) control, and i) simulated nanofiltered pores. The solid green lines are the quotient of the fits in a) and d), while the dotted line in i) is the quotient of the fits to simulated data.

results in significantly lower standard deviations than the control case (Figure 6.8e).

Experimental data with the nanofilter is fitted by a two-power law:

$$\sigma(N) = \sigma_0 \left[\left(\frac{N}{N^\star} \right)^q + \left(\frac{N}{N^\star} \right)^r \right]. \tag{6.22}$$

The experimental best-fit exponents for this form are $q_{exp} = 0.5 \pm 0.3$ and $r_{exp} = 2.0 \pm 0.6$, in reasonable agreement with $q_{sim} = 0.3 \pm 0.5$ and $r_{sim} = 2.1 \pm 0.2$ for the simulated data. The standard deviation thus exhibits a cross-over between different power laws for small and large N, as discussed below.

As a consequence of the mean and standard deviation passage times scaling behavior, the coefficient of variation $\sigma\tau^{-1}$ exhibits non-monotonic behavior, and has a global minimum which can be seen in Figures 6.8g and 6.8i. The origins of this minimum can be explained by examining the simulation data for the translocation time and standard deviation (Figures 6.8c and 6.8f). At short lengths, the standard deviation grows weakly with increasing DNA length. In this limit, the DNA is rod-like and thus increasing the length of the DNA causes minute variations in the available conformations at the start of translocation. On the other hand, the friction coefficient grows approximately with the length of the rod[51] and thus the translocation time does increase significantly. Hence, a weakly growing standard deviation normalized by an increasing translocation time yields a decreasing coefficient of variation. This rod-like limit breaks down around the Kuhn length, where variation of initial conformations increasingly influences the distribution of translocation times. Indeed, the standard deviation is seen to increase strongly with increasing length for $N > 300$ bp (slightly above the Kuhn length in simulations). The onset of this additional source of variation causes the increase in standard deviation to outpace that in the mean passage time, thus increasing the coefficient of variation. The combination of these effects is a minimum between these two regimes.

In the controls (Figure 6.8e), we see that deviations from the fit to nanofiltered pore data are always biased toward larger standard deviations (note the log scale). For a given molecular size, sensing pores equipped with a nanofilter set a lower bound for the standard deviation that is achievable by the sensing pore. To understand this trend, we consider recent simulation work which showed that the gradient in the electric field outside of nanopores can stretch out polymers as they are captured prior to translocation since polymer segments that are closer to the pore experience a larger electrophoretic force than those further away[23,42]. The distance from the pore at which elongation occurs can be estimated by considering the capture distance at which the electrophoretic force overcomes diffusion, which is proportional to the square of the pore diameter[52]. The experimental data in Figure 6.9 are collected for several devices in which the sensing pore diameter was varied between 3 and 14 nm. This translates into a variation of the capture distance over more than an order of magnitude. Hence, in the absence of the nanofilter, the DNA will be consistently elongated for large pores but much less so for small pores. The effects of this are experimentally observed in the control data in Figure 6.8b: large pores exhibit a smaller variation in the conformation of the dsDNA prior to translocation and thus a smaller standard deviation in the translocation times compared to the more variable conformations expected for smaller pores, though the effect is less reliable than that which is seen when using the nanofilter. In the presence of the nanofilter, sufficiently long dsDNA must uncoil in order to thread through the nanofilter and is thus biased to approach the sensing pore in an elongated conformation independent of the sensing pore size. Consequently, the nanofilter reduces the variability in the initial conformation and improves the standard deviation beyond what can be consistently achieved with large sensing pores alone, and more importantly removes the dependence of passage time standard deviation on sensing pore size and stability.

In order to further elucidate the origin of the minimum in the coefficient of variation and to confirm that molecules which pass through the nanofilter tend to be more elongated than those that do not, additional simulations were conducted wherein the dsDNA was initialized by equilibrating with one end fixed in the sensing pore (Figure 6.9c). In this configuration, DNA are much less elongated on average. However, in these simulations where the nanofilter plays little to no role, the crossover in the standard deviation of the passage time and the global minimum in the coefficient of variation are still observed, albeit at slightly shorter chain lengths. The fact that this cross-over behavior is also visible as the lower bound in the control experiments for both standard deviation (Figure 6.8d) and the coefficient of variation (Figure 6.8g) point to a molecular property of the polymers, namely the polymer stiffness, being responsible for the presence of the minimum in the coefficient of variation, rather than the presence of the nanofilter. The nanofilter is the mechanism by which the sensing pore can achieve the minimal standard deviation required to actually map the transition. Therefore, fundamental physics of polymer translocations are revealed by the presence of the nanofilter. This crossover behavior has always been present but has until now been indistinguishable from noise.

In principle, pre-stretching of the polymer is not the only way in which to achieve a reduction in the standard deviation of the passage time. As long as the conformational entropy is reduced, the passage time will be more consistent regardless of the subset of conformation space that is selected. Different confining geometries prior to translocation through the pore can in theory produce similar effects[24]. However, Figure 6.9a suggests that membrane interactions may play an important role in variability in the translocation process. Pre-stretching is capable of mitigating membrane interactions while simultaneously reducing conformational entropy, which need not be the case for any confining geometries.

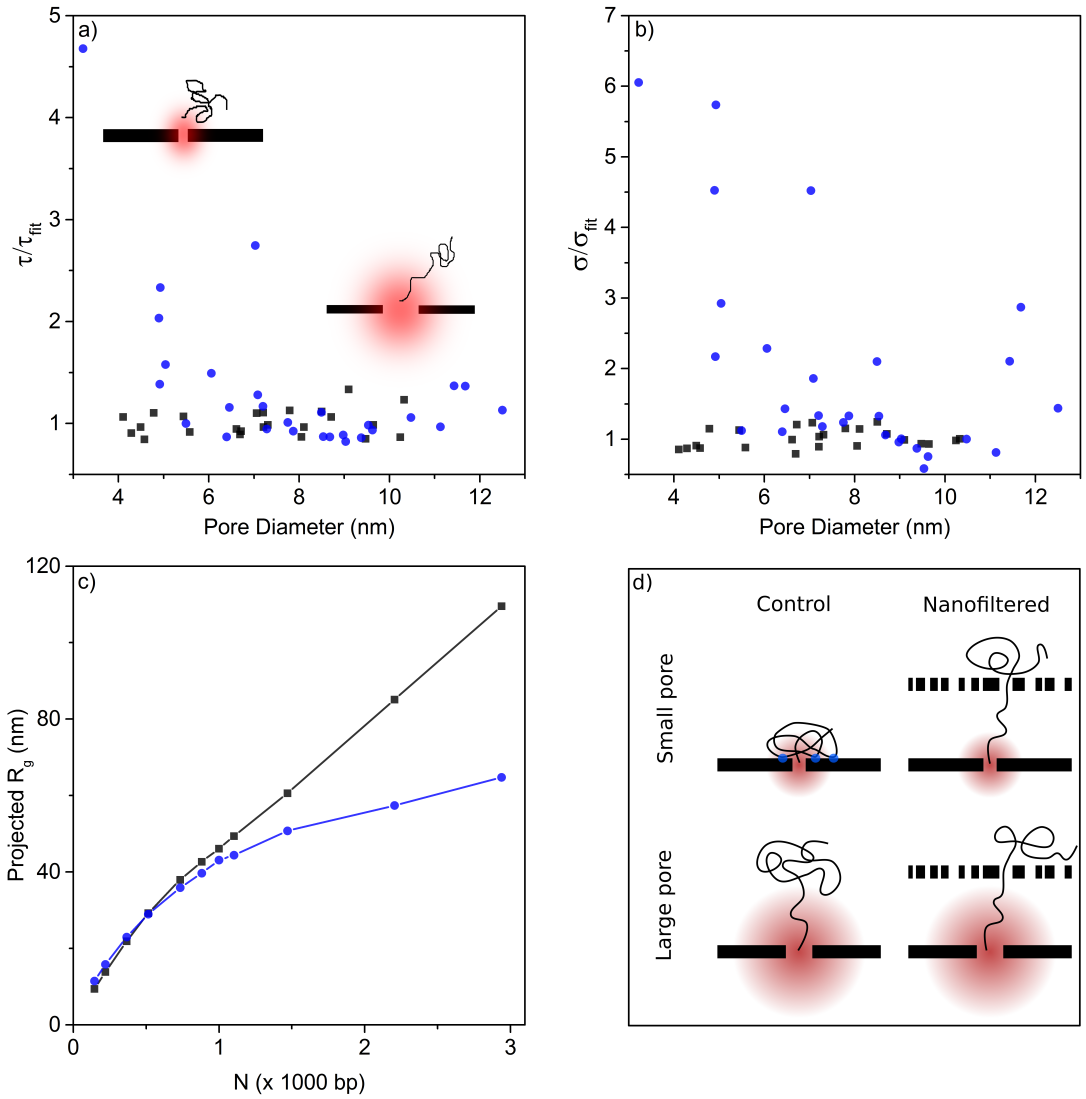

Figure 6.9: a) Experimental mean passage times normalized by the fit of Equation 6.21 as a function of sensing pore size for both nanofiltered (black squares) and control pores (blue circles). Inset schematics show stretching of the polymer as it enters the capture radius of control pores for two different pore sizes. b) Experimental standard deviation normalized by the fit of Equation 6.22 as a function of sensing pore size c) Simulated projection of the radius of gyration on the vector connecting the sensing pore and the center of mass of the DNA at the moment of capture, for molecules initialized with one end in the nanofilter (black squares) versus one end in the sensing pore (blue circles). d) Schematics illustrating the expected conformations of polymers at the onset of translocation for small and large pores with and without the nanofilter. Red gradients depict the electric profile outside the pore, while blue dots represent the potential interaction sites between the polymer and the membrane outside the pore.

While large control pores can sometimes approach the performance of nanofiltered pores, the results presented in Figures 6.8 and 6.9 show that the presence of the nanofilter idealizes the sensing pore, allowing the system to consistently achieve a minimal standard deviation and coefficient of variation. In addition, a remarkable feature of nanofiltered pores is the fact that this minimization happens independent of sensing pore size. In several cases the pore size was observed to grow over the course of a single experiment (Tables 6.1 and 6.2) without compromising the improvement to the passage time characteristics. This independence of the sensor on both pore size and pore stability, made possible by the presence of the nanofilter within nanoscale distances of the sensing pore, is a feature of clear importance to many solid-state nanopore-based technologies.

It is also interesting to note that the normalized mean passage time has a pore size dependence, with smaller control pores actually leading to slower translocation than their nanofiltered counterparts. Since an elongated polymer is expected to have more drag and thus take more time to translocate[7], this is counterintuitive. We attribute this observation to additional friction arising from interactions between the coiled polymers that approach small control pore both with itself (coil-coil interactions) and the surrounding membrane (coil-membrane interactions), as depicted in Figure 6.9d. Because these polymers are not elongated, their conformation renders them more prone to interact with the membrane surrounding the mouth of the pore, potentially leading to temporary weak sticking, whereas elongated polymers will not be subject to this slowing effect.

In support of this, as illustrated in Figure 6.9a, the mean passage time through unfiltered pores fluctuates above that seen with filtered pores of the same size. This is attributed to two mechanisms: small unfiltered pores lead to coiled conformations at the onset of translocation, which are prone to self-interactions and interactions

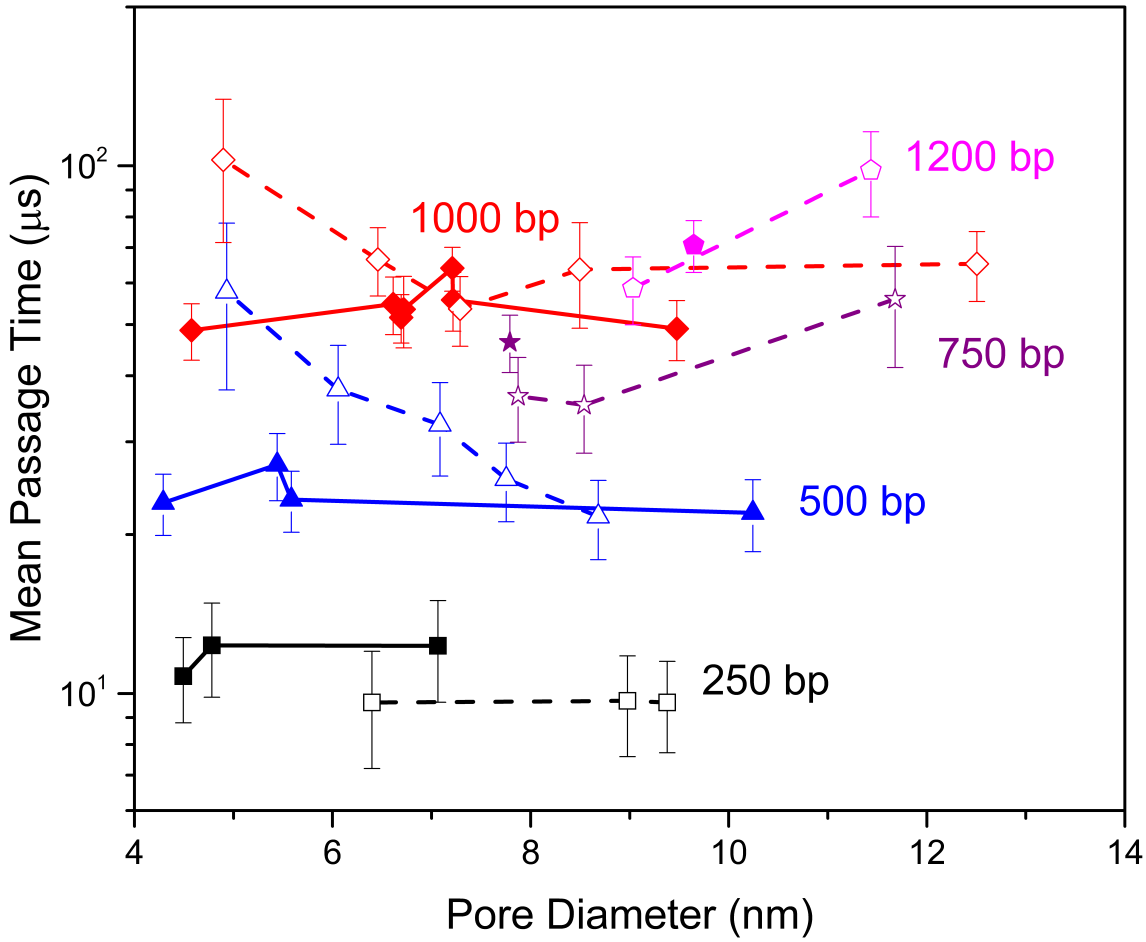

Figure 6.10: Dependence of mean passage time on pore diameter for a selection of given dsDNA lengths. Dashed lines indicate control pores, while solid lines indicate nanofiltered pores.

with the membrane; and large unfiltered pores have large capture radii, leading to elongated conformations at the onset. Figure 6.10 provides additional evidence for these interpretations. It shows the mean passage times for filtered and unfiltered pores as a function of pore diameter for chain lengths of 250, 500, 750, 1000, and 1200 basepairs.

The 250 bp case demonstrates that these chains are too small for their translocation to be affected by the filter, which is consistent with Figure 6.9c. In the 500 bp and 1000 bp cases, the mean passage times increase for small pore diameters

in the unfiltered pores but not the filtered pores. The increase occurs in a smooth fashion as pore diameter is reduced at fixed chain length, strongly suggesting that pore diameter is the driving factor causing the increase. Furthermore, the filtered pores consistently lack the increase, indicating that the filter reliably eliminates this phenomenon regardless of its origin.

Conversely, in the 750 and 1200 bp cases, the mean passage times increase with increasing pore diameter for unfiltered pores. This effect is not clearly visible in the 1000 bp case, but this is likely due to statistical fluctuations. The trend is not visible among filtered pores, as the dataset does not include sufficiently many large filtered pores to deduce a trend. However, those large filtered pores that are present have passage times consistent with the trends observed in the control pores.

Additionally, translocation is slower in larger pores, as expected due to polymer elongation. Thus, the largest of the control pores lead to slower translocation than the nanofiltered pores. It is important to note, however, that the dataset contains more large control pores than large nanofiltered pores, so it is unclear whether large nanofiltered pores would also exhibit slower translocation than smaller nanofiltered pores. However, it is clear from Figure 6.9 that the nanofilter reduces both variability within a given pore (Figure 6.9b) as well as variation between pores (Figure 6.9a).

6.3.3 Long Passage Time Events

There are a number of plausible explanations for the long tail of passage times which appear in Figures 6.7e and 6.7f. First, simulations performed for a polymer corresponding to approximately 2200 bp ($R_g \approx 82$ nm) indicate that the average translocation time is dependent on the elongation state of the polymer. Taking into account the gap height, for $N \geq 1300$ bp there will be a significant population of

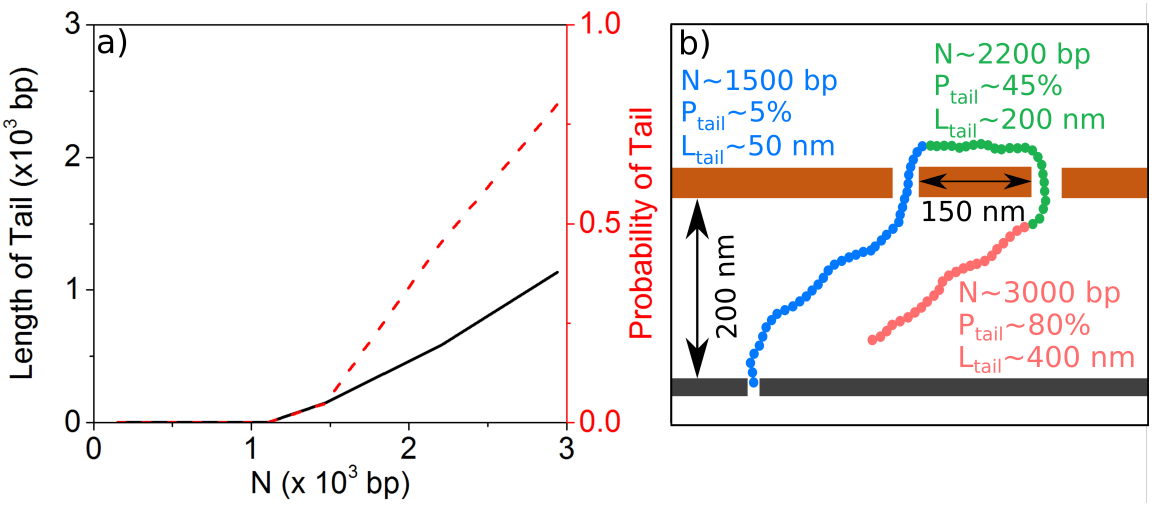

Figure 6.11: a) Simulated probability and average length of a segment (tail) of DNA remaining on the cis side of the nanofilter at the moment of capture by the sensing pore, which could be captured by a second pore in the nanofilter. b) Schematic representation of the capture of DNA tails by a second pore in the nanofilter.

molecules which still have part of their length on the cis side of the nanofilter when captured by the sensing pore, resulting in a highly elongated conformation with high fluid drag (Figure 6.11a). This is in line with the experimental onset of the long tail of events. However, while our simulations show that increased drag for elongated events can account for some increase in the translocation time, it is insufficient to explain the multiple orders of magnitude increase in passage times seen in the longest events.

Second, we note that for sufficiently long dsDNA, it is possible to thread through two pores in the nanofilter and for both arms of the polymer to come close to the sensing pore. In this case, not only is the polymer highly elongated, but there are competing pulling forces which further extend the passage time[53]. While these double-threaded events do occur, as shown Figure 6.12, our simulations indicate that these competing forces are still insufficient to explain the long passage times in the tail of the distribution unless both ends of the polymer are actually captured by the sensing pore, and the events in the long tail spend most of their time in a single-

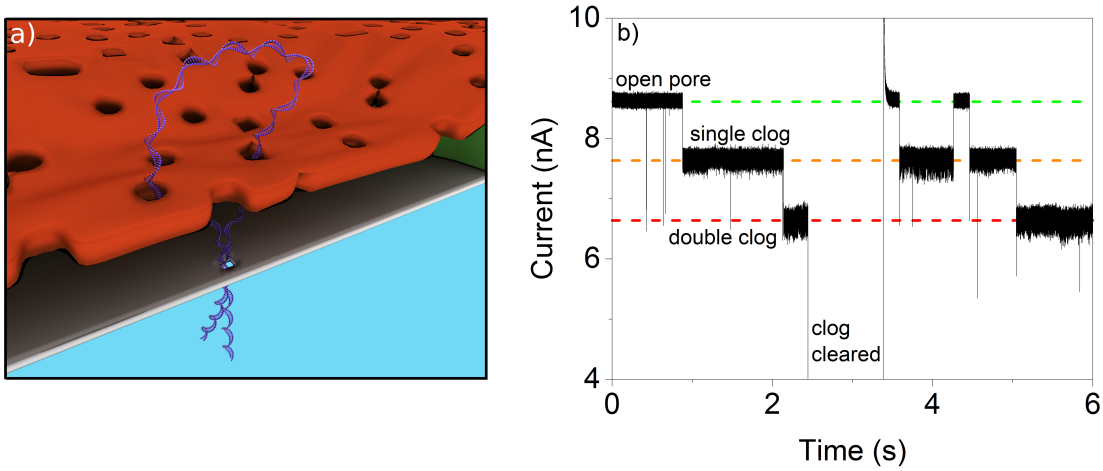

Figure 6.12: a) Long molecules are prone to double-threading into the sensing pore while straddling two nanofilter pores. b) Current trace for 3000 bp dsDNA traversing the nanofiltered pore, showing persistent clogging modes corresponding to single- and double-threading through the sensing pore. The clog can be temporarily removed by reversing the applied voltage, but it always quickly returns. Data is low-pass Bessel filtered at 300 kHz and down-sampled to 600 kHz for display purposes.

occupation state which is incompatible with this picture. In such cases, the sensing pore exhibits very consistent clogging modes consisting of two sequential blockage levels corresponding to one and two strands of dsDNA present in the sensing pore. Reversing the voltage polarity can temporarily clear the clog, but it reappears after a short interval of normal baseline (Figure 6.12b). Once this clogging mode occurs, even flushing out the flow cell with clean buffer is unable to remove it permanently, indicating that the offending dsDNA strand is most likely tangled in the nanofilter, a very clear molecular signature which is incomaptible with most of the observed long passage time events.

Finally, we attribute the long events to translocation which has one end of the dsDNA temporarily adsorbed to the nanofilter during capture of the other end by the sensing pore. To support this picture, we define adsorbed events as events with passage times exceeding four standard deviations above the mean for the log-normal

portion of the passage time distribution on a log-scale. Figure 6.13a shows the sublevel blockage depth as a function of duration for all of the events with long passage times for 3000 bp molecules translocating a nanofiltered pore. It can be compared to the full set of sublevels for a similar control pore (Figure 6.13b), which does not have the extended tail of long events. While most long events show a single blockage level (Figurse 6.13c and 6.13h), blockage states corresponding to occupation of the pore by more than one dsDNA molecule are present in some events. These deeper blockage levels are always very short compared to the unfolded sublevel, and for the majority of events appear only at the very start of events (type 21, Figures 6.13f and 6.13i). These latter events correspond to a dsDNA adsorbed on the nanofilter which is captured in a folded configuration very near an end, and then proceeds to occupy the pore in an unfolded conformation for the remainder of its length. However, there is a significant population of complex events which contain levels corresponding to two and three times the single occupation level in the middle of an extended stretch of single-occupancy, which cannot generally be explained by interactions of a single molecule with the pore (Figures 6.13g and 6.13j). We attribute these superimposed events to simultaneous translocation of a second, unhindered dsDNA molecule while the pore is partially occluded by a single DNA molecule adsorbed on the nanofilter. To support this, we note that the passage time distributions for superimposed events are similar to those for regular unhindered events (Figure 6.13c). The inter-event time distributions for superimposed events are also consistent with the unhindered translocations (Figures 6.13d).

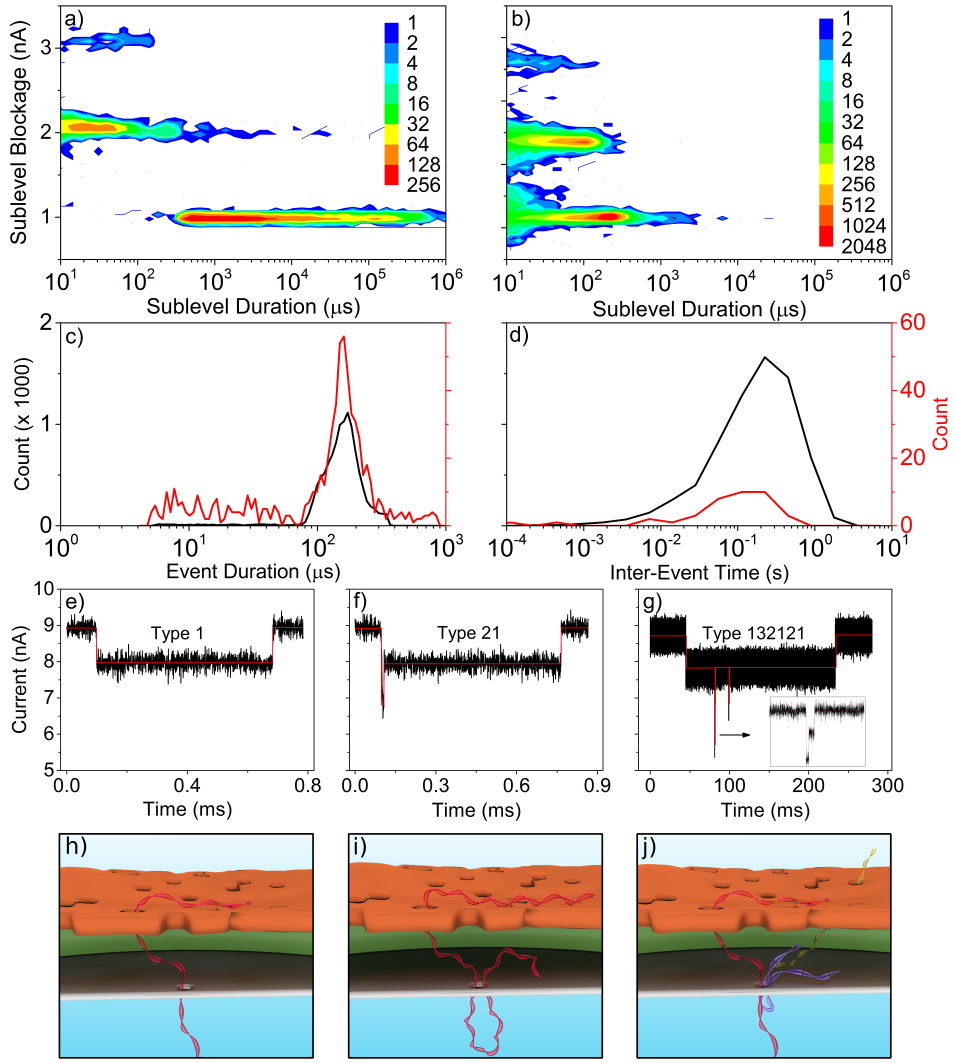

Figure 6.13: a) Heat map of sublevels within events, showing blockage depth as a function of sub-level duration for events which fall within the tail of long events for 3000 bp dsDNA in an 8.0 nm nanofiltered pore. b) For comparison, the sublevel breakdown for a control pore (no nanofilter), showing that the long tail of events is absent c, d) Distribution of passage times and inter-event times respectively for superimposed events within long single-level events (red) compared to the passage time distribution for unhindered events from the same pore (black). e-g) Examples of a single-level, unfolded type 1 event, a briefly initially folded type 21 event, and a more complex event, respectively, from among the 3000 bp double-threaded events. h-j) schematic representations of the molecular conformations giving rise to each of the corresponding event signatures above. Red DNA represents a polymer which is adsorbed to the filter while other colors translocate freely.

6.3.4 Nanopore Size Spectroscopy

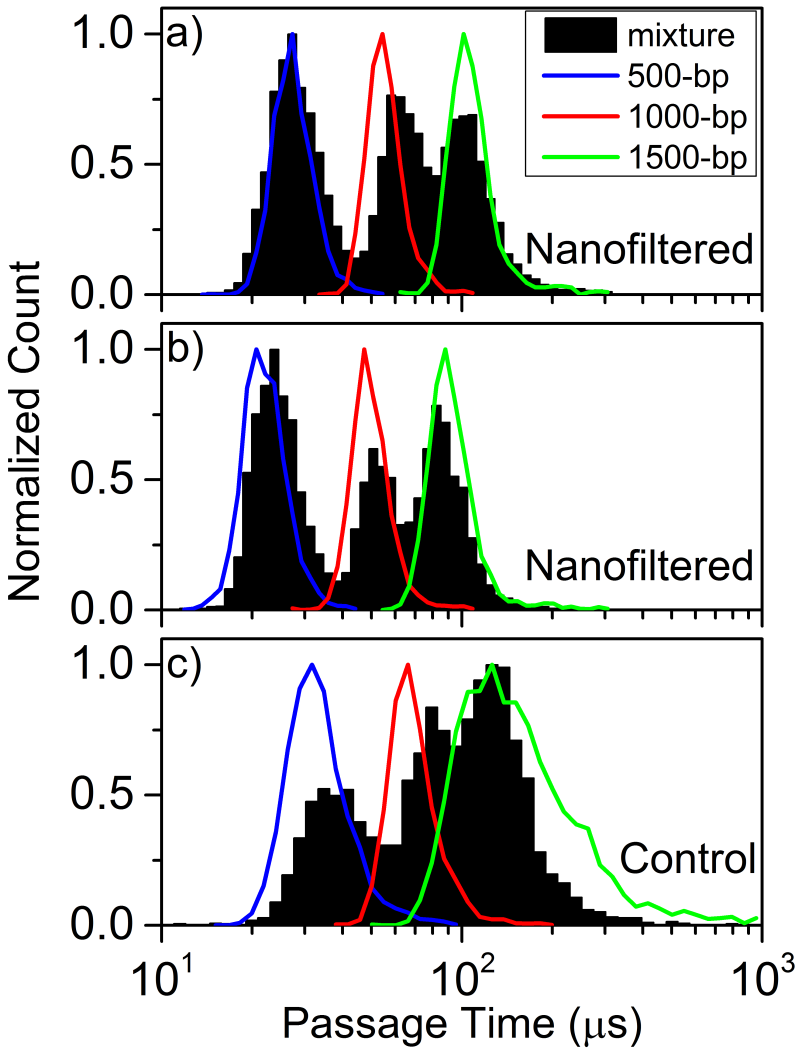

Figure 6.14: a, b) Passage time distributions for single-file translocation events using equimolar mixtures of 500 bp, 1000 bp, and 1500 bp dsDNA strands with a nanofilter. The line plots in each case shows the distribution for each species alone on the same nanopore, while the black histogram gives the distribution of the mixture. c) The same data for the case of a pore without the nanofilter.

Regular solid-state nanopores are usually unable to distinguish populations of different dsDNA sizes with better than 1000 bp[54] resolution, unless their diameter is very well controlled to precisely 3 nm so as to minimize any DNA self-interaction[19]. This poor resolution is to due the entropic effects already discussed, but also do

transient polymer-pore and polymer-polymer interactions, all of which contribute additional passage time variance. Here, the reduced standard deviation in passage times through nanofiltered pores can be leveraged to improve resolution without the need to precisely control the pore diameter. We investigate this effect by translocating equimolar mixtures of different DNA sizes in a single device. Figure 6.14 shows the results of using equimolar mixtures of 500 bp, 1000 bp, and 1500 bp dsDNA. The passage time distributions clearly show all three well-separated peaks (Figures 6.14a and 6.14b). Since LiCl is known to broaden passage time distributions compared to KCl[13], the resolution can most likely be further improved by using a different electrolyte, albeit for a different range of polymer lengths. While some control pores can also reveal the presence of three peaks in passage time distribution (Figure 6.14c), the nanofiltered pores have a tighter distribution and more reliable peak separation.

6.3.5 Folding Distributions

In addition to augmenting the standard deviation of molecular passage time distributions through a nanopore, the large degree of conformational entropy available to semi-flexible polymers also leads to folded translocation, in which a polymer is captured from somewhere along the length of the molecule and translocates in a hairpin conformation. This is particularly problematic for genomic mapping and barcoding schemes in which a DNA molecule is tagged with a marker, either to determine the presence or location of a particular sequence[55–57], the presence of a target[21], or to map the velocity profile of translocating molecules[20]. In such applications, folded translocations are generally excluded from data analysis, which can result in having to ignore many translocation events entirely. As a result, ensuring single-file passage of dsDNA through pores of any size is of high technological importance for many diag-

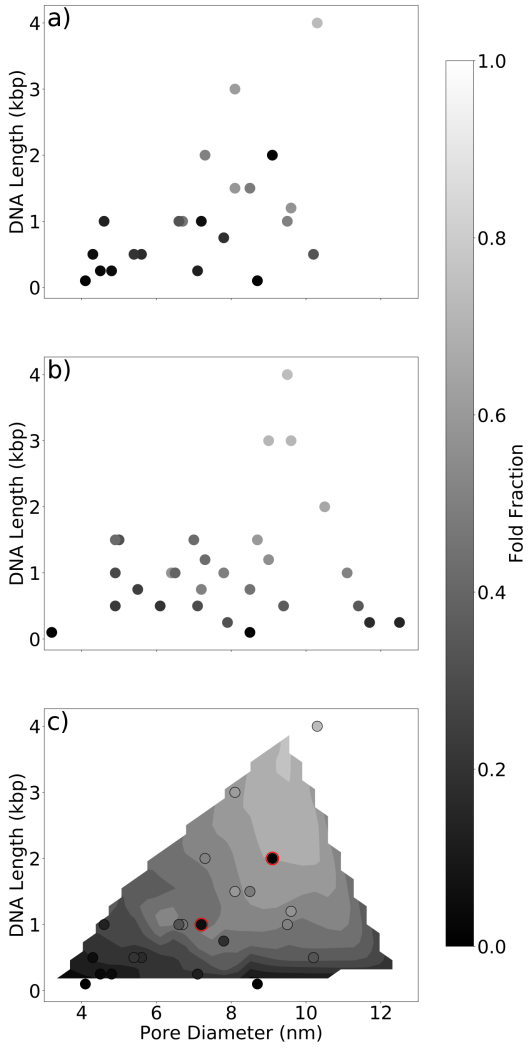

Figure 6.15: Folding fraction for nanofiltered pores as a function of pore size and dsDNA length, showing that folding probability increases strongly with chain length and weakly with pore diameter once the pore is past the minimum size to allow folding at all. b) The same plot for control pores. c) Control pores are used to interpolate contours of constant folding fraction, and nanofiltered pores are overlaid as circular symbols. Two symbols, circled in red, stand out as being significantly different from the control case. K478 (see Table 6.1) also showed folding suppression, but is excluded from this plot since data was acquired at a different voltage.

nostic and genomics applications[21,55,57,58] that rely on detecting and mapping bound probes. While it is possible to restrict folding by using a nanopore too small to allow

it, this is often incompatible with bulky labeling schemes and can be sensitive to pore instability[59,60].

We observed complete elimination of dsDNA folding during translocation through the sensing pore in two nanofiltered pore devices, despite the sensing pore being sufficiently large in both cases to allow for folded passage. The first of these pores is presented in Figure 6.15, which shows the folding behavior of molecules passing control pores and nanofiltered pores as a function of both pore diameter and dsDNA length. One of the nanofiltered pores (red circles in Figure 6.15c) completely suppressed folding even though both the pore and the dsDNA chains were large enough to support significant folding.

Both of the devices which suppressed folding had in common a low event rate compared to the rest of the nanofiltered devices. Due to the variability of folding behavior between nanofiltered devices, the origin of this effect must lie with the particular details of each individual nanofilter. We hypothesize that the mechanism behind folding suppression is the variation in the local distribution of nanofilter pore positions in the vicinity of the sensing pore. As is discussed in detail shortly, only a small number of nanofilter pores which are very close to the sensing pore are active and have a sufficiently high electric field to capture dsDNA, so the local nanofilter pore distribution can be different between devices. In particular, if a device has two active nanofilter pores which are very close together compared to the extent of the dsDNA, the probability of a dsDNA molecule threading through both nanofilter pores will be high. Because of the electric field gradient between the two membranes, double-threaded polymers will tend to favor capture by one end, and translocation will proceed unfolded due to the resulting elongation.

If we assume the nanofilter causes only a weak perturbation to the field and that the electric field $E(\rho, z)$ is cylindrically symmetric and decays as the second power of

radial distance from the pore[61], the electric field on the nanofilter a lateral distance from the sensing pore will be roughly

$$E(\rho, h) = \frac{E(0, h)}{1 + \left(\frac{\rho}{h}\right)^2}, \tag{6.23}$$

where h is the height of the nanocavity. Because passage through the nanofilter is an energy barrier process mediated by the tiny voltage drop present there, the probability of capture by a particular pore in the nanofilter will decrease rapidly with lateral distance from the sensing pore.

Assuming a weak electric field and an energy barrier limited passage of polymers through the nanofilter, the capture probability for a particular pore in the nanofilter should be roughly linear in the electric field, and the probability density for capture by a pore in the nanofilter at a lateral distance from the sensing pore will then be proportional to $\rho E(\rho)$, which is strongly peaked near $\rho = h$. Most of the translocations through the sensing pore will therefore be due to passage through pores in the nanofilter which are near the sensing pore. For the nanofilter used in this work, the average number of active pores in the nanofilter (defined as pores within $\rho < h$ of the sensing pore) is 3.4 ± 1.4, so variation in device behavior due to variation in the local porosity of the nanofilter can be quite significant.

To test this hypothesis, we performed experiments using a different nanofilter material, which had slightly smaller pores (38 ± 12 nm) but higher porosity ($16 \pm 3\%$), yielding more closely-spaced nanofilter pores which would promote double-threading. Due to the smaller nanofilter pores, a higher voltage of 400 mV was required to obtain a sufficiently high event rate to gather statistics.

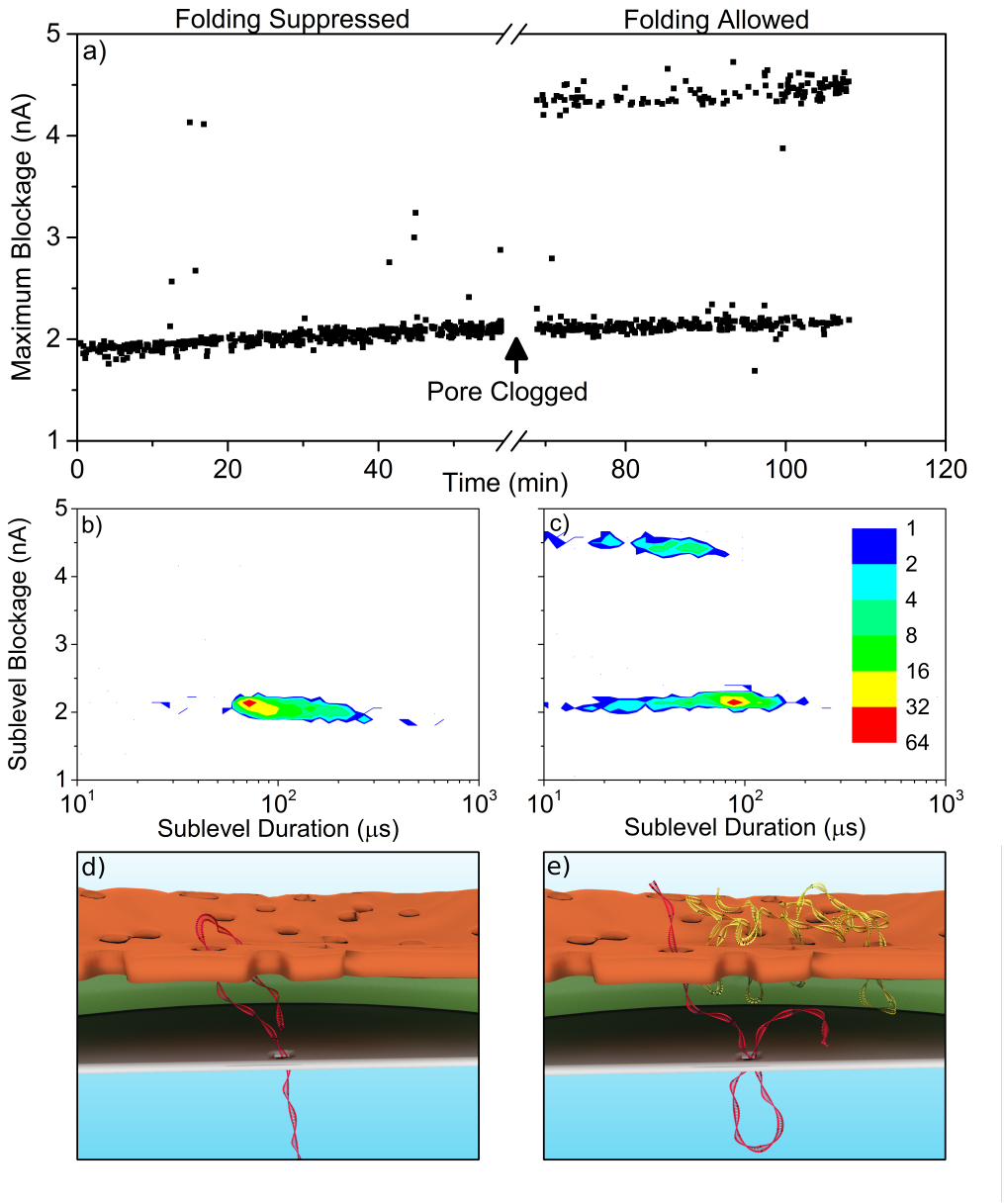

Figure 6.16: a) Maximum blockage as a function of experiment time, showing near-complete suppression of folding during the first half of the experiment, followed by allowing folding after a period of prolonged clogging. The single-occupancy blockage level is around 2 nA for this 5.4 nm sensing pore. b) Heat map of the sub-levels for events from the folding-suppressed half of the experiment. c) Heat map of the sub-levels for events from the folding-allowed half of the experiment, following clogging of the sensing pore. d) Schematic of the hypothesized mechanism of folding suppression consisting of two closely-spaced nanofilter pores. e) Schematic depicting how the folding suppression can be lost when one or more of the active nanofilter pores is clogged.

A dramatic demonstration of the hypothesized physical picture is shown in Figure 6.16. The device suppressed folding almost completely during the first part of the experiment (Figures 6.16a and 6.16b). Subsequently, the sensing pore clogged and exhibited increased noise centered around a single-occupancy clog for a few minutes. When the clog cleared the sensing pore, with the open pore current baseline returning to its previous value, subsequent events presented folding (Figures 6.16a and 6.16c). The most likely explanation is that one of the two closely-spaced nanofilter pores was permanently clogged during the period in which the sensing pore was clogged, and since the local properties of the nanofilter no longer promoted double-threading, folding was no longer suppressed.

In light of this, we expect that folding suppression can be achieved reliably if the nanofilter parameters can be chosen so as to promote double threading of DNA molecules en route to the sensing pore. As long as the edge-to-edge distance between adjacent active nanofilter pores is smaller than the free solution radius of gyration of the polymer we expect this probability to be high, while small nanofilter pores will promote unwinding of the dsDNA molecule as it passes into the space between the membranes.

In order to further study the effect of the local pore size distribution on the translocation kinetics, we reduced the size of the pores in the nanofilter by depositing hafnia by ALD (160 cycles) on the NPN material prior to membrane transfer. This had the effect of reducing the average pore size from 48 ± 4 nm to 16 ± 4 nm without significantly changing the number of pores per unit area. Figure 6.17 shows TEM imaging of ALD-coated nanofilter pores from a low-porosity section of the wafer. The reduced pore size did not have a significant effect on folding behavior, again pointing more toward the distance between active pores as the important controlling parameter in suppressing folding.

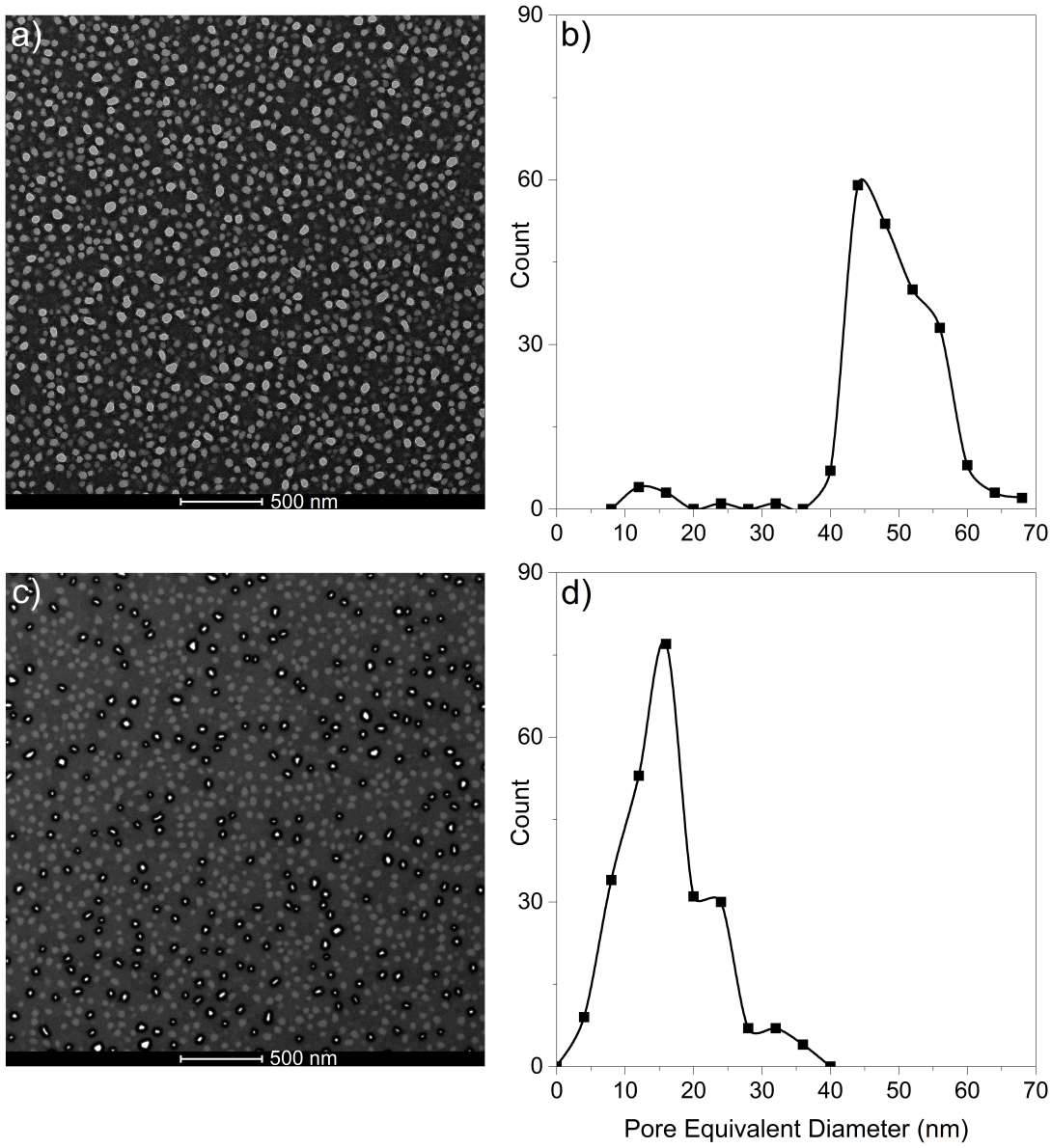

Figure 6.17: ALD coated pore distribution. a) TEM images of NPN material before conformal ALD deposition b) Pore diameter histogram for through holes in the image in a). c) TEM image of a different section of the same NPN wafer after 160 cycles of ALD hafnia deposition. d) Histogram of ALD-coated pore diameters for the through holes, with significant reduction in the average pore diameter. Only through-holes receive a visible ALD coating (black outline).

Unsurprisingly, the smaller pore sizes present in the hafnia-coated nanofilter required a larger applied voltage before translocations were observed. While almost no

translocations were observed at an applied voltage of 200mV, the capture rate at 400 mV of ALD-coated nanofiltered pores was comparable to the capture rate of uncoated nanofiltered pores at 200 mV. This is simply a consequence of the fact that smaller pores on thicker NPN membranes present a higher energy barrier to translocation. This is especially significant since the reduction in average pore size and the increase in nanofilter membrane thickness would increase the total electrical resistance of the nanofilter, and therefore the voltage drop across it, for a given applied voltage. Since even the uncoated nanofilter already shows size-selectivity properties in the capture rate, we expect that even more dramatic filtering effects will be accessible to nanofiltered systems with significantly smaller average pore size.

6.4 Conclusion

One of the reasons preconfinement of molecules through the use of two-membrane systems has proven experimentally challenging is the difficulty inherent in producing two adequately-spaced, precisely-sized, serial nanopores while having fluidic access to the nanoscale gap between them for the purposes of wetting. The nanofiltered pore device presented herein creates a composite structure which achieves an optimal balance between these requirements while keeping the complexity minimal: the ultrathin, porous nanofilter material allows easy wetting and simple fluidic and electrical access to the intermediate space for the purposes of nanopore fabrication by CBD, which guarantees the presence of appropriately aligned nanopores without requiring visual confirmation, and eliminates both the requirement for precise nanopore size and the deleterious effects of size instability during sensing.

The combined simulation and experimental results obtained on this nanofiltered pore device demonstrate the strong influence the capture process has on the dynamics

of DNA translocation and reveal the presence, previously hidden in the noise, of a minimum in the normalized variance of translocation times that is inherent to semi-flexible polymers. The presence of the nanofilter upstream of the nanopore sensor pre-stretches the polymer, which offers a significant reduction in variation of passage times even when compared to the effect stretching in the electric field gradient present around large nanopores. This composite structure will enable a broad range of applications and provide enhanced sensing capabilities. It can be leveraged to provide more precise polymer size separation and to suppress folded translocations, thus forcing single-file passage, of critical importance for many life science and health applications, including DNA sizing, barcoded target detection and genome mapping.

6.5 Materials and Methods

6.5.1 Nanofilter Assembly

The NPN nanofilter membranes and SiN_x/oxide microwell substrate chips (SiM-Pore Inc., West Henrietta, NY) are cleaned with a nitrogen flow, followed by 38 W air plasma for 40s to make all surfaces hydrophilic. Both the substrate and nanofilter chips are placed into gentle contact using a custom aluminum jig and placed in a $-15\,^{\circ}C$ freezer for 2 minutes to cool below room temperature. The assembly is then exposed to fine mist produced by a vaporizer, which condenses on the cooled surface and fills the cavity between the two membranes. As the liquid evaporates through the nanofilter, surface tension pulls the two membranes into contact, which then remain sealed together once all the liquid has evaporated. The two chips are then separated mechanically, and the nanofilter is left behind in contact with the substrate chip. In order to completely seal the nanofilter and to reduce chip capacitance, PDMS is then

painted over the entire chip surface, leaving only the free-standing membrane portion exposed. This assembly can be stored until use.

Just before use, the assembly is air plasma cleaned at 38 W for 40 s to make all surfaces hydrophilic. The cleaned assembly is then placed in a sealed container with ambient air (40% humidity) and this container is placed in the $-15\,^{\circ}\mathrm{C}$ freezer for up to 5 minutes. The cooling condenses humidity in the microwell, wetting the gap between the two membranes.

6.5.2 Nanopore Fabrication by CBD

Nanopores are fabricated in nanofilter assemblies via CBD, which is described elsewhere[46]. Briefly, pores are formed in 1 M KCl pH 10 using a slowly increasing voltage ramp from -10 V to -18 V applied to the nanofilter side of the assembly, with the trans side grounded. Typical fabrication times are between 5 and 10 minutes. Once fabricated, the salt solution is changed to 3.6 M LiCl pH 8 and, depending on the initial pore size, diameter is adjusted using $3-4$ V 4s square voltage pulses until the desired pore in the range of $3-14$ nm is achieved. Depending on the IV and noise characteristics, pores are sometimes aged before use[8].

6.5.3 Data Acquisition and Analysis

NoLimits dsDNA molecules (Life Technologies Inc.) in the range of 100 bp to 4000 bp are pre-mixed to the desired concentration (between $3-76$ nM) and injected into the vicinity of the pore using a custom PEEK flow cell.

Data is acquired in MATLAB R2013a (32-bit) using the Chimera VC100 current amplifier with 200 mV applied unless otherwise noted, sampled at 4.166 MHz, with a hardware 2-pole low-pass Bessel filter at 1 MHz cutoff frequency. Data is post-

filtered for analysis at 900 kHz using a digital low-pass Bessel filter, and analysed to extract passage times and sub-level structure using both the adept2state module of MOSAIC[62,63], (https://pages.nist.gov/mosaic/) for 100 bp molecules which do not fold, and a custom implementation of the CUSUM+ algorithm[63,64] for the rest of the events (https://github.com/shadowk29/CUSUM). Both analysis programs are available freely online. Nonlinear fitting results are obtained using Origin 9.1.

Acknowledgements

The authors would like to thank James Roussie and SiMPore Inc. for generous donations of expertise and NPN membrane materials. Kyle Briggs acknowledges the financial support provided by the NSERC Vanier program for postgraduate fellowships

Competing Financial Interest

JLM declares a competing financial interest as a co-founder and equity holder of SiMPore Inc., a commercial manufacturer of NPN and silicon-based membrane materials. VTC and KB declare a competing financial interest in the form of a patent on the nanofiltered nanopore device. All other authors declare no competing financial interest.

Bibliography

[1] K. Briggs, G. Madejski, M. Magill, K. Kastritis, H. W. de Haan, J. L. McGrath, and V. Tabard-Cossa, "DNA Translocations Through Nanopores Under Nanoscale Preconfinement," *Nano Letters*, vol. 18, no. 2, pp. 660–668, 2017.

[2] S. Carson and M. Wanunu, "Challenges in DNA motion control and sequence readout using nanopore devices," *Nanotechnology*, vol. 26, no. 7, p. 074004, 2015.

[3] S. J. Heerema and C. Dekker, "Graphene nanodevices for DNA sequencing," *Nature Nanotechnology*, vol. 11, no. 2, pp. 127–136, 2016.
[4] C. Dekker, R. Article, and C. Dekker, "Solid-state nanopores," *Nature Nanotechnology*, vol. 2, no. 4, pp. 209–215, 2007.
[5] S. van Dorp, U. F. Keyser, N. H. Dekker, C. Dekker, and S. G. Lemay, "Origin of the electrophoretic force on DNA in solid-state nanopores," *Nature Physics*, vol. 5, pp. 347–351, mar 2009.
[6] M. Gershow and J. A. Golovchenko, "Recapturing and trapping single molecules with a solid-state nanopore," *Nature Nanotechnology*, vol. 2, no. 12, pp. 775–779, 2007.
[7] B. Lu, F. Albertorio, D. P. Hoogerheide, and J. A. Golovchenko, "Origins and Consequences of Velocity Fluctuations during DNA Passage through a Nanopore," *Biophysical Journal*, vol. 101, pp. 70–79, 2011.
[8] K. Briggs, H. Kwok, and V. Tabard-Cossa, "Automated Fabrication of 2-nm Solid-State Nanopores for Nucleic Acid Analysis," *Small*, vol. 10, no. 10, pp. 2077–2086, 2014.
[9] Y. He, M. Tsutsui, C. Fan, M. Taniguchi, and T. Kawai, "Controlling DNA translocation through gate modulation of nanopore wall surface charges," *ACS Nano*, vol. 5, pp. 5509–5518, jul 2011.
[10] A. Aksimentiev, J. B. Heng, G. Timp, and K. Schulten, "Microscopic Kinetics of DNA Translocation through synthetic nanopores.," *Biophysical journal*, vol. 87, no. 3, pp. 2086–97, 2004.
[11] M. Waugh, A. Carlsen, D. Sean, G. W. G. Slater, K. Briggs, H. Kwok, and V. Tabard-Cossa, "Interfacing solid-state nanopores with gel media to slow DNA translocations," *Electrophoresis*, vol. 36, no. 15, pp. 1759–1767, 2015.
[12] A. H. Squires, J. S. Hersey, M. W. Grinstaff, and A. Meller, "A nanopore-nanofiber mesh biosensor to control DNA translocation," *Journal of the American Chemical Society*, vol. 135, pp. 16304–16307, nov 2013.
[13] S. W. Kowalczyk, D. B. Wells, A. Aksimentiev, and C. Dekker, "Slowing down DNA translocation through a nanopore in lithium chloride.," *Nano Letters*, vol. 12, pp. 1038–44, feb 2012.
[14] J. Feng, K. Liu, R. D. Bulushev, S. Khlybov, D. Dumcenco, A. Kis, and A. Radenovic, "Identification of single nucleotides in MoS2 nanopores," *Nature Nanotechnology*, vol. 10, no. 12, pp. 1070–1076, 2015.
[15] N. Di Fiori, A. Squires, D. Bar, T. Gilboa, T. D. Moustakas, and A. Meller, "Optoelectronic control of surface charge and translocation dynamics in solid-state nanopores," *Nature Nanotechnology*, vol. 8, pp. 946–951, nov 2013.
[16] D. Fologea, J. Uplinger, B. Thomas, D. S. McNabb, and J. Li, "Slowing DNA Translocation in a Solid-State Nanopore," *Nano Letters*, vol. 5, pp. 1734–1737, sep 2005.

[17] J. Larkin, R. Henley, D. C. Bell, T. Cohen-Karni, J. K. Rosenstein, and M. Wanunu, "Slow DNA transport through nanopores in hafnium oxide membranes.," *ACS Nano*, vol. 7, pp. 10121–8, nov 2013.

[18] H. Kwok, M. Waugh, J. Bustamante, K. Briggs, and V. Tabard-Cossa, "Long passage times of short ssDNA molecules through metallized nanopores fabricated by controlled breakdown," *Advanced Functional Materials*, vol. 24, no. 48, pp. 7745–7753, 2014.

[19] S. Carson, J. Wilson, A. Aksimentiev, and M. Wanunu, "Smooth DNA Transport through a Narrowed Pore Geometry," *Biophysical Journal*, vol. 107, no. 10, pp. 2381–2393, 2014.

[20] C. Plesa, N. V. Loo, P. Ketterer, H. Dietz, and C. Dekker, "Velocity of DNA during translocation through a solid state nanopore," *Nano Letters*, vol. 15, no. 1, pp. 732–737, 2015.

[21] N. A. W. Bell and U. F. Keyser, "Digitally encoded DNA nanostructures for multiplexed , single-molecule protein sensing with nanopores," *Nature nanotechnology*, vol. 11, no. 7, pp. 1–28, 2016.

[22] N. A. W. Bell and U. F. Keyser, "Direct measurements reveal non-Markovian fluctuations of DNA threading through a solid-state nanopore," *arXiv*, pp. 1–5, 2016.

[23] S. C. Vollmer and H. W. de Haan, "Translocation is a nonequilibrium process at all stages: Simulating the capture and translocation of a polymer by a nanopore," *The Journal of Chemical Physics*, vol. 145, no. 15, p. 154902, 2016.

[24] D. Sean, H. W. de Haan, and G. W. Slater, "Translocation of a polymer through a nanopore starting from a confining nanotube," *Electrophoresis*, vol. 36, no. 5, pp. 682–691, 2015.

[25] X. Liu, M. M. Skanata, and D. Stein, "Entropic cages for trapping DNA near a nanopore," *Nature Communications*, vol. 6, p. 6222, 2015.

[26] M. Langecker, D. Pedone, F. C. Simmel, and U. Rant, "Electrophoretic time-of-flight measurements of single DNA molecules with two stacked nanopores," *Nano Letters*, vol. 11, no. 11, pp. 5002–5007, 2011.

[27] Z. D. Harms, K. B. Mogensen, P. S. Nunes, K. Zhou, B. W. Hildenbrand, I. Mitra, Z. Tan, A. Zlotnick, J. P. Kutter, and S. C. Jacobson, "Nanofluidic devices with two pores in series for resistive-pulse sensing of single virus capsids," *Analytical Chemistry*, vol. 83, no. 24, pp. 9573–9578, 2011.

[28] D. Pedone, M. Langecker, G. Abstreiter, and U. Rant, "A pore-cavity-pore device to trap and investigate single nanoparticles and DNA molecules in a femtoliter compartment: Confined diffusion and narrow escape," *Nano Letters*, vol. 11, no. 4, pp. 1561–1567, 2011.

[29] N. A. W. Bell, K. Chen, S. Ghosal, M. Ricci, and U. F. Keyser, "Asymmetric dynamics of DNA entering and exiting a strongly confining nanopore," *Nature Communications*, vol. 8, no. 1, p. 380, 2017.

[30] J. P. S. DesOrmeaux, J. D. Winans, S. E. Wayson, T. R. Gaborski, T. S. Khire, C. C. Striemer, and J. L. McGrath, "Nanoporous silicon nitride membranes fabricated from porous nanocrystalline silicon templates," *Nanoscale*, vol. 6, no. 18, p. 10798, 2014.

[31] S. R. Gillmer, D. Z. Fang, S. E. Wayson, J. D. Winans, N. Abdolrahim, J.-P. S. DesOrmeaux, J. Getpreecharsawas, J. D. Ellis, P. M. Fauchet, and J. L. McGrath, "Predicting the failure of ultrathin porous membranes in bulge tests," *Thin Solid Films*, vol. 631, pp. 152–160, 2017.

[32] K. Briggs, M. Charron, H. Kwok, T. Le, S. Chahal, J. Bustamante, M. Waugh, and V. Tabard-Cossa, "Kinetics of nanopore fabrication during controlled breakdown of dielectric membranes in solution," *Nanotechnology*, vol. 26, no. 8, 2015.

[33] E. Beamish, H. Kwok, V. Tabard-Cossa, and M. Godin, "Precise control of the size and noise of solid-state nanopores using high electric fields.," *Nanotechnology*, vol. 23, p. 405301, oct 2012.

[34] G. W. Slater, C. Holm, M. V. Chubynsky, H. W. de Haan, A. Dube, K. Grass, O. A. Hickey, C. Kingsburry, D. Sean, T. N. Shendruk, and L. Zhan, "Modeling the separation of macromolecules: A review of current computer simulation methods," *Electrophoresis*, vol. 30, no. 5, pp. 792–818, 2009.

[35] H. J. Limbach, A. Arnold, B. A. Mann, and C. Holm, "ESPResSo – An Extensible Simulation Package for Research on Soft Matter Systems," *Comp. Phys. Comm.*, vol. 174, pp. 704–727, may 2006.

[36] G. S. Grest and K. Kremer, "Molecular dynamics simulation for polymers in the presence of a heat bath," *Physical Review A*, vol. 33, no. 5, pp. 3628–3631, 1986.

[37] D. Stigter, "Interactions of Highly Charged Colloidal Cylinders with Applications to Double-Stranded DNA," *Biopolymers*, vol. 16, no. 7, pp. 1435–1448, 1977.

[38] E. S. Sobel and J. A. Harpst, "Effects of Na+ on the persistence length and excluded volume of T7 bacteriophage DNA," *Biopolymers*, vol. 31, no. 13, pp. 1559–1564, 1991.

[39] A. Savelyev, "Do monovalent mobile ions affect DNA's flexibility at high salt content?," *Physical Chemistry Chemical Physics*, vol. 14, no. 7, p. 2250, 2012.

[40] A. R. Klotz, L. Duong, M. Mamaev, H. W. De Haan, J. Z. Y. Chen, and W. W. Reisner, "Measuring the Confinement Free Energy and Effective Width of Single Polymer Chains via Single-Molecule Tetris," *Macromolecules*, vol. 48, no. 14, pp. 5028–5033, 2015.

[41] E. Anderson, Z. Bai, C. Bischof, S. Blackford, J. Demmel, J. Dongarra, J. Du Croz, A. Greenbaum, S. Hammarling, A. McKenney, and D. Sorensen, *LAPACK Users' Guide*. Philadelphia, PA: Society for Industrial and Applied Mathematics, third ed., 1999.

[42] F. Farahpour, A. Maleknejad, F. Varnik, and M. R. Ejtehadi, "Chain deformation in translocation phenomena," *Soft Matter*, vol. 9, no. 9, pp. 2750–2759, 2013.

[43] P. D. Ross and R. L. Scruggs, "Electrophoresis of DNA. III. The effect of several univalent electrolytes on the mobility of DNA," *Biopolymers*, vol. 2, no. 3, pp. 231–236, 1964.
[44] M. Mihovilovic, N. Hagerty, and D. Stein, "Statistics of DNA Capture by a Solid-State Nanopore," *Physical Review Letters*, vol. 110, no. 2, pp. 1–5, 2013.
[45] A. T. Carlsen, O. K. Zahid, J. Ruzicka, E. W. Taylor, and A. R. Hall, "Interpreting the conductance blockades of DNA translocations through solid-state nanopores," *ACS Nano*, vol. 8, no. 5, pp. 4754–4760, 2014.
[46] H. Kwok, K. Briggs, and V. Tabard-Cossa, "Nanopore fabrication by controlled dielectric breakdown.," *PLoS One*, vol. 9, p. e92880, jan 2014.
[47] M. Muthukumar and H. H. Katkar, "Reading nanopore clocks in single-molecule electrophoresis experiments," *Biophysical Journal*, vol. 108, no. 1, pp. 17–19, 2015.
[48] A. J. Storm, J. H. Chen, H. W. Zandbergen, and C. Dekker, "Translocation of double-strand DNA through a silicon oxide nanopore," *Physical Review E*, vol. 71, p. 051903, may 2005.
[49] H. W. De Haan, D. Sean, and G. W. Slater, "Using a Pèclet number for the translocation of a polymer through a nanopore to tune coarse-grained simulations to experimental conditions," *Physical Review E*, vol. 91, no. 2, pp. 1–10, 2015.
[50] T. Ikonen, A. Bhattacharya, T. Ala-Nissila, and W. Sung, "Unifying model of driven polymer translocation," *Physical Review E*, vol. 85, no. 5, pp. 1–7, 2012.
[51] I. Teraoka, *Polymer Solutions: An Introduction to Physical Properties*. John Wiley & Sons, Inc., 2002.
[52] P. Rowghanian and A. Y. Grosberg, "Electrophoretic capture of a DNA chain into a nanopore," *Physical Review E*, vol. 87, no. 4, pp. 1–8, 2013.
[53] S. Pud, S.-H. Chao, M. Belkin, D. Verschueren, T. Huijben, C. van Engelenburg, C. Dekker, and A. Aksimentiev, "Mechanical Trapping of DNA in a Double-Nanopore System," *Nano Letters*, vol. 16, no. 12, pp. 8021–8028, 2016.
[54] N. A. W. Bell, M. Muthukumar, and U. F. Keyser, "Translocation frequency of double-stranded DNA through a solid-state nanopore," *Physical Review E*, vol. 93, p. 022401, 2016.
[55] T. T. J. Morin, T. Shropshire, X. Liu, K. Briggs, C. Huynh, V. Tabard-Cossa, H. Wang, and W. W. B. Dunbar, "Nanopore-Based Target Sequence Detection.," *PLoS One*, vol. 11, no. 5, p. e0154426, 2016.
[56] A. Singer, M. Wanunu, W. Morrison, H. Kuhn, M. Frank-Kamenetskii, and A. Meller, "Nanopore based sequence specific detection of duplex DNA for genomic profiling," *Nano Letters*, vol. 10, no. 2, pp. 738–742, 2010.
[57] E. Atas, A. Singer, and A. Meller, "DNA sequencing and bar-coding using solid-state nanopores," *Electrophoresis*, vol. 33, no. 23, pp. 3437–3447, 2012.
[58] C. Plesa, J. W. Ruitenberg, M. J. Witteveen, and C. Dekker, "Detection of individual proteins bound along DNA using solid-state nanopores," *Nano Letters*, vol. 15, no. 5, pp. 3153–3158, 2015.

[59] M. van den Hout, A. R. Hall, M. Y. Wu, H. W. Zandbergen, C. Dekker, and N. H. Dekker, "Controlling nanopore size, shape and stability.," *Nanotechnology*, vol. 21, no. 11, p. 115304, 2010.

[60] R. Rollings, E. Graef, N. Walsh, S. Nandivada, M. Benamara, and J. Li, "The Effects of Geometry and Stability of Solid-state Nanopores on Detecting Single DNA molecules," *Nanotechnology*, vol. 26, no. 4, pp. 997–1003, 2015.

[61] M. Wanunu, W. Morrison, Y. Rabin, A. Y. Grosberg, and A. Meller, "Electrostatic focusing of unlabelled DNA into nanoscale pores using a salt gradient," *Nature Nanotechnology*, vol. 5, pp. 160–165, feb 2010.

[62] A. Balijepalli, J. Ettedgui, A. T. Cornio, J. W. F. Robertson, K. P. Cheung, J. J. Kasianowicz, and C. Vaz, "Quantifying short-lived events in multistate ionic current measurements.," *ACS Nano*, vol. 8, pp. 1547–53, feb 2014.

[63] J. H. Forstater, K. Briggs, J. W. F. Robertson, J. Ettedgui, O. Marie-Rose, C. Vaz, J. J. Kasianowicz, V. Tabard-Cossa, and A. Balijepalli, "MOSAIC: A Modular Single Molecule Analysis Interface for Decoding Multi-state Nanopore Data," *Analytical Chemistry*, vol. 88, no. 23, pp. 11900–11907, 2016.

[64] C. Raillon, P. Granjon, M. Graf, L. J. Steinbock, and A. Radenovic, "Fast and automatic processing of multi-level events in nanopore translocation experiments.," *Nanoscale*, vol. 4, pp. 4916–24, aug 2012.

Chapter 7

MOSAIC: A Modular Single-Molecule Analysis Interface for Decoding Multistate Nanopore Data

Jacob H. Forstater[1,3], Kyle Briggs[2], Joseph W.F. Robertson[1], Jessica Ettedgui[1,3], Olivier Marie-Rose[4], Canute Vaz[1], John J. Kasianowicz[1], Vincent Tabard-Cossa[2], and Arvind Balijepalli[1]

1 – Physical Measurement Laboratory, National Institute of Standards and Technology, Gaithersburg, Maryland 20899
2 – Department of Physics, University of Ottawa, Ottawa, Ontario K1N 6N5
3 – Department of Chemical Engineering, Columbia University, New York, New York 10027
4 – Information Technology Laboratory, National Institute of Standards and Technology, Gaithersburg, Maryland 20899

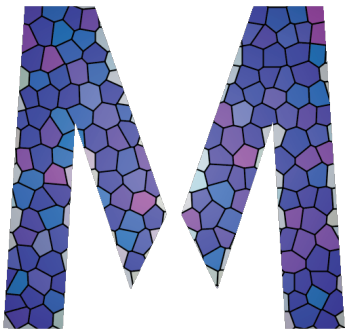

Adapted with permission from [J. H. Forstater, K. Briggs, J. W. F. Robertson, J. Ettedgui, O. Marie-Rose, C. Vaz, J. J. Kasianowicz, V. Tabard-Cossa, and A. Balijepalli, "MOSAIC: A Modular Single Molecule Analysis Interface for Decoding Multi-state Nanopore Data," *Analytical Chemistry*, vol. 88, no. 23, pp. 11900–11907, 2016]

Abstract

Biological and solid-state nanometer-scale pores are the basis for numerous emerging analytical technologies for use in precision medicine. We developed MOSAIC (Modular Single-molecule Analysis Interface), an open source analysis software that improves the accuracy and throughput of nanopore-based measurements. Two key algorithms are implemented: ADEPT, which uses a physical model of the nanopore system to characterize short-lived events that do not reach their steady state current, and CUSUM+, a version of the cumulative sum statistical method optimized for longer events that do. We show that ADEPT detects previously unreported conductance states that occur as double-stranded DNA translocates through a 2.4 nm solid-state nanopore, and reveals new interactions between short single-stranded DNA and the vestibule of a biological pore. These findings demonstrate the utility of MOSAIC and the ADEPT algorithm and offer a new tool that can improve the analysis of nanopore-based measurements.

7.1 Introduction

Protein and solid-state nanopores (Figure 7.1A) are the basis for single molecule measurements of a variety of analytes including ions[2,3], single-stranded RNA and DNA (ssDNA)[4–11] double-stranded DNA[12,13], proteins[14–20], synthetic polymers[21–24], and metallic nanoparticles[25,26]. The method is conceptually simple. An electric potential applied across a nanopore that spans two electrically isolated chambers (filled with electrolyte solution) results in an ionic current with a mean value $\langle i_0 \rangle$, and single molecules that reversibly partition into the pore cause a series of pulses or current blockades (Figure 7.1B). The change in pore conductance is caused by the volume exclusion of mobile ions from the pore[21,22] and interactions between the ions

and the analyte[6,22,27]. The change in conductance[5,21,22,27,28] and the residence time of analytes in the pore[9,21,22] are used to estimate the analyte size[21,22], effective charge[22], and dipole moment[29].

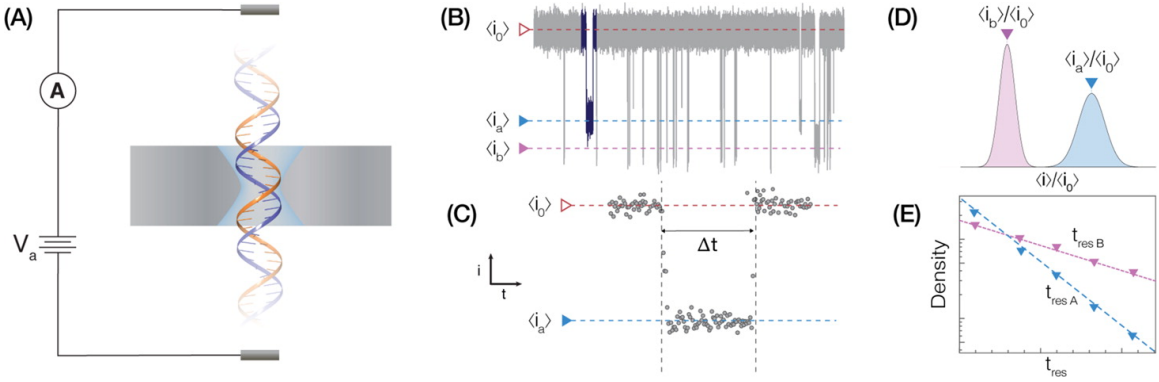

Figure 7.1: (A) Schematic illustration of DNA translocation through a solid-state nanopore. An electric potential applied across the pore produces an ionic current. (B) The partitioning of DNA into the pore causes well-defined current reduction with different mean current blockade amplitudes (e.g., $\langle i_a \rangle$ and $\langle i_b \rangle$). (C) A single level event is characterized by the ratio of the mean currents for the occupied and fully open pore ($\langle i_a \rangle / \langle i_b \rangle$ and the level residence time (Δt). (D) A histogram illustrating the relative current blockade depth for two species obtained by analysing the events. (E) Residence time distributions for the two blockade depths in the two populations. The mean residence times are estimated from fits to the distributions.

Analyte-induced events appear as single or multiple conductance state levels, arising from changes in the analyte conformation or interactions in the pore[10,12,21,22,28,30,31] (Figure 7.1C). Multiple conductance level events differ from the gating of ion channels, where the channel fluctuates between two states, open and closed[32]. These fluctuations are well characterized using hidden Markov models[33–35] and kinetic simulations[35,36]. On the other hand, several analysis techniques have been applied to analyse nanopore-based single-molecule data including threshold detection[5,22], slope- or area-based techniques[37,38], the cumulative sum (CUSUM) algorithm[39], charge conservation[38], and probabilistic machine-learning techniques[21,40]. While these approaches are effective when the residence times of analytes in the nanopore are long (compared

to the characteristic time constant of the system), they are not useful for characterizing short-lived events. To more accurately characterize these events, we developed a technique that models the ionic current response with an equivalent electrical circuit[27,41]. This algorithm, when applied to the interaction of a polydisperse mixture of a synthetic polymer with the *Staphylococcus aureus* α-hemolysin (αHL) nanopore, recovered 18-fold more events per unit time at high measurement bandwidth ($B = 100$ kHz), reduced the constraints on data acquisition by permitting polymers to be separated at lower bandwidth ($B = 10$ kHz), and improved the resolving power in the low mass regime (to polymers with molecular weight approximately 370 g/mol).

Here, we describe MOSAIC (Modular Single-molecule Analysis Interface), an improved data analysis tool for analysing nanopore data. We implemented two algorithms in MOSAIC: ADEPT, the equivalent electrical circuit model described previously[27,41], and an improved version of CUSUM that is suitable for analysing events with relatively long residence times in the pore. The software is extensible, and allows many commonly used data formats, signal conditioning, and data processing algorithms to be seamlessly integrated. Below, we demonstrate the features and utility of MOSAIC when applied to data measured with both biological and solid-state nanopores.

7.2 Architecture

MOSAIC consists of a modular data processing pipeline, shown schematically in Fig. 7.2. Five self-contained modules provide the building blocks of the pipeline, which together allows the analysis of data from single-molecule nanopore experiments: (i) load data, (ii) optional signal conditioning and filtering, (iii) event detection, (iv) event analysis, and (v) results storage. MOSAIC was designed using object-oriented

concepts. This allowed us to leverage polymorphism within individual modules to customize functionality and promote interoperability. Module interoperability is also ensured through a well-defined interface. This approach makes it straightforward for users to implement new features into the software, such as other analysis algorithms or loading custom data formats. In most cases, users interact with MOSAIC using a custom graphical user interface (Figure 7.11) that uses the pipeline architecture. Here we briefly describe the key elements of that pipeline architecture.

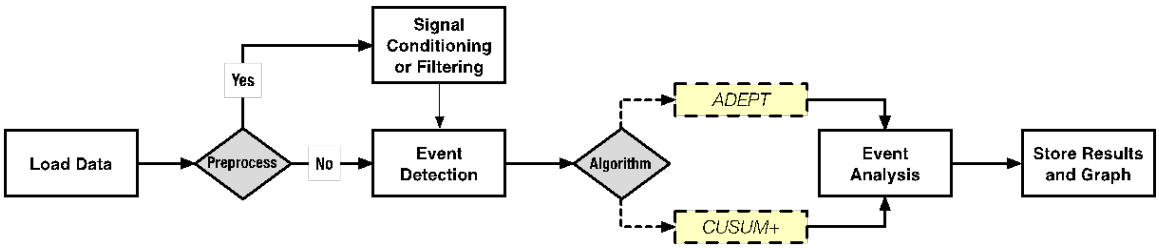

Figure 7.2: The MOSAIC processing pipeline comprises of five modules that perform well-defined functions. By enforcing a common interface, individual functions can be easily customized in a manner that allows them to interoperate with other parts of the pipeline. Choices in this diagram are made by the user prior to analysis.

7.2.1 Load Data

This module allows users to load raw current traces from nanopore experiments into MOSAIC. Axon binary format (ABF) by Molecular Devices Axopatch amplifiers and QUB data files (QDF) are supported natively. In addition, MOSAIC can read a wide variety of raw binary file format for data saved with custom hardware. Data from disk is first loaded into a first-in, first-out (FIFO) queue after applying the specified signal conditioning steps (setting amplifier scale and offsets, correcting for systematic artefacts, etc.). Downstream modules request data in blocks for subsequent processing. The Load Data module adds data to the FIFO queue on demand until the end of the data set is reached. Because the logic for the data access is implemented as

part of the common interface, new data types can be added to MOSAIC by simply reading in individual files and making the data available to the FIFO queue.

7.2.2 Filtering

MOSAIC allows acquired data to be filtered prior to analysis by applying the optional Filtering module. While this module is not a substitute for anti-alias filtering, it allows the data bandwidth and sampling to be controlled in software[42]. High frequency noise, resulting from amplifier noise or charge trapping in solid-state measurements can hinder the measurement of short events (shorter than 100 μs). In some cases, the signal-to-noise ratio (SNR) can be improved by filtering data, albeit with distortion of the signal shape[37]. MOSAIC provides multiple options for data filtering including Bessel which has a well-behaved response to signal transients. Alternatively, arbitrary filters (finite impulse response filters, weighted moving averages, etc.) can be implemented using a tap-delay line[43]. Finally, this module provides experimental support for wavelet-based filtering[43], which allows a signal to be denoised while preserving SNR and pulse shape.

7.2.3 Event Detection

This module partitions the time-series to detect individual interactions of single molecules with the nanopore. Currently, we have implemented a simple thresholding algorithm that detects deviations of the ionic current from the open channel baseline value[21,22,37]. To discern statistically meaningful events, we heuristically set the current threshold. Typical values range from 2.5 to 6 times the standard deviation of the open channel current, σ. The end of an event is registered when the ionic current returns to the open-channel baseline. The segment of the time-series corresponding to the

event is then processed further using the Event Fitting/Analysis module.

7.2.4 Event Analysis

Detected events are analysed using the user-selected algorithm as described in the main text. Currently two algorithms, ADEPT and CUSUM+, are available. However, additional algorithms can be added. The parameters and associated metadata of successfully analysed events are stored in a SQLite database (Figure 7.3) for future analysis. Events with processing or analysis errors are flagged within the database.

7.2.5 Store Results and Graph

The results generated by the Event Fitting/Analysis module are stored in a SQLite database. The use of a relational database for storage enables rapid, non-platform specific data storage and access and allows users to explore the data and analyse it further using external applications. The database schema for the ADEPT is shown in Figure 7.3A. Primary metadata generated from the analysis of individual events in a time-series are stored in the metadata table. The `analysisinfo` table holds additional analysis information needed to make the database self-contained. Finally, the `analysissettings` table holds the settings used to run the analysis and the output log of the analysis is stored in the `analysislog` table. A brief description of the metadata generated by the ADEPT algorithm is presented in Figure 7.3B. An up-to-date listing of metadata of all algorithms available in MOSAIC is available at https://pages.nist.gov/mosaic/.

A

metadata	[table]
recIDX	INTEGER
ProcessingStatus	TEXT
OpenChCurrent	REAL
NStates	INTEGER
CurrentStep	BLOB
BlockDepth	BLOB
EventStart	REAL
EventEnd	REAL
EventDelay	BLOB
StateResTime	BLOB
ResTime	REAL
RCConstant	BLOB
AbsEventStart	REAL
ReducedChiSquared	REAL
ProcessTime	REAL
TimeSeries	BLOB

analysisinfo	[table]
datPath	TEXT
dataType	TEXT
partitionAlgorithm	TEXT
processingAlgorithm	TEXT
filteringAlgorithm	TEXT
analysisTimeSec	REAL
dataLengthSec	REAL
FsHz	REAL
mosaicVer	TEXT
mosaicBuild	TEXT
recIDX	INTEGER

analysissettings	[table]
settings	TEXT
recIDX	INTEGER

analysislog	[table]
logstring	TEXT
recIDX	INTEGER

B

metadata	
recIDX	Record index
ProcessingStatus	Status of the analysis
OpenChCurrent	Open channel current in pA.
NStates	Number of detected states.
CurrentStep	Blocked current steps in pA.
BlockDepth	BlockedCurrent/OpenChCurrent for each state.
EventStart	Event start in ms.
EventEnd	Event end in ms.
EventDelay	Start time of each state in ms.
StateResTime	Residence time of each state in ms.
ResTime	EventEnd-EventStart in ms.
RCConstant	System RC constant in ms.
AbsEventStart	Global event start time in ms.
ReducedChiSquared	Reduced Chi-squared of fit.
ProcessTime	Analysis time in ms.
TimeSeries	Event time-series data.

Figure 7.3: (A) Database schema for ADEPT algorithm output in MOSAIC. Primary metadata associated with processed events are stored in the metadata table. (B) A description of the metadata columns of ADEPT.

7.3 Algorithms

In this section, we discuss two algorithms implemented in MOSAIC: (i) CUSUM+, an improved version of the CUSUM algorithm[39] that provides robust statistical analysis of events which converge to a steady state, and (ii) ADEPT, an implementation of a previously developed theory[27,41] that uses a physical model of the nanopore system to accurately characterize very short events that do not approach a steady state ionic current.

7.3.1 Cumulative Sum Analysis (CUSUM+)

Cumulative Sum (CUSUM) is a commonly used method to detect step-like changes in time-series data[44], but was only recently implemented in nanopore analysis[39]. It assumes that the interaction of an analyte with the pore causes a series of instantaneous changes in the ionic current from its baseline value (defined as states, and well-approximated by step functions[44]), and that the ionic current noise follows a known distribution (e.g., Gaussian, which is generally the case for nanopore data). A statistical test identifies when the current level changes. The instantaneous log-likelihood ratios of sequential data points for both positive and negative step changes are calculated. The positive values of these ratios are independently summed and a negative log-likelihood resets the sum to zero. These form a two-sided decision function, which detects level changes that correspond to either an increase or decrease in the current level. A new state is identified when one of the decision functions exceeds a threshold determined automatically by the software. The locations of state changes are determined from the minima of related functions[44], and the mean ionic current between sequential states is calculated and used to determine the local blockade depth, defined as ratio of the ionic current when the pore is occupied to that of the open pore ($\langle i \rangle / \langle i_0 \rangle$, Figure 7.1C).

We implemented an improved version of the CUSUM algorithm in MOSAIC called CUSUM+, which is less sensitive to artifacts that can be falsely identified as a state change. This is achieved by specifying a minimum time between successive triggers (to exclude transients from the state change detection and blockade depth calculations) and by requiring that identified state levels differ by a minimum value (corresponding to a physically significant change). State changes are not required to be quantized. Efficiency is improved by eliminating or reducing the computations (e.g., maintaining

running calculations of the mean and variance).

7.3.2 Adaptive Time-Series Analysis (ADEPT)

For very long events (longer than 5τ, Figure 7.4 left), the blockade depth is easily estimated (e.g., with CUSUM+). However, that process fails for short-lived events (shorter than 5τ, Figure 7.4 right) that do not reach a steady-state mean value. In this case, the blockade depths are estimated by fitting the data to an electrical circuit model of the nanopore (implemented as ADEPT[27,41] in MOSAIC). The algorithm assumes a molecule partitioning into the nanopore instantaneously increases the nanopore resistance (R_p) by ΔR. However, the system capacitance causes the ionic current change to occur over a finite time. For a constant applied voltage, V_a, the predicted ionic current is

$$i(t) = i_0 - \beta\left(1 - \exp\left(-\frac{t}{\tau}\right)\right), \tag{7.1}$$

where

$$i_0 = \frac{V_a}{R_s + R_p}, \tag{7.2}$$

$$\beta = \frac{V_a \Delta R}{(R_s + R_p + \Delta R)(R_s + R_p)}, \tag{7.3}$$

and

$$\tau = \frac{C_m R_s (R_p + \Delta R)}{R_s + R_p + \Delta R}. \tag{7.4}$$

The actual difference between the time constants leading up to and following an event are considerably shorter than the sampling rate used in most experiments. For example, the partitioning of DNA into an αHL nanopore, discussed in paper, produces

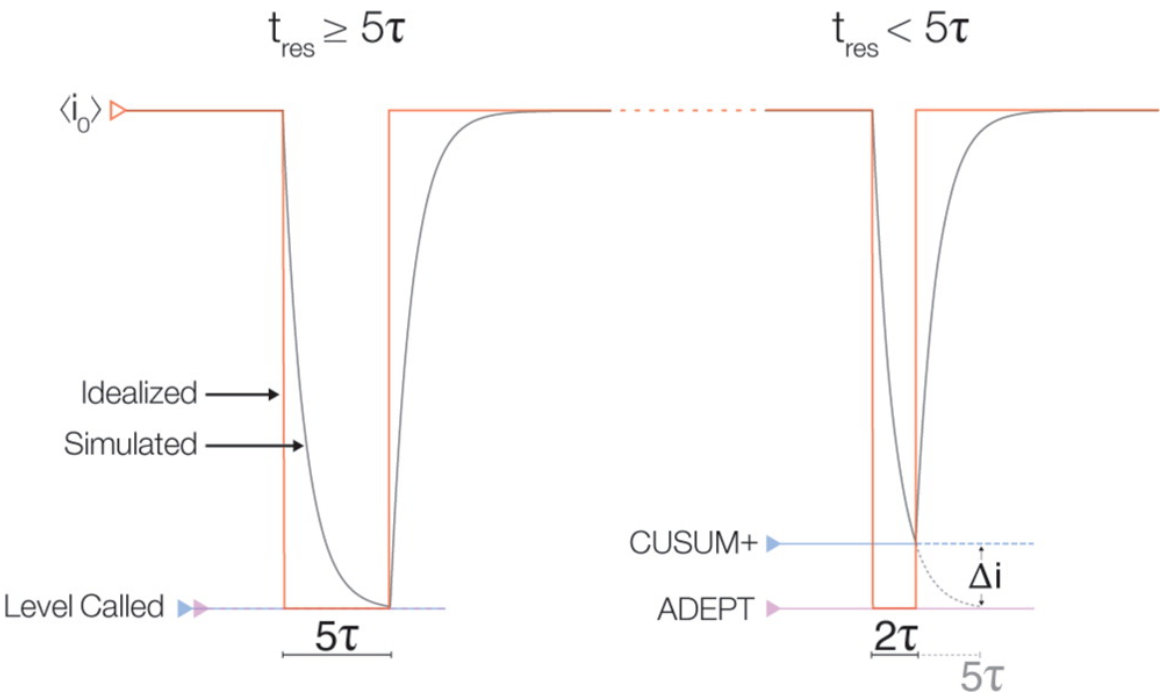

Figure 7.4: ADEPT and CUSUM+ analysis applied to a simulated nanopore measurement generated using Equation 7.1 (gray). Two events with the same current blockade (red), but different residence times (tres), with respect to the system characteristic relaxation time (τ) are shown. (Left) For a long event ($t_{res} \geq 5\tau$), the ionic current converges close to its steady-state value, and the current levels estimated by ADEPT and CUSUM+ are equivalent. (Right) For short events (e.g., $t_{res} \approx 2\tau$), the current does not reach the steady state value of the idealized pulse (red). In this case, CUSUM+ and other algorithms used in nanopore analysis systematically underestimate the steady-state current (blue) by an amount Δi (gray; dashed). In contrast, the physical model underlying ADEPT allows the algorithm to accurately estimate an event's steady-state current.

a blockade depth ratio, $\langle i \rangle / \langle i_0 \rangle \approx 0.1$. For typical experimental parameters, the time constant associated with entry and exit of the DNA into the nanopore will differ by by 293 ns (assuming $R_p = 0.8$ GΩ, $R_s = 50$ MΩ, $C_m = 2$ pF, and ΔR = 7.2 GΩ). This change is even smaller (237 ps) for solid state nanopores[45,46]. Because these differences are 10^3 times shorter than the duration between sampled points (2 μs) at a sampling rate $F_s = 500$ kHz, they cannot be resolved by our measurements. We therefore utilize a single fit parameter for τ, which reduces the degrees of freedom in

the fit. For cases where these assumptions do not hold, there is an option to override this constraint in the software.

7.4 Results and Discussion

7.4.1 Analysis of Short dsDNA Fragments in SiN_x Nanopores

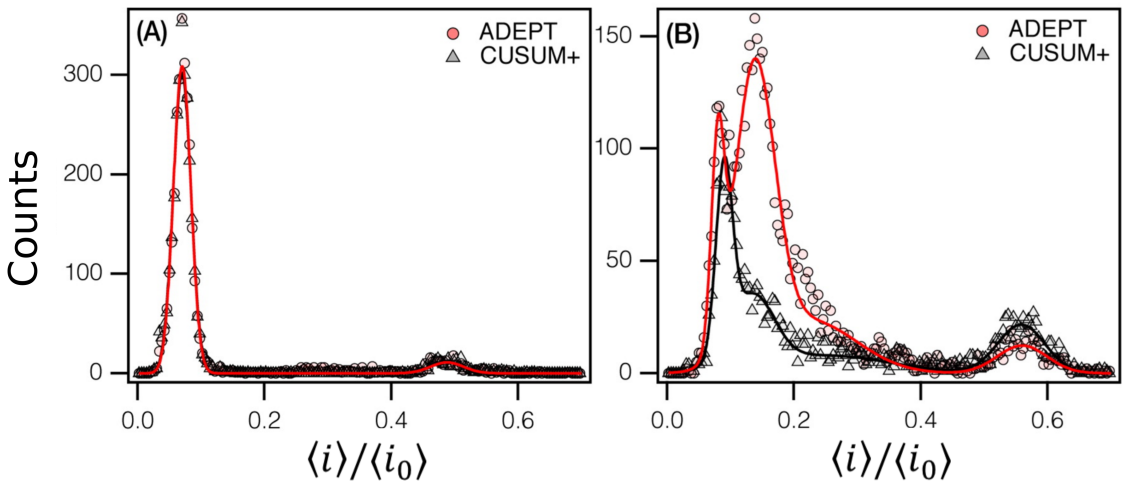

Figure 7.5: Blockade depth histograms for a 50 base pair double-stranded DNA measured with a 2.4 nm diameter SiN_x nanopore[46]. (A) At 400 mV, dsDNA, both CUSUM+ (gray) and ADEPT (red) are in excellent agreement. (B) At 800 mV, the mean residence time decreases to 36 μs (estimated from ADEPT analysis). The analyses by ADEPT and CUSUM+ are markedly different.

We compared the results of CUSUM+ and ADEPT on measurements of 50 base pair (bp) double-stranded DNA (dsDNA) translocating through a 2.4 nm diameter SiN_x nanopore ($2,800$ events)[46]. At an applied potential of 400 mV, the mean residence time of dsDNA in the pore is 440 μs, more than an order of magnitude longer than the characteristic time constant of the system ($\tau \approx 10$ μs; $B = 100$ kHz). Both algorithms produce two distinct peaks in the blockade depth histogram

Table 7.1: Parameters used in the analysis of dsDNA with a solid-state nanopore.

Parameter	ADEPT 400 mV	ADEPT 800 mV	CUSUM+ 400 mV	CUSUM+ 800 mV
Event Identificaiton Threshold ($\times\sigma$)	5	5	5	5
Min. Event Length (samples)	5	5	5	5
Block Size (s)	2	2	2	2
StepSize	9	9	9	18
Min. Threshold			0.1	0.1
Min. State Length (samples)	10	10	10	10
Max. Event Length (samples)	15000	15000	-	-
Fit Iterations	50000	5000	-	-
Fit Tolerance	10^{-7}	10^{-7}	-	-

($\langle i\rangle/\langle i_0\rangle = 0.070 \pm 0.001$ and 0.488 ± 0.004. Peak positions were obtained using an error-weighted Gaussian fit and are reported with an expanded uncertainty, $k = 2$ (see Table 7.1 for a full listing of the analysis and fit parameters). The leftmost peak corresponds to DNA translocation, whereas the rightmost peak is likely due to the helical structure of dsDNA unwinding to transition from the B-form to the S-form dsDNA[47,48] where the chain elongates by 1.7× because of the strong electric field gradient across the pore[46].

At 800 mV, the blockade depth histogram produced by ADEPT has two overlapping peaks (Figure 7.5B) consisting of a narrow peak ($\langle i\rangle/\langle i_0\rangle = 0.080 \pm 0.002$), the expected location for B-form dsDNA[47], and a broader peak ($\langle i\rangle/\langle i_0\rangle = 0.138 \pm 0.002$). The latter is comprised of short, single-level events, which likely result from transient interactions between the dsDNA and the access region outside the pore[49]. This was not accurately identified in our previous analysis[46]. A third, low amplitude, broad

Table 7.2: Blockade depth peaks and amplitude, as a function of voltage and algorithm, for 50 bp dsDNA interaction with a solid-state nanopore. Peak locations are obtained from an error-weighted fit of the data to a sum of three Gaussians; individual bin errors were assumed to follow a Poisson error distribution. Expanded uncertainty for individual fit parameters ($k = 2$) is reported.

	$\langle i \rangle / \langle i_0 \rangle$	Amplitude
ADEPT 400 mV	0.070 ± 0.001	309.0 ± 15.1
	0.488 ± 0.004	11.0 ± 1.1
CUSUM+ 400 mV	0.070 ± 0.001	301.6 ± 7.4
	0.486 ± 0.004	11.7 ± 1.1
ADEPT 800 mV	0.080 ± 0.002	86.5 ± 6.5
	0.138 ± 0.002	128.7 ± 3.9
	0.226 ± 0.018	23.1 ± 1.9
	0.260 ± 0.005	12.6 ± 0.9
CUSUM+ 800 mV	0.090 ± 0.002	80.8 ± 5.7
	0.134 ± 0.010	31.3 ± 2.7
	0.250 ± 0.030	8.0 ± 0.7
	0.559 ± 0.004	21.6 ± 1.2

peak is visible at $\langle i \rangle / \langle i_0 \rangle = 0.226 \pm 0.018$. It is probable that this peak is associated with these access-region interactions, although it is possible that these events could represent partial unwinding of the dsDNA secondary structure at forces below the B-S stretching transition threshold[48]. As seen in Figure 37.5, CUSUM+ also detects the first peak, $\langle i \rangle / \langle i_0 \rangle = 0.090 \pm 0.002$ (albeit slightly shifted compared to the ADEPT value). However, it only characterizes approximately 20% of the events in the second peak ($\langle i \rangle / \langle i_0 \rangle = 0.134 \pm 0.010$), where the mean residence time of the events ($\langle t_{res} \rangle = 47 \pm 4$ μs) is less than 5τ. In addition, CUSUM+ misses most of the events from the third peak detected with ADEPT. While CUSUM+ could be allowed to characterize events with lifetimes less than 5τ, it will underestimate the blockade depth ratios, as shown in Figure 7.6. Both algorithms identify the fourth peak ($\langle i \rangle / \langle i_0 \rangle \approx 0.56$), which arises from the stretching transition of dsDNA noted above

(S-form of dsDNA[47,48]). CUSUM+ recovers more events here than ADEPT, which utilizes a fitting routine that may not converge for some very long events ($t_{res} > 25$ ms; $50,000$ points; $F_s = 500$ kHz). Because CUSUM+ can only correctly identify states that have reached their steady state value (with residence times greater than 5τ) we normally exclude events less than 5τ from CUSUM+ analysis.

Relaxing this constraint results in a systematic underestimation of the ionic current when DNA occupies the pore, causing the blockade depth histogram to shift to the right (7.6). This underestimation will also apply to sub-states shorter than 5τ within a longer event.

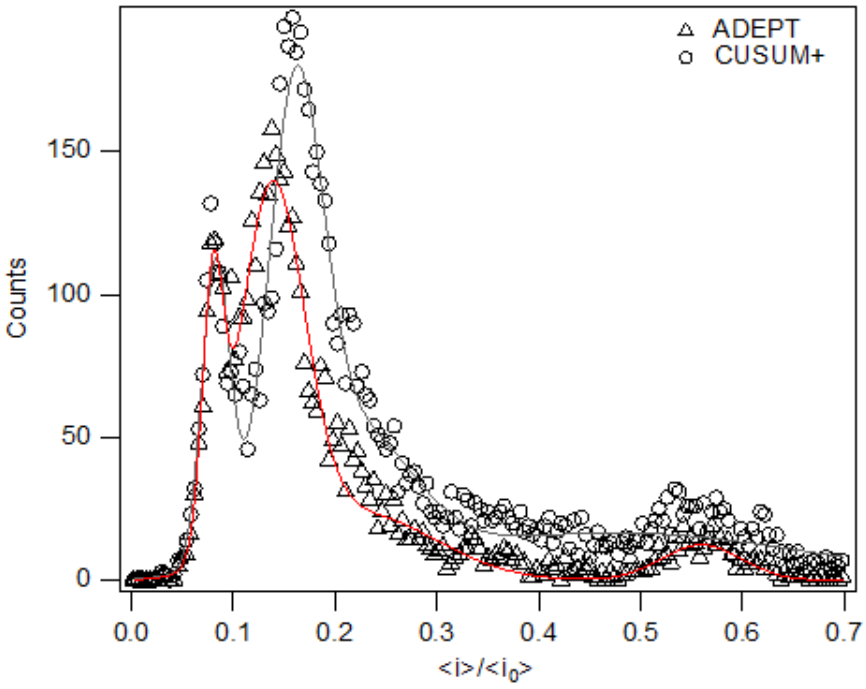

Figure 7.6: A comparison of ADEPT (red) and CUSUM+ (grey) blockade depths for dsDNA events with a minimum length of 2τ. Including events in CUSUM+ that do not converge to a steady state (less than 5τ) results in a systematic shift in the peak positions.

In some instances, ADEPT exhibits poor convergence for events with more than 10^4 points. This is seen in Figure 7.5B, where CUSUM+ recovers around 11% more

events for the peak at $\langle i \rangle / \langle i_0 \rangle = 0.56 \pm 0.01$, which contains characteristically long events. Therefore, the overall result can be improved when both algorithms are used in a complementary manner using ADEPT to fit short events and CUSUM+ to fit long ones, as seen in Figure 7.7.

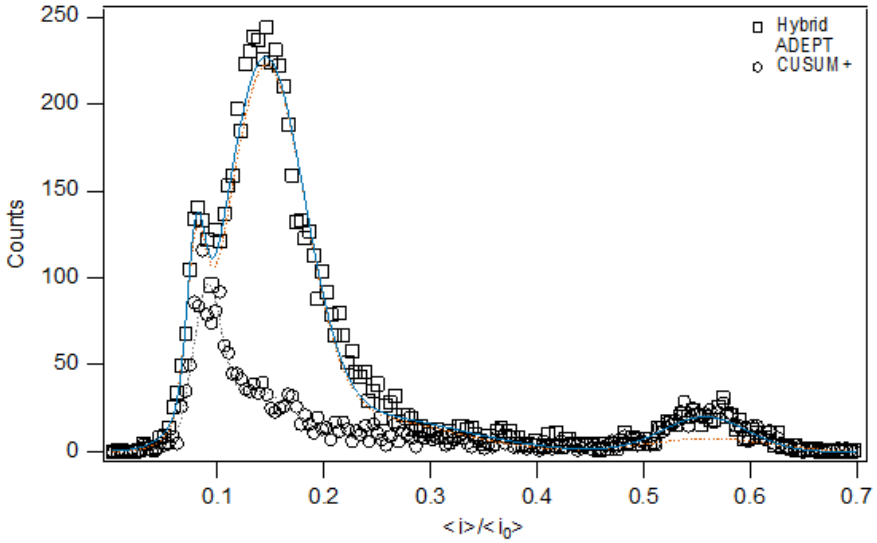

Figure 7.7: A proof of concept hybrid approach (Blue, rectangles) that merges the results of ADEPT (Orange, triangles) and CUSUM+ (Gray, circles) improves the analysis of the dsDNA data.

Clearly, the results would be improved if ADEPT is used for relatively short-lived events (shorter than 5τ) and CUSUM+ used on events with residence times longer than 5τ (Figure 7.7). This functionality will be implemented in a future version of MOSAIC.

While both CUSUM+ and ADEPT produce comparable results for events with residence times greater than 5τ, the statistical approach used in CUSUM+ is on average approximately $10\times$ faster than the Levenberg-Marquardt least squares fitting used in ADEPT[49]. Therefore, CUSUM+ is preferred for events with mean residence times considerably longer than the recovery time of the system (greater than 5τ). Furthermore, the processing time per event for each algorithm scales linearly with

the residence time, and therefore the number of data points in an event. Table 7.2 summarizes the fitting results with both algorithms.

7.4.2 Analysis of ssDNA Oligonucleotides with ADEPT

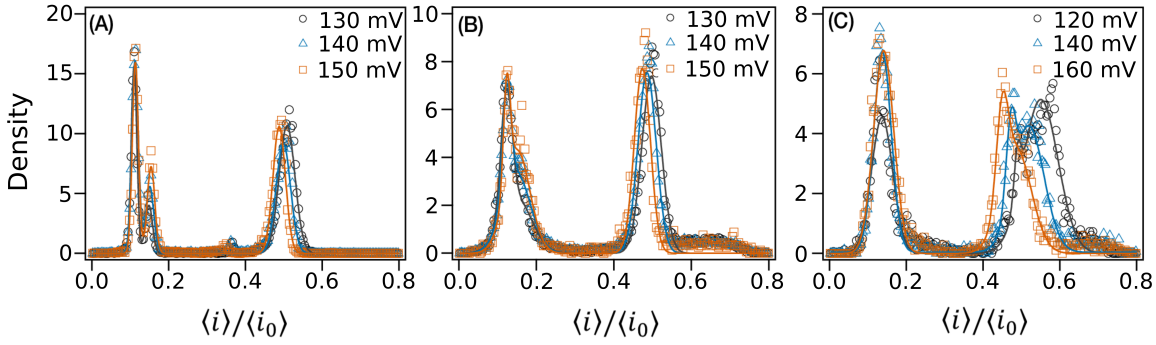

Figure 7.8: Blockade depth histograms for dA_{100}, dA_{40} and dA_{20} ssDNA translocation from the cis side of αHL nanopore at as a function of voltage. Peak fits shown were obtained using an error-weighted fit to a sum of Gaussians, as indicated in the text.

We use ADEPT to determine the blockade depth ratio histograms for three different length single stranded DNA (ssDNA) homopolymers (dA_{100}, dA_{40} and dA_{20}) entering an αHL nanopore from the cis side[50]. We consider events with up to 6 discrete states, with each state containing at least 5 data points ($t_{res} > 10$ μs, $F_s = 500$ kHz). Events are partitioned from the time series data with a thresholding algorithm that identifies when the current changes by more than 5 standard deviations from the mean open channel current. A complete listing of the analysis parameters is shown in Table 7.3.

We examine the translocation of homopolymer poly$(dA)_n$ through the nanopore (cis)[50], as a function of hompolymer length and applied potential. The blockade depth produced by the oligonucleotides as they enter from the cis side of the pore are shown in Figure 7.8 as a function of applied potential. At an applied potential of 130 mV, the blockade depth histogram of dA_{100} has three distinct peaks, $\langle i \rangle / \langle i_0 \rangle = (0.11 \pm$

Table 7.3: Parameters used in the analysis of ssDNA with a protein nanopore with ADEPT

Parameter	dA_{100}	dA_{40}	dA_{20}
Event Identification Threshold ($\times\sigma$)	5	5	5
Min. Event Length (data points)	5	5	5
Block Size (s)	0.5	0.5	0.5
StepSize	9	9	9
Min. State Length (data points)	5	5	5
Max. Event Length (data points)	50000	100000	10000
Fit Iterations	5000	5000	5000
Fit Tolerance	10^{-7}	10^{-7}	10^{-7}

0.01), (0.15 ± 0.03), and (0.51 ± 0.02). The first two peaks (denoted $\langle i \rangle / \langle i_0 \rangle_{3'}$ and $\langle i \rangle / \langle i_0 \rangle_{5'}$) are consistent with the dependence of the blockade depth on the orientation of the leading end of the DNA entering the pore ($3'$ vs $5'$)[5,51,52]. The location of these two peaks agrees with previous measurements of dA_{100}, where two broad overlapping peaks were observed at similar locations[7].

These differences are not as clearly observed in the shorter ssDNA. As seen in Figures 7.8B—C, the position of the $3'$ peak of dA_{40} and dA_{20} does not change with voltage. The amplitude of the $5'$ peak decreases substantially for measurements of dA_{40} (Fig 7.8B) and is not observed for dA_{20} (Figure 7.8C), likely due to both the lower probability of $5'$ entry as well as the decreasing residence time of shorter ssDNA[51].

The current blockades observed with poly(dA) appear as either one level (a shallow or deep blockade) or two levels (a shallow blockade followed by a deeper one[9,53,54]), and approximately 60% of the events have two levels. As shown in the blockade depth ratio histograms for dA_{100}, dA_{40}, and dA_{20} (Figure 7.8, blue), these two observed levels are comprised of several different states. Figure 7.8A, shows that the blockade depth

histogram for dA_{100} has three peaks, $\langle i \rangle / \langle i_0 \rangle = (0.11 \pm 0.03)(0.11 \pm 0.03)$, (0.15 ± 0.05), and (0.50 ± 0.05). The first two peaks (denoted $\langle i \rangle / \langle i_0 \rangle 3'$ and $\langle i \rangle / \langle i_0 \rangle 5'$) are consistent with the dependence of the blockade depth on the orientation of the leading end of the DNA ($3'$ vs. $5'$) entering the pore[5,51,52]. The location of these two peaks agrees with previous measurements of dA_{100}, where two highly overlapping peaks were observed at these locations[7]. In contrast to earlier measurements, we resolve the $3'$ and $5'$ events with a separation better than 3σ.

The differences between the $3'$ and $5'$ blockade depth peaks (Figure 7.8A, two left-most peaks) are progressively more difficult to discern for the shorter polynucleotides (Figures 7.8B and 7.8C). The amplitude of the $5'$ peak decreases substantially for dA_{40} (Figure 7.8B) and is not resolved for dA_{20} (Figure 7.8C). These results are likely due to the lower probability of the $5'$-end's entry into the pore and the decreasing residence time of shorter ssDNA molecules[5,51].

Interestingly, the shallow blockade level ($\langle i \rangle / \langle i_0 \rangle \approx 0.5$) is characterized by a single peak for dA_{100} and dA_{40}, and two peaks for dA_{20}, as seen in Figure 7.8. Previous studies have either not reported this peak[7], or noted it for molecules as short as dA_{50}[53]. Furthermore, the sharp decrease in residence time associated with shorter polymers complicates their analysis and has thus far limited the analysis of nucleotides as short as dA_{20}.

The algorithms within MOSAIC improve the characterization of short polynucleotides. Figure 7.9 shows the voltage dependent behavior of the dA_{20} shallow blockade peaks and their residence time distributions. The shallow blockade depth distributions are qualitatively different than those measured for longer polymers (Figure 7.8) as noted previously. Furthermore, we observe a change in the morphology of the peaks with increasing voltage as seen in Figure 7.9A. In particular, increasing the magnitude of the applied potential: i) shifts the peaks to smaller $\langle i \rangle / \langle i_0 \rangle$ values,

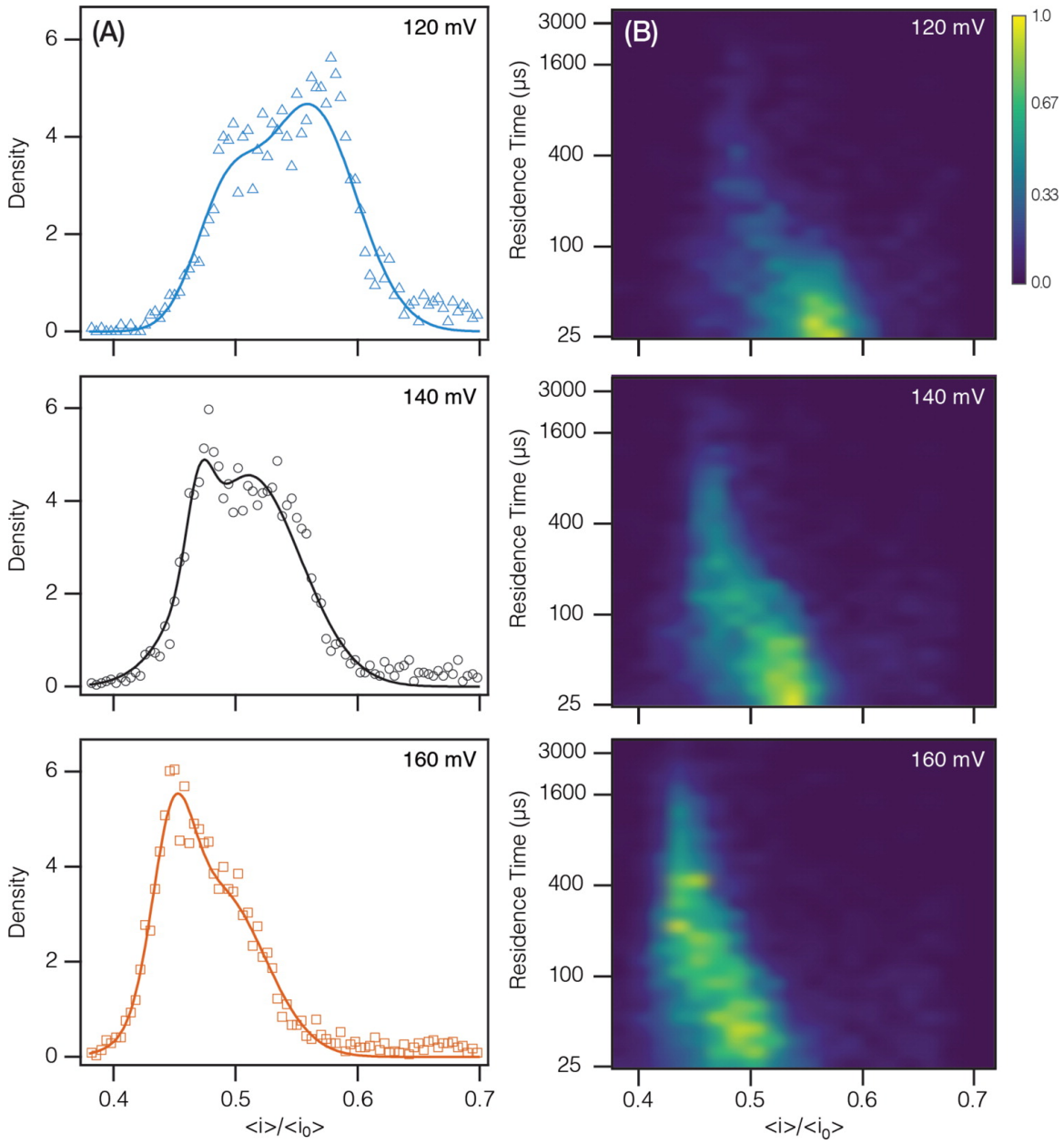

Figure 7.9: Voltage dependence of dA_{20} shallow blockade depth and residence time. (a) Blockade depth histogram from $\langle i \rangle / \langle i_0 \rangle = 0.38$ to 0.7 as a function of voltage. Each blockade depth histogram was normalized to yield a probability density. (B) A joint residence time-blockade depth distribution (log-linear) as a function of voltage. Z-scale (color) was normalized and smoothed using a Gaussian interpolation.

i.e., the polynucleotide blocks more current (Figure 7.9A), ii) increases the residence times (Figure 7.9B) (in contrast to the mean residence time of the deep blockades in

Figure 7.8 that are associated with translocation)[3,6], and iii) increases the number of events observed per unit time (capture rate) (Figure 7.10). With increasing voltage, the shallow blockades were more likely to exhibit two states with the shallow blockade preceding a deep blockade.

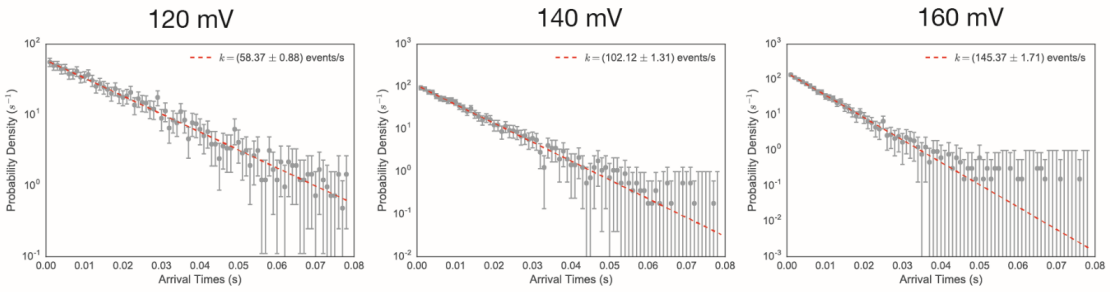

Figure 7.10: Normalized probability distribution of arrival times (log-linear plot) for dA_{20}. Error bars indicate the standard error for Poisson counting; bins with zero counts were assigned an error of $\sigma = 1$. Mean residence times for each voltage are shown in the plot legend. To accurately calculate the mean capture rate from the arrival times we include all events with 4 or more data points, regardless of whether they can be fit by ADEPT. The arrival times (defined as the time between the start of adjacent events) follow an exponential distribution.

The above results strongly suggest that the shallow blockade peaks correspond to dA_{20} interacting with the vestibule, but not translocating through the pore. Moreover, the observed increase in the residence time of the shallow blockade (Figure 7.9B) with voltage suggests that the change in the leftmost peak amplitude in Figure 7.9A is likely due to interactions between the analyte and different regions of the vestibule, rather than a loss of signal. Interestingly, of the three measured analytes (dA_{100}, dA_{40}, dA_{20}), this voltage dependent change in peak structure was only observed with dA_{20}, indicating that the phenomenon may be length-dependent[50,55]. Table 7.4 summarizes fitting results for these polymers.

Table 7.4: Blockade depth peaks, as a function of voltage, for different lengths of dA interaction with αHL. Peak locations are obtained from an error-weighted fit of the data to a sum of three Gaussians; individual bin errors were assumed to follow a Poisson error distribution. Expanded uncertainty for individual fit parameters ($k = 2$) is reported.

	Voltage (mV)	$\langle i \rangle / \langle i_0 \rangle_{3'}$	$\langle i \rangle / \langle i_0 \rangle_{5'}$	$\langle i \rangle / \langle i_0 \rangle_{a}$	$\langle i \rangle / \langle i_0 \rangle_{b}$
dA_{100}	130	0.11 ± 0.02	0.15 ± 0.08	0.51 ± 0.07	-
	140	0.11 ± 0.02	0.15 ± 0.05	0.50 ± 0.05	-
	150	0.11 ± 0.01	0.16 ± 0.02	0.49 ± 0.02	-
dA_{40}	130	0.12 ± 0.06	0.15 ± 0.13	0.49 ± 0.02	-
	140	0.12 ± 0.07	0.15 ± 0.11	0.50 ± 0.04	-
	150	0.12 ± 0.03	0.15 ± 0.04	0.47 ± 0.02	-
dA_{20}	130	0.13 ± 0.02	-	0.49 ± 0.25	0.56 ± 0.12
	140	0.14 ± 0.02	-	0.47 ± 0.08	0.51 ± 0.05
	150	0.14 ± 0.02	-	0.45 ± 0.07	0.49 ± 0.10

7.4.3 Single Molecule Mass Spectrometry with a Biological Nanopore

We show a typical analysis using MOSAIC's graphical user interface. Specifically, we use both CUSUM+ and ADEPT to identify polymers by size in polydisperse PEG samples with an αHL nanopore[21–23,27,56,57]. Note that due to their lower isoelectric point, in the pH 7.2 buffer used here, PEG molecules are weakly negatively charged. Previous studies showed that the blockade depth ratio ($\langle i \rangle / \langle i_0 \rangle$) and mean residence time of these events scale monotonically with polymer size.

Analysis of the PEG data is set up using the GUI shown in Figure 7.11, and is configured using drop down menus. Table 7.5 summarizes the fitting parameters. After selecting a data source (MOSAIC accepts most common electrophysiology data formats: Axon ABF, QUB QDF, as well as raw binary and comma separated value, CSV, data), a segment of the time series is displayed, which assists in determining the mean open channel current ($\langle i_0 \rangle$), noise (σ_{i_0}) and threshold values for preliminary

event identification.

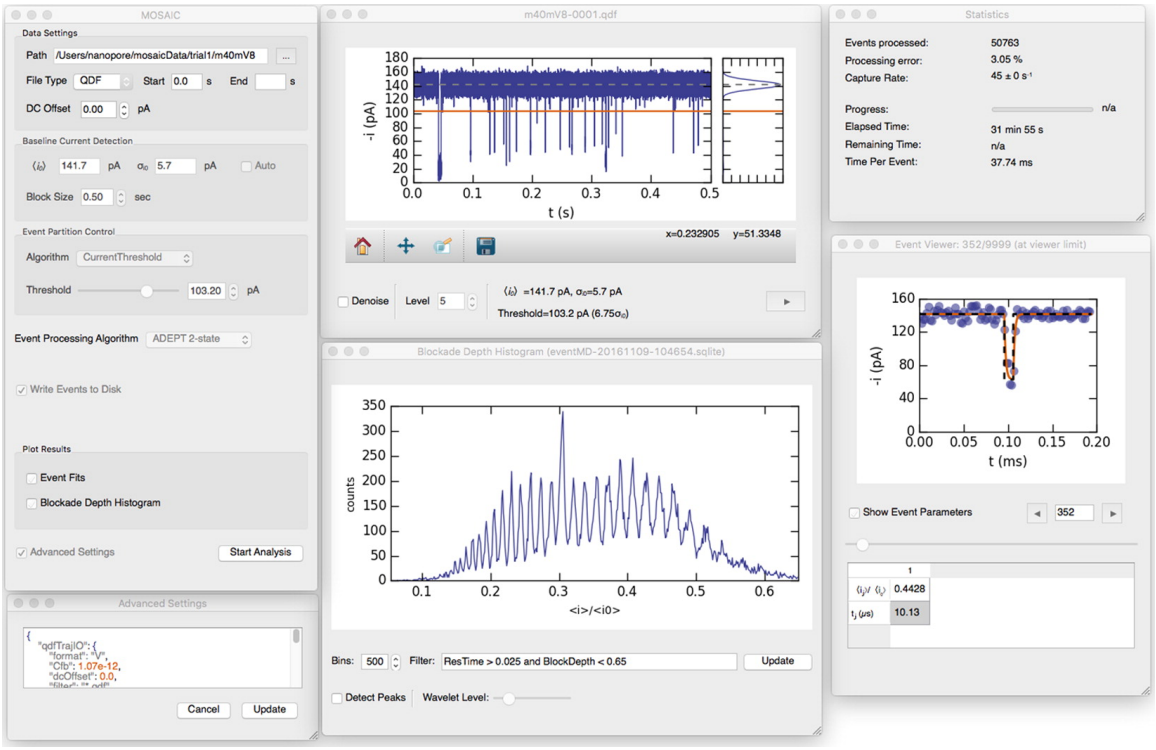

Figure 7.11: The graphical user interface (GUI) used to setup and run an analysis in MOSAIC. A main settings window is used to configure the analysis. The results of an analysis are displayed in real-time in the adjacent panels. Completed analysis can also be reexamined within the GUI by opening the saved database files.

A key feature of MOSAIC is the ability to integrate custom algorithms into the processing pipeline. Within the GUI, the user can select the analysis algorithm. The PEG data were analysed independently using both the ADEPT and CUSUM+ algorithms. The blockade depth histogram of the events and the processing statistics are presented in real time. Fits of the physical model (ADEPT) or detected states (CUSUM+) of individual analysed events are also displayed to monitor the progress and quality of the analysis. The results are stored in a SQLite database (or can be exported as a CSV file from within the GUI) for further analysis.

This example further demonstrates the differences between the CUSUM+ and ADEPT algorithms. Only events that deviate from the open channel current baseline

Table 7.5: Parameters used in the analysis of PEG with an αHL nanopore

Parameter	ADEPT Small PEG	ADEPT Large PEG	CUSUM+ Small PEG	CUSUM+ Large PEG
Event Identificaiton Threshold ($\times\sigma$)	2.75	4.0	2.75	4.0
Min. Event Length (samples)	5	5	5	5
Block Size (s)	0.5	0.5	0.5	0.5
StepSize	-	-	3	3
Min. Threshold	-	-	2	2
Max. Threshold	-	-	100	100
Fit Iterations	50000	5000	-	-
Fit Tolerance	10^{-7}	10^{-7}	-	-

by at least 2.7σ were analysed. Events shorter than 5τ were excluded from the CUSUM+ analysis (the default value when running CUSUM+ from the GUI). On the other hand, when using ADEPT, we excluded events shorter than 2.5τ (25 μs) to minimize fitting errors (set with the Advanced Settings dialog in the GUI).

Both algorithms produce well-resolved peaks for PEGs larger than 17-mers (Figure 7.12). For smaller PEGs that have shorter mean residence times, CUSUM+ shows a single broad peak whereas ADEPT easily identifies additional individual species. Here, CUSUM+ recovers significantly fewer events than ADEPT because only a fraction of the total events (those with $t_{res} > 5\tau$) are considered. This effect is particularly significant because it amounts to examining the tail of exponentially distributed lifetimes[21,22].

In Figure 7.12, we directly compare the peak signal to noise ratio of peak, defined as the logarithm of the ratio of the peak amplitude, to the residual fit error. For larger polymers ($n > 20$) the SNR is similar, however for small species ($n < 20$) the SNR of the CUSUM+ peaks are on average $14.3 \pm 0.3\%$ lower than those recovered

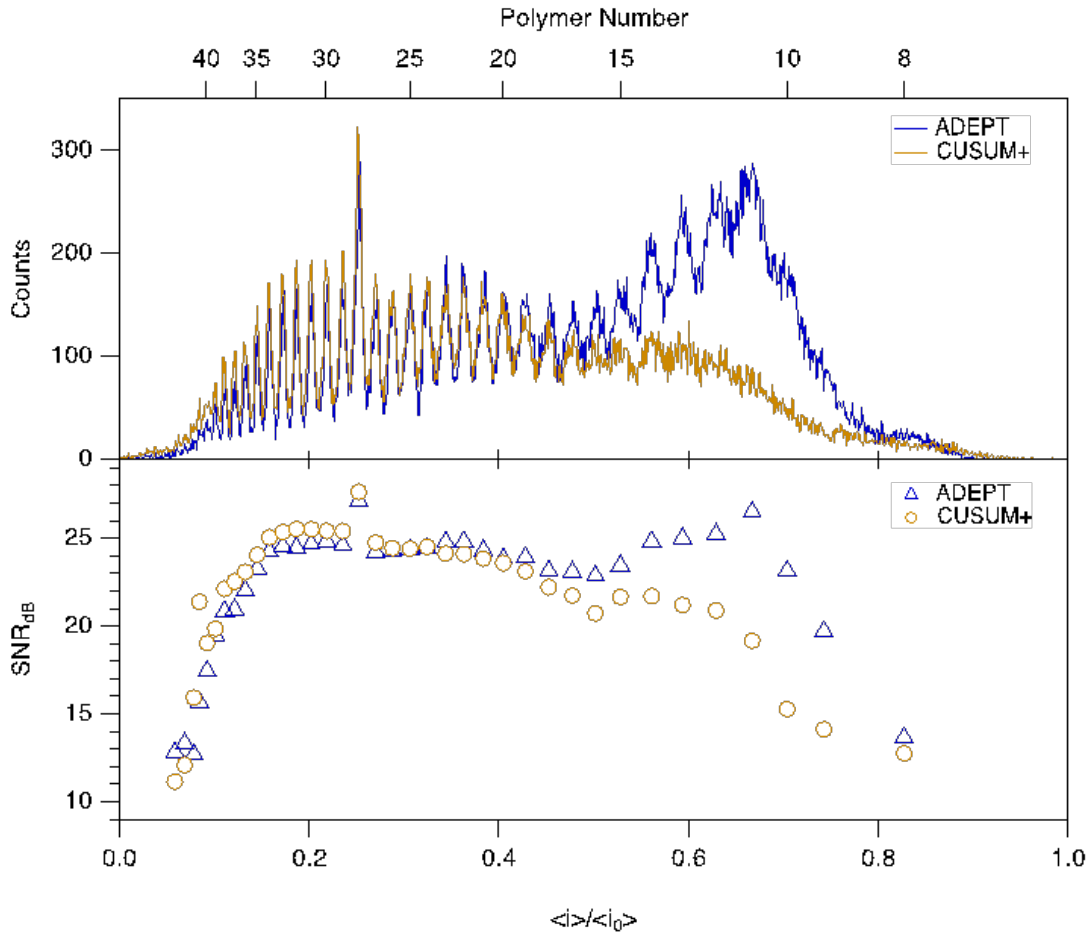

Figure 7.12: A comparison of ADEPT (blue) and CUSUM+(orange) analysis of a polydisperse PEG solution measured with an HL nanopore. Blockade depth histogram of events recovered by each algorithm and comparison of signal to noise of each peak. The number of events recovered by CUSUM+ decreases sharply for small polymers ($N < 20$) that exhibit fast residence times (below 5τ) in the pore.

by ADEPT.

The histograms in Figure 7.12 are fit to a sum of Lorentzian functions using Igor Pro 6.3 (Wavemetrics Inc., Portland, OR). To directly compare the blockade depth histograms, we use the peak positions from the ADEPT dataset as initial guesses for a fit of the CUSUM+-derived blockade depth distribution (Figure 7.12, gray). As expected, for both algorithms, where the peaks are resolved, the peak positions are

in good agreement. For PEGs ($n < 17$), the signal-to-noise ratio of the CUSUM+ peaks is lower than those recovered by ADEPT (Figure 7.12), consistent with the lower number of events recovered by CUSUM+ in this region.

7.5 Conclusion

We developed a new open source platform for the analysis of single molecule data (MOSAIC), and implemented two robust optimized algorithms (ADEPT and CUSUM+) for biological or solid-state nanopore measurements. When applied to dsDNA measurements with a 2.4 nm SiN_x nanopore, MOSAIC found previously undetected states most likely arising from the transient interactions between dsDNA and the access region of the solid-state pore. Additionally, when measuring short oligonucleotides poly$(dA)_n$, MOSAIC accurately analysed events with residence times below 5τ, thereby characterizing previously unreported interactions of dA_{20} with the αHL nanopore. Such analysis can be used to provide greater insight into the underlying physics of analyte-nanopore interactions.

Disclaimer

Certain commercial entities, equipment, or materials may be identified in this document in order to describe an experimental procedure or concept adequately. Such identification is not intended to imply recommendation or endorsement by the National Institute of Standards and Technology, nor is it intended to imply that the entities, materials, or equipment are necessarily the best available for the purpose.

Acknowledgements

This work was supported in part by grant R01HG007415 from the National Human Genome Research Initiative (J.J.K), and by the Natural Sciences and Engineering Research Council of Canada (NSERC). K.B. acknowledges the financial support provided by NSERC and the Vanier CGS program for postgraduate fellowships. We gratefully acknowledge the Ju Laboratory (Columbia University) for providing the pre-heptamerized alpha-hemolysin used in some of these studies. We thank the numerous research groups who provided feedback on the software during its development.

7.6 Materials and Methods

7.6.1 Solid-State Nanopore Measurements

Solid-state nanopore data were re-analysed from Briggs *et al.*[46]. Briefly, nanopores were fabricated in 50×50 μm^2, 10 nm thick low-stress silicon nitride (SiN_x) TEM windows (Norcada, Canada) via the controlled breakdown (CBD) method[58] in a 1 M NaCl buffer (pH 10, 10 mM $NaHCO_3$). Nanopore measurements of double-stranded DNA (dsDNA) were performed in 3.6 M LiCl, 10 mM HEPES (pH 8) using highly purified 50 base pair (bp) dsDNA fragments (NoLimits # SM1421, Life Technologies, USA). Data were low-pass filtered at 100 kHz with a hardware 4-pole Bessel filter (Axopatch 200B), and digitized using a National Instruments USB-6351 DAQ card (Austin, TX) at a sampling rate of $F_s = 500$ kHz.

7.6.2 Biological Nanopore Measurements

Nanopore measurements were performed using quartz capillaries with a (roughly 1 μm diameter) aperture on one end[27,59,60], within a custom polycarbonate test cell (roughly 200 μL volume) (Electronic Biosciences, San Diego, CA). Analytes were dissolved in the working buffer and added directly into the capillary or to the external test cell.

For single stranded DNA measurements, the quartz capillary was filled with a 10 μM to 20 μM solution of different length homopolymeric adenosine dA_{20}, dA_{40}, or dA_{100} (Integrated DNA Technologies, Coralville, IA) dissolved in 1 M NaCl, 1X TE buffer (10 mM Tris, 1 mM EDTA in DNase-free water, titrated to pH 7.2 with 3 M HCl).

For poly(ethylene glycol) measurements (PEG), data from two previous studies that span a wide range of polymer sizes were combined[23,27]. In both cases, the capillary was filled with a solution containing a combination of polydisperse PEG (Fluka, Switzerland) and a highly purified calibration standard (Polypure, Oslo, Norway), dissolved in 4 M KCl (Sigma-Aldrich, St. Louis, MO), buffered with 10 mM Tris (Schwarz/Mann Biotech, Cleveland, OH) and titrated to pH 7.2 with 3 M citric acid. Since the isoelectric point of PEG is lower than 7.2, the PEG molecules will be weakly negatively charged. The two different solutions were as follows: (a) 20 μM PEG-600 (MW_{avg} = 600 g/mol), 40 μM PEG-400 (MW_{avg} = 400 g/mol) and 2 μM purified PEG-502 (MW = 502 g/mol) or (b) 30 μM PEG-1000 (MW_{avg} = 1000 g/mol), 30 μM PEG-1500 (MW_{avg} = 1500 g/mol), and 1 μM purified PEG-1251 (MW = 1251 g/mol).

Planar lipid bilayers were formed across the quartz capillary aperture using a 10 mg/mL solution of 1,2 diphytanolyl-sn-glycero-3-phosphatidylcholine (DPhyPC;

Avanti Polar Lipids, Alabaster, AL) in n-decane (Sigma Aldrich)[27]. Subsequently, wild-type *S. aureus* α-Hemolysin (αHL) was introduced to the test cell by adding a solution containing either approximately 250 ng of monomeric αHL (List Biological Laboratories, Campbell, CA) or approximately 2.5 ng of purified preformed heptamers. To facilitate channel incorporation, the bilayer was thinned and enlarged by applying a transmembrane potential of around 300 mV and a static back pressure within the capillary. Following the insertion of a single channel, the static pressure was reduced and the voltage decreased to the value used for the measurement to prevent further channel incorporation.

The potential was applied across the membrane by a pair of Ag/AgCl electrodes. Immediately prior to use, the electrode placed within in the capillary was prepared by abrading a Ag wire (Alfa Aesar) with 600 grit sandpaper and soaking it in bleach for around 10 min. The external electrode in the test cell bath was a 2 mm Ag/AgCl disk electrode (E202, In Vivo Metric). Data were acquired with a custom high-impedance amplifier system (Electronic BioSciences, San Diego, CA) and conditioned with a low-pass an anti-aliasing filter. The analog signal was digitized by a National Instruments PCI-6120 DAQ card with a sampling rate (F_s) of 1 MHz, further conditioned using a software-based 8-pole low pass Bessel filter with a cutoff frequency of 100 kHz, and resampled at 500 kHz.

7.6.3 Data Processing and Analysis

Nanopore data were processed using a Python based program (MOSAIC) developed in-house. The software implements the ADEPT and CUSUM+ algorithms, which are described below. The compiled program and source code are freely available at https://pages.nist.gov/mosaic/. MOSAIC consists of a modular data processing

pipeline which allows the user to analyse ionic current data from single-molecule nanopore experiments. The software is designed using object-oriented principles, which ensures that modules remain interoperable. This also makes it straightforward to implement new features into the software, such as alternative analysis algorithms or custom data formats. In many cases, users can interact with MOSAIC using a front end graphical user interface.

Bibliography

[1] J. H. Forstater, K. Briggs, J. W. F. Robertson, J. Ettedgui, O. Marie-Rose, C. Vaz, J. J. Kasianowicz, V. Tabard-Cossa, and A. Balijepalli, "MOSAIC: A Modular Single Molecule Analysis Interface for Decoding Multi-state Nanopore Data," *Analytical Chemistry*, vol. 88, no. 23, pp. 11900–11907, 2016.

[2] S. M. Bezrukov and J. J. Kasianowicz, "Current noise reveals protonation kinetics and number of ionizable sites in an open protein ion channel," *Physical Review Letters*, vol. 70, no. 15, pp. 2352–2355, 1993.

[3] J. J. Kasianowicz and S. M. Bezrukov, "Protonation dynamics of the alpha-toxin ion channel from spectral analysis of pH-dependent current fluctuations," *Biophysical Journal*, vol. 69, no. 1, pp. 94–105, 1995.

[4] O. K. Zahid, F. Wang, J. A. Ruzicka, E. W. Taylor, and A. R. Hall, "Sequence-Specific Recognition of MicroRNAs and Other Short Nucleic Acids with Solid-State Nanopores," *Nano Letters*, vol. 16, no. 3, pp. 2033–2039, 2016.

[5] J. J. Kasianowicz, E. Brandin, D. Branton, and D. W. Deamer, "Characterization of individual polynucleotide molecules using a membrane channel," *Proc. Natl. Acad. Sci. U.S.A.*, vol. 93, no. November, p. 13770, 1996.

[6] S. E. Henrickson, M. Misakian, B. Robertson, and J. J. Kasianowicz, "Driven DNA transport into an asymmetric nanometer-scale pore," *Physical Review Letters*, vol. 85, no. 14, pp. 3057–3060, 2000.

[7] A. Meller, L. Nivon, E. Brandin, J. Golovchenko, and D. Branton, "Rapid nanopore discrimination between single polynucleotide molecules.," *Proceedings of the National Academy of Sciences of the United States of America*, vol. 97, pp. 1079–84, feb 2000.

[8] J. Clarke, H.-C. Wu, L. Jayasinghe, A. Patel, S. Reid, and H. Bayley, "Continuous base identification for single-molecule nanopore DNA sequencing," *Nature Nanotechnology*, vol. 4, no. 4, pp. 265–270, 2009.

[9] S. E. Henrickson, E. A. Dimarzio, Q. Wang, V. M. Stanford, and J. J. Kasianowicz, "Probing single nanometer-scale pores with polymeric molecular rulers," *Journal of Chemical Physics*, vol. 132, no. 13, 2010.

[10] E. A. Manrao, I. M. Derrington, A. H. Laszlo, K. W. Langford, M. K. Hopper, N. Gillgren, M. Pavlenok, M. Niederweis, and J. H. Gundlach, "Reading DNA at single-nucleotide resolution with a mutant MspA nanopore and phi29 DNA polymerase.," *Nature Biotechnology*, vol. 30, pp. 349–53, apr 2012.

[11] G. M. Cherf, K. R. Lieberman, H. Rashid, C. E. Lam, K. Karplus, and M. Akeson, "Automated forward and reverse ratcheting of DNA in a nanopore at 5-Å precision.," *Nature Biotechnology*, vol. 30, pp. 344–8, apr 2012.

[12] C. A. Merchant, K. Healy, M. Wanunu, V. Ray, N. Peterman, J. Bartel, M. D. Fischbein, K. Venta, Z. Luo, A. T. C. Johnson, and M. Drndić, "DNA translocation through graphene nanopores," *Nano Letters*, vol. 10, no. 8, pp. 2915–2921, 2010.

[13] J. A. Rodríguez-Manzo, M. Puster, A. Nicolaï, V. Meunier, and M. Drndić, "DNA Translocation in Nanometer Thick Silicon Nanopores," *ACS Nano*, vol. 9, no. 6, pp. 6555–6564, 2015.

[14] M. M. Marshall, J. Ruzicka, O. K. Zahid, V. C. Henrich, E. W. Taylor, and A. R. Hall, "Nanopore analysis of single-stranded binding protein interactions with DNA," *Langmuir*, vol. 31, no. 15, pp. 4582–4588, 2015.

[15] J. J. Kasianowicz, S. E. Henrickson, H. H. Weetall, and B. Robertson, "Simultaneous multianalyte detection with a nanometer-scale pore," *Analytical Chemistry*, vol. 73, no. 10, pp. 2268–2272, 2001.

[16] G. Oukhaled, J. Mathé, A. L. Biance, L. Bacri, J. M. Betton, D. Lairez, J. Pelta, and L. Auvray, "Unfolding of proteins and long transient conformations detected by single nanopore recording," *Physical Review Letters*, vol. 98, no. 15, pp. 98–101, 2007.

[17] A. Oukhaled, B. Cressiot, L. Bacri, M. Pastoriza-Gallego, J. M. Betton, E. Bourhis, R. Jede, J. Gierak, L. Auvray, and J. Pelta, "Dynamics of completely unfolded and native proteins through solid-state nanopores as a function of electric driving force," *ACS Nano*, vol. 5, no. 5, pp. 3628–3638, 2011.

[18] M. Pastoriza-Gallego, L. Rabah, G. Gibrat, B. Thiebot, F. G. Van Der Goot, L. Auvray, J. M. Betton, and J. Pelta, "Dynamics of unfolded protein transport through an aerolysin pore," *Journal of the American Chemical Society*, vol. 133, no. 9, pp. 2923–2931, 2011.

[19] D. Rotem, L. Jayasinghe, M. Salichou, and H. Bayley, "Protein detection by nanopores equipped with aptamers.," *Journal of the American Chemical Society*, vol. 134, pp. 2781–7, feb 2012.

[20] J. Larkin, R. Y. Henley, M. Muthukumar, J. K. Rosenstein, and M. Wanunu, "High-bandwidth protein analysis using solid-state nanopores," *Biophysical Journal*, vol. 106, no. 3, pp. 696–704, 2014.

[21] J. W. F. Robertson, C. G. Rodrigues, V. M. Stanford, K. A. Rubinson, O. V. Krasilnikov, and J. J. Kasianowicz, "Single-molecule mass spectrometry in solution using a solitary nanopore," *Proceedings of the National Academy of Sciences*, vol. 104, no. 20, pp. 8207–8211, 2007.

[22] J. E. Reiner, J. J. Kasianowicz, B. J. Nablo, and J. W. F. Robertson, "Theory for polymer analysis using nanopore-based single-molecule mass spectrometry," *Pnas*, vol. 107, no. 27, pp. 12080–12085, 2010.

[23] A. Balijepalli, J. W. Robertson, J. E. Reiner, J. J. Kasianowicz, and R. W. Pastor, "Theory of polymer-nanopore interactions refined using molecular dynamics simulations," *Journal of the American Chemical Society*, vol. 135, no. 18, pp. 7064–7072, 2013.

[24] G. Baaken, I. Halimeh, L. Bacri, J. Pelta, A. Oukhaled, and J. C. Behrends, "High-Resolution Size-Discrimination of Single Nonionic Synthetic Polymers with a Highly Charged Biological Nanopore," *ACS Nano*, vol. 9, no. 6, pp. 6443–6449, 2015.

[25] C. E. Angevine, A. E. Chavis, N. Kothalawala, A. Dass, and J. E. Reiner, "Enhanced single molecule mass spectrometry via charged metallic clusters," *Analytical Chemistry*, vol. 86, no. 22, pp. 11077–11085, 2014.

[26] J. Ettedgui, J. J. Kasianowicz, and A. Balijepalli, "Single Molecule Discrimination of Heteropolytungstates and Their Isomers in Solution with a Nanometer-Scale Pore," *Journal of the American Chemical Society*, vol. 138, no. 23, pp. 7228–7231, 2016.

[27] A. Balijepalli, J. Ettedgui, A. T. Cornio, J. W. F. Robertson, K. P. Cheung, J. J. Kasianowicz, and C. Vaz, "Quantifying short-lived events in multistate ionic current measurements.," *ACS Nano*, vol. 8, pp. 1547–53, feb 2014.

[28] L. Movileanu, S. Cheley, and H. Bayley, "Partitioning of individual flexible polymers into a nanoscopic protein pore," *Biophysical Journal*, vol. 85, no. 2, pp. 897–910, 2003.

[29] E. C. Yusko, B. R. Bruhn, O. Eggenberger, J. Houghtaling, C. Ryan, N. C. Walsh, S. Nandivada, M. Pindrus, and A. R. Hall, "Real-time shape approximation and 5-D fingerprinting of single proteins," *arXiv*, 2015.

[30] G. F. Schneider, S. W. Kowalczyk, V. E. Calado, G. Pandraud, H. W. Zandbergen, L. M. K. Vandersypen, and C. Dekker, "DNA translocation through graphene nanopores," *Nano Letters*, vol. 10, no. 8, pp. 2915–2921, 2010.

[31] A. B. Farimani, K. Min, and N. R. Aluru, "DNA base detection using a single-layer MoS2," *ACS Nano*, vol. 8, no. 8, pp. 7914–7922, 2014.

[32] F. Bezanilla, "The voltage sensor in voltage-dependent ion channels.," *Physiological reviews*, vol. 80, no. 2, pp. 555–92, 2000.

[33] L. Rabiner and B. Juang, "An introduction to hidden Markov models," *IEEE ASSP Magazine*, vol. 3, no. January, p. Appendix 3A, 1986.

[34] F. Qin, A. Auerbach, and F. Sachs, "A direct optimization approach to hidden markov modeling for single channel kinetics," *Biophysical Journal*, vol. 79, no. 4, pp. 1915–1927, 2000.

[35] K. L. Magleby and D. S. Weiss, "Estimating kinetic parameters for single channels with simulation. A general method that resolves the missed event problem and accounts for noise," *Biophysical Journal*, vol. 58, no. 6, pp. 1411–1426, 1990.

[36] D. Colquhoun, C. J. Hatton, and A. G. Hawkes, "The quality of maximum likelihood estimates of ion channel rate constants," *Journal of Physiology*, vol. 547, no. 3, pp. 699–728, 2003.

[37] D. Pedone, M. Firnkes, and U. Rant, "Data analysis of translocation events in nanopore experiments," *Analytical Chemistry*, vol. 81, no. 23, pp. 9689–9694, 2009.

[38] Z. Gu, Y. L. Ying, C. Cao, P. He, and Y. T. Long, "Accurate data process for nanopore analysis," *Analytical Chemistry*, vol. 87, no. 2, pp. 907–913, 2015.

[39] C. Raillon, P. Granjon, M. Graf, L. J. Steinbock, and A. Radenovic, "Fast and automatic processing of multi-level events in nanopore translocation experiments.," *Nanoscale*, vol. 4, pp. 4916–24, aug 2012.

[40] J. Schreiber and K. Karplus, "Analysis of nanopore data using hidden Markov models," *Bioinformatics*, vol. 31, no. 12, pp. 1897–1903, 2015.

[41] A. Balijepalli, J. Ettedgui, A. T. Cornio, J. W. F. Robertson, K. P. Cheung, J. J. Kasianowicz, and C. Vaz, "Correction to Quantifying Short-Lived Events in Multistate Ionic Channel Measurements," *ACS Nano*, vol. 9, no. 12, pp. 12583–12583, 2015.

[42] D. K. Lathrop, E. N. Ervin, G. A. Barrall, M. G. Keehan, R. Kawano, M. A. Krupka, H. S. White, and A. H. Hibbs, "Monitoring the escape of DNA from a nanopore using an alternating current signal," *Journal of the American Chemical Society*, vol. 132, no. 6, pp. 1878–1885, 2010.

[43] W. H. Press, S. A. Teukolsky, W. T. Vetterling, and B. P. Flannery, *Numerical recipes: The art of scientific computing 3rd Edition*. Cambridge University Press, 2007.

[44] E. S. Page, "Continuous Inspection Schemes," *Biometrika*, vol. 41, no. 1/2, p. 100, 1954.

[45] V. Dimitrov, U. Mirsaidov, D. Wang, T. Sorsch, W. Mansfield, J. Miner, F. Klemens, R. Cirelli, S. Yemenicioglu, and G. Timp, "Nanopores in solid-state membranes engineered for single molecule detection," *Nanotechnology*, vol. 21, no. 6, p. 065502, 2010.

[46] K. Briggs, H. Kwok, and V. Tabard-Cossa, "Automated Fabrication of 2-nm Solid-State Nanopores for Nucleic Acid Analysis," *Small*, vol. 10, no. 10, pp. 2077–2086, 2014.

[47] P. Cluzel, A. Lebrun, C. Heller, R. Lavery, J.-L. Viovy, D. Chatenay, and F. Caron, "DNA: An Extensible Molecule," *Science*, vol. 271, no. 5250, pp. 792–794, 1996.

[48] T. R. Strick, J.-F. Allemand, D. Bensimon, A. Bensimon, and V. Croquette, "The Elasticity of a Single Supercoiled DNA Molecule," *Science*, vol. 271, no. 5257, pp. 1835–1837, 1996.

[49] M. Newville, T. Stensitzki, D. B. Allen, and A. Ingargiola, "LMFIT: Non-Linear Least-Square Minimization and Curve-Fitting for Python," 2014.

[50] L. Song, M. R. Hobaugh, C. Shustak, S. Cheley, and J. E. Gouaux, "Structure of Staphylococcal α-Hemolysin , a Heptameric Transmembrane Pore," *Science*, vol. 274, no. 5294, pp. 1859–1866, 1996.

[51] J. Muzard, M. Martinho, J. Mathé, U. Bockelmann, and V. Viasnoff, "DNA translocation and unzipping through a nanopore: Some geometrical effects," *Biophysical Journal*, vol. 98, no. 10, pp. 2170–2178, 2010.

[52] J. Mathe, A. Aksimentiev, D. R. Nelson, K. Schulten, and A. Meller, "Orientation discrimination of single-stranded DNA inside the -hemolysin membrane channel," *Proceedings of the National Academy of Sciences*, vol. 102, no. 35, pp. 12377–12382, 2005.

[53] T. Z. Butler, J. H. Gundlach, and M. Troll, "Ionic current blockades from DNA and RNA molecules in the α-hemolysin nanopore," *Biophysical Journal*, vol. 93, no. 9, pp. 3229–3240, 2007.

[54] T. Z. Butler, J. H. Gundlach, and M. A. Troll, "Determination of RNA orientation during translocation through a biological nanopore," *Biophysical Journal*, vol. 90, no. 1, pp. 190–199, 2006.

[55] J. Mathé, H. Visram, V. Viasnoff, Y. Rabin, and A. Meller, "Nanopore unzipping of individual DNA hairpin molecules," *Biophysical Journal*, vol. 87, no. 5, pp. 3205–3212, 2004.

[56] O. V. Krasilnikov, C. G. Rodrigues, and S. M. Bezrukov, "Single polymer molecules in a protein nanopore in the limit of a strong polymer-pore attraction," *Physical Review Letters*, vol. 97, no. 1, pp. 1–4, 2006.

[57] S. M. Bezrukov, I. Vodyanoy, R. A. Brutyan, and J. J. Kasianowicz, "Dynamics and free energy of polymers partitioning into a nanoscale pore," *Macromolecules*, vol. 29, no. 26, pp. 8517–8522, 1996.

[58] H. Kwok, K. Briggs, and V. Tabard-Cossa, "Nanopore fabrication by controlled dielectric breakdown.," *PLoS One*, vol. 9, p. e92880, jan 2014.

[59] R. J. White, E. N. Ervin, T. Yang, X. Chen, S. Daniel, P. S. Cremer, and H. S. White, "Single Ion-Channel Recordings Using Glass Nanopore Membranes Single Ion-Channel Recordings Using Glass Nanopore Membranes," *Journal of the American Chemical Society*, vol. 129, no. 15, pp. 11766–11775, 2007.

[60] S. Kumar, C. Tao, M. Chien, B. Hellner, A. Balijepalli, J. W. F. Robertson, Z. Li, J. J. Russo, J. E. Reiner, J. J. Kasianowicz, and J. Ju, "PEG-Labeled Nucleotides and Nanopore Detection for Single Molecule DNASequencing by Synthesis," *Scientific Reports*, vol. 2, no. 1, p. 684, 2012.

Chapter 8

Digital Signal Processing for Nanopore Data

Kyle Briggs

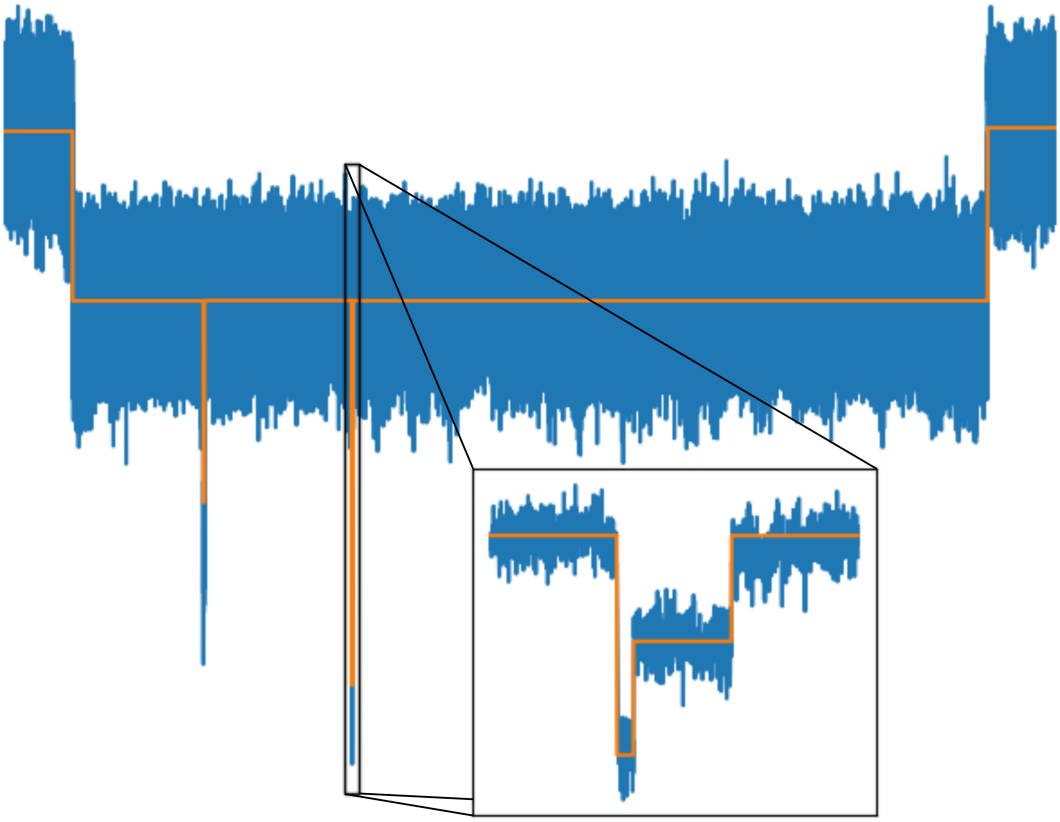

8.1 Introduction

Nanopores have until recently been limited in scope to research settings in well-equipped research labs. Because of this, very few tools, commercial or otherwise, are available to aid in analysis of biomolecular translocations through nanopores. This chapter describes the theory, implementation, and use of an open source nanopore analysis software suite called CUSUM that addresses the general problem of identifying step changes in a uniformly digitized timeseries. The software combines several statistical and physical models of the nanopore in order to accurately and automatically extract a host of useful metrics from nanopore time-series data. The software package is written in C, is released under the GNU General Public License version 3, and is freely available online[1].

Due to extensive optimization for both speed and memory footprint, CUSUM processes nanopore data orders of magnitude faster than it can be acquired using the fastest current amplifier commercially available at the time of writing (the Chimera VC100) on a typical desktop computer, meaning that high-quality signal analysis need no longer be the bottle neck in nanopore experiments.

In addition to the C package above, the improved CUSUM algorithm has also been ported to MOSAIC, another open-source nanopore analysis toolkit developed at NIST, which is in use in several nanopore labs globally[2,3], and is discussed in detail in the previous chapter.

Unless otherwise noted, the data plotted in this chapter is simulated using simple Gaussian random number generators for the purposes of illustrating particular use cases.

8.2 Setting up CUSUM

8.2.1 Compilation and Execution

CUSUM requires a 64-bit operating system/compiler. With a suitable compiler aliased to `cc` and all of the source files in the active directory on a linux system, the command

```
cc -o [executable name] -D_GNU_SOURCE -O3 -lm *.c -static
```

will compile a statically linked version of CUSUM. For a Windows executable, cross-compiling an executable on Linux using MinGW is the preferred method, though support and instructions for compiling natively on Windows is available upon request. The `-D_GNU_SOURCE` flag is necessary for large file support on some systems. MAC is currently not supported and remains untested, though in principle there is nothing OS-specific in the code that would be expected to cause problems.

Once it is compiled, CUSUM requires three things in order to run:

1. A configuration file called `config.txt` in the same directory as the executable.

2. A valid data file in one of the supported I/O formats (16- or 64-bit big-endian raw binary files, or Chimera VC100 output logfiles). Support for additional formats can be implemented with relative ease upon request.

3. A pre-existing output folder specified in the configuration file that contains a pre-existing empty sub-directory called `events`.

For the sake of keeping all of the code OS-agnostic and portable, CUSUM does not interact directly with the file system except to create output files, so the user is responsible for creating the required output directory structure and ensuring cleanup between runs if the same output directory is used for a different run.

Once the above requirements are satisfied, the program can be started simply by running the executable without additional arguments.

8.2.2 Configuration File Format

The configuration file must be called config.txt, and follows a simple .ini format, wherein parameters are specified, one per line, in the form `parameter_name=value`. Throughout this chapter, wherever possible, a default value which can be used most of the time is given. Note that default parameters must still be supplied in the configuration file.

8.3 Data I/O

The file to be read is specified in the configuration file using the `input_file` parameter. CUSUM currently supports three file formats, chosen using the `datatype` parameter. A `datatype` of 0 indicates a file generated using the Chimera VC100, which consists of 16-bit adc codes encoding current. Currently CUSUM only supports single file analysis, so VC100 files must be separately concatenated into a continuous time-series before analysis. A `datatype` of 16 indicates interleaved 16-bit signed integer values alternating between current and voltage. Finally, a `datatype` of 64 indicates interleaved 64-bit double values alternating between current and voltage.

All three data types require that the sampling frequency be specified using the `samplingfreq` parameter. Note that this value is rounded down to the nearest integer. The section of file to be analyzed is specified using the `start` and `finish` parameters, which have units of sample numbers. Setting both to zero will read the whole file.

The length of data to be read in each segment is set by the `readlength` param-

eter. This parameter denotes the number of current samples to work with at a time, and should be set to be at least twice as long as the longest event that is desired to be fitted, but sufficiently short that the baseline current does not vary significantly within a single data segment. Because slow variation in the baseline current is characteristic of low-frequency noise, generally pores with a lot of low-frequency noise will require a smaller `readlength` value, as will pores whose size is unstable during the course of an experiment. Generally a value of a few seconds is appropriate.

In the case of Chimera files (`datatype=0`), the ADC settings must also be supplied, as output by the Chimera itself. The required parameters are `SETUP_mVoffset`, `SETUP_ADCSAMPLERATE`, `SETUP_pAoffset`, `SETUP_ADCVREF`, `SETUP_ADCBITS`, and finally `SETUP_preADCgain`, all of which are saved during data acquisition and can be accessed either using MATLAB, or additional tools that are discussed later in this chapter. CUSUM assumes that these settings do not change during the file being read. Segmented VC100 data with different ADC parameters must be concatenated and analyzed separately.

During reading of the data file an optional low-pass digital Bessel filter can be applied, which is discussed in detail in a later section of this report.

8.4 Event Identification

The first task in extracting useful metrics from nanopore time-series data is identification of the sections of the time-series that are physically interesting: the blocked states, which typically comprise less than 1% of the actual measurement time. In CUSUM, this initial event identification is achieved using simple adaptive thresholding. The algorithm proceeds as follows.

8.4.1 Characterization of Open Pore Current

Once a segment of data is read into the program, a histogram of the current values is constructed. The range over which the program will look for the open pore current is specified by the user using the `baseline_min` and `baseline_max` parameters, which are signed quantities given in pA. In cases where the open pore current is well-behaved the algorithm is not particularly sensitive to the actual values specified here. As long as the mean current trace is contained between the two baseline bounds specified, the algorithm will extract the correct value.

In order to extract open pore current statistics, a Gaussian noise distribution for the current $i(t) \sim \mathcal{N}(i_0, \sigma)$ is assumed. However, because each section of data can also include blocked states that can in principle overlap with the mean open pore peak in the histogram, the histogram peak corresponding to the open state must first be identified. This is done simply by assuming that the pore spends more time open than blocked, so that the location of the global maximum value of the histogram that falls between the specified baseline bounds corresponds roughly to the mean open pore current i_0. Care must be taken in cases where the current signal contains more than one closely-spaced open current states, such as when channel gating occurs. The baseline calculator will estimate the baseline to be the global histogram maximum while remaining inside the specified bounds. If a different state is desired, for example if the pore spends more time in the blocked state than the open one, the baseline bounds must be explicitly set to exclude other possibilities. Note that just because it is possible to set tight baseline bounds does not mean one should; generally, larger bounds provide a more robust fit, and tight bounds should only be used to explicitly exclude some pathological case. The number of bins in the histogram is internally optimized to provide good peak resolution and a smooth histogram.

To avoid biasing the fit by fitting sections where the open state overlaps with the first blocked state, we identify the approximate standard deviation by finding the point above (away from 0) the global maximum i_0 where the histogram decays to 1% of the maximum value, which corresponds roughly to the 3σ point. With this rough estimate of σ, we then perform the fit between

$$|i_0| - \sqrt{2\ln 2}\,\sigma \leq |i_k| \leq |i_0| + 2\sigma, \tag{8.1}$$

where i_k denotes the current in bin k. If either baseline bound intersects the range above, the range is truncated at that point. If the first blocked state overlaps the baseline histogram past the half-width at half-max, the fit might come out skewed and accuracy cannot be guaranteed.

It is also important to note that the simple estimate of mean and standard deviation employed here assume that the current histogram on each segment is sufficiently smooth that the global maximum corresponds to the actual location of the baseline mean. Since this requirement simply means that as many current samples as possible is desired, so that the relative error in the histogram bin counts satisfies $N^{-\frac{1}{2}} \ll 1$, `readlength` should be set as large as is possible while ensuring that no baseline drift occurs on each segment, and should generally correspond to at least a few seconds of data.

Several examples of baseline fitting setups for a few particularly pathological cases, along with the required baseline bounds, are shown in Figure 8.1. In cases where such tricks are necessary, it is important that the user perform at least some manual quality control to ensure accurate baseline identification during post-processing.

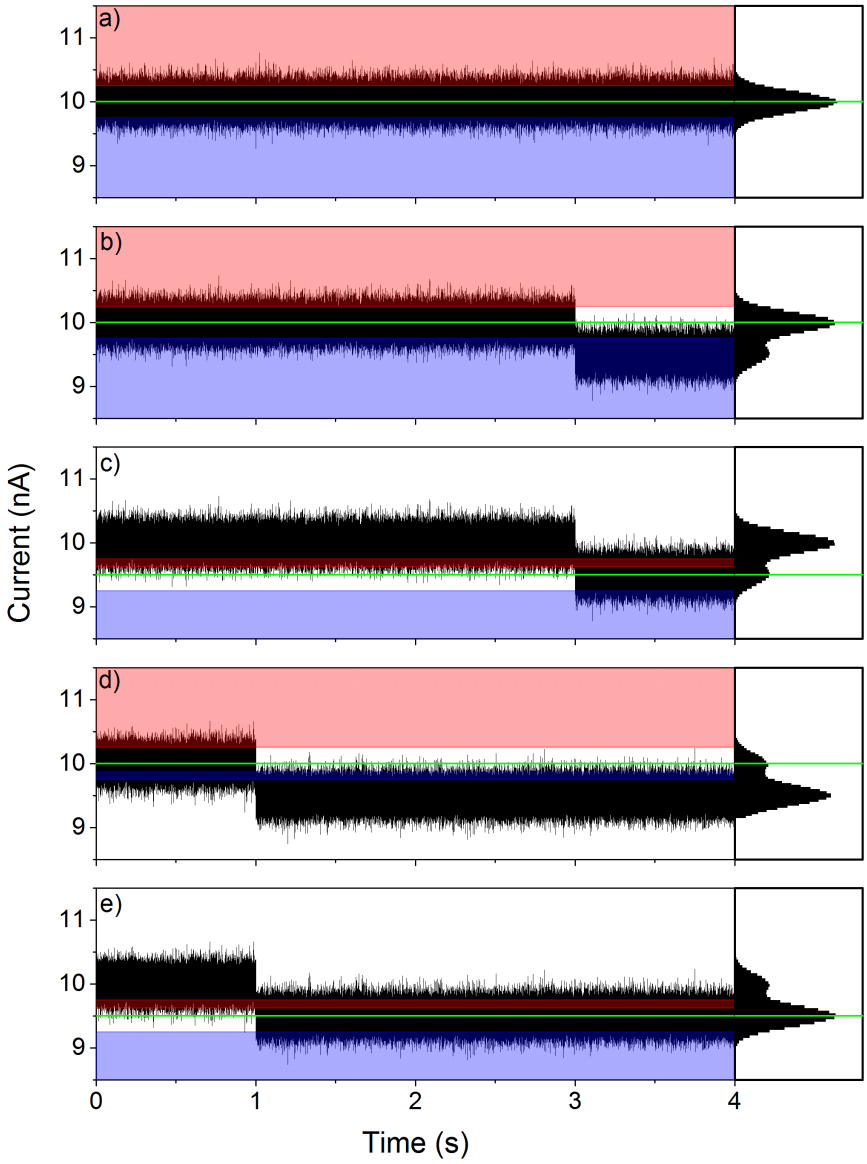

Figure 8.1: Examples of baseline extraction parameters when using CUSUM. In each case, setting `baseline_max` anywhere in the red region and `baseline_min` anywhere in the blue region results in CUSUM selecting the green line as the local mean open pore current. a) In the case of a single well-behaved baseline value, baseline extraction is largely insensitive to the bounds. b) in the case of a bimodal peak, as long as the peak that is being selected for has higher amplitude, baseline bounds can once again be set liberally. c,d) If a lower-amplitude peak is desired as the baseline, baseline bounds must be set to explicitly exclude the higher one. e) In the case where the peak to be selected has higher amplitude but smaller absolute current value, baseline bounds must be set to inhibit the fit range in the direction away from zero, or else CUSUM will attempt to fit a single Gaussian to both peaks.

In order to ensure numerical robustness, the current is approximately normalized to $\mathcal{N}(0,1)$ by defining $z = \frac{i-i_0}{\sigma}$ using the above method of guessing i_0 and σ. The actual fitting is done using a linearized least-squares model for a Gaussian fit, which assumes the histogram of the open pore current is given by

$$h_i \approx A \exp\left(-\frac{i_k - i_0}{2\sigma^2}\right), \tag{8.2}$$

where k denotes the bin index. Linearizing by taking the logarithm of both sides and solving the linear least-squares problem for a quadratic model immediately gives

$$\begin{pmatrix} -\frac{1}{2\sigma^2} \\ \frac{i_0}{\sigma^2} \\ \ln A - \frac{i_0^2}{2\sigma^2} \end{pmatrix} = \begin{pmatrix} \sum_k i_k^4 & \sum_k i_k^3 & \sum_k i_k^2 \\ \sum_k i_k^3 & \sum_k i_k^2 & \sum_k i_k \\ \sum_k i_k^2 & \sum_k i_k & N \end{pmatrix}^{-1} \begin{pmatrix} \sum_k i_k^2 \ln h_k \\ \sum_k i_k \ln h_k \\ \sum_k \ln h_k \end{pmatrix}. \tag{8.3}$$

While this solves the problem analytically, there is an issue: because the histogram can have zeros in some bins, $\ln h_k$ is not always defined, and bins with very small values of h_k get artificially more weight in the linearized model. We can get around this difficulty by multiplying both sides of the equation by h_k, effectively weighting each bin by its own amplitude, and rearranging so that we instead have

$$\begin{pmatrix} -\frac{1}{2\sigma^2} \\ \frac{i_0}{\sigma^2} \\ \ln A - \frac{i_0^2}{2\sigma^2} \end{pmatrix} = \begin{pmatrix} \sum_k i_k^4 h_k & \sum_k i_k^3 h_k & \sum_k i_k^2 h_k \\ \sum_k i_k^3 h_k & \sum_k i_k^2 h_k & \sum_k i_k h_k \\ \sum_k i_k^2 h_k & \sum_k i_k h_k & N h_k \end{pmatrix}^{-1} \begin{pmatrix} \sum_k i_k^2 h_k \ln h_k \\ \sum_k i_k h_k \ln h_k \\ \sum_k h_k \ln h_k \end{pmatrix}. \tag{8.4}$$

This gives approximately the same solution as the nonlinear least-squares problem

while avoiding the issue of small bin values by defining $h_k \ln h_k = 0$ if $h_k = 0$. To see the equivalence, we note that the residuals for this model are given by

$$r_k = h_{k,fit} \ln h_{k,fit} - h_k \ln h_k \approx h_k \ln \left(1 + \frac{h_{k,fit} - h_k}{h_k}\right). \tag{8.5}$$

Since we only perform the fit over the central region of the actual histogram peak, the residuals $h_{k,fit} - h_k \approx \sqrt{h_k}$ are small relative to the actual bin counts h_k, so we can expand the logarithm to first order, giving

$$r_i \approx h_{k,fit} - h_k, \tag{8.6}$$

which is equivalent to the residual for the nonlinear least-squares problem. We then have an approximate analytical solution to the nonlinear least-squares problem that uses a linearized model to avoid the computational complexity of actually iterating numerically.

8.4.2 Approximate Event Location

Once the local open pore baseline and standard deviation are determined, events can be located. To do so, the user supplies two values, `threshold` t and `hysteresis` y, which determine by how much a data point must deviate from the local state to constitute the start or end of an event. When the pore is in the open state, any point that deviates from the baseline and passes $i_0 - \text{sign}(i_0)t\sigma$ is designated the start of an event, and the pore is marked as being in a blocked state. While in a blocked state, any point that passes $i_0 - \text{sign}(i_0)(t-y)\sigma$ is designated the end of an event. Generally speaking, threshold should be set at least 5σ away from the baseline current ($t \geq 5$) to avoid false positives. y is best set such that the signal must return slightly past

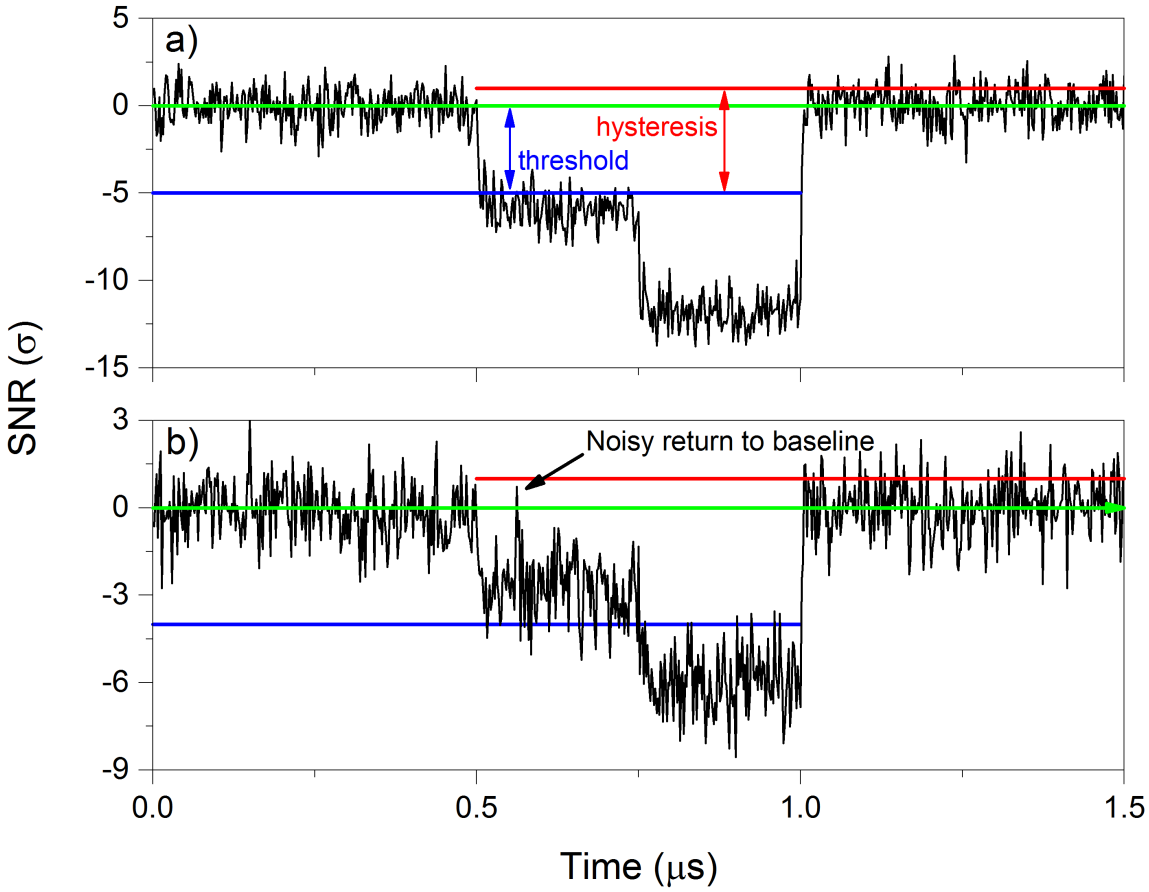

Figure 8.2: Examples of `threshold` and `hysteresis` signalling the approximate start and end of an event. Blue lines represent the current threshold at which an event start is indicated, while read lines indicate the current at which event ends are indicated. Green shows the local baseline. a) A well-behaved event (SNR of 6) can use the default settings of $t = 5$ and $y = 6$ to detect events. In cases with a lower SNR of 3 such as in b), $t = 4$ is necessary to reliably detect the event. Note that setting the hysteresis level above the current baseline avoids early even ends and subsequent double counting of the event.

the mean baseline to indicate the end of an event to avoid premature signalling in the case where the blocked state partially overlaps the baseline. To this end, it is usually optimal to set $y = t + 1$ so that an event end is signalled when the current passes $i_0 + \sigma$. The default settings of $t = 5$ and $y = 6$ will accurately pick out events in the vast majority of cases. In cases where the signal-to-noise ratio (SNR) is barely sufficient, threshold can be reduced as low as $t = 4$ at the cost of slightly higher false

positive rate, though false positives can usually be easily identified by the automated quality control discussed later in this manual. Two examples of setting `threshold` and `hysteresis` are show in Figure 8.2.

Passing through the whole file using this test, a linked list of start and end points, the edges of all events, is built. If an event straddles the end of one data section and the start of the next, the program will record two event start locations in a row, the second of which is ignored. After building the full list, edges are paired up, with a start location being paired with the next consecutive end location to determine the approximate sections of data that constitute interesting events.

8.5 Sublevel Identification using CUSUM

The Cumulative Sums (CUSUM) algorithm is a general statistical method for detecting changes in a time-series, which has historically been used for process control applications[4]. More recently, the algorithm was implemented as a black box model for nanopore data analysis by Raillon *et al*[5]. The implementation defined here further improves the method to a grey box model that takes advantage of the physics of nanopore translocation to achieve more accurate fitting[2].

In the implementation given in CUSUM we make the assumption of Gaussian noise, which is generally a reasonable approximation for solid-state nanopore data, though the method can easily be adapted to other noise profiles for which an analytical form for the distribution can be approximated. We assume that the current through the nanopore at any given time is well-described by its mean i_0 and standard deviation σ, so that each current value i_k follows the probability distribution

$$p_0(i_k) = \frac{1}{\sqrt{2\pi\sigma^2}} \exp\left(-\frac{(i_k - i_0)^2}{2\sigma^2}\right). \tag{8.7}$$

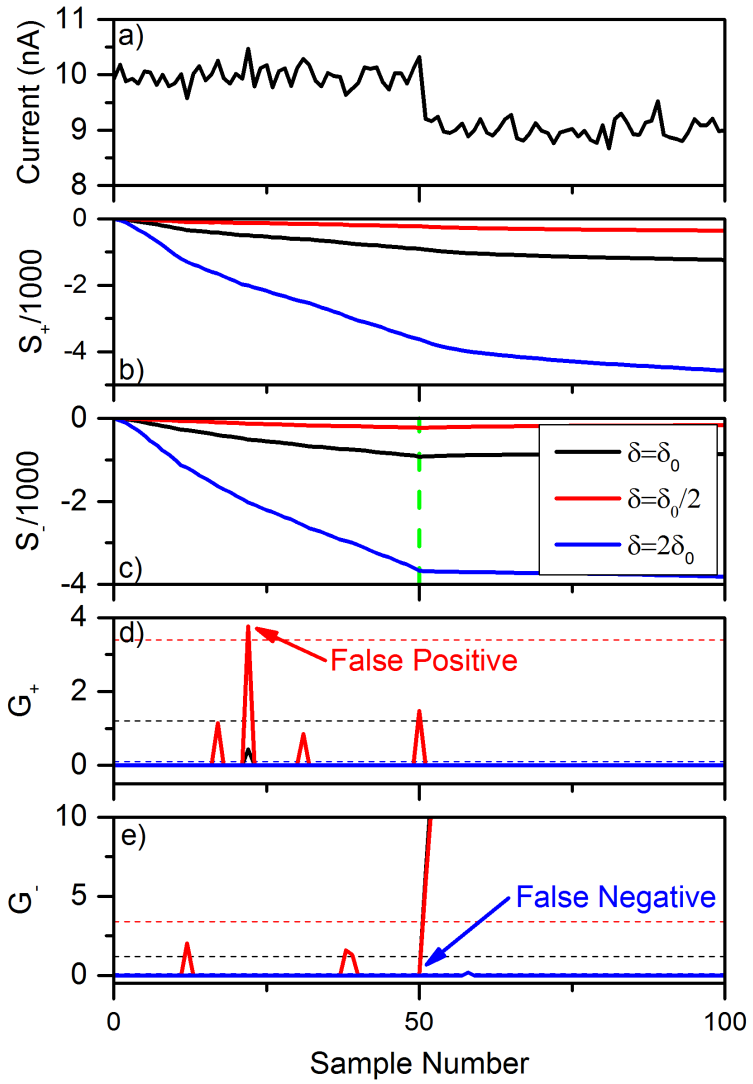

Figure 8.3: a) The current signal to which CUSUM is applied, which has a $\delta_0 = 6$ change at sample 50. b) The cumulative log-likelihood function for a positive change in current mean, showing no local minima for any value of δ. c) The cumulative log-likelihood for a negative change, show local minima at sample 50 as required. d) The threshold function for a negative current change. Change detection occurs when the threshold function crosses the dashed line of matching color. Setting δ too small results in a false positive. e) The threshold function for a positive current change. Setting δ too large results in a false negative. Note that for the purpose of illustration, the accumulators are not reset to zero when the change is detected.

In this definition, k denotes the number of samples since either the start of the signal or the last detected change in the mean.

At each data point, we apply a simple statistical test with the alternative hypothesis that the mean value has changed abruptly by a user-supplied value $\pm\delta$ as compared to the null hypothesis of no change in the mean. This parameter is defined in the configuration file as `cusum_delta`, given as a multiple of the open pore current standard deviation. This quantity is generally set equal to the smallest significant change that the user wants to detect.

We calculate the probabilities that the observed current sample belongs to either the unchanged distribution p_0 or the changed distributions

$$p_{\pm}(i_k;\delta) = \frac{1}{\sqrt{2\pi\sigma_k^2}} \exp\left(-\frac{(i_k - (\mu_k \pm \delta))^2}{2\sigma_k^2}\right). \tag{8.8}$$

Here, μ_k and σ_k are the local mean and standard deviation calculated using all points in the interval since the last detected change, and therefore do depend weakly on k as each new data point contributes slightly to both values. In order to evaluate this, we define the log-likelihoods

$$s_{k,\pm}(i_k;\delta) = \ln\left(\frac{p_{\pm}(i_k;\delta)}{p_0(i_k)}\right) = \pm\frac{\delta}{\sigma_k^2}\left[i_k - \left(\mu_k \pm \frac{\delta}{2}\right)\right]. \tag{8.9}$$

Note that while this form explicitly assumes a Gaussian noise distribution, the algorithm can easily be modified to use any other noise distribution simply by changing to an appropriate expression for the log-likelihood. A positive log-likelihood indicates that the more probable distribution is the one with the changed mean, while a negative log-likelihood supports the null hypothesis of no change.

At each data point, we define two accumulators for each possible sign of δ, both starting initialized at 0:

$$S_{k,\pm} = S_{k-1,\pm} + s_{k,\pm}, \tag{8.10}$$

and

$$G_{k,\pm} = \max\left(G_{k-1,\pm} + s_{k,\pm},\, 0\right). \tag{8.11}$$

$S_\pm$ accumulates all log-likelihoods, while $G_\pm$ accumulates log-likelihoods but resets to zero when a negative one is found. When the value of $G_\pm$ passes a pre-determined threshold h, discussed in more detail below, which occurs when several positive log-likelihoods are detected in sequence, it signals that a significant change has occurred in the mean current. Since there is a delay before triggering as $G_\pm$ accumulates values, the actual location of the step change must be back-calculated from $S_\pm$. Because the sign of the log-likehoods changes from negative to positive when a step change occurs, $S_\pm$ has a global minimum at the exact location of the step change. Because $S_\pm$ and $G_\pm$ are time-integrals of log-likelihood, they are actually quite robust against noise in the signal. These quantities are reset to zero every time a change in the mean is found, and the process starts over again from that location. The time-evolution of these quantities in response to a simulated step change is shown in Figure 8.3. Note that the actual current states are not calculated at this stage of the algorithm. Rather, CUSUM itself only detects and records the time-points at which the mean changes between two significantly different values.

The threshold value h that the $G_\pm$ must cross to indicate a change depends on the length of the event and the desired δ value. It is a statistical approximation that sets h as the smallest possible value that keeps the expectation value of the number of false positives to one, assuming that there is no actual significant change in the signal. Since any region of interest by definition contains a significant change, the algorithm will find a true positive before finding a false positive with overwhelming

probability. The optimal threshold is determined using the function

$$f(h) = \frac{2}{\delta^2}\left[\exp\left(h + 1.166\delta\right) - 1 - \left(h + 1.166\delta\right)\right] - 2N, \tag{8.12}$$

where N is the number of data points in the event of interest[6].

The optimal threshold is the value of h for which $f(h) = 0$, which is determined using a simple linear search over $h \in (0.1, 100)$. If a zero does not exist in this range, CUSUM defaults to $h = 0.1$. This is a rough approximation that generally results in a larger number of false positives than predicted, but false positives are relatively easy to correct internally, as is discussed shortly.

We have implemented several major improvements over the basic CUSUM algorithm, leveraging what we know of the physics of nanopore translocations. First, one of the assumptions that governs the CUSUM algorithm is that any changes occur instantaneously. However, in real systems that are bandwidth-limited, this is not the case. When the nanopore current changes state from open to blocked, there is a transient rise time during which the current has a nonzero derivative. This rise time is discussed in greater detail in the next section. Depending on the input settings to CUSUM, this rise in current can be detected as a series of closely-spaced step changes. One of the major improvements to CUSUM implemented here is to explicitly exclude these regions from the fitting altogether, via the `subevent_minpoints` parameter. This parameter defines the minimum number of data points that must elapse between consecutive detected step changes for the change to be considered valid, and should usually be set to approximately 4 times the rise time of the system to ensure complete stabilization of the signal. Once all of the locations at which the mean changes are determined, the program will average over the current between adjacent change points to determine the local current state. In order to avoid rise times skewing the

average, `subevent_minpoints` samples are excluded from the start of each section when performing averaging.

Second, while δ is generally set equal to the smallest step change that one wants to detect, the algorithm can and will detect step changes smaller than δ, provided they are sustained long enough to trigger the threshold crossing. Step changes smaller than δ simply result in log-likelihoods that accumulate slower, requiring maintenance of the new mean for longer before triggering. When a false positive occurs, it results in two adjacent sections of data with essentially identical mean. The `cusum_minstep` parameter can be used to define the minimum size of the step change between adjacent sections of current for the detection to be considered a true positive. It is usually set to be equal to $\frac{\delta}{2}$. Any change detected that is smaller than this will be ignored and the two sections of data on either side will be considered to be a single state. This provides a very sensitive way to distinguish true positives from false positives, and as a result it is not necessarily a problem to use a sensitive value of δ, since an easily-corrected false positive is preferable to a much more difficult to fix false negative. However, care must be taken with the interaction between false positive probability and the `subevent_minpoints` parameter, since every time a false positive occurs, another state change detection cannot occur until that many more points have passed. If a false positive occurs within `subevent_minpoints` samples of a true state change, it will result in a false negative, which is not so easily corrected.

Finally, translocation events can occasioanally end with an overshoot of the baseline current due to electric double-layer effects, particularly in low-concentration salt solutions. The `padding_wait` parameter specifies a number of data points to exclude from both level identification and baseline averaging after an event has returned to baseline, and can be used to avoid erroneous sublevel detection on event characteristics that have nothing to do with the polymer itself. This paramter is optional, and

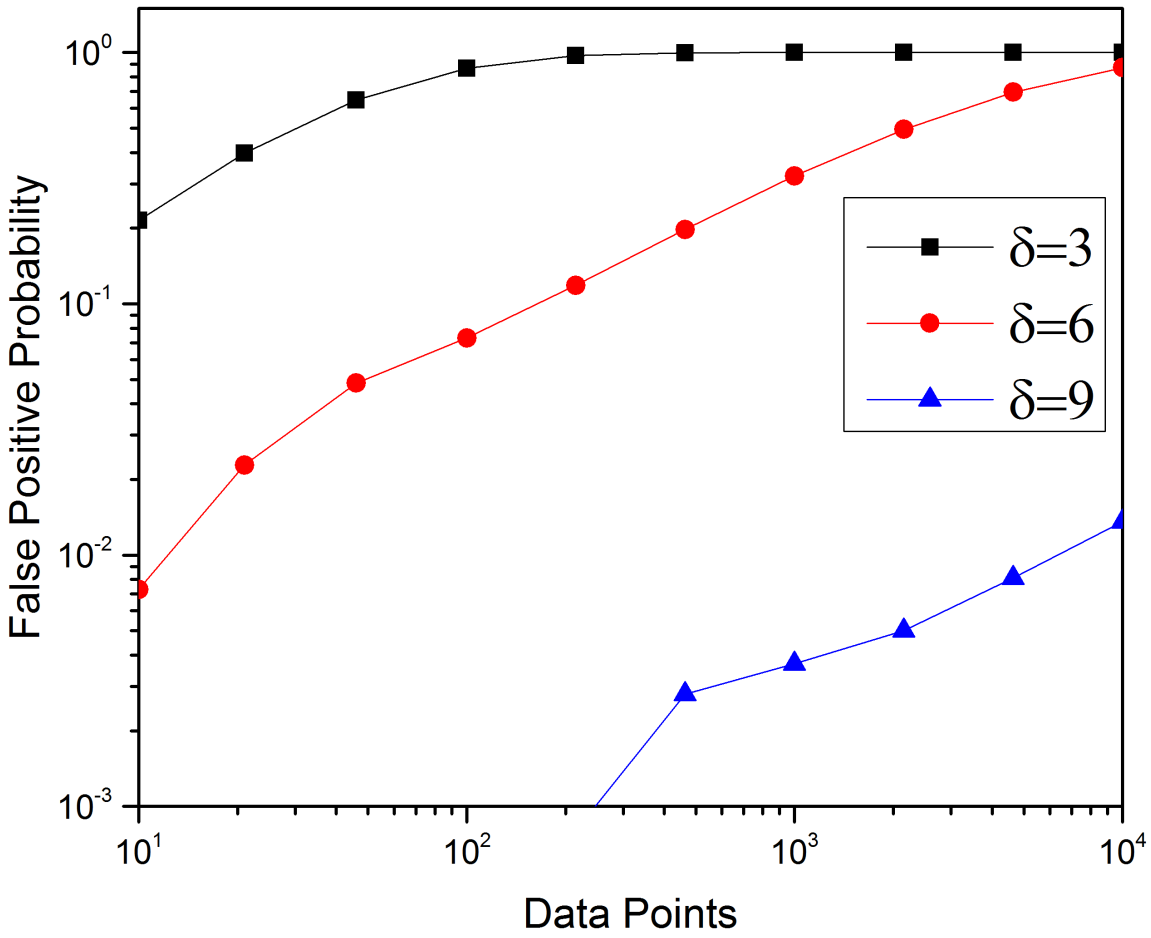

Figure 8.4: The probability of a false positive occurring somewhere in the event as a function of the length of time series with no actual change in the mean for a variety of input settings. Data here is simulated to match the spectral content of actual nanopore data, and each point is averaged over 10^4 realizations of a nanopore-typical noise process of the given length.

will default to 0 if not supplied.

Because CUSUM applies a statistical test to noisy data, it will eventually find a false positive detection given a sufficiently long time-series even if no real change occurs. In order to simulate the probability of this happening, we follow the recipe laid out by Owens[7], which allows us to generate time series which have arbitrary spectral content. By matching our simulated data to the PSD from an actual nanopore, we are able to simulate high quality statistics for the performance of CUSUM. Using

this method, the probability of a false positive detection for various values of δ and lengths of data with constant means is shown in Figure 8.4.

As a final improvement over existing implementations, CUSUM implements running calculations of the local mean and variance to avoid repeated calculation at each data set. As a result, CUSUM has $\mathcal{O}(N)$ time complexity and can typically analyze data orders of magnitude faster than it can be acquired.

8.6 Sublevel Identification using STEPFIT

As discussed in the previous chapter, the I-V response of a solid-state nanopore can be approximated by a simple RC circuit[2,8], shown below. This circuit models the pore as a single resistor R_p in parallel with the capacitance C of the membrane, all in series with an access resistance term R_a that accounts for the voltage drop in the electrolyte outside the pore mouth. When a molecule enters the pore, it causes an instantaneous (as compared to the sampling frequency) step change in the resistance of the pore, which causes a corresponding change in the current. However, this change that is actually measured is not instantaneous. The time-domain response of the RC circuit leads to a single-exponential decay between current states, so that a step change in the resistance of the pore ΔR under constant applied voltage V at time 0 leads to a current response of the form[2]:

$$i(t) = i_0 - \Delta i \left(1 - \exp\left(-\frac{t}{\tau}\right)\right), \tag{8.13}$$

where

$$i_0 = \frac{V}{R_a + R_p}, \tag{8.14}$$

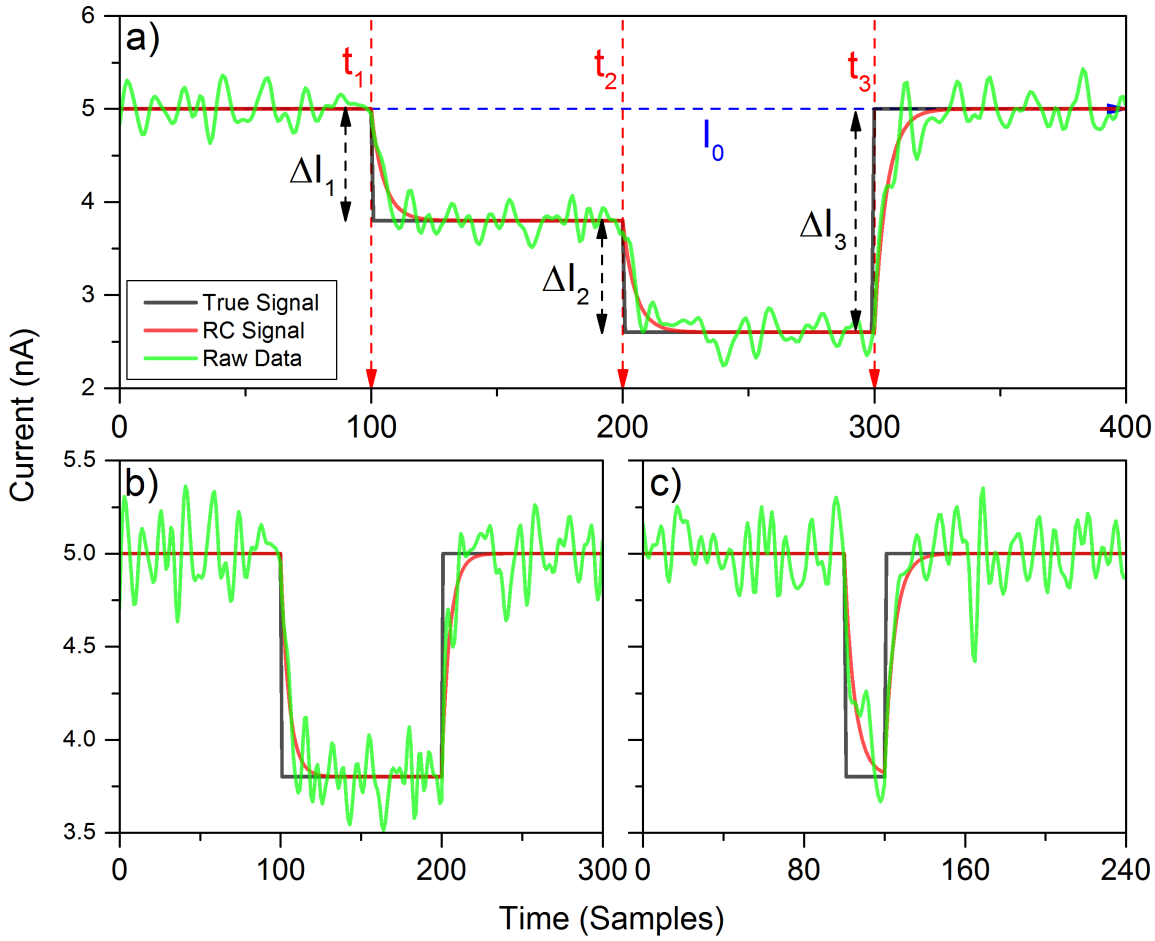

Figure 8.5: a) an example of an event with 2 levels as modelled by STEPFIT with parameters labelled. b) For events much longer than the rise time the current will reach a steady state. Events like this can be fitted accurately using either algorithm. c) Events that do not reach a steady state can only be recovered by STEPFIT.

$$\Delta i = \frac{\Delta R}{R_a + R_p + \Delta R} i_0, \tag{8.15}$$

and

$$\tau = R_a C \frac{R_p + \Delta R}{R_a + R_p + \Delta R}. \tag{8.16}$$

For multi-state events, these single exponentials are chained together, so that the current response for an N-sublevel event will be of the form

$$i(t) = i_0 + \sum_{k=1}^{N} \Delta i_k \left(1 - \exp\left(-\frac{t - t_k}{\tau_k}\right)\right) \Theta(t - t_k), \tag{8.17}$$

where ΔR_k is now the difference in resistance between state $k-1$ and k, and $R_p \rightarrow R_{p,k-1}$ is the total resistance in state $k-1$, a change that occurs with time response τ_k. Θ is the Heaviside step function, which determines the start times t_k of each step change in the series. Examples of this function are shown in Figure 8.5. Note that while in principle all of the time constants are different, the differences between them are typically much smaller than the sampling rate and are therefore undetectable experimentally[2]. We will therefore refer to *the* time constant of the nanopore system. It is possible to build high-order circuit models to more accurately depict the nanopore system, but each additional resistance-capacitance pair introduces a new time constant, all of which are faster than τ_k and which are therefore irrelevant for the sampling frequencies and bandwidths being used here[2,8]. The time constant is typically on the order of $\tau \sim 10^0 - 10^1$ μs for the nanopores throughout this work.

Given a current time-series, it is possible to perform a nonlinear fit to this functional form to extract the parameters that define the translocation event. CUSUM implements this form only for single-state functions in the STEPFIT module, so that

$$i(t) = i_0 \pm \Delta i_1 \left(1 - \exp\left(-\frac{t - t_1}{\tau_1}\right)\right) \Theta(t - t_1) \mp \Delta i_2 \left(1 - \exp\left(-\frac{t - t_2}{\tau_2}\right)\right) \Theta(t - t_2) \tag{8.18}$$

In principle $|\Delta i_1| \approx |\Delta i_2|$, and $\tau_1 \approx \tau_2$ in most cases, but all are left as free parameters

in the fitting, since discrepancies here can serve as sensitive quality control metrics. Good initial guesses for all of the parameters are easily extracted the simple thresholding algorithm discussed above. Whereas CUSUM is unable to fit events that do not achieve a steady state, this functional form is able to recover the true translocation event shape corresponding to the observed transient even when the event is too short to achieve a steady state (less than 4τ), though it becomes highly sensitive to the current noise and is inadvisable to use for events shorter than 2.5τ. CUSUM and STEPFIT are best used in conjunction with one another, using STEPFIT for short events and CUSUM for long ones. This is controlled in the configuration file by the `stepfit_samples` parameter that sets the cutoff number of samples below which the event is analyzed by STEPFIT instead of CUSUM, and the `attempt_recovery` setting, which is a boolean value which indicates that events for which CUSUM fails to find a significant level change should be refitted by STEPFIT. `stepfit_samples` is usually best set to about 4τ.

The actual fitting is performed using the Levenberg-Marquardt least-squares fitting algorithm using a slightly modified version of lmfit, a C port of the FORTRAN package MINPACK by Joachim Wuttke, which is available in its unmodified form under the FreeBSD license (apps.jcns.fz-juelich.de/lmfit)[9]. Modifications from its original form for use in CUSUM include the use of 64-bit integers for all calculations to enable indexing of very long time-series events, and the elimination of unsafe floating-point equality comparison operations.

Care needs to be taken when using nonlinear fitting techniques, particularly for low capacitance devices with very short rise times. Because the rise time is on the order of the sampling rate in these devices, very few points are actually recorded during the rise times, which can lead to overfitting of noise for the rise times in particular. Accurate identification of rise times is only possible on very short events, so that a

significant portion of the total event time is spent in a non-steady state. Even then, the rise time fits will often appear to be bimodal, with a small population of rise times much faster than the rest. These are not physical values, but rather reflect events for which insufficient data was available to achieve a good fit. If the device is able to achieve a near-steady state then the blockage depths and start and end times are usually robust against a poorly-fitted rise time, but for events shorter than 2.5τ, a bad rise time fit will also lead to incorrect values for Δi. When STEPFIT is needed, it is best to sample as fast as the hardware will allow. Even though the extra sampling frequency contributes no additional spectral information, it will provide a better sampling of the signal in the vicinity of rise times and consequently improve the accuracy of the nonlinear fit.

In order to improve the numerical robustness of the fitting algorithm and to properly bound the fit parameters, we use a change of variables. The allowed values of Δi_k fall on the interval $(0, \Delta i_{\max})$, where $\Delta i_{\max}$ is the largest absolute difference between two current samples in an event. We define a parameter p_k, and set

$$\Delta i_k = \pm \frac{\Delta i_{\max}}{2} \left(1 + \tanh p_k\right). \tag{8.19}$$

Similarly, t_k lies between $(0, T)$ where T is the total length of the event and the padding on either side. We define a parameter q_k and set

$$t_k = \pm \frac{T}{2} \left(1 + \tanh t_k\right). \tag{8.20}$$

We constrain the time constants τ_k to be positive by defining parameters r_k, choosing

an approximate time constant τ_0 and setting

$$\tau_k = \tau_0 \exp r_k. \tag{8.21}$$

Finally, the value of i_0 is constrained using $i_{\max} = \max |i(t)|$ using a parameter s_0 as

$$i_0 = \pm \frac{i_{\max}}{2} \left(1 + \tanh s_0\right). \tag{8.22}$$

While they are mathematically equivalent, these normalized functional forms have the numerical advantage that all of the parameters are of order unity and are constrained to within physical bounds. These constraints allow for robust floating-point arithmetic and improved numerical performance of the nonlinear fitting algorithm when the proper substitutions are made in Equation 8.18.

The time complexity of nonlinear fitting scales as $\mathcal{O}(Np^2)$ where p is the number of parameters. For a single step event ($p = 7$) this is reasonable, but quickly becomes computationally prohibitive as the number of sublevels increases, since $p = 3n + 1$ for an event with n sublevels. Since CUSUM is generally able to provide the same quality of fitting as STEPFIT for long, multi-level events, we use the nonlinear fitting approach only for very short, single step events. If there is a need to fit multilevel events that have sublevels which are individually too short for CUSUM to process, using MOSAIC for fitting is preferred[2].

8.7 Digital Filtering

8.7.1 Definition and Implementation

In order to extract signals with sufficient signal-to-noise ratio in nanopore experiments it is often necessary to digitally low-pass filter the signal to remove some of the contribution of high-frequency noise. As discussed in Section 1.2.3, in nanopore systems the limiting noise components scaling with frequency and are due to capacitance arising from the membrane and support structure and from parasitic capacitance within the sensing electronics.

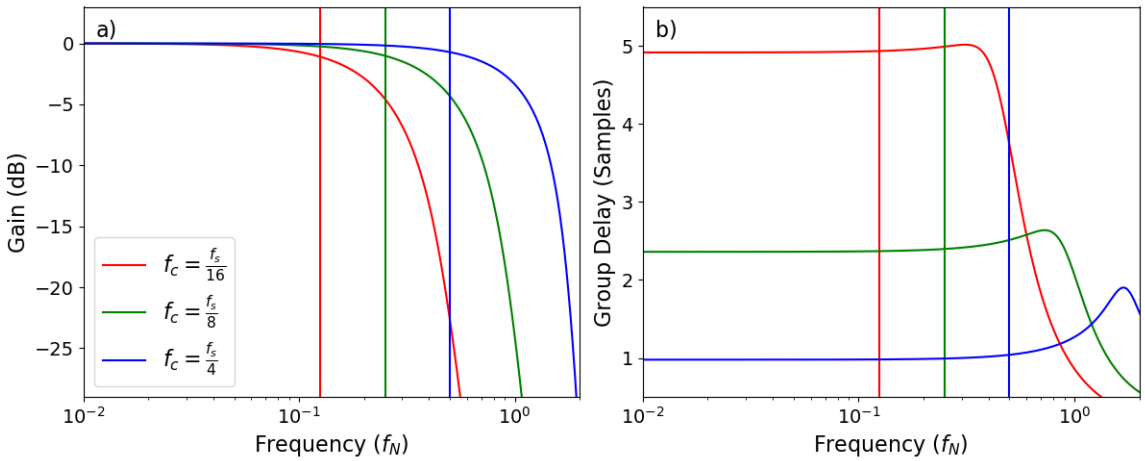

Figure 8.6: a) the gain of an 8 pole Bessel filter with various cutoff frequencies. b) the group delay of the same filters as in a), showing that as the cutoff frequency (vertical lines) increases, the group delay for frequency components near the cutoff start to experience distortion. Frequencies are normalized by the Nyquist frequency.

The Bessel filter is specified in the analysis software with four parameters. The `use_filter` boolean keyword determines whether or not a filter is applied during the thresholding step. The `event_filter` boolean keyword determines whether or not a filter is applied during event fitting. If either one of these is active, then the `cutoff` parameter sets the cutoff frequency f_c in Hz, while the `order` parameter

determines the number of poles. This is currently limited to even integers up to 10.

Digital filters are complex objects, and we make no attempt to comprehensively describe the theory behind their general implementation. Instead we focus only on aspects of the theory that are required for a practical understanding of their application to nanopore data. For more detailed information about digital filters in general, we refer the interested reader to dedicated publications in the field.

Bessel filters are a member of the class of infinite impulse response filters. Because they are implemented in the time domain as a weighted sum of the previous data points, in principle the response to an impulse at time t_0 extends to infinity. This weighted sum also introduces a phase delay between the raw and filtered signals.

The analog Bessel filter is designed such that its phase delay is maximally flat below the cut-off frequency, so that all passband frequencies are shifted equally. Moving to the digital the digital domain requires using the approximation of the bilinear transform, which does not preserve the group delay, so that the digital Bessel filter actually distorts the phase near the cut-off frequency if this occurs too close to the sampling frequency f_s, with maximal distortion occurring at $f_c = \frac{f_s}{4}$. The true maximally flat digital filter is the Thiran filter[10], though this is not currently supported by CUSUM. Figure 8.6 shows the phase and amplitude response of several digital Bessel filters.

In order to undo the effects of this phase delay and the errors associated with the bilinear transform approximation, we run the filter twice: once forward in time, and then again backwards in time on the output of the first filter. The second pass of the filter perfectly undoes the phase shift caused by the forward pass, and applies the same frequency gain as the forward pass. However, zeroing the phase delay comes at the cost of causality, since the value of the filtered current at time t now depends on the current values both before and after. Since we are not performing analysis

in real time, this is of little concern, but any future work aimed at real-time signal processing must take this into account.

The first pass of a p pole digital filter is implemented numerically for an input signal indexed as i_n as

$$a_0 y_n = b_0 i_n + \sum_{k=1}^{p} \left(b_k i_{n-k} - a_k y_{n-k} \right), \tag{8.23}$$

where y_n is now the causal, phase-shifted, filtered signal and n runs from 0 to $N-1$ in that order. To avoid edge effects, the signal is padded on both ends with values equal to the end-most value. The second pass of the filter then applies

$$a_0 x_n = b_0 y_n + \sum_{k=1}^{p} \left(b_k y_{n+k} - a_k x_{n+k} \right), \tag{8.24}$$

where x_n is then the zero-phase non-causal filtered signal and n now runs from $N-1$ to 0 in that order.

The filter coefficients $\{a_k, b_k\}_{0 \leq k \leq p}$ are determined by the filter transfer function in the $\mathcal{Z}$ domain

$$H(z) = \frac{\sum_{k=0}^{p} b_k z^{-k}}{\sum_{k=0}^{p} a_k z^{-k}}, \tag{8.25}$$

and are implemented in CUSUM as a lookup table for even orders of $p \in \{2, 4, 6, 8, 10\}$, using values ported from the Scientific Python (scipy) library implementation contained in `scipy.signal.bessel` [11,12].

Due to the padding at either end of the filter, there is a mismatch between the edges of adjacent filtered data sections, though in practice the discrepancies are negligibly small compared to the noise in the system and do not affect the accuracy of

fitting. Zero-phase filtering also doubles the effective order of the filter, since the transfer function for the combined filter is $|H(z)|^2$.

It is difficult in general to say what the best filter parameters are for any given experiment. An effective rule of thumb is to set the cutoff frequency as high as possible while maintaining an SNR of at least 6. Filtering minimally is always the preferred option, and if sufficient SNR exists it should be avoided entirely, both because of the possibility of distortion of fast features within the signal, and because it is by far the slowest process in CUSUM computationally. Leaving the filter off can reduce the run time by up to 50%.

8.7.2 Digital Filtering of RC-Limited Signals

While we have been referring to a single timescale in the discussion so far, there are actually two important timescales that determine the measured response of the system to changes in the nanopore resistance as molecules translocate. The first is the RC time constant already discussed:

$$\tau_{RC} = \frac{CR_aR_p}{R_a + R_p}. \tag{8.26}$$

Since the nanopore is well-approximated as a linear circuit element, we can build up the response to more complex events as linear sums of the single step response. The RC time-domain current response of the nanopore system to a step change in the resistance has already been discussed in some detail, and is well approximated by a one-sided exponential decay between constant current states:

$$i(t) = i_0 - \Delta i \left(1 - \exp\left(-\frac{t}{\tau_{RC}}\right)\right). \tag{8.27}$$

The second timescale is the rise time of the digital filter used, which is proportional to, though generally smaller than the inverse cutoff frequency of the Bessel filter:

$$\tau_B \propto f_c^{-1}. \tag{8.28}$$

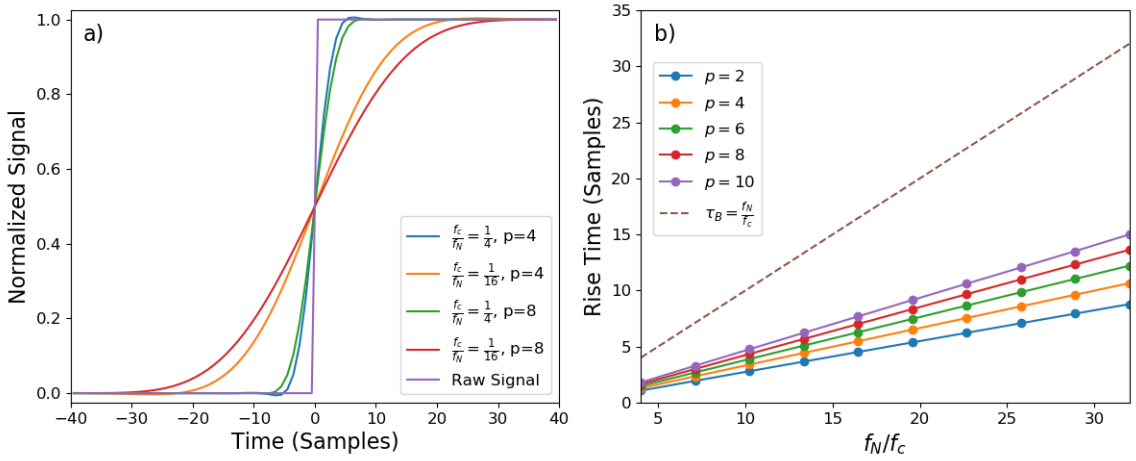

Figure 8.7: a) The step response of various zero-phase Bessel filters, showing that while the two-sided exponential is not a perfect fit due to the slight time-domain ringing of a digital Bessel filter, it is a good approximation. b) The rise times of various zero-phase Bessel filters as a function of filter order and cutoff frequency, showing the expected linear relation between rise time and inverse cutoff frequency.

The time-domain response of a Bessel filter to a step change in the current is much more difficult to represent than the RC response. Making use of the $\mathcal{Z}$ transform, which generalizes the Laplace transform to digital signals, it is possible to represent the digital time-domain response of a single pass of the filter on a single step change Δi by

$$i_k = \mathcal{Z}^{-1}\left(\Delta i \frac{z^{1-n}}{z-1} H(z)\right), \tag{8.29}$$

where n is the index of the point t_0 at which the step change occurs. While this is analytically solvable, the solution is an impractically long rational form containing very large exponents that is neither useful nor well-behaved numerically. A purely empir-

ical approximation to the response, which suffices to extract the relevant timescales while failing to capture the time-domain ringing that occurs near the actual step, is the two-sided exponential sigmoidal function

$$i(t) = i_0 - \frac{\Delta i}{1 + \exp\left(-\frac{t-t_0}{\tau_B}\right)}. \tag{8.30}$$

The two-sided nature of this form comes from the non-causal nature of the dual-pass filter. Note that the infinite impulse response nature of the function means that the impulse affects the entire current signal. Far away from t_0, when $|t - t_0| \gg \tau_B$, the RC and filtered response of the system agree, as expected. Figure 8.7 shows the step response and τ_B for zero-phase Bessel filters as a function of $\frac{f_N}{f_c}$ for various filter orders p.

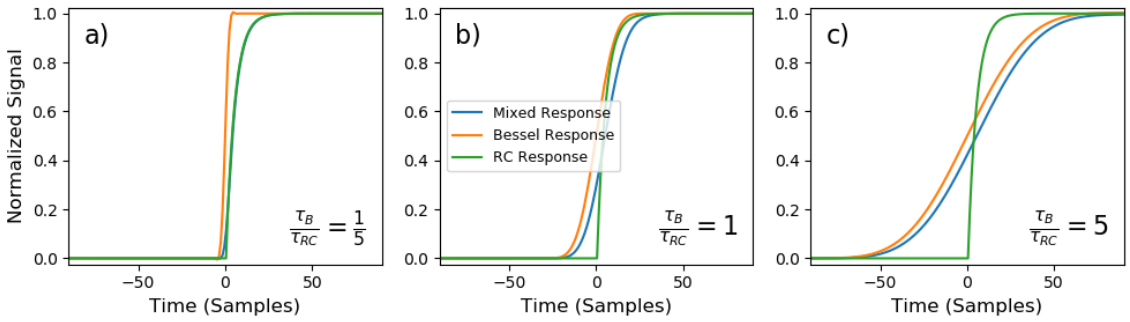

Figure 8.8: a) The The RC response, Bessel filtered response, and mixed response for the case where the RC time constant dominates. The mixed response closely approximates the RC response, which is the ideal case for fitting using either algorithm. b) The case in which the RC time and filter rise time coincide. The mixed response both underestimates the event start time, and does not follow either the filter or the RC response, making accurate fitting by either algorithm impossible. c) The case in which the Bessel filter timescale dominates. Because the mixed response reasonably approximates the response of the Bessel filter alone this could in principle be fitted using the Bessel step response equation, but this is not currently implemented.

If $\tau_{RC} \gg \tau_B$, the measured response of the system is dominated by the RC time constant and the Bessel filter response can be ignored. When the opposite is true,

the Bessel filter response dominates. If $\tau_B \sim \tau_{RC}$, one obtains a convolution of the two responses, which has no simple analytical form and should be avoided if at all possible. Figure 8.8 shows the filtered step response, the filtered RC response, and the raw RC response for the three cases discussed above. Because STEPFIT assumes the RC-limited form of the signal, it is vitally important that the first condition hold in any context where STEPFIT is used; the analysis software presented here does not implement a nonlinear fitting form for a Bessel-filter dominated time-domain response. Even when using CUSUM, it is important that the dominant timescale be the τ_{RC}, since the location of the step change the CUSUM detects will correspond to the point at which the current begins to deviate from the local mean, which will happen too early if τ_B is dominant. For this reason, it is important to filter minimally, only as much as is needed to allow sufficient SNR for accurate event threshold detection. Implementation of a nonlinear fitting analog of STEPFIT for Bessel-dominated events is possible using a linear combination of instances of Equation 8.30 instead of Equation 8.27 for the fit, but it has thus far proven unnecessary since this case is very rare and can usually be avoided entirely by filtering less heavily.

8.8 Quality Control

CUSUM has a number of built in checks that are performed at various stages of event fitting to ensure that the fits actually correspond to physical translocation events. Events that are flagged by one of these filters are assigned an error code and are excluded from the main set of outputs, though details of the excluded events can be found in the `rate.csv` output file. The error codes are summarized in table 8.1.

When the program is first run, it executes a very simple quality control check that verifies consistency between dependent configuration parameters. If the relationships

between any parameters are inconsistent, it will either internally correct the problem, or issue a warning. In either case, changes and warnings are logged and printed to the console. It is vitally important to check these messages, as they can change the outcome of an analysis run. Work is ongoing to reduce the number of configuration parameters to a minimal set of mutually independent parameters for which these relationships will be irrelevant.

The first quality control check applied to the actual detected events is to filter out events that are either too short to be fitted, or too long to be translocations, which are determined by user-provided `event_minpoints` and `event_maxpoints`

Table 8.1: A list of possible error codes relating to event fitting with CUSUM and STEPFIT

Code	Meaning	Possible Solution
0	Successful CUSUM fit	
1	Successful STEPFIT fit	
2	Baseline before and after event are different	Increase `hysteresis`
3	Event length longer than `event_maxpoints`	Increase `event_maxpoints`
4	Event length shorter than `event_minpoints`	Decrease `event_minpoints`
5	CUSUM fit fewer than 3 levels including baseline	Decrease `cusum_delta`, `cusum_minstep`, and/or `subevent_minpoints`
6	Unable to read the current data	Verify that the data file was not changed
7	Unable to extract sufficient padding	Decrease concentration of analyte
8	STEPFIT found a change smaller than `cusum_minstep`	Decrease `cusum_minstep`
$9 - 18$	lmfit encountered a numerical error	Submit a bug report

configuration parameters respectively. These filters are applied twice: once during the first initial threshold event finding, and again after events have been fitted either by CUSUM or STEPFIT. The `event_minpoints` parameter should be set to $2.5\tau_{RC}f_s$ if STEPFIT is used for short events, and to $4\tau_{RC}f_s$ if only CUSUM is used.

If CUSUM fitting fails to find at least three distinct current states in a segment of data, the event is optionally fed to STEPFIT before being labelled a failed fit and rejected. This optional step accounts for the possibility that due to statistical fluctuations the event detected was too short for CUSUM to properly fit it despite passing the initial duration tests. If STEPFIT also fails, the event is rejected. If the program is generating many of this error type on what should be valid events, the most likely culprit is either that that `cusum_delta` and `cusum_minstep` are too large, making the algorithm insensitive, or that the `subevent_minpoints` is too large, precluding CUSUM from properly detecting the second current step change. A similar error mode occurs if STEPFIT finds a current change that is smaller than `cusum_minstep`.

If two events are very close together, such that the program is unable to extract sufficient padding from the region between them to determine an accurate baseline, then both events are rejected. Care should be taken when using high concentrations of analytes to ensure that the time between events is still significantly longer than the average event duration. Finally, if the baseline current before and after an event differ by more than 2.5σ, the event is rejected as incomplete. The most likely cause is that `hysteresis` is too small, resulting in the thresholding algorithm marking the end of an event before it actually returns to baseline.

Finally, the lmfit library has a host of internal error codes related to detection of various numerical pathologies that can arise when using the black box that is the Levenberg-Marquardt algorithm.

It is important to note that the presence of a significant population of events with particular error codes does not necessarily mean that there is a problem. Indeed, using parameters that are overly sensitive and relying on the internal quality control metrics to clean up the resulting data set is a perfectly valid option in some pathological cases. Determining whether or not the presence of error codes represents a problem with the fitting or a problem with the data itself requires careful consideration by the user and depends entirely on the context of the experiment being analyzed.

8.9 Data Visualization and Post-Processing

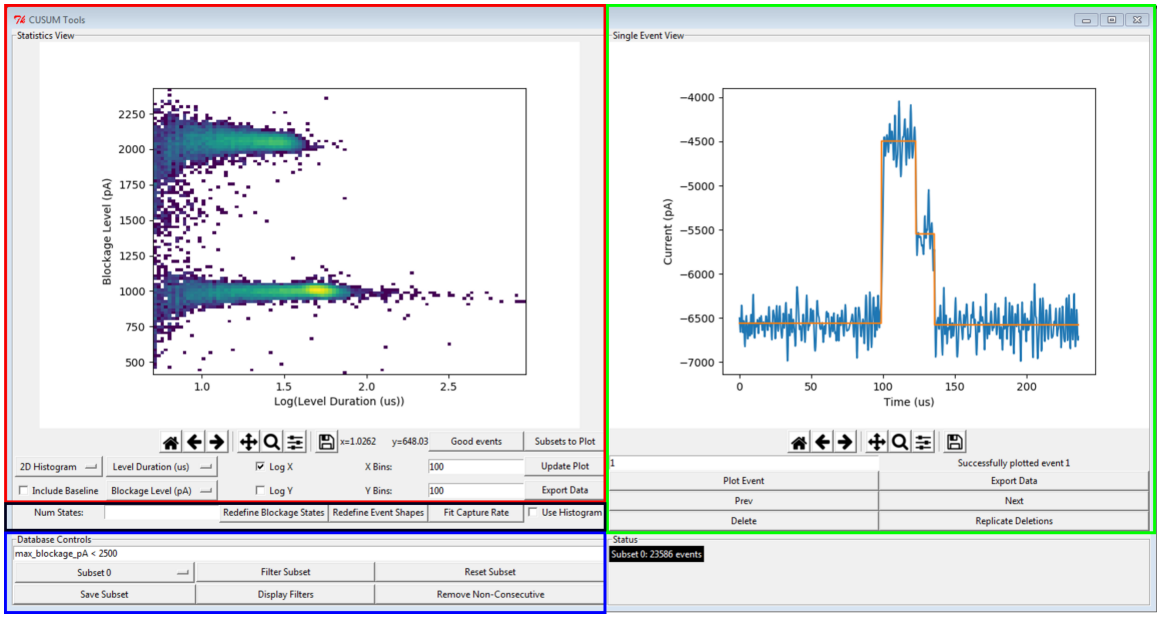

Figure 8.9: The main GUI for `readevents.py`. Red box: the statistics view window, which allow any two columns from `events.csv` to be plotted against one another as scatterplots or heatmaps, or any single column to be plotted as a histogram. Green box: The single event viewer, which plots the timeseries and fit for each event by index. Black box: the analysis box, which allows event shapes to be defined by blockage level, and capture rates to be fitted for a given experiment. Blue box: database controls, which provides tools for filtering event databases to isolate populations of interest.

The output of CUSUM can be visualized with `readevents.py`, an open source data viewer and analyzer available at online[13]. When first run, the user will be prompted to enter an input file, which should be the output file `events.csv` from a previous CUSUM analysis run. The main viewer of the GUI is presented in Figure 8.9. There are four main components to this tool.

8.9.1 Data Viewer

The main area of the GUI, outlined in red in Figure 8.9, is the statistics view window. This area provides plotting controls for the output of CUSUM, allowing any two columns from `events.csv` to be plotted against one another either as scatter plots or 2D histograms, as shown in the example. Plot types and columns to be plotted are selected via dropdown menus, and scales can be linear or logarithmic. The plot itself, as well as the data underlying it, can both be easily and independently exported for use in other software.

On the right, labelled in the green box in Figure 8.9, the user can view the traces and fits of each individual event labelled by index in order to verify fit quality.

8.9.2 Data Stratification

One of the most useful features of `readevents.py` is its ability to stratify experimental data into any number of subsets and view the resulting statistics for each population at the same time. This data filtering is implemented using SQL-style database queries entered into the database controls box. Any valid SQL query of the form `select * from [table] where [condition]` can be applied, where `[condition]` can be any numerical restriction on one or more of the columns in `events.csv`. For example, to keep only events with a maximum blockage less than

2000 pA, the user would enter `max_blockage_pA < 2000`. Equality must be tested using the `==` operator.

More complex filter are also possible. For example, if one wishes to keep only the events inside an ellipse on an $x-y$ plot with columns x and y corresponding to columns in `events.csv`, the user could enter `((x-h)/a)**2 + ((y-k)/b)**2 < 1`, where a and b are the desired major and minor axes and (h, k) is the centroid. The filter also understands elementary trigonometric operations and logarithms. For example, to select all events within an ellipse on the a scatterplot of x versus $\log y$ rotated an arbitrary angle θ counter-clockwise about its own centroid, one would enter

`(((x-h)`$\cos\theta$`+(log y-k)`$\sin\theta$`)/a)**2 + (((x-h)`$\sin\theta$`+(log y-k)`$\cos\theta$`)/b)**2 < 1.`

The user can also use boolean expressions `and` / `&` and `or` / `|` to combine filters as needed, or chain filters together successively to build complex conditions out of simple rules. Subsets can be saved directly into files that can be reopened using `readevents.py` at a later date.

8.9.3 Event Shape Fitting

The black box in the example provides controls for two useful functions. The first allows a user to assign event shapes to every event which encode the blockage states for every sublevel in order into a single integer. An example is shown in Figure 8.10. To achieve these results, the user must plot the `Blockage Level (pA)` column as a histogram, and indicate in the `Num States` box the number of discrete states to fit. Once this is done, the user clicks the `Redefine Blockage States` button, and clicks on the graph at the edges of each blockage state that is desired to be fit. Once this is finished, the user clicks the `Redefine Event Shapes` button to finish. This defines two new columns in `events.csv`, which encodes an integer for every event

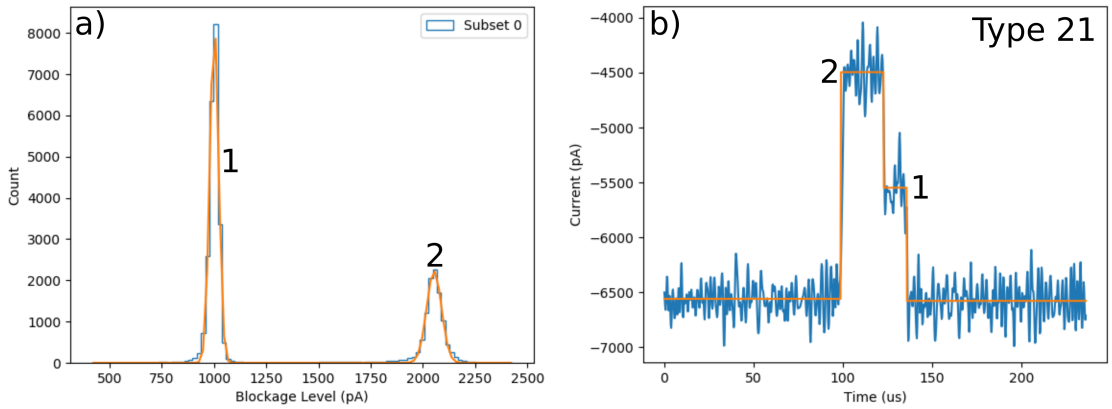

Figure 8.10: a) Fits to the two blockage levels as indicated by the user, which assigns an integer to each blockage state. b) The resulting event shape classification for a typical type 21 event.

that indicates to which blockage state each consecutive level belongs to. Events that contain levels not defined by the user are assigned a shape of -1. Once event shapes are defined, two new columns are defined in the internal data structure, `event_shape` and `trimmed_shape`. The former encodes an integer for which each digit corresponds to a current blockage level, while the latter concatenates any repeated levels into a single one. Once these columns are defined, saving the active subset will save these columns as well.

8.9.4 Event Rate Fitting

The event rate for a given experiment is exponentially distributed since in the concentration regimes studied with nanopores it is limited by the rate of diffusion of polymers into the capture region of the nanopore. The natural way to determine the event rate for a given experiment is then to fit an exponential distribution to the interevent times observed. However, there is a complication arising from the fact that event fitting occasionally rejects good events due to fitting artefacts that are unrelated to the physics of passage, resulting in an interevent time that is not representative of

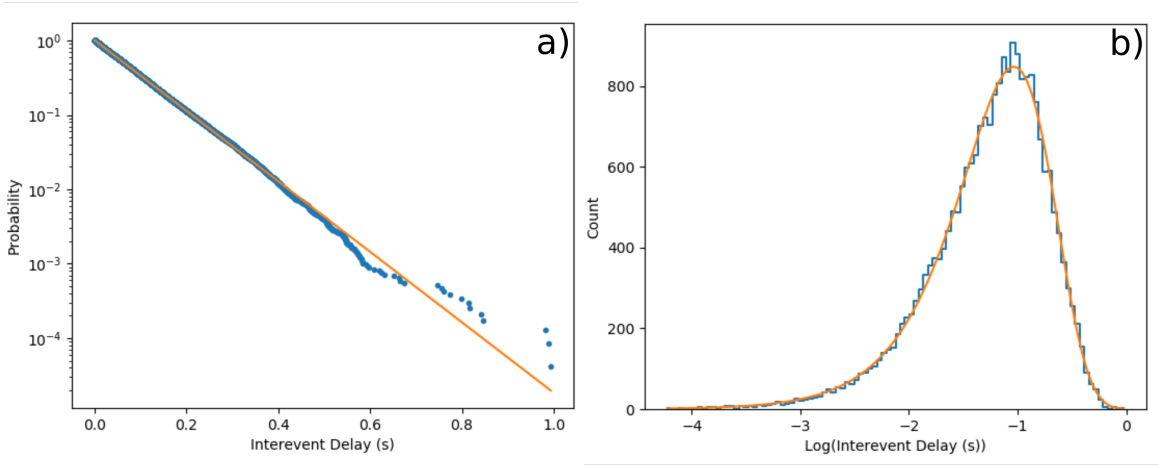

Figure 8.11: a) Event rate for an experiment fitted using the survival probability, i.e. the cumulative distribution function of the probability distribution. b) Event rate for the same experiment fitted using the probability density function after log-transforming.

the underlying distribution.

In order to avoid this problem, `readevents.py` internally picks off only interevent times for which the indices of adjacent events differ by only 1, which indicates that no events were discarded in between. Because CUSUM has a negligibly small false negative probability thanks to the sensitive nature of the thresholding algorithm used to find the events in the first place, this allows us to assume that any such interevent times are valid. Care should be taken in any situation in which this assumption does not hold, since the event rate extracted will no longer be valid in that case.

Once valid interevent times are identified, the user can choose to either fit the distribution using the survival probability, which is related to the cumulative distribution function

$$s(t) = 1 - \exp\left(-\lambda t\right) \tag{8.31}$$

or the probability density function

$$p(t) = \lambda \exp(-\lambda t), \tag{8.32}$$

after log-transforming. These fits are shown in Figures 8.11a and 8.11b respectively. In either case λ is the capture rate for the given experiment, and should in principle be the same independent of the method chosen, though sometimes one fitting method will outperform the other depending on the quality of statistics available. The former method is more sensitive to outliers, but performs well even with a small dataset, while the latter method is robust against outliers but requires more comprehensive statistics to produce meaningful results.

This framework is also able to simultaneously fit the event rate for multiple subsets simultaneously within the same overall experiment. To do so, good events must be indicated manually with the `Good Events` button, after which these events can be stratified with the database filters and each subset can be independently fitted for event rate without needing to discard non-consecutive events within each subset.

8.10 Conclusion

This chapter has presented a number of tools for the analysis of nanopore time-series data and visualization of the results that represent the state of the art in nanopore signal processing. While development is ongoing in order to streamline the user experience, these tools should already be useful to researchers in the field.

Planned development going forward consists mainly quality-of-life improvements to the user experience in order to make it more accessible to newcomers to the field and to facilitate setup in remote labs. In particular, it is clear from the discussion

above that in many cases there are dependencies between configuration parameters, which would allow for streamlining of the setup of configuration files by hiding these dependencies from the user by default. This relatively simple optimization will be implemented in the near future. The process by which CUSUM is actually run is also fairly opaque, and could be integrated into a simple GUI interface from which configuration files could be generated graphically.

On the backend side, while CUSUM performs very well for long events, and for short single-file events, it fails when fitting events that contain multiple sublevels shorter than 4τ. While this use case is covered by MOSAIC currently, plans exist to implement a hybrid approach in CUSUM that is able to locally apply STEPFIT within a subsection of an event containing a single short sublevel in order to extract these structures without the need to resort to high parameter-count nonlinear fits.

Finally, CUSUM is very nearly in the class of embarrassingly parallel problems that could achieve linear speedup through parallelism. The groundwork for this improvement has already been laid, and should enable a further order of magnitude speedup in nanopore timeseries analysis.

Acknowledgements

The author would like to thank Martin Charron, Eric Beamish and Phillip Karau for their contributions to the cusumtools software suite, and all the members of the Tabard-Cossa and Godin labs for their help testing and debugging the various nanopore analysis tools developed in this chapter. The author acknowledges Arvind Ballijepalli and the MOSAIC developers for their open source implementation of the STEPFIT algorithm, Joachim Wuttke for the lmfit nonlinear fitting library[9], and Enthought Inc. and the Scipy developers, in particular endolith for their open-source

implementation of digital Bessel filters. Finally, the author acknowledges Salem for their help debugging a parallelized version of CUSUM.

Bibliography

[1] K. Briggs, "CUSUM." https://github.com/shadowk29/CUSUM, 2015.

[2] J. H. Forstater, K. Briggs, J. W. F. Robertson, J. Ettedgui, O. Marie-Rose, C. Vaz, J. J. Kasianowicz, V. Tabard-Cossa, and A. Balijepalli, "MOSAIC: A Modular Single Molecule Analysis Interface for Decoding Multi-state Nanopore Data," *Analytical Chemistry*, vol. 88, no. 23, pp. 11900–11907, 2016.

[3] A. Balijepalli, K. Briggs, J. Forstater, Robertson Joseph, and C. Vaz, "MOSAIC: A Modular Single-Molecule Analysis Interface." https://github.com/usnistgov/mosaic, 2014.

[4] E. S. Page, "Continuous Inspection Schemes," *Biometrika*, vol. 41, no. 1/2, p. 100, 1954.

[5] C. Raillon, P. Granjon, M. Graf, L. J. Steinbock, and A. Radenovic, "Fast and automatic processing of multi-level events in nanopore translocation experiments.," *Nanoscale*, vol. 4, pp. 4916–24, aug 2012.

[6] D. Seigmund, *Sequential Analysis: Tests Confidence Intervals*. Springer Series in Statistics, 1985.

[7] A. J. Owens, "An algorithm for generating fluctuations having any arbitrary power spectrum," *Journal of Geophysical Research*, vol. 83, no. A4, pp. 1673–1675, 1978.

[8] A. Balijepalli, J. Ettedgui, A. T. Cornio, J. W. F. Robertson, K. P. Cheung, J. J. Kasianowicz, and C. Vaz, "Quantifying short-lived events in multistate ionic current measurements.," *ACS Nano*, vol. 8, pp. 1547–53, feb 2014.

[9] J. Wuttke, "LMFIT: Levenberg-Marquardt least squares fitting." http://apps.jcns.fz-juelich.de/doku/sc/lmfit, 2004.

[10] J.-P. Thiran, "Recursive digital filters with maximally flat group delay," *IEEE Transactions on Circuit Theory*, vol. 18, no. 6, pp. 659–664, 1971.

[11] E. Jones, T. Oliphant, P. Peterson, and Others, "SciPy: Open source scientific tools for Python," 2001.

[12] B. W. E. Thomson, "Delay Networks Having Maximally Flat Frequency Characteristics," *Proceedings of the IEE-Part III: Radio and Communication Engineering*, vol. 96, no. 44, pp. 487 – 490, 1949.

[13] K. Briggs, M. Charron, E. Beamish, and P. Karau, "cusumtools." https://github.com/shadowk29/cusumtools, 2015.

Chapter 9

Outlook

Kyle Briggs

9.1 Possibilities

The bar of novelty and complexity that must be met in this field for work to be of interest has moved at an astonishing and accelerating pace over the past few years. From early work in which researchers marvelled that the nanopores could detect DNA at all and sequencing was a seemingly distant pipe dream, nanopore technology is now at a point where solid-state nanopores can detect genetic markers of disease and characterize proteins[1,2], and where biological nanopores have actually been used to sequence human DNA, more or less as originally envisioned[3]. The focus of the solid-state nanopore research in our group has also shifted significantly in the last few years thanks in large part to the development of CBD, from fabrication and characterization of the nanopore sensing elements themselves to the development of novel applications for the single-molecule sensing capabilities of nanopores.

With these advances comes the possibility of a revolution in medical diagnostics, in which treatment can be easily and cheaply tailored to an individual genomic profile. However, standing between solid-state nanopores and these promised applications are still several major problems.

9.2 Open Problems

9.2.1 Consistency

Even though nanopores formed with CBD are now easy to make and use, they suffer from issues of instability and inconsistency that make them difficult to deploy in a clinical setting where highly repeatable and consistent performance is of utmost importance. Because nanopores are small enough to make the atomic nature of matter relevant to their performance, even slight dissolution of the nanopore material will

result in a significant change in size alter its performance as a sensor[4]. The exact chemical and physical processes by which this size instability occurs have not been explored in great detail in the nanopore field. While the work presented in Chapter 6 begins to address this by decoupling sensor performance from stability, it still does not present a solution for the long term stability required for clinical use. While in principle CBD could be used to fabricate pores at the point of care directly and thus avoid the long term stability problem entirely, this runs into regulatory problems with fabricating the sensing element for a test on the fly, which makes quality control challenging.

In addition to pore size changes, small differences in the pore geometry (local membrane thickness variation, deviation from cylindrical geometry, etc.) can cause the shape of signals generated by translocating molecules to differ between two different pores, or even between signals generated on the same pore at different times. This makes it difficult to automate and quality-check analysis of nanopore signals, which is a requirement for any medical assay based on a nanopore sensing element. Geometry differences and other uncontrolled factors also lead to wildly varying capture rates for DNA between ostensibly identical pores and operating conditions, making it difficult to relate capture rate of a target molecule to its concentration with any degree of accuracy.

Some work on alternative membrane materials has shown that there exist more stable options than SiN_x, such as HfO_2[5], though there is limited data available on this type of membrane as compared to SiN_x. A thorough exploration of novel membrane types and architectures will be needed in order to find one that is suitable for clinical use. The near-infinite variety of transition metal dichalcogenides will provide a fertile ground for experimentation, with MoS_2 being the first to be explored as a potential basis for nanopores[6]. The ideal material must be highly inert and non-reactive

with the target analyte and permit the existence of stable, free-standing membranes with nanometre thickness while being highly resistant to dissolution in an aqueous environment. Needless to say, this is a challenging problem given the size of the available parameter space, but one that certainly has a solution waiting to be discovered, though it may require some complex layered structure to achieve the ideal electrical properties.

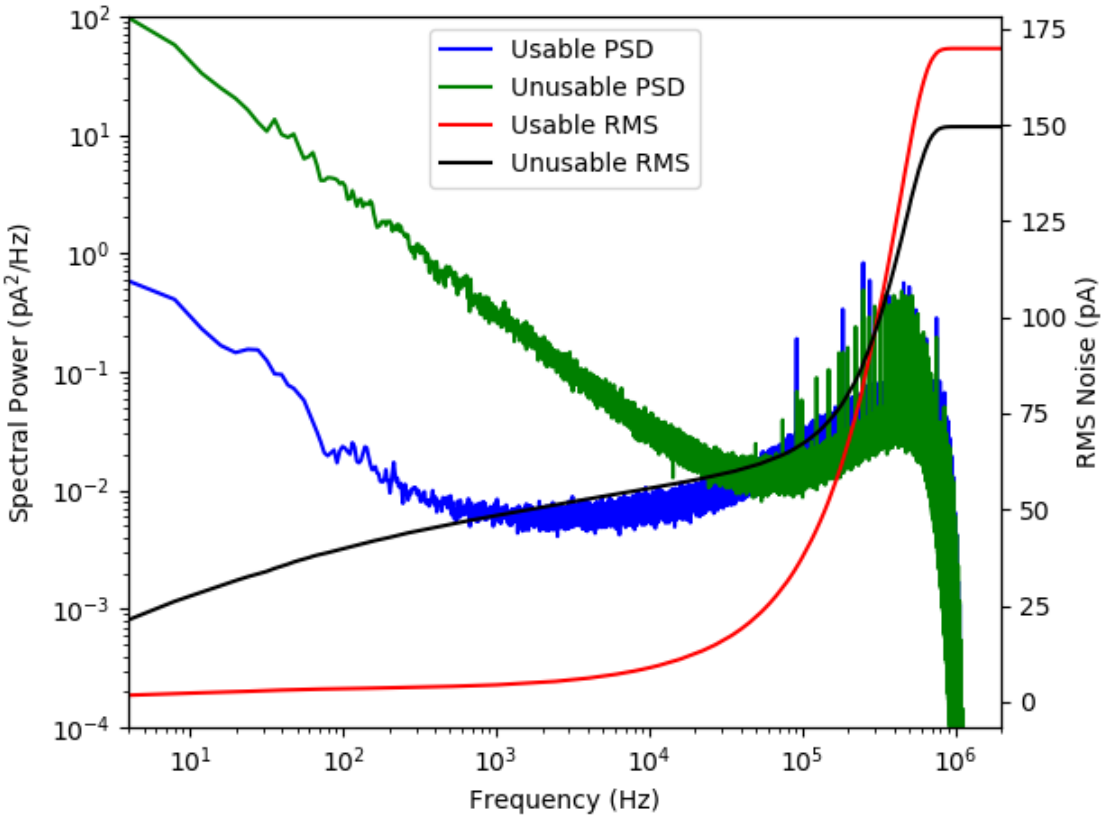

Figure 9.1: Two similar nanopores prepared with the same protocol can have dramatically different power spectra in the low-frequency regime, with one being entirely useless for biomolecule sensing. Despite having lower RMS noise, the pore with high low-frequency noise is useless for sensing and will likely not allow DNA passage at all. The left axis corresponds to the power spectrum, while the right axis corresponds to the integrated RMS noise.

The second major problem facing nanopores as clinical sensors is inconsistency in

the noise performance between ostensibly identical nanopores. Two pores made using the same protocol and from the same membrane source can have dramatically different low-frequency noise spectra, for reasons that are poorly understood at best. Even worse, pores with high $\frac{1}{f}$-type noise often fail to pass DNA at all. The nanopore field has a serious knowledge gap when it comes to the low-frequency part of the nanopore power spectrum, a gap that accounts for a significant segment of failed nanopore experiments. While some very elegant experiments have identified nanobubbles as a source of low-frequency noise[7], there are certainly more noise sources in this frequency range that are not yet understood. While some effort has been put toward understanding the specific low-frequency noise sources that correlate to failed nanopores[7,8], it's clear that additional work is needed in order to eliminate this issue.

Fortunately, there is a shortcut that can allow solid-state nanopores to overcome these challenges without actually solving them. Due to the ease with which solid-state nanopores can now be integrated into complex fluidic geometries using CBD, it is in principle possible to massively parallelize nanopore fabrication, with techniques already existing for quickly serially fabricating many nanopores on a single support membrane[9–11]. The only thing standing between these integration schemes and true parallization is the development of appropriately miniaturized and parallelized CMOS electronics, which is already well underway[12]. Given a sufficiently large number of pores, the failure of many of them will not compromise sensor performance. This approach is already being used by Oxford Nanopore in their commercial nanopore sequencers, which employ several thousand biological nanopores in parallel, of which some fraction fail in every device without causing complete failure of the sequencer. Solid-state nanopores are cheap and require only only simple, low-bandwidth electronics to fabricate using CBD, so the limits in their potential degree of parallelization are of an engineering nature rather than one requiring any additional fundamental

research.

9.2.2 Nanopore Theory

There exists a significant divide in the nanopore field between theoretical work on translocation dynamics and experimental results. In particular, there is currently very little experimentally validated theoretical work that attempts to address the problem of mapping temporal information in the electrical signal to spatial position along the analyte in the pore[13–17]. This is due in large part to the complexity of analysing a dynamic object such as a polymer translocating a nanopore theoretically. So many idealizing assumptions must be made to make progress theoretically that the results are difficult to match up with experiments performed on non-ideal pores (i.e. pores which are not cylindrical, surface charge variations, etc.). As nanopore sensor consistency and characterization methods improve so will agreement between theory and experiment, but significant efforts will be required both from theorists and experimentalists to find a middle ground.

This is especially important for analysis of tagged polymers[1,18–22], where the position of tags along the DNA backbone can only be approximately matched to the position of corresponding signals within a translocation event, a problem further compounded by the contribution of stochasticity in the polymer motion. Further complications arise from folded passage of polymers, since in order to have sufficient SNR to accurately resolve translocation events the driving voltage must be high enough that DNA can form hairpins during translocation. Elimination of these hairpins can greatly increase the rate at which usable translocation events can be collected in a single experiments. Chapter 6 is a step in the right direction in both motion control of the polymer and suppression of folding, but the folding suppression property of the

nanofilter is still poorly understood and is the subject of ongoing work[23].

9.3 Ease of Use

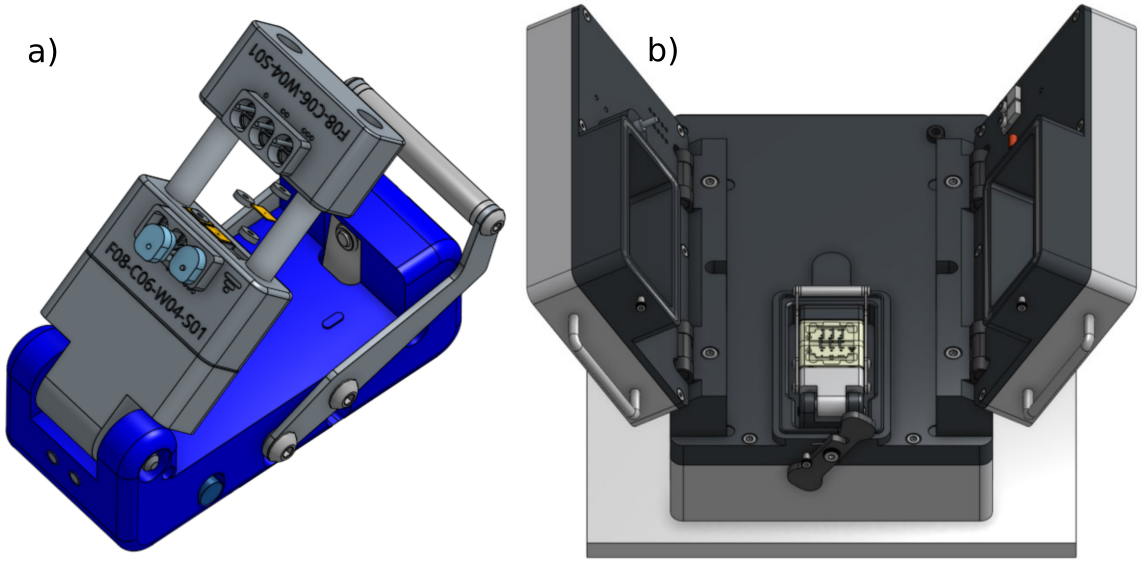

Figure 9.2: a) An early version of a three-channel fluidic cell which holds nanopore support chips and electrodes in place for both fabrication and sensing. The two half-cells are contained in a simple clamping mechanism which provides enough force for a fluidic seal. b) The nanpore fabrication and sensing instrument, containing the clamped flow cell from a). One of the lids permits 3-channel fabrication of solid-state nanopores, while the other allows for serial sensing on one of the channels.

The ultimate goal of most nanopore research is to achieve a sensor for use in a clinical or industrial setting, and the field is sufficiently mature that this is a realistic goal within the next few years. Since it is unreasonable to assume that everyone who might use these tools will be an expert, methods of nanopore fabrication, sensing, and analysis must be developed that are sufficiently simple and automated that a non-expert user can obtain useful results quickly, hiding most if not all of the detail of the backend from the user. Our lab has taken the first steps toward that goal, developing instrumentation and software which simplifies the task of fabricating use-

ful nanopores to the point that a group of high school students were able to make and use a solid-state nanopore on their first attempt. The workflow that has been developed is detailed in Figure 9.2, which depicts fluidic cells and electronics that enable simple assembly and fabrication of three solid-state nanopores in parallel. The current process flow requires minimal user intervention to perform quality control during fabrication of the nanopores, in the near future the fabrication process and quality control processes will be automated to the point that no user intervention will be required at all between insertion of the nanopore chips into the flow cell and sensing of clinically relevant samples.

9.4 Ongoing Work

Addressing the issues raised in the previous section will provide for several years of research alone, some of which has already begun. First, driven mainly by Matthew Waugh, a research associate in the lab, an invited manuscript is currently in preparation for Nature Protocols which explores the fabrication and operating conditions and membrane properties which promote consistent noise performance and nanopore stability, and which will present the instrument detailed in Figure 9.2 to the community. Preliminary data suggest that the surface properties of the membranes correlates strongly to noise performance, and that yield of stable, low-noise pores can be greatly improved with careful preparation of nanopore chips prior to CBD fabrication.

Second, a manuscript is in preparation which explores the possibility of using an internal calibration standard of a known concentration of DNA of a particular length in order to normalize away the influence of pore geometry on molecular capture rate. Preliminary data show that the ratio of capture rates of two molecules simultaneously has lower time-variation than either capture rate alone, allowing for more sensitive

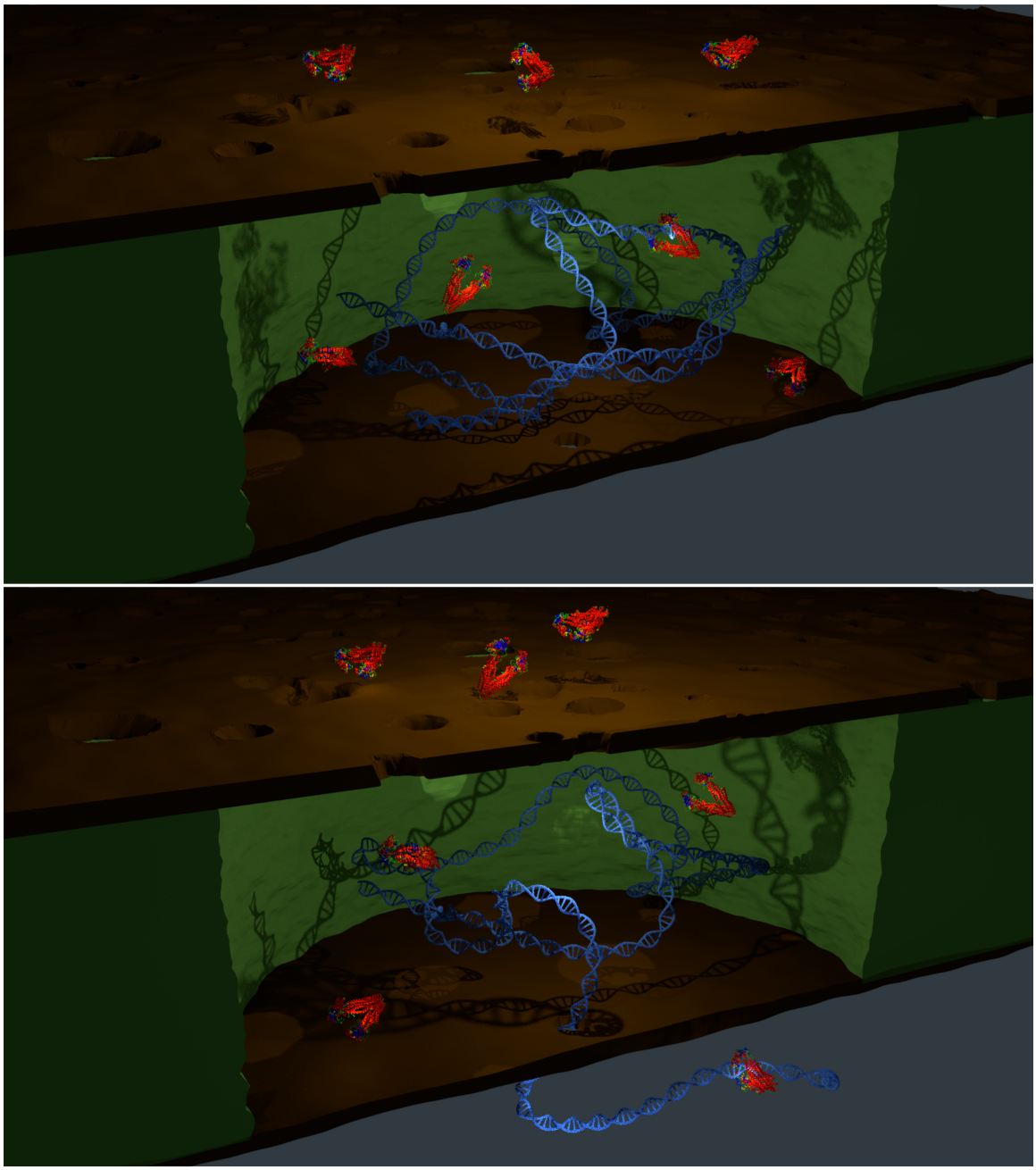

Figure 9.3: DNA that has been trapped in the cavity can be made to react with biomolecules such as methyl-binding protein (top) before recapture and analysis of the reaction products (bottom).

concentration measurements, consistent with theory work which shows that capture rate depends sensitively on pore geometry, a dependence which is lost when taking a

ratio of the capture rates of two species in the same pore[24].

The work presented in Chapter 6 in particular has given rise to a host of interesting projects regarding the kinetics of polymer translocation in confined environments. Among the many possible avenues of research to which the nanofiltered nanopore device could be applied, a few stand out as being particularly interesting given the open problems already discussed.

In collaboration with Simpore Inc. and the Univeristy of Rochester, a manuscript is being drafted which describes monolithic fabrication of the nanofiltered nanopore device on the wafer scale, obviating the need for manual assembly of complex nanofluidic devices and greatly speeding up the process of further exploring the novel translocation kinetics available to the serial nanopore device.

Folding suppression in DNA translocations through the nanofilter needs to be better understood and controlled, since being able to reliably suppress folding will greatly facilitate analysis of nanopore translocation results[23]. Recent work with neural networks has resulted in the development of analysis tools that can deconvolute folded translocation signals with attached tags[25], but a solution that simply removes the folding entirely at the source would obviate the need for extensive training of neural networks and would greatly simplify analysis.

The nanofiltered nanopore device can also be run in reverse as an entropic trap, pulling polymers through the sensing pore to trap polymers in the gap between the two membranes. While the field can drive polymers to escape through the filter, as long as the field can be removed faster than the polymer can transit the gap, the nanofilter will serve as an excellent entropic trap for any polymers with radius of gyration smaller than the nanofilter pore size. This could be used as a nanoreactor, pulling DNA or other target biomolecules into the gap to react with small molecules that diffuse in through the NPN. The reaction products could then be recaptured in order

to analyze the results of single biomolecular reactions one at a time, as illustrated in Figure 9.3. One can then not only study single molecules with a nanopore, but also study the kinetics of biomolecular reactions one at a time in an environment with a controlled degree of confinement. A manuscript is currently being prepared, driven mainly by Michelle Lam, a co-op student in the lab.

This entropic trap could also be used as a means to vary the level of confinement experienced by the polymer by changing the trap geometry, which would in turn provide a way to vary the Flory exponent for trapped polymers and serve as a sensitive method by which to test and compare the various competing models of polymer translocation kinetics on the single-molecule level. Similar entropic traps have been studied in the past[26], but the unique combination of high entropic cost of passing through the unbiased NPN makes this system a more stable long term trap, while the easy wetting of the cavity between the two membranes due to the high permeability of the NPN allows for more complex and more confining geometries to be explored than have previously been accessible.

As is clear from the sheer number of interesting questions to be explored by just the first novel nanodevice enabled by CBD nanopore fabrication, the completion of a thesis represents not so much having reached a conclusion as it does the acknowledgement that the rabbit hole is truly bottomless.

Acknowledgements

Chapter cover art: tricorderunbox4, from from Bobbie Johnson, licensed under the CC BY-SA 2.0.

Bibliography

[1] T. T. J. Morin, T. Shropshire, X. Liu, K. Briggs, C. Huynh, V. Tabard-Cossa, H. Wang, and W. W. B. Dunbar, "Nanopore-Based Target Sequence Detection.," *PLoS One*, vol. 11, no. 5, p. e0154426, 2016.

[2] E. C. Yusko, B. R. Bruhn, O. M. Eggenberger, J. Houghtaling, R. C. Rollings, N. C. Walsh, S. Nandivada, M. Pindrus, A. R. Hall, D. Sept, J. Li, D. S. Kalonia, and M. Mayer, "Real-time shape approximation and fingerprinting of single proteins using a nanopore," *Nature Nanotechnology*, vol. 12, no. 4, pp. 360–367, 2017.

[3] H. Bayley, "Nanopore sequencing: From imagination to reality," *Clinical Chemistry*, vol. 61, no. 1, pp. 25–31, 2015.

[4] M. van den Hout, A. R. Hall, M. Y. Wu, H. W. Zandbergen, C. Dekker, and N. H. Dekker, "Controlling nanopore size, shape and stability.," *Nanotechnology*, vol. 21, no. 11, p. 115304, 2010.

[5] J. Larkin, R. Henley, D. C. Bell, T. Cohen-Karni, J. K. Rosenstein, and M. Wanunu, "Slow DNA transport through nanopores in hafnium oxide membranes.," *ACS Nano*, vol. 7, pp. 10121–8, nov 2013.

[6] J. Feng, K. Liu, M. Graf, M. Lihter, R. D. Bulushev, D. Dumcenco, D. T. L. Alexander, D. Krasnozhon, T. Vuletic, A. Kis, and A. Radenovic, "Electrochemical reaction in single layer MoS2: Nanopores opened atom by atom," *Nano Letters*, vol. 15, no. 5, pp. 3431–3438, 2015.

[7] R. M. M. Smeets, U. F. Keyser, M. Y. Wu, N. H. Dekker, and C. Dekker, "Nanobubbles in solid-state nanopores," *Physical Review Letters*, vol. 97, no. 8, pp. 1–4, 2006.

[8] V. Tabard-Cossa, D. Trivedi, M. Wiggin, N. N. Jetha, and A. Marziali, "Noise analysis and reduction in solid-state nanopores," *Nanotechnology*, vol. 18, no. 30, p. 305505, 2007.

[9] C. E. Arcadia, C. C. Reyes, and J. K. Rosenstein, "In Situ Nanopore Fabrication and Single-Molecule Sensing with Microscale Liquid Contacts," *ACS Nano*, vol. 11, no. 5, pp. 4907–4915, 2017.

[10] R. Tahvildari, E. Beamish, K. Briggs, S. Chagnon-Lessard, A. N. Sohi, S. Han, B. Watts, V. Tabard-Cossa, and M. Godin, "Manipulating Electrical and Fluidic Access in Integrated Nanopore-Microfluidic Arrays Using Microvalves," *Small*, vol. 13, no. 10, pp. 1–7, 2017.

[11] R. Tahvildari, E. Beamish, V. Tabard-Cossa, and M. Godin, "Integrating nanopore sensors within microfluidic channel arrays using controlled breakdown," *Lab Chip*, vol. 15, no. 6, pp. 1407–1411, 2015.

[12] S. Shekar, D. J. Niedzwiecki, C. C. Chien, P. Ong, D. A. Fleischer, J. Lin, J. K. Rosenstein, M. Drndić, and K. L. Shepard, "Measurement of DNA translocation dynamics in a solid-state nanopore at 100 ns temporal resolution," *Nano Letters*, vol. 16, no. 7, pp. 4483–4489, 2016.

[13] T. Ikonen, A. Bhattacharya, T. Ala-Nissila, and W. Sung, "Unifying model of driven polymer translocation," *Physical Review E*, vol. 85, no. 5, pp. 1–7, 2012.
[14] T. Saito and T. Sakaue, "Dynamical diagram and scaling in polymer driven translocation," *European Physical Journal E*, vol. 34, no. 12, 2011.
[15] T. Sakaue, "Nonequilibrium dynamics of polymer translocation and straightening," *Physical Review E - Statistical, Nonlinear, and Soft Matter Physics*, vol. 76, no. 2, pp. 1–7, 2007.
[16] T. Sakaue, "Sucking genes into pores: Insight into driven translocation," *Physical Review E - Statistical, Nonlinear, and Soft Matter Physics*, vol. 81, no. 4, pp. 1–6, 2010.
[17] J. L. A. Dubbeldam, V. G. Rostiashvili, A. Milchev, and T. A. Vilgis, "Forced translocation of a polymer: Dynamical scaling versus molecular dynamics simulation," *Physical Review E - Statistical, Nonlinear, and Soft Matter Physics*, vol. 85, no. 4, pp. 1–12, 2012.
[18] C. Plesa, N. V. Loo, P. Ketterer, H. Dietz, and C. Dekker, "Velocity of DNA during translocation through a solid state nanopore," *Nano Letters*, vol. 15, no. 1, pp. 732–737, 2015.
[19] N. A. W. Bell and U. F. Keyser, "Digitally encoded DNA nanostructures for multiplexed , single-molecule protein sensing with nanopores," *Nature nanotechnology*, vol. 11, no. 7, pp. 1–28, 2016.
[20] A. Singer, M. Wanunu, W. Morrison, H. Kuhn, M. Frank-Kamenetskii, and A. Meller, "Nanopore based sequence specific detection of duplex DNA for genomic profiling," *Nano Letters*, vol. 10, no. 2, pp. 738–742, 2010.
[21] E. Atas, A. Singer, and A. Meller, "DNA sequencing and bar-coding using solid-state nanopores," *Electrophoresis*, vol. 33, no. 23, pp. 3437–3447, 2012.
[22] C. Plesa, J. W. Ruitenberg, M. J. Witteveen, and C. Dekker, "Detection of individual proteins bound along DNA using solid-state nanopores," *Nano Letters*, vol. 15, no. 5, pp. 3153–3158, 2015.
[23] K. Briggs, G. Madejski, M. Magill, K. Kastritis, H. W. De Haan, J. L. McGrath, and V. Tabard-Cossa, "DNA Translocations through Nanopores under Nanoscale Preconfinement," *Nano Letters*, vol. 18, no. 2, pp. 660–668, 2018.
[24] P. Rowghanian and A. Y. Grosberg, "Electrophoretic capture of a DNA chain into a nanopore," *Physical Review E*, vol. 87, no. 4, pp. 1–8, 2013.
[25] K. Misiunas, N. Ermann, and U. F. Keyser, "QuipuNet: convolutional neural network for single-molecule nanopore sensing," *ArXiv e-prints*, 2018.
[26] X. Liu, M. M. Skanata, and D. Stein, "Entropic cages for trapping DNA near a nanopore," *Nature Communications*, vol. 6, p. 6222, 2015.